

Some pages of this thesis may have been removed for copyright restrictions.

If you have discovered material in Aston Research Explorer which is unlawful e.g. breaches copyright, (either yours or that of a third party) or any other law, including but not limited to those relating to patent, trademark, confidentiality, data protection, obscenity, defamation, libel, then please read our [Takedown policy](#) and contact the service immediately (openaccess@aston.ac.uk)

**Development of novel Delivery systems for
nose-to-brain drug delivery**

SHITAL LUNGARE
Doctor of Philosophy

ASTON UNIVERSITY

June 2016

©Shital Lungare, 2016

Shital Lungare asserts his moral right to be identified as
the author of this thesis

This copy of the thesis has been supplied on condition that anyone who consults it is understood to recognise that its copyright rests with its author and that no quotation from the thesis and no information derived from it may be published without appropriate permission or acknowledgement.

Aston University
Development Of Novel Delivery Systems For Nose-To-Brain Drug Delivery

Shital Lungare

Doctor of philosophy
2016

Thesis Summary

The blood brain barrier (BBB) poses a significant hurdle to brain drug delivery. However, the location of the olfactory mucosa, within the nasal cavity, is a viable target site for direct nose-to-brain (N2B) delivery, thereby bypassing the BBB. To exploit this target site innovative nasal formulations are required for targeting and increasing residency within the olfactory mucosa. We developed and characterised three formulation systems for N2B delivery, (i) thermoresponsive mucoadhesion nasal gels sprays; (ii) mesoporous silica nanoparticles and (iii) nasal pMDI devices.

We developed an optimal mucoadhesive formulation system incorporating amantadine as a model, water-soluble anti-Parkinson's drug using carboxymethyl cellulose and chitosan as mucoadhesives. Formulations demonstrated droplet sizes of < 130 μ m and stability over 8-weeks when stored at refrigeration conditions with no significant cellular toxicity against olfactory bulb (OBGF400) and nasal epithelial (RPMI 2650) cells.

Mesoporous silica nanoparticles (MSNP) were prepared (~220nm) and demonstrated cellular uptake into OBGF400 within 2-hours of incubation with minimal toxicity. MSNP were loaded with two novel phytochemicals known to possess CNS activity, curcumin and chrysin, with loading efficiencies of ~12% confirmed through TGA, DSC and HPLC-UV analysis. Furthermore, a pH dependant release profile was identified with curcumin with greater release at nasal cavity pH 5.5 compared to pH 7.4. Furthermore, successful incorporation of MSNP into nasal gels was demonstrated through rheological studies with a decrease in $T_{sol-gel}$.

A pilot study was conducted to assess the feasibility of modified existing pulmonary pMDI to deliver diazepam intranasally, targeting the olfactory mucosa. Diazepam was formulated with HFA134a and using ethanol as a co-solvent, and demonstrated stability in formulation over 3 months. Deposition studies within a nasal cast model demonstrated 5-6% deposition onto the olfactory mucosa under optimal administration conditions in the absence of any nozzle attachments.

Our studies have provided a basis for the development to innovative intranasal formulation systems potentially capable of targeting the olfactory mucosa for both water soluble and poorly soluble drugs.

Key words: Olfactory, mucoadhesive, mesoporous silica nanoparticles, pMDI,

To

My wife Madhu, daughter Urvee

&

Ma, Aba, Amar, Didi, Padu Bhavaji, Deepu,

Shraddha, Premveer & Preetam.

Acknowledgements

Firstly, I would like to express my sincere gratitude to my supervisor Dr. Raj K Singh Badhan for his invaluable guidance, encouragement, constant support and patience throughout this journey for the past few years, especially during the writing of my thesis, thank you for everything.

I am thankful to my associate supervisor Dr James Bowen (Birmingham University, now Open University) for showing interest in my project, training & letting me use the Rheometer for my project. I would also like to thank Dr Gail Scherba (University of Illinois) for providing the neuronal cell lines for my project.

I must also like to thank all the lab technicians: Jit, Tom, Christine for providing all the lab and technical support throughout my project. Special thanks to Mike Davis for being such a kind person apart from his enormous help in the medicinal chemistry lab, unfortunately he is not with us today.

I would like to thank my only group colleague Manjit and other group colleagues/ fellow researchers Swapnil, Sameer, Ali, Craig, Amr, Eman, Affiong, Jas, Liz, Tom, Mandeep, Hamad, Ehsan, Floren, Pranav, Shibu for their direct or indirect help.

Thanks to ARCHA and Charlie for the training and letting us use their facility.

I would like to thanks Aston University for giving the bursary for this PhD.

I would like to thank Dr Keith Hallam for conducting the BET analysis

I would like to thank 3M Healthcare Ltd. for collaborating with Chapter 4 and providing assistance and materials.

Finally, I reserve my greatest expression of gratitude to my wife Madhu, who has always been there for me and my daughter Urvee and for tolerating my absence.

List of Publications

Peer Reviewed Articles

1. **Lungare, S.**, Hallam, K., & Badhan, R. K. S. (2016). Phytochemical-loaded mesoporous silica nanoparticles for nose-to-brain olfactory drug delivery. *International Journal of Pharmaceutics*, 513(1-2), 280-293.
2. **Lungare, S.**, Bowen, J. & Badhan, R. (2016). Development and Evaluation of a Novel Intranasal Spray for the Delivery of Amantadine. *J Pharm Sci*, 105, 1209-20.
3. Badhan RK, Kaur M, **Lungare S** and Obuobi S., (2014). Improving brain drug targeting through exploitation of the nose-to-brain route: a physiological and pharmacokinetic perspective. *Current Drug Delivery*.11 (4):458-71.

Abstracts

1. **Shital Lungare**, James Bowen and Raj K Singh Badhan, 2015. Development of drug delivery system to target the brain via olfactory route. LHS PG Research day, Aston University, Birmingham, UK.
2. **Shital Lungare**, James Bowen and Raj K Singh Badhan., 2014. Exploiting nose to brain delivery route using flavonoid loaded mesoporous nanoparticles. M5 Biomedical imaging conference, University of Nottingham, Nottingham, UK.
3. **Shital Lungare**, James Bowen and Raj k Singh Badhan., 2013. Overcoming Parkinson's disease: direct nose-to-brain delivery of amantadine. UKICRS. The University of Reading, Reading. UK.
4. **Shital Lungare**, James Bowen, Raj K Singh Badhan. 2014. Optimisation of Mesoporous nanoparticles for delivering flavonoids to the brain via olfactory route. APS Pharmasci University of Hertfordshire, Hatfield, UK.
5. **Shital Lungare**, James Bowen, Raj K Singh Badhan. 2015. Mesoporous nanoparticles for nose to brain drug delivery via olfactory route. 1st Annual Keele Nanopharmaceutics Symposium. Keele University, Keele, UK.

Table of Contents

Acknowledgements	4
List of Publications	5
Peer Reviewed Articles	5
<u>Chapter 1: Introduction</u>	18
1.1 Background	19
1.2 Blood-brain barriers: functional role in limiting CNS drug disposition	19
1.3 The nasal route as an administration route for CNS drug delivery	21
1.3.1 The nasal cavity anatomy and physiology	21
1.3.2 Nose-to-brain pathways	23
1.3.2.1 Olfactory pathways	24
1.3.2.2 Trigeminal nerve pathways	26
1.4 Pharmacokinetic aspects of nose-to-brain delivery	26
1.4.1 Absorption considerations	27
1.4.2 Distribution considerations	27
1.5 Olfactory delivery of macromolecules	29
1.6 Human studies demonstrating olfactory drug delivery	30
1.7 Formulation factors influencing olfactory drug delivery	32
1.7.1 Nasal solutions/sprays	33
1.7.2 Nasal Gels	34
1.7.3 Nanoparticulate drug carriers for olfactory drug delivery	39
1.7.4 Pressure metered dose inhaler	42
1.8 Novel CNS drug candidates: phytochemicals	43
1.9 Models for studying nasal drug delivery	46
1.9.1 Models for studying nasal drug delivery: <i>ex-vivo</i> models	46
1.9.2 Models for studying nasal drug delivery: cell culture models	46
1.10 Aims and Objectives	48
<u>Chapter 2: Development of thermosensitive mucoadhesive polymer hydrogel formulations for olfactory drug delivery</u>	50
2.1. Introduction	51
2.2. Aims and objectives	53
2.3. Materials and Methods	54
2.3.1. Materials	54
2.3.2. Formulation development	54
2.3.3. Assessment of sol-gel transition ($T_{sol-gel}$): visually	55
2.3.4. Assessment of formulation mucoadhesion	56
2.3.4.1. Texture analysis	56
2.3.4.2. Displacement method	57
2.3.5. Pre-column derivatisation of AMT and HPLC detection	58
2.3.6. Stability of formulations	59
2.3.7. Membrane-less release kinetics	60
2.3.8. Human nasal epithelial cell culture: RPMI 2650	61
2.3.8.1. Human nasal epithelial airway cell culture model	62
2.3.9. Porcine olfactory bulb neuroblastoma cell culture: OBG400	64
2.3.10. Formulation cellular viability: 3-(4,5-Dimethylthiazol-2-yl)-2,5-Diphenyltetrazolium Bromide (MTT) assay	65
2.3.11. AMT release and transport across an <i>in-vitro</i> human nasal epithelial cell culture model	66
2.3.12. Nasal spray systems: droplet size distribution	66
2.3.13. Nasal spray system: human nasal cast deposition	67
2.3.14. Statistical analysis	68
2.4 Results	69
2.4.1. Formulation development and optimisation	69
2.4.1.1. Optimisation of thermoresponsive polymer content	69
2.4.2. The impact of mucoadhesive polymers on formulation $T_{sol-gel}$.	72
2.4.3. Formulation characterisation	73

2.4.3.1.	Sol-gel transition ($T_{\text{sol-gel}}$) by rheology	73
2.4.3.2.	Assessment of formulation mucoadhesion: texture analysis	79
2.4.3.3.	Assessment of formulation mucoadhesion: displacement method	80
2.4.3.4.	Validation of a pre-column derivatisation method to detect AMT	81
2.4.3.5.	Human nasal epithelial cell culture model: MTT assay	85
2.4.3.6.	Porcine olfactory bulb cell culture model: MTT assay	87
2.4.3.7.	The development of a human nasal epithelial airway cell culture model	89
2.4.3.8.	Human nasal epithelial airway cell culture model: AMT transport	90
2.4.4.	Stability and AMT release from optimised formulations	91
2.4.5.	Nasal spray systems: droplet size distribution	97
2.4.5.1.	Nasal spray system: human nasal cast deposition	101
2.5.	Discussion	104
2.5.1.	Development of thermosensitive mucoadhesive hydrogel formulations	106
2.5.2.	Rheological assessment of thermosensitive formulations	109
2.5.3.	Evaluation of <i>in-vitro</i> mucoadhesion	112
2.5.4.	Cellular toxicity associated with formulation exposure	114
2.5.5.	AMT release and transport across a permeable insert model of the human nasal epithelia	115
2.5.6.	Stability and release of AMT from optimised formulations	117
2.5.7.	Nasal spray system	119
2.6.	Conclusion	122

Chapter 3: Development and characterisation of mesoporous nanoparticles for olfactory drug delivery 123

3.1.	Introduction	124
3.2.	Aims and objectives	128
3.3.	Materials and Methods	129
3.3.1.	Fluorescent bead uptake in porcine olfactory bulb neuroblastoma (OBGF400) cells	129
3.3.2.	Preparation of mesoporous nanoparticles (MSNP)	130
3.3.2.1.	Synthesis of MSNPs: template removal by calcination (Gul-MSNP)	130
3.3.2.2.	Synthesis of MSNPs: charged template approach (Pro-2-MSNPs)	131
3.3.2.3.	Synthesis of MSNPs: template removal by refluxing (Fan-MSNPs)	131
3.3.3.	Assessment of MSNP particle size distribution and zeta-potential (ζ)	131
3.3.4.	Scanning electron microscopy based assessment of the morphology of MSNP	132
3.3.5.	Porosity assessments using nitrogen adsorption/desorption isotherm analysis	132
3.3.6.	Thermogravimetric analysis (TGA) of MSNP	132
3.3.7.	Loading of fluorescein isothiocyanate (FITC) and targeting to OBGF400	133
3.3.8.	Differential scanning calorimetry (DSC)	134
3.3.9.	Fourier transform infrared (FT-IR)	134
3.3.10.	HPLC analytical detection of curcumin	134
3.3.11.	HPLC method for chrysin	135
3.3.12.	Toxicity of MSNP towards olfactory cells	135
3.3.13.	Cellular toxicity of phytochemicals	136
3.3.14.	Live cell imaging: Cell-IQ [®]	136
3.3.15.	Phytochemical loading of MSNP Drug loading	136
3.3.16.	<i>In-vitro</i> drug release studies	137
3.3.17.	Incorporation of Fan-MSNP into thermoresponsive nasal gel systems	138
3.3.18.	Statistical analysis	138
3.4.	Results	139
3.4.1.	Fluorescent bead uptake	139
3.4.2.	Synthesis and characterisation of MSNP	141
3.4.2.1.	Scanning electron microscopy based assessment of the morphology of MSNP	141
3.4.2.2.	Surface porosity of MSNP using nitrogen adsorption-desorption studies	145
3.4.2.3.	FTIR assessment of MSNP	147

3.4.3.	FITC loading of MSNPs for cellular uptake studies	150
3.4.4.	FITC release from Fan-MSNPs	150
3.4.5.	Cellular uptake of FITC-Fan-MSNPs	151
3.4.6.	Phytochemical loading of Fan-MSNPs	155
3.4.7.	HPLC-UV detection of curcumin	165
3.4.8.	HPLC-UV detection of chrysin	169
3.4.9.	Cytotoxicity study	173
3.4.10.	Cellular toxicity of MSNP: live-cell time-lapse phase-contrast microscopy	176
3.4.11.	Drug release study from the mesoporous silica nanoparticles	180
3.4.12.	Incorporation of Fan-MSNPs into thermoresponsive nasal gel	182
3.5.	Discussion	190
3.5.1.	Target MSNP size range for olfactory uptake	191
3.5.2.	Formulation of MSNP	192
3.5.3.	Surface porosity and pore size determination	193
3.5.4.	FT-IR assessment of Fan-MSNPs	194
3.5.5.	FITC loading and release in Fan-MSNPs	195
3.5.6.	FITC-MSNPs cellular uptake	195
3.5.7.	Phytochemical loading into Fan-MSNPs	196
3.5.8.	HPLC-UV detection of phytochemicals	199
3.5.9.	Cellular toxicity of MSNP	200
3.5.10.	Phytochemical release from MSNP	202
3.5.10.1.	Curcumin	202
3.5.10.2.	Chrysin	206
3.5.11.	Incorporation of Fan-MSNPs into the thermoresponsive nasal gel	206
3.6.	Conclusion	208

Chapter 4: Adaptation of a pMDI spray device for targeted delivery onto the olfactory mucosa: a feasibility study 209

4.1.	Introduction	210
4.2.	Aims and objectives	212
4.3.	Materials and Methods	213
4.3.1.	Materials	213
4.3.2.	Assessment of diazepam solubility in ethanol	213
4.3.3.	Assessment of diazepam solubility in propellant	213
4.3.4.	HPLC-UV detection of diazepam	214
4.3.5.	Canister stability studies	214
4.3.6.	Nasal pMDI spray: droplet size distribution	215
4.3.7.	Nasal pMDI spray deposition within a nasal cast model: brilliant blue visualisation	216
4.3.8.	Nasal pMDI spray deposition within a nasal cast model: diazepam localisation	218
4.3.9.	Cellular toxicity of diazepam	218
4.4.	Results	219
4.4.1.	Assessment of diazepam solubility in ethanol	219
4.4.2.	Assessment of diazepam solubility in propellant	219
4.4.3.	HPLC-UV detection of diazepam	220
4.4.4.	Canister stability studies	223
4.4.5.	Nasal pMDI spray: droplet size distribution	224
4.4.6.	Nasal pMDI spray deposition within a nasal cast model: brilliant blue visualisation	225
4.4.7.	Diazepam deposition in a nasal cast model	228
4.4.8.	Cellular toxicity of diazepam	229
4.5.	Discussion	231
4.6.	Conclusion	235

Chapter 5: Conclusion 236

List of Figures

Figure 1-1: The blood-brain barrier (BBB) is formed from brain microvascular endothelial cells, astrocytes and pericytes (Chen and Liu, 2012).20

Figure 1-2: Anatomy and histology of human nasal cavity (Pires et al., 2009).....22

Figure 1-3: Drug transfer routes to the brain, adapted from (Chen et al., 2016).24

Figure 1-4: Olfactory area showing epithelium, bulb and tract (Mistry et al., 2009).25

Figure 1-5: Nasal (solution) formulation.33

Figure 1-6: Chemical structure of widely used thermoresponsive polymers36

Figure 1-7: The gelation of poloxamer 407 in water37

Figure 1-8: Schematic representation of mesoporous silica nanoparticles. Taken from(Yuan *et al.*, 2011).41

Figure 1-9: Stöber reaction for preparation of mesoporous silica nanoparticles {Yan, 2014 #814}.42

Figure 1-10: Example of pMDI systems used for pulmonary and nasal (olfactory) drug delivery.43

Figure 1-11: The structure of flavonoid (Heim et al., 2002).44

Figure 2-1: Tensile strength apparatus57

Figure 2-2: Displacement measurement apparatus.....58

Figure 2-3: Fmoc reaction and complex formation with amines (Bahrami and Mohammadi, 2007)...59

Figure 2-4: Morphology of RPMI 2650 cells.....62

Figure 2-5: Morphology of OBGf400 cells.....65

Figure 2-6: Assessment of nasal deposition in a human nasal cast model using a multidose nasal spray.....68

Figure 2-7: Impact of differing heating rates on FCMC temperature sweep properties.....74

Figure 2-8: Temperature sweep of AMT containing formulations76

Figure 2-9: Time sweep of AMT containing formulations.....77

Figure 2-10: Steady shear behaviour of AMT containing formulations78

Figure 2-11: Assessment of formulation mucoadhesion through tensile strength measurements80

Figure 2-12: Assessment of formulation mucoadhesion through displacement measurements81

Figure 2-13: HPLC chromatogram of derivatised amantadine at retention time 4.911 min.....82

Figure 2-14: Linearity plot for a AMT pre-column derivatisation method85

Figure 2-15: Cellular toxicity of amantadine (A), CMC (B), PEG4000 (C), F127 (D) and CS (E) on RPMI-2650 cells.	86
Figure 2-16: Cellular toxicity of amantadine (A), CMC (B), PEG4000 (C), F127 (D) and CS (E) on OBGF400.	88
Figure 2-17: Monolayer resistance of RPMI 2650 cells grown on permeable inserts.	89
Figure 2-18: Release and transport of AMT from formulations.....	90
Figure 2-19: Amantadine cumulative% release for optimised formulations at week 0 and stored at 4°C, (A) FCMC; (B) FCS and (C) FPEG	92
Figure 2-20: Amantadine cumulative % release for optimised formulations at week 1 and stored at 4°C, (A) FCMC; (B) FCS and (C) FPEG	93
Figure 2-21: Amantadine cumulative % release for optimised formulations at week 8 and stored at 4°C, (A) FCMC; (B) FCS.	94
Figure 2-22: Amantadine cumulative % release for FCS at week 1 and 2 stored at 25°C.	95
Figure 2-23: Nasal spray droplet size distribution graph for FPEG	98
Figure 2-24: Nasal spray droplet size distribution graph for FCS.	99
Figure 2-25: Nasal spray droplet size distribution graph for FCMC.....	100
Figure 2-26: Representative nasal deposition patterns of FCS.	102
Figure 2-27: Representative nasal deposition patterns of FCMC.....	103
Figure 3-1: Cellular uptake of fluorescent latex beads in OBGF400	140
Figure 3-2: Scanning electron micrograph of Gul-MSNP.....	142
Figure 3-3: Scanning electron micrograph of Pro 2 MSNP.....	143
Figure 3-4: Scanning electron micrograph of Fan-MSNP.....	144
Figure 3-5: Nitrogen adsorption/desorption isotherms of Fan-MSNP.....	146
Figure 3-6: BJH pore radius distribution of Fan-MSNP.....	146
Figure 3-7: BJH pore width distribution of Fan-MSNP.	147
Figure 3-8: FT-IR spectra of Fan-MSNP.	148
Figure 3-9: FT-IR spectra of Fan-MSNP prior to CTAB removal (green) and immediately after CTAB removal (red).	149
Figure 3-10: FT-IR spectra of FITC-MSNP	150
Figure 3-11: Release of FITC from FITC-MSNP.....	151
Figure 3-12: Cellular localisation of FITC-MSNP	152
Figure 3-13: z-dimension cellular localisation of FITC-MSNP (stage 1)	153

Figure 3-14: z-dimension cellular localisation of FITC-MSNPs (stage 2)	154
Figure 3-15: FTIR spectra of (A) Fan-MSNPs; (B) and (C) Curc-MSNPs	156
Figure 3-16: DSC thermograms of curcumin, Fan-MSNPs and Curc-MSNPs	157
Figure 3-17: TGA thermograms of curcumin, Fan-MSNPs and Curc-MSNPs	158
Figure 3-18: Fan-MSNPs size and PDI before and after loading with curcumin	159
Figure 3-19: Fan-MSNPs zeta potential before and after loading of flavonoid curcumin	160
Figure 3-20: FTIR spectra of chrysin, blank MSNPs and Chry-MSNPs	161
Figure 3-21: DSC thermograms of chrysin, Fan-MSNPs and Chry-MSNPs	162
Figure 3-22: TGA thermograms of chrysin, Fan-MSNPs and Chry-MSNPs	163
Figure 3-23: Fan-MSNPs size and PDI before and after loading with chrysin	164
Figure 3-24: Zeta potential before and after loading of flavonoid chrysin.....	165
Figure 3-25: HPLC chromatogram of curcumin	166
Figure 3-26: Linearity plot for curcumin.....	169
Figure 3-27: Chrysin HPLC chromatogram.....	170
Figure 3-28: Linearity plot for chrysin.....	173
Figure 3-29: Cellular toxicity of Fan-MSNPs on OBG400 cells.	174
Figure 3-30: Cellular toxicity of curcumin on OBG400 cells	175
Figure 3-31: Cellular toxicity of chrysin on OBG400 cells.....	175
Figure 3-32: Cell-IQ live cell imaging of OBG400 cells (top) and Fan-MSNPs at 150µg/mL (middle) and 50µg/mL (bottom).	177
Figure 3-33: Cell-IQ live cell imaging of OBG400 cells (top) and Chry-MSNPs at 150µg/mL (middle) and 50µg/mL (bottom).	178
Figure 3-34: Cell-IQ live cell imaging of OBG400 cells (top), Curc-MSNPs at 150µg/mL (middle) and 50µg/mL (bottom).	179
Figure 3-35: Cumulative percentage release of curcumin from Curc-MSNPs.....	180
Figure 3-36: Cumulative percentage release of chrysin from Chry-MSNPs.....	181
Figure 3-37: Temperature sweep of FCMC following incorporation of Fan-MSNPs	183
Figure 3-38: Temperature sweep of FCS following Incorporation of Fan-MSNPs.	184
Figure 3-39: Temperature sweep of FPEG following Incorporation of Fan-MSNPs.....	185
Figure 3-40: Steady shear behaviour of FCMC incorporating Fan-MSNPs.	187
Figure 3-41: Steady shear behaviour of FCS incorporating Fan-MSNPs.....	188

Figure 3-42: Steady shear behaviour of FPEG incorporating of Fan-MSNP.	189
Figure 3-43: Chemical structures of (A) curcumin, (B) demethoxycurcumin and (C) and bisdemethoxycurcumin.....	200
Figure 3-44: Curcumin degradation products	203
Figure 3-45: HPLC-UV chromatogram of curcumin at pH 7.4.	204
Figure 3-46: HPLC-UV chromatogram of curcumin at pH 5.5.	205
Figure 4-1: A pressured metered dose inhaler (Lavorini, 2013).	211
Figure 4-2: The 3M fabricated nasal pMDI actuator (termed the 'Aardvark' system).	215
Figure 4-3: Spray angle used within the nasal pMDI actuators.	216
Figure 4-4: Nozzle attachments	217
Figure 4-5: Stability of diazepam formulated in 5% or 10% w/w ethanol and HF134a following 3-week storage.....	219
Figure 4-6: Diazepam HPLC chromatogram.....	220
Figure 4-7: Linearity plot for diazepam.....	223
Figure 4-8: Diazepam content assay of 5 and 10% w/w ethanol canisters.	224
Figure 4-9: Spray particle size distribution.	225
Figure 4-10: Nasal cast deposition of BB pMDI under static and dynamic airflow.	226
Figure 4-11: Nasal cast deposition of BB pMDI under static air flow and with the 'short' and 'long' nozzle attachments.	227
Figure 4-12: Olfactory deposition of diazepam.	229
Figure 4-13: Cellular toxicity of diazepam on OBGF400 cells.	230

List of Tables

Table 2-1: Impact of PF127 on $T_{\text{sol-gel}}$, indicating the inverse relationship between concentration and $T_{\text{sol-gel}}$ in Pluronic only formulations.	69
Table 2-2: Effect of addition of amantadine and excipients on gelation temperature	70
Table 2-3: Effect of addition of CMC on gelation temperature	70
Table 2-4: Effect of addition of amantadine on gelation temperature	71
Table 2-5: Effect of Increase in PF127 content on gelation temperature.....	71
Table 2-6: Optimised formulation based on CMC as mucoadhesive	72
Table 2-7: Impact of mucoadhesive polymers on formulation gelation	72
Table 2-8: Power law rheological analysis of AMT at ambient and nasal temperatures.....	79
Table 2-9: System precision assessment for AMT pre-column derivitisation method.....	83
Table 2-10: Method precision assessment for AMT pre-column derivitisation method.....	84
Table 2-11: Drug release kinetics analysis of formulations stored at refrigerated (4°C) and ambient (25°C) temperature for up to 8 weeks.	96
Table 2-12: Laser diffraction particle size analysis.....	97
Table 3-1: Particle size and zeta-potential of different MSNPs.....	141
Table 3-2: Nitrogen adsorption desorption data for Fan-MSNPs	145
Table 3-3: System precision assessment for curcumin HPLC-UV detection	167
Table 3-4: Method precision assessment for curcumin.....	168
Table 3-5: System precision assessment for chrysin HPLC-UV detection	171
Table 3-6: Method precision assessment for chrysin	172
Table 4-1: pMDI canister composition	214
Table 4-2: Dimensions of nozzle attachments	217
Table 4-3: System precision assessment for diazepam.....	221
Table 4-4: Method precision assessment for diazepam.....	222

List of abbreviations

AD	Alzheimer's disease
AEP	Auditory-evoked brain potentials
ALI	air liquid interface
AMT	Amantadine
ANE	Artificial nasal electrolyte solution
ANOVA	Analysis of variance
API	Active pharmaceutical ingredient
AUC	Area under the curve
BB	Brilliant blue
BBB	Blood brain barrier
BCRP	Breast cancer resistance protein
BCS	Biopharmaceutical classification system
BCS	Bovine calf serum
BCSFB	Blood cerebrospinal fluid barrier
BLK	Benzalkonium chloride
CBF	Ciliary beat frequency
Chry-MSNP	Crysin loaded MSNP
CNS	Central nervous system
CO ₂	Carbon dioxide
CS	Chitosan
CSF	Cerebrospinal fluid
CST	Critical solution temperature
CTAB	Cetyltrimethylammonium bromide

Curc-MSNP	Curcumin loaded MSNP
DFT	density functional theory
DMEM	Dulbecco's Modified Eagle Medium
DMEM-F12	Dulbecco's Modified Eagle Medium: Nutrient Mixture F12
DMF	Dimethylformamide
DMSO	Dimethylsulphoxide
DSC	Differential scanning calorimetry
DUSA	Dosage unit sampling apparatus
DZP	Diazepam
EE	Entrapment efficiency
Fan-MSNP	Fan method Mesoporous Nanoparticles
FBS	Foetal bovine serum
FDA	US Food and Drug Administration
FITC	Fluorescein isothiocyanate- Dextran
FMOOC	9-Fluorenylmethyl chloroformate
FTIR	Fourier transform infrared
HBSS	Hank's Balanced Salt Solution
HEPES	4-(2-hydroxyethyl)-1-piperazineethanesulfonic acid
HFA	Hydrofluroalkanes
HPC	Hydroxypropyl cellulose
HPLC	High performance liquid chromatography
HPMC	Hydroxypropyl methylcellulose
HRP	Horseradish peroxidase
IGF-1	Insulin like growth factor-1
IN	Intra-nasal
LC	loading content

LCST	Low critical solution temperature
LOB	Left olfactory bulb
LOD	Limit of detection
LOQ	Limit of quantification
LY	Lucifer yellow
MCC	Mucocilliary clearance
MCI	Mild cognitive impairment
ME	Microemulsion
MEM	Eagle's minimal essential medium
MSNP	Mesoporous nanoparticles
MTB	Sodium metabisulphate
MTT	3-(4, 5-dimethylthiazol-2-yl)-2,5-diphenyl tetrazolium bromide
Na CMC	Sodium carboxymethyl cellulose
NEAA	Non-essential amino acid
NP	nanoparticles
OB	Olfactory bulb
OE	olfactory epithelium
OEC	olfactory ensheathing cells
ORN	olfactory receptor neurons
PAA	poly (acrylic acid)
PBS	posphate buffered saline
PD	Parkinson's disease
PDI	Polydispersity index
PEG	Polyethylene glycol
PEO	Poly (ethylene oxide)
PF127	Pluronic F127

PHE	Phenylephrine
pMDI	Pressurised meter dose inhaler
PNIPAAm	Poly (N-isopropyleacrylamide)
PPO	Poly (propylene oxide)
PVP	Polyvinylpyrrolidone
QS	Quantity sufficient
RCF	Relative centrifugal force
RH	Relative humidity
ROB	right olfactory bulb
RPM	Revolutions per minute
RT	Room temperature
SD	Standard deviation
SEM	Scanning electron microscopy
SFM	Serum free media
TEER	Transendothelial electrical resistance
TEOS	Tetraethoxysilane
TGA	Thermogravimetric analysis
TJ	Tight junction
UCST	Upper critical solution temperature
UV	Ultraviolet
WGA-HRP	Wheatgerm agglutin-horseraddish peroxidase
WHO	World Health Organisation

Chapter 1

Introduction

1.1 Background

The World Health Organisation (WHO) have highlighted that neurological disorders are one of the biggest threats to public health (WHO, 2006). Furthermore with an increasingly ageing population, by the year 2020 one in every three people alive will suffer from a central nervous system (CNS) related disorders (WHO, 2006). Disorders of the CNS account for approximately 1% of deaths but this is associated with a worldwide disease burden of almost 11%, and it is thought that approximately 1.5 billion people worldwide suffer from some kind of brain or CNS disorder. Less than 8% of CNS-indicated drugs successfully enter clinical trials and this has been accompanied by an overall drop in the success rate of delivering a candidate to market (Kola and Landis, 2004), with the US Food and Drug Administration (FDA) only approving between 15-25 new compounds per year (Kola and Landis, 2004).

Despite advances in drug delivery technologies, CNS drug targeting and delivery is still a limiting factor with less than 1% of all CNS-targeted compounds showing activity against CNS diseases (Pardridge, 2005, Lipinski, 2000). This is despite many of these compounds possessing physicochemical properties that would normally predispose them to good membrane permeability (e.g, molecular weight < 500 and highly lipid soluble) (Pardridge, 1998).

Blood-brain barriers: functional role in limiting CNS drug disposition

The brain is a very highly vascularised organ with a microvascular surface area of 150-200cm² g. tissue (12-18m²) in humans (Abbott and Romero, 1996). However, the primary cause of poor brain disposition of therapeutics is often associated with highly selective barrier termed as the blood-brain barrier (BBB), formed from brain microvascular endothelial cells which are highly selective in controlling the entry of endogenous and exogenous compounds into the brain (Figure 1-1).



Figure 1-1: The blood-brain barrier (BBB) is formed from brain microvascular endothelial cells, astrocytes and pericytes (Chen and Liu, 2012).

The three key features of the BBB which specifically govern and restrict passage of therapeutic drugs are: 1) an extensive network of tight junction (TJ) proteins limiting the transfer of molecules between endothelial cells; 2) Limited transcellular transport of molecules due to a lack of fenestrations and limited transcytosis; 3) An extensive network of membrane drug transporter proteins which hinder molecular trafficking across the BBB but also provide a mechanism to deliver or remove required substances such as amino acids and glucose into the brain (Dauchy *et al.*, 2008, Dutheil *et al.*, 2010).

Conventional drug therapy targeting the CNS has largely failed to yield successful results, and this is thought to be a result of the impermeable nature of the BBB in hindering molecular flux, and hence limiting the extent to which therapeutic agents can accumulate within the brain biophase before yielding a clinical response (Pardridge, 2012, Pardridge, 2010, Pardridge, 2007a, Pardridge, 2007c, Pardridge, 2005, Neuwelt *et al.*, 2008, Abbott *et al.*, 2010a).

1.2 The nasal route as an administration route for CNS drug delivery

Although the nasal route has traditionally been used to treat local symptoms, many studies have demonstrated the systemic delivery of therapeutic agents through intranasal (IN) drug delivery. A major advantage of the nasal route is the highly perfused nature of the nasal cavity which allows the rapid systemic delivery of drug, and which further offers the ability to bypass first-pass metabolism and extraction of drugs, posing as an attractive route for drugs otherwise delivered through parenteral or oral routes (Illum, 2012, Bitter *et al.*, 2011). The first recorded success in the delivery of a therapeutic agent into the brain in humans, following IN administration, was in a patent application by William Frey II (Frey, 1997a),(Frey, 1997b) reporting the successful delivery of neurological agents and macromolecules (insulin) (Frey, 2001) targeting Alzheimer's disease. These reports established a novel approach to target CNS drug delivery through potentially bypassing the BBB.

1.2.1 The nasal cavity anatomy and physiology

The surface area of the human nasal cavity is approximately 150cm² with a total volume of 15-20mL (Morrison and Costanzo, 1992). The primary function of the nasal cavity is respiration and olfaction, and is divided into two symmetrical halves with each half further divided into four areas termed the vestibules, atrium, respiratory region and olfactory region (Figure 1-2).



Figure 1-2: Anatomy and histology of human nasal cavity (Pires et al., 2009).

Nasal vestibule: the nasal vestibules cover an area of approximately 0.6cm^2 and forms part of the anterior area of the nasal cavity (Figure 1-2). The vestibules are formed from stratified squamous and keratinised epithelium and sebaceous glands, and the absorption of drugs is difficult.

Atrium: the area close to vestibules is comprised of stratified squamous epithelium whereas the area close to respiratory region has pseudostratified columnar cells with microvilli.

Respiratory region: this is the largest region within the nasal cavity and is the primary target for systemic drug delivery (Figure 1-2). It is divided into the superior, middle and inferior turbinates which project from the lateral wall. A range of cell types are present here and include

pseudostratified columnar epithelial cells, goblet cells, basal cells, mucous and serous glands. Basal cells are thought to provide a source of stem cells for the replenishing of olfactory or supporting cell structure within the nasal region (Mackay-Sim and Kittel, 1991, Leung *et al.*, 2007, Carter *et al.*, 2004). Furthermore, the nasal epithelium in this region has a thick layer of mucous which is secreted by secretory glands and goblet cells. This secreted mucus is high in water content (95%) and contains a variety of electrolytes, proteins, lipids, enzymes, antibodies, bacterial products and the specific glycoprotein mucin (Pires *et al.*, 2009).

Olfactory Region: this regions covers the upper part of the nasal cavity with an approximate surface area of 2.5-10cm² in humans (Figure 1-2) (Gizurason, 2012). It is primarily comprised of approximately 12 million olfactory receptor cells (Purves, 2007) and is the only known part of the CNS which is in direct contact with the external environment (Illum, 2000, Pires *et al.*, 2009). The olfactory mucosa is a pseudostratified columnar epithelium made up of supporting cells, basal cells, microvillar cells and olfactory or receptor cells (Morrison and Costanzo, 1990a). The olfacotry region has been the focus of one of the major 'nose-to-brain' pathways to deliver drugs directly to the brain through olfacotry deposition.

1.2.2 Nose-to-brain pathways

Following the IN administration of drug, entry into the brain and CNS primarily occurs through either the olfactory or trigeminal nerve pathways (Illum, 2000), and to a lesser extent by diffusion into the cerebrospinal fluid (CSF) and lymphatic circulations (Dhuria *et al.*, 2010) (Figure 1-3).

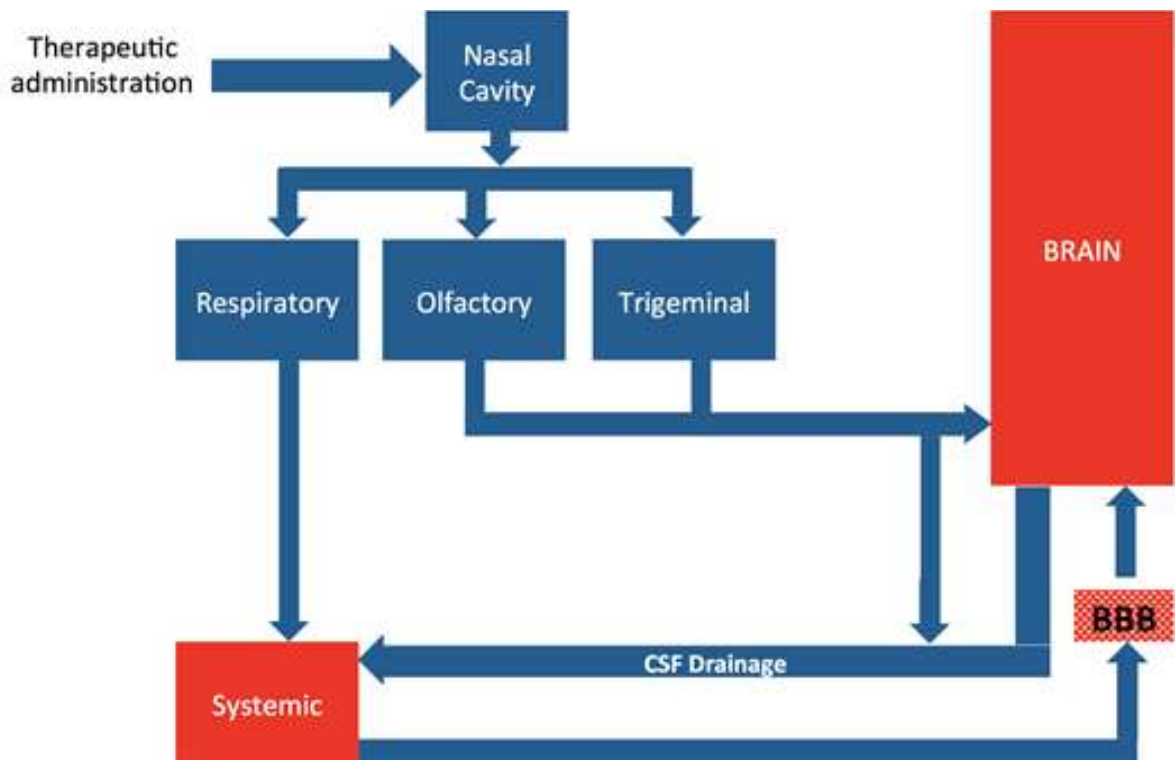


Figure 1-3: Drug transfer routes to the brain, adapted from (Chen et al., 2016).

Following therapeutic administration into the nasal cavity, compounds may enter the brain and CNS through at least three possible mechanisms: (i) nasal respiratory epithelia-leading to systemic absorption and brain deposition; (ii) delivery onto the olfactory epithelium leading to olfactory transfer into the olfactory bulb and diffusion into the brain parenchyma; (iii) delivery into the trigeminal network and transfer into the brain

1.2.2.1 Olfactory pathways

The olfactory region of the nasal cavity consists of olfactory receptor neurons (ORNs) which are responsible for providing information associated with olfaction (smell) from the external environment into the CNS (Figure 1-4).

Beneath the olfactory epithelium lies the lamina propria which contains mucus secreting Bowman's glands, axons, blood vessels, lymphatic vessels and connective tissues. Dendrites associated with the ORNs extend into the mucus layer of the olfactory epithelium, and the axons of ORN pass through the lamina propria through the gaps in cribriform plate and ethmoid bone of the skull (Figure 1-4) before terminating in the olfactory bulb (Djupesland, 2013, Leopold *et al.*, 2000, Feron *et al.*, 1998).



Figure 1-4: Olfactory area showing epithelium, bulb and tract (Mistry et al., 2009).

The transfer of therapeutic molecules to the olfactory bulb begins at the olfactory receptor neurons, whose endogenous function is to process olfaction signals to the brain in response to odorant stimulation. Therapeutic molecules are thought to be able to be endocytosed into olfactory receptor neurons (ORN) or permeate through the olfactory epithelium and travel along intracellular or extracellular (perineural) pathways towards the olfactory bulb.

The olfactory nerve pathway provides a non-invasive route to obtain CNS drug delivery and was demonstrated in studies using fluorescent tracers which were tracked as they passed through the olfactory nerves, the cribriform plate and finally within the olfactory bulb (OB) (Lochhead and Thorne, 2012, Renner *et al.*, 2012). The process of movement through these routes are thought to occur either because of intracellular or extracellular mechanisms. Fast extracellular movement (typically within 30 minutes) from the nasal epithelium to the CNS is likely to occur as a result of channels created by the olfactory ensheathing cells (OEC) (Thorne *et al.*, 2004). Balin *et al.* (1986) observed that IN administered native horseradish peroxidase reached the OB of rats and squirrel monkeys extracellularly within 45-90min. Intracellular transport involves passive diffusion, receptor mediated endocytosis or adsorptive endocytosis

by which the molecules are taken up into ORNs and then axonal transport taking hours to days to take these molecules to different regions of the brain (van Woensel *et al.*, 2013).

1.2.2.2 Trigeminal nerve pathways

The trigeminal nerves have been somewhat less investigated as a route for nose to brain delivery. Trigeminal nerves are located within the nasal epithelia respiratory region and the olfactory epithelium and passes through to the CNS through the pons with some contact with the olfactory bulb (Chapman *et al.*, 2012, Dhuria *et al.*, 2010).

1.3 Pharmacokinetic aspects of nose-to-brain delivery

There is an increasing interest in exploiting the physiology of the nasal cavity and the olfactory pathway route to gain access to the CNS for small-molecular weight compounds. A key advantage of any IN route of administration is the ability to overcome hepatic metabolic clearance and first pass metabolism, which hinders the bioavailability of many orally administered drugs. In addition, because of this bypassing effect the doses required to achieve comparable clinical outcomes is lower and hence reduces the burden of systemic and central adverse drug reactions.

Demonstration of 'nose-to-brain' delivery has been widely conducted in rodents, however it is important to highlight that the olfactory region in rodents (13-15cm²) (Gross *et al.*, 1982) is larger and more accessible than that found in humans (2-10cm²) (Morrison and Costanzo, 1990b) although the total number of olfactory receptor cells are thought to be similar (15 million and 12 million, respectively). Furthermore, the transport rates of particles interacting with the olfactory epithelia is approximately 14mm/min in both species (Gizurason, 1990). Thus, despite some differences between humans and rodents, the anatomical similarities would suggest that the rat model is a reasonable model for drug delivery studies.

1.3.1 Absorption considerations

A major challenge to CNS disposition is the targeted delivery of drug at the olfactory mucosa rather than the entire nasal mucosa. The challenges lie in the fact that the nasal mucosa covers most of the nasal surface area with the olfactory mucosa being posterior in the nasal cavity, posing difficulties from a formulation/delivery perspective.

The vascularized nature of the olfactory and nasal mucosa would suggest that small molecular weight and highly lipophilic compounds are expected to preferentially be absorbed (Illum, 2003). However, as with drug absorption at other absorption sites within the body, larger molecular weight compounds (> 500Da) show limited membrane permeation (McMartin *et al.*, 1987). An added difficulty is the fact that membrane localized xenobiotic transporter proteins at the olfactory bulb and olfactory epithelial may provide a further 'barrier', in a similar way to their expression at the BBB, and thereby potentially limiting the ability of drug substrate of these membrane transporters from utilizing efficient olfactory transport (Thiebaud *et al.*, 2011, Molinas *et al.*, 2012, Manzini and Schild, 2003, Kandimalla and Donovan, 2005, Graff and Pollack, 2005, Bauer *et al.*, 2010).

1.3.2 Distribution considerations

Assuming a drug has been delivered sufficiently high enough into the nasal cavity to deposit onto the olfactory mucosa, two specific pathways exist for the subsequent delivery of drug to the brain, namely axonal transport and epithelial pathways (Shi and Pardridge, 2000). Axonal transport pathways are slow mechanisms involving endocytic movement into the neurons and ante-retrograde transport to transverse along olfactory neurons to the OB and brain, with typical distribution rates of 0.1 to 400mm/day (Vallee and Bloom, 1991). This has been demonstrated with dopamine where concentrations were found to reach a peak in the olfactory bulb 4 hours post dosing in mice (Dahlin *et al.*, 2000)

Epithelial pathways are faster and drugs pass paracellularly across the olfactory epithelium (OE) perineural spaces, followed by diffusion into the brain tissue. This rapid transfer has been

demonstrated for cocaine and benzoylecgonine following IN administration to rats with peak concentrations attained within 10–15 minutes post-dosing (Chow *et al.*, 1999, Chow *et al.*, 2001). The rapid brain delivery of the centrally acting acetylcholinesterase inhibitor tacrine was reported in both mice and rabbits following IN administration (Jogani *et al.*, 2007). Biodistribution studies in BALB/c mice, using radiolabeled tacrine, showed brain distribution to be more rapid following IN administration ($t_{max}=60$ minutes) when compared to IV administration ($t_{max}=120$ minutes). In addition the brain:blood ratio of tacrine and brain tacrine concentrations were reported to be higher at all time points during the experiment following IN administration (Jogani *et al.*, 2007).

More direct evidence of the use of olfactory pathways for drug absorption has been demonstrated with morphine, Westin *et al.* (Westin *et al.*, 2005, Westin *et al.*, 2006b) quantified right olfactory bulb (ROB) morphine disposition following right-sided nasal administration as a marker for olfactory deposition and CNS delivery, and used the left olfactory bulb (LOB) as a control for systemic distribution. They reported that levels of morphine in the ROB were significantly higher than those in the LOB following IN administration with similar levels in both olfactory bulbs and in the rest of the brain following IV administration. Furthermore, the appearance of morphine in the ROB was rapid and detected in a 5-minute autoradiogram, however clear species differences in peak levels were reported in mice (60 minutes) and rats (15 minutes).

This rapid appearance of morphine in the olfactory bulbs was further quantified in rats at 5- and 15-minute time points following IN and IV administration of morphine (Westin *et al.*, 2006b). Brain morphine concentrations were similar at both time points, despite lower plasma concentrations following IN administration, and with significantly higher area under the curve ($AUC_{0-5 \text{ minute}}$) brain:plasma for IN administration compared to IV administration (3 and 0.1 respectively) indicating that direct olfactory transfer makes a significant early contribution to brain morphine concentrations. This suggests that although IV administration yields delivery

of morphine into the systemic circulation and subsequent delivery across the BBB and into the brain, IN administration may provide a rapid delivery effect because of combination of distribution across the BBB and transfer through the olfactory pathways.

Interestingly at 0-5, 0-15, 0-60, and 0-240 minutes the right brain hemisphere:plasma morphine AUC ratios were 2,200, 348, 91, and 11% higher, respectively, compared to IV administration, and the overall proportion of morphine which reached the right hemisphere (as a result of olfactory transfer) was 95, 71, 48, and 10% for the studied time points (Westin *et al.*, 2006a). This subsequent study by Westin highlights an important aspect of assessing nose-to-brain pharmacokinetics, namely that the olfactory transfer effect is potentially rapid and decreases with time and is an important experimental consideration in such studies. Furthermore, the overall contribution of the olfactory route to brain penetration (following IN administration) may well be masked for highly lipophilic drugs where BBB penetration and brain disposition may be extensive (Sakane *et al.*, 1991).

1.4 Olfactory delivery of macromolecules

The connection between the nasal cavity and brain was first established for solute diffusion studies, where dyes were injected into the CSF and were shown to penetrate through the cribriform plate and enter the mucosal layers of the nasal cavity (Kristensson and Olsson, 1971). The first direct and quantitative study of the exploitation of the nasal route to deliver drug into the brain was reported by Thorne *et al* (1995) (Thorne *et al.*, 1995), who demonstrated that delivery of wheatgerm agglutinin-horseradish peroxidase (WGA-HRP) into the olfactory bulbs of rats.

The exact transfer mechanism of macromolecules is thought to occur through axonal transport through the olfactory neurone and olfactory bulb or trigeminal nerve and along extracellular pathways to the brain. Dendritic uptake is thought to occur through endocytotic or pinocytotic mechanism which internalises the macromolecule (De Lorenzo, 1970, Baker and Spencer,

1986). Once internalised, the macromolecular is thought to be transported axonally along the olfactory filaments and passes through the cribriform plate before reaching the olfactory bulb.

The process of internalisation of the macromolecules is an important factor in governing whether it undergoes trans-neuronal transport away from the olfactory bulb or whether it simply accumulates within the olfactory bulb (Baker, 2003). For example, the mechanisms of intracellular transport of unconjugated HRP within the olfactory neurones was found to be through a lysosomal endocytosis pathway as a result of the lack of HRP binding sites on the neurone (Broadwell and Balin, 1985). In contrast, the lectin-conjugated form (WGA-HRP) was demonstrated to be capable of binding to cell surface glycoproteins and undergo receptor-mediated endocytosis followed by trans-neuronal transport and brain deposition (Broadwell and Balin, 1985, Baker and Spencer, 1986, Shipley *et al.*, 1985). As with small molecular weight compounds, extracellular transport pathways are also a potential route of entry of macromolecules into the brain and CNS (Mathison *et al.*, 1998b, Balin *et al.*, 1986).

1.5 Human studies demonstrating olfactory drug delivery

Although the reports presented thus far deal with *in-vitro* or pre-clinical animal models of IN delivery, a number of human clinical trials and studies have also conclusively demonstrated the ability to deliver drugs into the brain following IN delivery. Many of these studies have focussed on insulin therapeutic agents for the reversal of Alzheimers-associated neurological degeneration with a view to examining either the disposition into the brain tissue or the effects on memory function.

In a double-blind study by Kern *et al* (1999) (Kern *et al.*, 1999), insulin and vehicle-placebo was dosed to 18 fasted healthy male volunteers and evaluated a possible nose-to-brain pathway by assessing auditory-evoked brain potentials (AEP). Whilst no changes were observed in systemic concentration (in line with previous reports of poor systemic absorption into the blood circulation following IN administration, in the absence of absorption enhancers (Watanabe *et al.*, 1992, Illum and Davis, 1992, Aungst *et al.*, 1988)), significant changes were

observed in elements of the AEP providing evidence of a direct route of transfer from the site of administration (IN) to the brain and CNS.

Furthermore, a study by Reger *et al* (Reger *et al.*, 2006), assessed the impact of saline vs 20 IU insulin vs 40 IU insulin on cognitive tests were examined. Their results demonstrated no significant impact on systemic plasma glucose but significant changes in total story recall and total list recall when compared to placebo groups. In a further study by the same group (Reger *et al.*, 2008), adults with Alzheimer's disease (AD) or mild cognitive impairment (MCI) along with normal healthy adults underwent a dose-escalation study of five intranasal doses of insulin (10, 20, 40, or 60 IU) or placebo, followed by a cognitive ability testing 15-minutes post-dosing and systemic insulin/glucose levels assessed 45-minutes post-dosing. Again, plasma and blood insulin/glucose levels were unchanged but a dose dependency in outcome was reported, with low doses improving verbal memory recall (word and story recall) in AD adults and in MCI adults who did not carry the APOEε4 allele.

The interest in IN delivery as a potential novel route to deliver therapeutic agents to the CNS, and thereby bypass the BBB, has gained much interested in recent years. As a relatively non-invasive approach, IN delivery (with olfactory/trigeminal nerve targeting) provides a route that has been demonstrated to bypass the BBB and target delivery to the brain and CNS. There is clear evidence amongst both small molecular weight compounds and macromolecules, that pathways including the olfactory neurons/bulb, trigeminal nerves, perivascular channels, the CSF, and lymphatic channels play a key role in transfer to the CNS.

To fully exploit this delivery approach urgent research is needed to examine the methods to enable specific regional delivery of compounds within the brain where treatment is required and the underlying mechanisms of which govern onwards distribution of therapeutic agents across the brain and wider CNS. Nose-to-brain drug delivery is a rapidly developing area, and the existing literature supports the view that olfactory transfer may bypass the BBB to achieve CNS delivery. Recent developments in nanotechnology and formulation development are

aiding the difficult challenge of olfactory-targeted delivery within the nasal cavity (Yang *et al.*, 2013, Xia *et al.*, 2011, Samia *et al.*, 2012, Ravouru *et al.*, 2013, Perez *et al.*, 2012, Chekhonin *et al.*, 2008, Zhao *et al.*, 2013, van Woensel *et al.*, 2013, Vaka *et al.*, 2013, Liu *et al.*, 2013, Liu *et al.*, 2012).

1.6 Formulation factors influencing olfactory drug delivery

When formulating a dosage form for intranasal administration intended to direct brain delivery, a number of aspects should be taken into consideration. Firstly, the olfactory region in man is situated higher up in the upper part of the nasal cavity making it difficult to reach with currently available nasal spray or powder devices (Ugwoke *et al.*, 2005). Secondly any nasally administered drugs will be rapidly cleared into the gastrointestinal tract through mucociliary clearance (Illum, 2003). Also, for large molecular weight or highly polar drugs the nasal mucosa can hinder the trans- and paracellular transport of polar drugs and also provide a significant metabolic barrier to systemic absorption (Costantino *et al.*, 2007, Khafagy el *et al.*, 2007).

To enhance the residency within the nasal cavity, many groups have developed smart polymer-based delivery systems which often employ both a 'responsive' polymer which can alter the properties of the formulation based on a trigger pH or temperature, coupled with the use of mucoadhesive polymers to enhance nasal residency (Agrawal and Maheshwari, 2014, Kumari *et al.*, 2012, Shin *et al.*, 2013, Jones *et al.*, 2009).(Ugwoke *et al.*, 2005, Zaki *et al.*, 2007a, Bhandwalkar and Avachat, 2013)

1.6.1 Nasal solutions/sprays

Liquid based preparations are the most widely used nasal dosage form and are based on aqueous formulation systems with the inclusion of excipients for osmolality and maintenance of pH coupled with the use of preservatives for multi-dose containers. The majority are

intended for local effects such as relief of nasal congestion, nasal allergy, and nasal infections (Figure 1-5).



Figure 1-5: Nasal (solution) formulation.

(A) Multi-dose nasal spray; (B) multi-dose liquid drops.

Solution systems are ideal for scenarios where a rapid onset of action is required. For example, intranasally administered methadone for pain relief in human volunteers has been reported to reach maximum plasma concentrations within 7 min and a peak pharmacodynamic response within 30 min post administration with a bioavailability of 85% (Dale *et al.*, 2002). Equally poorly soluble drugs can be formulated as their salt forms and administered intranasally, e.g. raloxifene and tamoxifen (Hussain and Dittert, 2001).

The administration of solution formulations can occur through the use of drops or sprays. The use of drops often requires a complex set of manoeuvres to ensure correct administration (Vidgren and Kublik, 1998) and often can lead to poor control of the volume delivered in addition to rapid clearance through laryngopharynx clearance if the head position is incorrect (Vidgren and Kublik, 1998). On the other hand, sprays can often deposit to a greater extent in the anterior regions of the nasal cavity and hence yields slower clearance than drops (Hardy *et al.*, 1985). For example the nasal bioavailability of desmopressin was increased following intranasal spray administration compared to drops (Harris *et al.*, 1986).

One type of approach to improve both residency of the formulation within the nasal cavity but to also enhance brain delivery is the use of microemulsions. Kumar *et al* (Kumar *et al.*, 2008) developed an IN microemulsion risperidone formulation and assessed distribution in rats using radiolabelled biodistribution studies. A significantly larger brain: blood was observed following IN administration for risperidone solution and nanoemulsion formulations when compared to IV administration at 30 minutes post dosing. A lower $t_{\max, \text{brain}}$ (1 hour) compared to blood (2 hours) also suggested rapid and preferential nose-to-brain delivery.

Triptan-based drugs are widely prescribed for both headaches and migraines (Jain *et al.*, 2010). Commonly prescribed types include sumatriptan and zolmitriptan and which are often delivered intranasally. Clearly, systemic absorption followed by CNS distribution would be the primary route of delivery into the CNS, but nose-to brain delivery has been reported in rats (Vyas *et al.*, 2006b, Vyas *et al.*, 2005a) using microemulsion (ME) based delivery systems. Such a ME-based system demonstrated drug concentrations in brain following IN administration to be significantly higher at all sampling time points compared with IV administration, with 2.5-3-fold higher brain: blood at the $t_{\max, \text{brain}}$ (0.5 hours) (Vyas *et al.*, 2006a).

1.6.2 Nasal Gels

To overcome the rapid and significant removal of solution from the nasal cavity as a result of mucocilliary clearance, the use of increased viscosity formulations and/or bioadhesion polymers is often employed to prolong the contact time with the nasal epithelia. Viscosity increasing polymers are often utilized in nasal formulations resulting in 'gel' like structures, often termed hydrogels. These are transparent, viscoelastic and thermodynamically stable systems consisting of a polar solvent and a polymer, where polar solvent is the external phase. The polymer used is often synthetic or natural in origin and will act to form a 3D- network which is capable of absorbing water. A variety of polymers used in these systems are of the 'responsive' type and the most widely studied for nasal drug delivery has been the temperature-sensitive category, of which poloxamer-based hydrogels are the most widely cited

(Zaki et al., 2007a, Shin et al., 2013, Nie et al., 2011, Majithiya et al., 2006, Kumari et al., 2012, Jones et al., 2009, Attwood et al., 1985, Miller and Drabik, 1984).

These systems undergo a phase transition, moving from a solid-to-liquid or a liquid-to-solid which is triggered by a change in the temperature, this is often termed the critical solution temperature (CST) or gelation temperature ($T_{\text{sol-gel}}$ or $T_{\text{gel-sol}}$). This transition can be positive or negative and the majority of polymers belong to positive temperature sensitive hydrogels, which undergo swelling in water as the temperature increases above a critical point (upper critical solution temperature (UCST)), and hence become a 'gel' with increasing temperature. Formulations which shrink with increasing temperature are termed negative hydrogels (Soppimath *et al.*, 2002).

The majority of polymers used in these formulations are hydroxypropyl methylcellulose (HPMC), N-isopropylacrylamide copolymers (PNIPAAm), poly(ethylene oxide) (PEO) and poly(propylene oxide) (PPO) (poloxamers, Tetronics® or Pluronics®) and poly (acrylic acid) (PAA) (Klouda and Mikos, 2008) (Figure 1-6). Of these polymer system, poloxamers block copolymers have been widely used in nasal hydrogel systems. Poloxamer consist of ethylene oxide and propylene oxide units which are arranged in a tri-block formation, with Pluronics ® being the most widely incorporated due to their general biocompatibility and stability (Dumortier et al., 2006b).

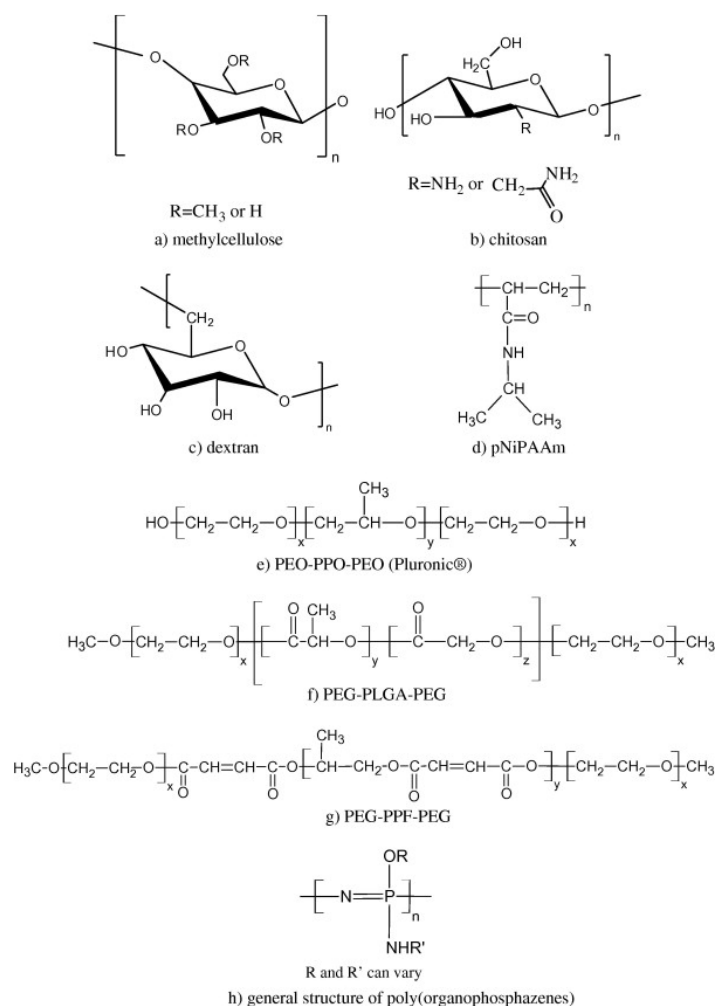


Figure 1-6: Chemical structure of widely used thermoresponsive polymers

Taken from (Klouda and Mikos, 2008)

Poloxamer 407 ($a=101$; $b=56$; molecular weight: 9840-14600) is the most widely used poloxamer and is also known as Pluronic F 127® ('F' for flakes). Hydrogels formed from these systems are thermoreversible and are capable of transferred from liquid-to-gel above the sol-gel transition temperature ($T_{\text{sol-gel}}$). In such systems the gelation occurs over two phases, as the temperature increases to the critical micelle temperature, poloxamer will aggregate to form micelles followed by a second step where the micellar structure will form an ordered system in the physical form of a gel (Figure 1-7).

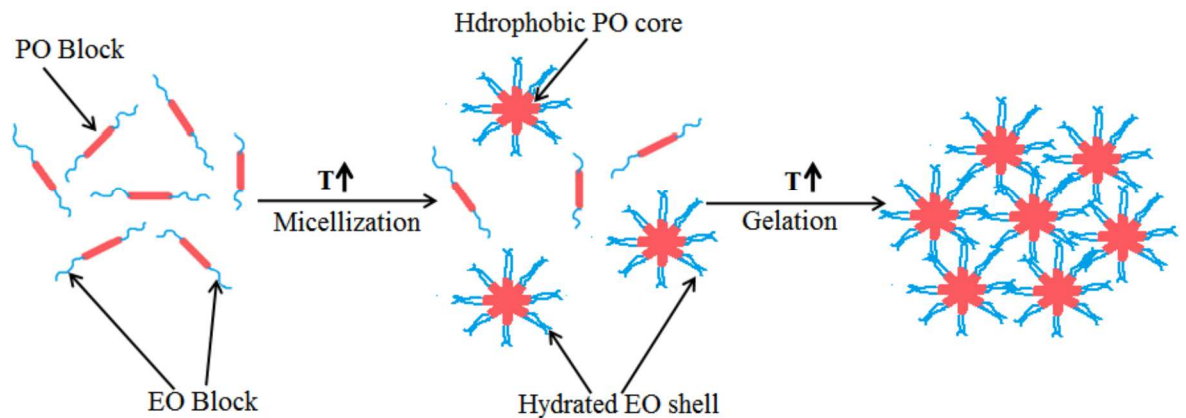


Figure 1-7: The gelation of poloxamer 407 in water

Adapted from (Dumortier et al., 2006a)

In addition to temperature, the process of gelation is highly dependent on the concentration of poloxamer utilised and is related to the selection of a concentration above the critical micellar concentration. For poloxamer solutions in the region of 20-30% w/v, a clear liquid is formed at refrigerated temperatures (4°C) and a hydrogel formed at room temperature (~25°C), with decreasing poloxamer concentration increasing the $T_{\text{sol-gel}}$ (Schmolka, 1972a).

To further enhance the residency within the nasal cavity, the use of bioadhesive polymers is widespread and often include, amongst others, xanthan gum, tamarind gum, sodium alginate, carrageenan, gelatin, pectin, chitosan, hydroxypropylcellulose and sodium carboxymethyl cellulose (Lee *et al.*, 2000, Nakamura *et al.*, 1996). Bioadhesion is the process of attachment of macromolecular polymer to the mucus network on cellular layers. Typically this process occurs through molecular forces such as covalent attachment, hydrogen bonding or electrostatic interactions (Lee *et al.*, 2000) and often through interaction with mucus containing proteins such as mucin (and termed 'mucoadhesion').

The process of bioadhesion/mucoadhesion is not widely understood and is based on numerous theories:

Electronic theory: The adhesive polymer and mucus layer have opposing charges which attract when in close contact (Derjaguin *et al.*, 1977).

Adsorption theory: Adhesion takes place as a result of forces such as van der Waals, hydrogen bonding or hydrophobic interactions (Wake, 1976) (Kaelble and Moacanin, 1977).

Diffusion theory: Chains of the adhesive and substrate can interact and penetrate one another to create a semi-permanent bond (Campion, 1975, Voiutskii, 1963, Wake, 1978).

Wetting Theory: It is the affinity of a liquid system towards the surface to spread over it (Boddupalli *et al.*, 2010).

Fracture Theory: This theory involves mechanical measurement of mucoadhesion, where force required to separate two surfaces is measured (Smart, 2005).

Examples of successful application of mucoadhesive systems include the use of haluronate solutions to enhance the nasal bioavailability of vasopressin in rats (Morimoto *et al.*, 1991), a range of mucoadhesive (Carbopol 934, PVP K30, HPMC K4M, sodium alginate, tamarind seed gum, and carrageenan) to enhance the bioavailability of venlafaxine in rats (Bhandwalkar and Avachat, 2013), natural extract mucoadhesive to enhance zolmitriptan absorption (Kumari *et al.*, 2012), Carbopol® polymers to enhance sumatriptan absorption (Majithiya *et al.*, 2006),

This issue of retention and residency time of formulations within the nasal cavity was further explored by (Kumar *et al.*, 2008), who demonstrated the added benefit of inclusion of a mucoadhesive agent on retention in the nasal cavity and subsequent drug pharmacokinetics, with the C_{max} (0.11 %/g) and AUC (0.48 h %/g) of mucoadhesive

ME formulations of risperidone significantly higher than non-mucoadhesive containing formulations.

Approaches aimed at retaining the drug within the nasal cavity for prolonged periods of time would undoubtedly aid in the overall retention and drug release within the nasal cavity. (Zaki et al., 2007b) explored approaches to enhance the residency time of the anti-emetic drug metoclopramide hydrochloride in the nasal cavity using a combination of thermosensitive and mucoadhesive polymers. The bioavailability of metoclopramide in rabbits was demonstrated to be significantly improved when given IN rather than orally (69.1% and 51.7% respectively) with more rapid (t_{max} = 42.5 minutes and 50 minutes respectively) and pronounced (C_{max} =3.41 $2.63\mu\text{g mL}^{-1}$ and $2.63\mu\text{g mL}^{-1}$ respectively) when using a poloxamer 407 thermosensitive gel system which incorporated polyethylene glycol (PEG) polymers to aid in mucoadhesion and retention within the nasal cavity.

1.6.3 Nanoparticulate drug carriers for olfactory drug delivery

The use of nanotechnology for drug delivery has developed significantly over the last decade. Principally the application of nanoparticles have focussed on poorly soluble active agents (Junghanns and Muller, 2008) with a view to increasing their solubility (Ambrus *et al.*, 2009) and to enhance permeability through mucosal barriers (Morgen *et al.*, 2012). Two basic approaches are involved in the production of nanoparticles, the bottom-up technologies (controlled precipitation, crystallization) and the top-down (high pressure homogenisation, wet milling, co-grinding) technologies. The result of such approaches is a wide variety of different types of nanomaterials including lipid systems (liposomes), metallic (gold, silver), polymeric and ceramic (silica, titanium) (Moreno-Vega *et al.*, 2012), that consist of a highly homogenous system of spherical particles in the nanometer scale range, with the European and other International Committees have defining

a nanoparticle as having three dimensions in the order of 100 nm or less, although materials up to 1000nm have often been described as 'nanoparticle' systems (Lövestam *et al.*, 2010). The inclusion of drugs into nanoparticles often aids to enhance the solubility, but also provides a vehicle through which the nanoparticle is able to, often, easily transverse mucus barriers (Kim *et al.*, 2012, Cario, 2012).

Of the range of nanocarriers developed for nose-to-brain delivery, example of successful delivery have been demonstrated with polymeric nanoparticles such as PLGA for lorazepam (Sharma *et al.*, 2014); lipid nanoparticles for delivery for the K3 receptor agonist senktide (De Luca *et al.*, 2015), duloxetine (Alam *et al.*, 2014), ondansetron (Devkar *et al.*, 2014); polysaccharide chitosan for mitotane (Severino *et al.*, 2013). In all cases, the inclusion of the drug into the nanoparticles has been demonstrated to result in a rapid and quantifying delivery into the olfactory bulb and wider CNS following administration.

The advantages of using formulation approaches to enhance CNS delivery was further demonstrated by (Jain *et al.*, 2010), through the development of a micellar nanocarrier for zolmitriptan. Significantly higher brain accumulation of zolmitriptan was observed in rats at all time points studied (30-240 minutes) compared to either IN solution or IV administration. Furthermore, it was reported that in the first 30 minutes post-administration, drug uptake was limited to the rostral brain region with limited radioactivity in mid-brain, cerebellum, pons and medulla. From 60-240 minutes an increase in distribution was seen in the midbrain and cerebellum regions. To elucidate the absorption pathway, autoradiographical studies using ^{99m}Tc -zolmitriptan demonstrated transport to the olfactory bulb along the olfactory and trigeminal systems with transport of the drug complex to the mid-brain and cerebellum along the trigeminal pathways. Finally (Jain *et al.*, 2010) were also able to demonstrate targeting of ^{99m}Tc -zolmitriptan to the axon terminals of the olfactory neurons, where the axon terminals of the olfactory receptor neuron contact the dendrites of the mitral and tufted cells. This pathway was able to allow ^{99m}Tc -zolmitriptan to distribute further into brain regions such as

the hippocampus and diencephalon and frontal cortex. Thereafter the compound was demonstrated to travel to the caudaputamen, hippocampus and diencephalon.

A class of biocompatible nanomaterials that has gained attention for drug delivery are silica based nanoparticles. Silica is biocompatible and is often used in inorganic nanoparticles (Bottini *et al.*, 2007, Gerion *et al.*, 2007). Silica nanoparticles are highly porous in nature, with the pore sizes, density and total surface area being highly tuneable making them excellent tools for biomolecule detection, drug delivery systems and for contrast agent protectors (Nehoff *et al.*, 2014, Liao *et al.*, 2014, Marzaioli *et al.*, 2014). Mesoporous material was first discovered by Mobil Corporation in 1992 (Kresge *et al.*, 1992b) and termed MCM-41, possessing a honeycomb-like porous structure with hundreds of pore channels (termed mesopores) that have the potential to absorb molecules (Figure 1-8).

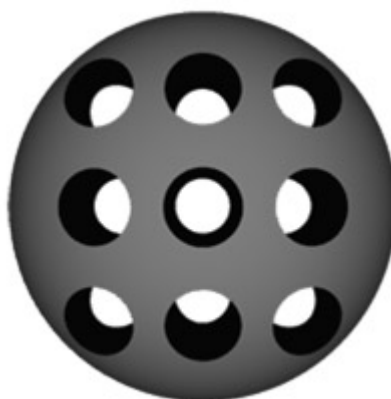


Figure 1-8: Schematic representation of mesoporous silica nanoparticles. Taken from(Yuan *et al.*, 2011).

This results in mesoporous nanoparticles (MSNP) having a high surface area ($> 900\text{m}^2/\text{g}$), large pore volume ($> 0.9\text{cm}^3/\text{g}$) with the added benefit of a tuneable pore size over a very narrow size distribution (2–10nm) (Slowing *et al.*, 2008a).

Unger, Stucky, and Zhao were one of the first groups to prepare micrometer-sized mesoporous silica spheres (Grün *et al.*, 1997, Huo *et al.*, 1997, Qi *et al.*, 1998), and their synthesis was based on the well-established Stöber reaction for the synthesis of monodisperse non-porous silica spheres. This reaction involves the co-hydrolysis and condensation of tetraethoxysilane (TEOS) and an alkyltrialkoxysilane (generating porosity) in a mixture of ethanol (co-solvent to form a homogenous solution), water, and aqueous ammonia (morphological catalyst) (Grün *et al.*, 1997) (Figure 1-9).

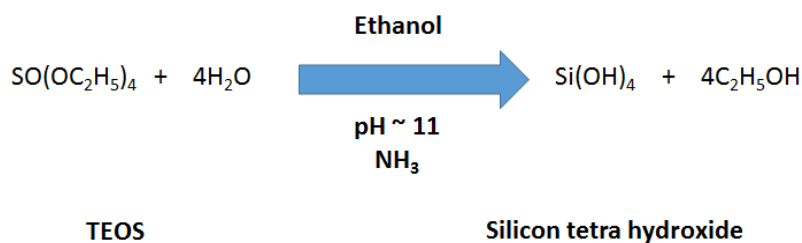


Figure 1-9: Stöber reaction for preparation of mesoporous silica nanoparticles (Yan *et al.*, 2014).

However, this first approach developed micrometer size particles, which are not considered suitable for cellular targeting and delivery. Adaptations of this method has developed mesoporous silica nanoparticles through the use of TEOS as a silica source, the cationic surfactant cetyltrimethylammonium bromide (CTAB) to act as a structure-directing agent, water as a solvent and sodium hydroxide as a morphological catalyst (Huh *et al.*, 2003). To remove the template surfactant a solvent extraction or calcination step is used to generate pores.

Given the relative ease of preparation of MSN and the tuneable nature of the nanomaterials, MSNP are an interesting group of nanoparticles which have not fully been exploited for nose-to-brain delivery.

1.6.4 Pressure metered dose inhaler

Although pressurized metered dose inhalers (pMDIs) have been widely utilized for pulmonary delivery of drugs, their use in nasal (and specifically olfactory) delivery has been limited. A pMDI system comprises of a drug dissolved directly into a propellant Hydrofloroalkane (HFA 134a (1,1,1,2-tetrafluoroethane) or 227 (1,1,1,2,3,3,3-Heptafluoropropane)) and, if solubility limitations exist, formulation with a co-solvent (e.g. ethanol). The formulation is housed under pressure within the canister, and a metering valve determines the overall spray volume (~60-100 μ L/actuation). For nasal drug delivery, very few actuator devices exist and are often utilized to the local treatment allergic rhinitis conditions (Djupestrand, 2013). Whilst actuator devices for nose-to-brain delivery are sparse and include technologies such as g. ArhcerFish® N2B (www.mysticpharmaceuticals.com), ViaNase® (www.kurvetechnology.com), POD (<http://impelnp.com/>), however there are no current marketed products based on these inhaler technologies (Figure 1-10).



Figure 1-10: Example of pMDI systems used for pulmonary and nasal (olfactory) drug delivery.

The requirement for localised delivery at the upper-most part of the nasal cavity poses significant challenges in directing the spray plume from a pMDI system and this may account for the limited progress in clinical translation of this widely used delivery system.

1.7 Novel CNS drug candidates: phytochemicals

A novel category of potential therapeutic agents for CNS disorders are phytochemicals, which are derived from natural extracts from plants. Over 8000 compounds have been identified as

belonging to the general category of polyphenols (Pandey and Rizvi, 2009). One of the major classes of these polyphenols are flavonoids. There are over 6500 compounds identified as flavonoids (Kong *et al.*, 2009). Flavonoids consist of a backbone of two aromatic rings (A and C ring) and a heterocyclic benzene ring (B ring) (Figure 1-11). The main subclasses includes: flavones (e.g. flavone), flavonols (e.g. quercetin, fistein), flavonones (e.g. flavanone, hesperetin and naringin), flavanonol (e.g. taxifolin), isoflavones (e.g. genistein, daidzein), flavan-3-ols (e.g. catechin , epicatechin) (Yao *et al.*, 2004).

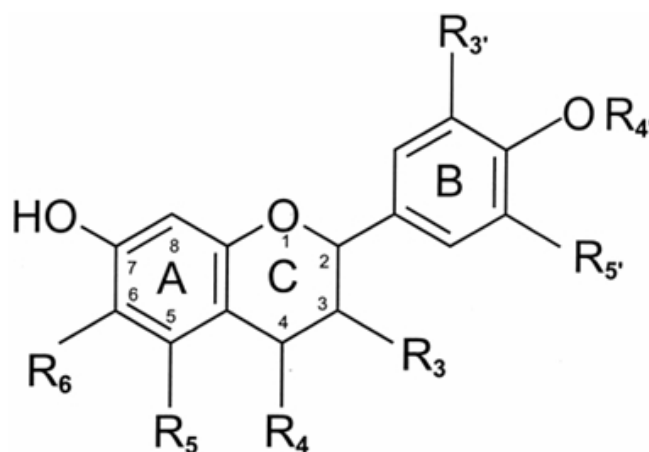


Figure 1-11: The structure of flavonoid (Heim *et al.*, 2002).

Flavonids consist of two aromatic rings (A and B) linked through three carbons that usually form a heterocyclic ring (C). Based on the pattern of hydroxylation and substitution (Rx), there are 7 subclasses of flavonoids.

Flavonoids offer a wide range of pharmacological actions which includes anti-inflammatory, antineoplastic, antioxidative, antiallergic, hepato- and gastro-protective, antidiabetic, and antiviral activities (Arts *et al.*, 2000) (Zand *et al.*, 2002) (Hertog *et al.*, 1993). These physiological actions are mostly believed to be due to their antioxidant and free-radical scavenging effects (Chu *et al.*, 2000), however new studies suggest that their mechanism of action is beyond these two properties (Nones *et al.*, 2010).

Many phytochemicals have been reported to possess CNS indicating effects including the protection of neurons from neurotoxins and neuro-inflammation in degenerative disease status such as Dementias (Williams and Spencer, 2012, Solanki *et al.*, 2015, Shukitt-Hale, 2012, Mecocci *et al.*, 2014, Macready *et al.*, 2009, Cherniack, 2012, Blumberg *et al.*, 2014). Furthermore, an increasing body of clinical evidence is supporting the view that flavonoids impart a protective function towards dopamine neurons through prevention of oxidative damage and apoptosis (Mercer *et al.*, 2005, Meng *et al.*, 2009). The target site for flavonoids is thought to be widespread within the CNS, but much attention has been focussed on the ability of phytochemicals to interact with the GABA_A receptor, one of the most important neurotransmitter sites within the CNS. Indeed, many phytochemicals demonstrated significant inhibitory actions on GABA_A in low micromolar concentration, e.g. chrysin (3µM) (Medina *et al.*, 1990) and 6-methylapigenin (495 nM) (Wasowski *et al.*, 2002). Furthermore, chrysin has been demonstrated to result in anxiolytic in mice at an intraperitoneal dose of 1mg/kg (Wolfman *et al.*, 1994). In addition to their action on receptor sites, a range of phytochemicals have been demonstrated to modulate the genome and proteome of the promiscuous network of membrane transporter proteins localised at the BBB (Kaur, 2016).

Phytochemical flavonoids are therefore a potentially novel multi-faceted class of molecules which show potential for a range of CNS patho-physiologies (Katayama *et al.*, 2007, Breedveld *et al.*, 2006b, Allen *et al.*, 2002b, Ashida *et al.*, 2000, Pick *et al.*, 2011, Fleisher *et al.*, 2015, Zhang *et al.*, 2004, van Zanden *et al.*, 2007, Zhang *et al.*, 2005, Robey *et al.*, 2004, Ferrandiz and Alcaraz, 1991, Breedveld *et al.*, 2006a, Allen *et al.*, 2002a). However, many phytochemicals are poorly soluble and are not immediately amenable to direct formulation into simple spray, solution or hydrogel based systems. To overcome this, many groups have demonstrated successful loading and delivery of phytochemicals into nanoparticle carrier systems to enhance their solubility, with the most commonly studied phytochemical being curcumin (Gupta *et al.*, 2009, Gupta and Dixit, 2011b, Gupta and Dixit, 2011a, Krausz *et al.*, 2015). Mesoporous silica nanoparticles have also recently been used recently to demonstrate

loading and release of curcumin (Kim *et al.*, 2015). Furthermore, in another study by (Du *et al.*, 2016) chrysin was encapsulated in PLGA-PEG nanoparticles for local treatment whereas other groups (Tamaddon *et al.*, 2015, Guideline, 2005) used β -cyclodextrin to increase the solubility of chrysin.

1.8 Models for studying nasal drug delivery

1.8.1 Models for studying nasal drug delivery: *ex-vivo* models

To assess the targeting and delivery of drugs within the nasal cavity, the use of established cell culture or *ex-vivo* tissue models are vital. Traditional, *ex-vivo* tissue extracts have been used from a range of animals or humans and these are mounted within a vertical Franz diffusion cell model to evaluate drug penetration from pharmaceutical preparations (Ng *et al.*, 2010). In this system, the donor and acceptor compartments are separated by a membrane of artificial, animal or human origin. However a key difficulty in this approach are species differences in the quality of the tissue and the associated enzyme activities or cell type distribution, particularly as these can differ when compared to humans (Chien and Chang, 1987) (Costantino *et al.*, 2007, Horvat *et al.*, 2009).

1.8.2 Models for studying nasal drug delivery: cell culture models

Although *ex-vivo* tissue models may be more historically and anatomically relevant for *in-vivo* delivery studies, *in-vitro* cell culture models of barrier sites are often utilised due to their ease of growth/proliferation and development of permeation assays. To ensure a representative nasal epithelial model, it is imperative the chosen cell culture model systems is capable of forming confluent cell layers; expresses correct intercellular junctional proteins; possess an appropriate functional barrier as measured by the transepithelial electric resistance and permeability coefficients for drug or marker molecules. The use of *in-vitro* cell culture models of the human nasal epithelium based on directly isolated cells from freshly extract nasal tissue

(primary cell culture) has been previously demonstrated to fulfil these criteria, but the limiting proliferation ability of primary cells coupled with batch-to-batch variability is often hinders their widespread use (Horvat *et al.*, 2009, Werner and Kissel, 1996).

Immortalized cell lines have the advantages of being relatively easy to culture and of lower costs with a greater level of genetic homogeneity (Werner and Kissel, 1996). Out of the available immortalised nasal epithelial cell line, the RPMI 2650 cell line is derived from a spontaneously formed anaplastic nasal septum tumour, but possess properties that are very closely related to normal human nasal epithelium (Moorhead, 1965, Moore and Sandberg, 1964, Moll *et al.*, 1983). Furthermore, reports have demonstrated that this cell line is suitable for drug transporter studies (Salib *et al.*, 2005, Reichl and Becker, 2012b, Lungare *et al.*, 2016, Kurti *et al.*, 2013, Kreft *et al.*, 2015, Dolberg and Reichl, 2016).

The availability of olfactory immortalised cell lines is relatively rare with only one model system published that is readily available, and isolated from the olfactory bulb of pigs. This cell line is termed OBG400 and was originally developed by Dr Gail Scherba (Uebing-Czipura *et al.*, 2008) and has been used as a continuous source of porcine neuronal-committed progenitors that can be used for the development of *in-vitro* neuropathogenic disease models (Uebing-Czipura *et al.*, 2009).

1.9 Aims and Objectives

The overall aim of this thesis was to examine approaches that can be used to selectively target and deliver drugs onto the olfactory mucosa following intranasal delivery. Thermoresponsive nasal gel systems, mesoporous silica nanoparticle carriers and adaptations of existing nasal pMDI systems were chosen as administration approaches/vehicles. Furthermore, the formulation of water-soluble (amantadine) and poorly soluble (chrysin, curcumin and diazepam) compounds were considered.

To achieve the aims, the overall objectives were:

Chapter 2: Thermoresponsive nasal gels

- To demonstrate successful formulation of a thermoresponsive nasal gel system for the delivery of amantadine
- To assess the stability of formulations and release mechanisms from gels
- To investigate the optimal administration techniques to ensure optimal olfactory deposition using a human nasal cast model
- To assess the cellular toxicity of formulation towards nasal epithelia cells and olfactory cells in culture

Chapter 3: Mesoporous silica nanoparticles

- To demonstrate successful formulation of a mesoporous silica nanoparticle capable of penetration into olfactory cells layer
- To assess the optimal size range for penetration of nanoparticles into OBGF400 cells
- To characterise the mesoporous material developed using FTIR, DSC, TGA, SEM
- To investigate the potential for loading and release of the phytochemicals chrysin and curcumin
- To assess the cellular toxicity of formulation towards olfactory cells in culture

Chapter 4: Nasal pMDI systems

- To formulate a pMDI canister containing diazepam for nasal delivery
- To assess the stability of diazepam in HFA134a
- To assess the deposition patterns of spray when actuating a nasal pMDI into a silicone nasal cast
- To quantify olfactory deposition of diazepam under optimal administration angles
- To assess the cellular toxicity of diazepam towards olfactory cells.

Chapter 2

Development of thermosensitive mucoadhesive polymer hydrogel formulations for olfactory drug delivery

2.1. Introduction

Approaches aimed at delivering a drug into the CNS to target CNS disorders are challenging due to the significant hurdle that the BBB poses in restricting the entry of xenobiotics across into the brain and wider CNS (Abbott, 2005, Abbott *et al.*, 2010b, Abbott and Romero, 1996, Pardridge, 2007b). Recently, there has been a growing interest in identifying and exploiting alternative pathways which may enable CNS drug delivery through bypassing the BBB, and much of this work has focussed on the olfactory mucosa and trigeminal neuronal regions within the nasal cavity as target sites which can enable CNS drug delivery, primarily as a virtue of the direct exposure of neurones to the external environment within the nasal cavity (Jogani *et al.*, 2008, Stewart, 1985, Reiss *et al.*, 1998, Sakane *et al.*, 1995). These regions provide direct access to the brain, without the limitation of the BBB to hinder drug delivery (Mathison *et al.*, 1998a) .

Although IN drug delivery offers many advantages to targeting the olfactory regions for nose-to-brain delivery, a key limitation is the short residence time of the formulation in the nasal cavity. The residency time is key to allow the absorption of the drug across the mucosa and the action of mucociliary clearance cycles (MCC) substantially reduces the half-life of substances administered intranasally to approximately 15-20 minutes (Vyas *et al.*, 2005b) (Soane *et al.*, 1999).

The optimal design of an olfactory targeting system would be one capable of prolonging the residence time of the formulation within the nasal cavity and therefore enhance the bioavailability of the drug. To achieve this goal, the use of intelligent polymer based systems have now become more commonplace in this field and particularly the use of responsive systems which may respond to the nasal cavity temperature have increased amongst researchers (Schmolka, 1972b, Wu *et al.*, 2007, Qian *et al.*, 2014, Nazar *et al.*, 2011, Li *et al.*, 2010, Li *et al.*, 2014, Jeong *et al.*, 2002, Chen *et al.*, 2013b, Alsarra *et al.*, 2009, Agrawal *et al.*, 2010) or at a specific trigger pH (Zaki *et al.*, 2007a, Nakamura *et al.*, 1999, Ikechukwu

Ugwoke et al., 1999, Hosny and Banjar, 2013, Basu and Maity, 2012). Furthermore, the use of mucoadhesive polymers to enhance the adhesion of the formulations onto the nasal mucosa (Zhou and Donovan, 1996, Ugwoke *et al.*, 1999, Soane *et al.*, 2001, Luessen *et al.*, 1996, Jain *et al.*, 2008, Ikechukwu Ugwoke *et al.*, 2000, Basu and Maity, 2012, Basu and Bandyopadhyay, 2010), has further demonstrated the ability to prolong contact time with the mucosa and hence increase drug bioavailability (Ugwoke et al., 2001, Qian et al., 2014, Li et al., 2014, Kumar et al., 2015, Ibrahim et al., 2015, Hosny and Hassan, 2014, Zaki et al., 2007a).

Thus, a thermosensitive polymeric system which undergoes solution-to-gel transition associated with a change in temperature, coupled with a mucoadhesive to enhance nasal cavity/olfactory residency, may provide a simple yet effective formulation and opportunities for drug absorption across the olfactory epithelia to enhance residency and delivery to the brain.

One of the major complications of PD is the emergence of dysphagia affecting the ability to ingest or swallow and is thought to affect between 45% and 95% of PD patients and has significant implications for orally dosed therapeutics, such as amantadine (Foltynie et al., 2004) and other anti-Parkinsonian therapeutics agents. Furthermore, the occurrence of bradykinesia and morning akinesia is often associated with delayed gastric emptying after the oral administration of anti-Parkinsonian therapeutics (Leopold and Kagel, 1997). To address these issues amantadine was selected as a model drug in these formulations.

Aims and objectives

The aim of this chapter was to develop a novel thermoresponsive and mucoadhesive hydrogel drug delivery system using amantadine as a model candidate compound which was capable of sol-gel transition at 34°C and stable over prolonged storage.

To achieve the aims, the overall objectives were:

- To identify and develop a thermosensitive nasal gel formulation using amantadine as a model drug.
- Identify the optimal formulation composition to ensure suitable sol-gel transition
- Understand the thixotropic behaviour of these gel formulations at molecular level both at room temperature and nasal temperature using rheology
- Evaluate and compare the mucoadhesive of the formulation following incorporation of different mucoadhesive polymers.
- Analyse the release kinetics of amantadine release from formulations
- Determine amantadine and excipient cellular toxicity against human nasal epithelia cells (RPMI 2650) and porcine olfactory mucosa cells (OBGF400).
- Assess the storage stability of formulations.
- Identify optimal administration parameter from a multi-dose spray system for olfactory deposition using a human nasal cavity cast

2.3. Materials and Methods

2.3.1. Materials

Dulbecco's Modified Eagle Medium (MEM), Dulbecco's Modified Medium: Nutrient Mixture F12 (DMEM-F12), Dulbecco's Phosphate buffered saline (PBS), L-glutamine 200mM, non-essential amino acids (NEAA), penicillin/streptomycin and trypsin-EDTA solution were obtained from PAA laboratories (Austria); foetal bovine serum (FBS) (Labtech, UK); polyethylene glycol 4000 (PEG4000), polyethylene glycol 12000 (PEG12000), chitosan-medium molecular weight (CS), sodium chloride, potassium chloride, magnesium sulphate, calcium chloride, acetonitrile, orthophosphoric acid, acetic acid, ethanol, sodium hydroxide, and sodium chloride were obtained from Fisher Scientific (Loughborough, UK); Acutase (Biolegend, UK) and unless otherwise indicated all other chemicals were obtained from Sigma (Dorset, UK), rat tail I collagen solution from First Link (Birmingham, UK) .

2.3.2. Formulation development

Formulations were prepared using a modified 'Cold method' approach as originally described by Schmolka (Schmolka, 1972b). Briefly, fixed quantities of excipients were utilised in all formulations and consisted of d-sorbitol (humectant) (0.5% w/w), sodium metabisulphate (antioxidant) (0.1% w/w) and benzalkonium chloride (surfactant) (0.1% w/w). Initially four mucoadhesive polymers were investigated (Na CMC (sodium carboxymethyl cellulose), CS, PEG4000 and PEG 12000) at concentrations of 0.5-1.5% w/w. These components were combined with ultrapure water under constant stirring, followed by the addition of amantadine (AMT) (0.5-1.5% w/w). The resulting solution was maintained for 2-hours in an ice bath prior to the slow addition of the thermoresponsive polymer pluronic-127 (P127) at concentrations of 15-20% w/w followed by storage at 4°C for 12 hours prior to use.

In the case of CS, the required quantity was first dissolved in 1% v/v acetic acid (Cho *et al.*, 2011) for 24 hours before being combined with the remaining formulations (prepared in ultrapure water) and stored at 4°C for at least 24 hours prior to analysis.

2.3.3. Assessment of sol-gel transition ($T_{\text{sol-gel}}$)

Visually: A modified method described by Zaki *et al* (Zaki et al., 2007b) was used to determine the sol-gel transition temperature ($T_{\text{sol-gel}}$). A sample of each formulation (1 g) was transferred into a glass vial and heated in a dry block (Techne Dri-Block[®] DB-2D), initiated at 20°C and increased by 1°C after every 5 minutes of equilibration time. The $T_{\text{sol-gel}}$ point was defined as the temperature whereby the upper meniscus of the gel did not move upon tilting the vial by 90 ° and this was used to demark optimal formulations. The optimal subset of formulations were then further characterised.

Rheologically: To assess the rheological properties of the formulations, samples were transferred to a AR-G2 Rheometer (TA instruments, USA). Throughout the tests a parallel plate geometry with 40mm steel plates having a gap 1.0mm were used. The approximate sample volume used was 1.26mL and the instrument was used in the oscillatory mode in the linear viscoelastic range. The rheological behaviour was characterised as a dynamic moduli G' and G'' as a function of frequency. Storage modulus (elastic) G' is a measure of energy stored and recovered for solid like component or how well structured a material is, loss modulus (viscous) G'' measures the energy lost for liquid like component of viscoelastic behaviour of the material, whereas loss tangent ($\tan \delta$) indicates overall viscoelasticity of the formulation measured (G''/G') (Madsen *et al.*, 1998). Tests conducted included:

Time sweep test: performed in a linear viscoelastic regime to ascertain any changes in formulation rheology over time at a fixed constant temperature (20°C or 34°C), stress (1 Pa) and frequency (1 Hz).

Temperature sweep test: performed to assess formulation behavior at a constant frequency and stress across a temperature range of 20-40°C, at different heating rates but at constant frequency (1 Hz) and stress (1 Pa). A temperature ramp of 5°C min⁻¹ was used in order to minimise dehydration or degradation of the formulation.

Steady shear viscosity: samples were subjected to shear rates ranging from 0.1 to 100 s⁻¹ and tests were conducted at 20°C and 34°C to identify the impact of temperature on viscosity.

To quantify the rheological properties, the Ostwald-de Waele relationship (often called the power law) was applied to relate the shear stress (σ) is related to a consistency coefficient (k), the shear rate ($\dot{\gamma}$) and an index value (n) (Bonacucina et al., 2004):

$$\sigma = k\dot{\gamma}^n$$

which is applicable to the formulations in light of the constant shear viscosity curves. In the context of rheology, the index value can be used to determine the type behavioural flow, with Newtonian behaviour when to $n \approx 1$ (where n is identical to the viscosity). When the magnitude of n is < 1 , the underlying rheological process is shear-thinning (pseudoplastic flow) and then when $n > 1$ the fluid is shear-thickening.

2.3.4. Assessment of formulation mucoadhesion

2.3.4.1. Texture analysis

To assess the mucoadhesive properties of formulations, a modified texture analysis method was utilized (Curran *et al.*, 2009) (Bruschi *et al.*, 2007) through the means of a Brookfield Texture Analyzer CT3 (Figure 2-1). Porcine mucin discs were prepared in a manual hydraulic press (SPECAC, UK) using 250mg mucin with the application of 10t force for 30s. The prepared mucin discs were then hydrated in 5% w/v mucin solution for 30s and excess mucin solution was carefully removed. Using double sided tape, the prepared discs were attached to a 13mm aluminum cylinder probe of the texture analyser and 1.5mL of formulations were placed on a 34°C heated surface of a dry block. The texture analyzer was programmed such that the probe of the texture analyzer was lowered at the speed of 0.10mm s⁻¹ until the mucin disc contacted the gel surface. A trigger load of 2g was then applied for 2mins, and then the probe was lifted at the same speed. The adhesive force required to detach the mucin disc from the gel was measured in grams and used as measure of mucoadhesion.

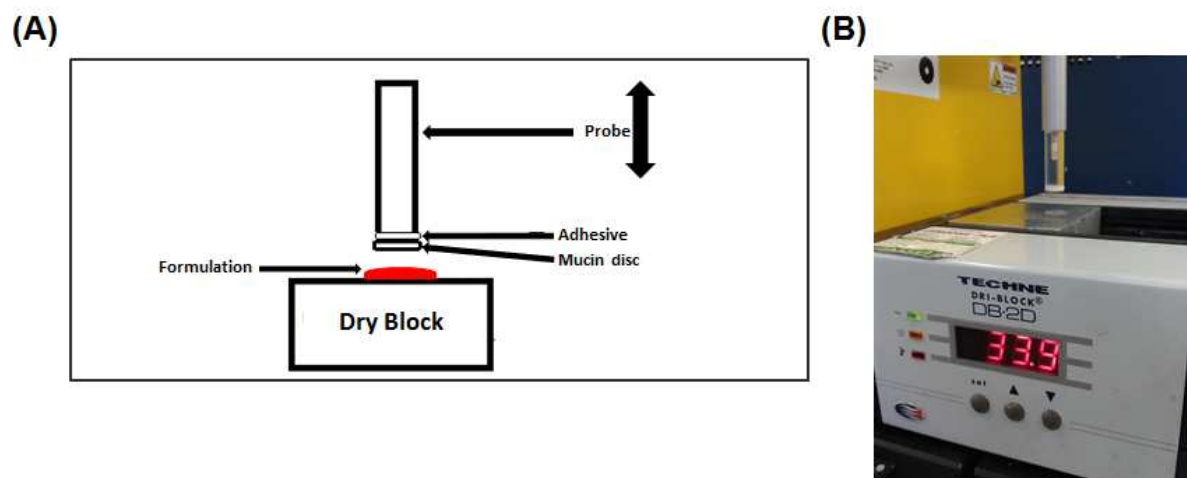


Figure 2-1: Tensile strength apparatus

(A) Schematic and (B) apparatus setup, to assess tensile strength using a dry block maintained at 34°C. A wetted (5% w/v mucin) compressed mucin disc was adhered onto the bottom of the probe of a texture analyser and tensile strength recorded as the force required to detach the probe from the formulation.

2.3.4.2. Displacement method

To further assess the mucoadhesion of formulations, an adapted inclined plate displacement method (Nakamura *et al.*, 1999) was developed. Briefly, 100mL of a hot 1% w/v agar and 2% w/v mucin mixture in PBS (pH 6.0) was cast onto a glass plate and left to dry at 4°C for 4 hours. The gel plate was then equilibrated at 34°C for 1 hour before formulation mucoadhesion was assessed through the application of a 250µL sample of each formulation with the plate kept at a 45° angle and maintained at 34°C in a heated incubator (Figure 2.2). The displacement (cm) of each formulation, measured for 1 minute, was used as a measure of the potential for adhesion.

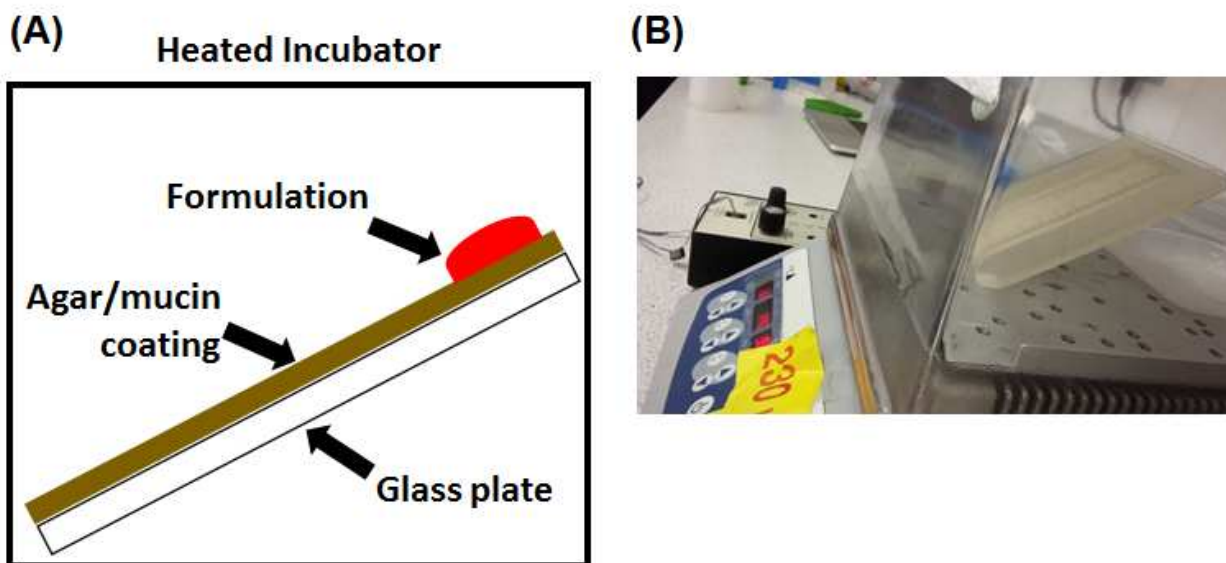


Figure 2-2: Displacement measurement apparatus

(A) Schematic and (B) apparatus setup, to measure displacement using a agar/mucin coated glass plate inclined at 45° and maintained in a 34°C environment.

2.3.5. Pre-column derivatisation of AMT and HPLC detection

To enable detection of AMT from formulations, a pre-column derivatisation method for memantine hydrochloride was modified in order to enable detection of AMT (Narola *et al.*, 2010). Amantadine lacks a chromophoric group to be detected by UV. 9-Fluorenylmethyl chloroformate (FMOC) is one of the derivatising agents which reacts with primary and secondary amines through ionic interactions (Bahrami and Mohammadi, 2007). Amantadine is a primary amine and its amino group can be trapped with FMOC to form amantadine-FMOC complex (Figure 2.3) which can be easily detected in the UV wavelength range.

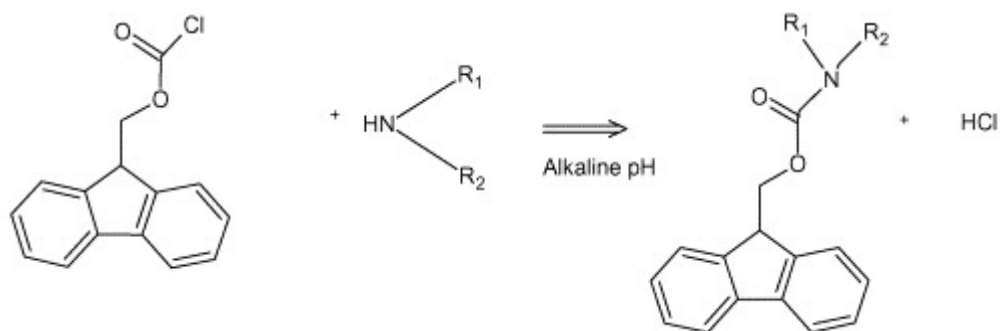


Figure 2-3: Fmoc reaction and complex formation with amines (Bahrami and Mohammadi, 2007).

In comparison to other derivatization methods of memantine hydrochloride, this method was found to be more reliable, sensitive and reproducible (Xie *et al.*, 2011). Briefly, to 50 μ L of sample or standard solution of AMT, 40 μ L of 0.015 M Fmoc and 50 μ L of 0.5 M acetate buffer were mixed well and kept at room temperature for 20 minutes prior to the addition of 360 μ L of diluent (0.05M borate buffer:acetonitrile (50:50 v/v)). A Shimadzu HPLC system was used with a Phenomenex Luna C18 (150 \times 4.6mm) 5 μ m column. The mobile phase consisted of premixed and degassed phosphate buffer:acetonitrile (20:80 v/v) which was filtered through 0.45 μ m membrane filter. The column was maintained at 30 $^{\circ}$ C and volume of injection was 10 μ L. The flow rate was maintained at 2mL/minute with run time 12 minutes. The software used for data collection and control of the system was LCsolution Version 1.24 SP1. The UV detection of derivatised amantadine was measured at 265nm. The intra/inter-day precision was determined and the limit of detection (LOD) and limit of quantitation (LOQ) were calibrated according to ICH (QR (R1) recommendations (Guideline, 2005),(Group, 2005) .

Stability of formulations

Optimised formulations were stored in stability cabinets maintained at 4 \pm 1 $^{\circ}$ C (Sanyo Medicoool, Loughborough, UK) and 25 \pm 2 $^{\circ}$ C (Firlabo, Paris, France) at a humidity of 60% \pm 5%. The stability of the formulation was assessed based on the gelation of a sample of the formulation at 34 $^{\circ}$ C within 5 minutes, followed by an assessment of the extent of drug release and drug content by HPLC as described in the section 2.3.5.

2.3.6. Membrane-less release kinetics

The release of AMT from the formulations were assessed by a 'membrane-less' diffusion system (Varshosaz *et al.*, 2006, Chen *et al.*, 2013b, Chi and Jun, 1991). A mass of formulation (0.25g) appropriate for the nasal cavity volume was transferred to a glass vial and allowed to equilibrate in a dry block at 34°C. Artificial nasa I electrolyte (ANE) (0.8g/L NaCl, 3g/L KCl, and 0.45g/L CaCl₂, pH 6.8) (Martinac *et al.*, 2005) was used as a release medium. 100µL of ANE was carefully layered on top of the gelled formulation. This volume was completely withdrawn and replaced with fresh ANE at each time point. Samples were analysed by a pre-column derivatisation method followed by HPLC analysis.

Several kinetic drug release mathematical models were used to assess drug release from the formulations (Tamaddon *et al.*, 2015). The best-fit to the mathematical models described below confirmed the appropriate release kinetics:

$$\text{Higuchi model: } \frac{M_t}{M_\infty} = kH \cdot t^{\frac{1}{2}}$$

where M_t/M_∞ is the drug fraction released at time t and kH is the Higuchi constant.

$$\text{Zero order model: } \frac{M_t}{M_\infty} = k_0 \cdot t$$

where M_t/M_∞ is the drug fraction released at time t and k_0 is the zero-order release constant.

$$\text{First order model: } \frac{M_t}{M_\infty} = 1 - e^{-k_1 t}$$

where M_t/M_∞ is the drug fraction released at time t and k_1 is the first-order release constant.

To assess the mechanism of drug release, the Korsmeyer-Peppas power law (Korsmeyer, 1983) has been used in many pharmaceutical formulations (Siepmann and Peppas, 2001, Kim and Fassihi, 1997, Bettini *et al.*, 1994, Peppas and Sahlin, 1989) and can be defined as:

$$\text{Power law: } \frac{M_t}{M_\infty} = kKP \cdot t^n$$

where M_t/M_∞ is the drug fraction released at time t , kKP is a kinetic constant which describes the structural and geometrical elements of the formulations and n is the release exponents which is used to indicate the mechanism of drug release. The value of n is important in understanding the mechanism of release when it is unknown and often polymeric formulations can be categorised accordingly to this scale. When $n \leq 0.45$ drug release is diffusion controlled and sometimes referred to as Fickian diffusion and when $n > 0.89$ the diffusion is indicative of erosion controlled drug release or class-II kinetics. For situations where $0.45 < n \leq 0.89$ the diffusion is a complex mixture of both processes and often termed anomalous transport. In all cases this is based on the assumption of release from a cylinder and applied to cumulative release rates $< 60\%$ (Korsmeyer, 1983).

2.3.7. Human nasal epithelial cell culture: RPMI 2650

The immortalised human nasal epithelial cell line RPMI 2650 (CLS, Germany) (Figure 2-4), was used to assess the compatibility of the formulations with human nasal epithelia and to develop an *in-vitro* nasal epithelial cell culture model (Reichl and Becker, 2012a) to assess drug release/transport. Cells were grown in MEM supplemented with 10% FBS, 1% L-glutamine, 1% NEAA, 1% penicillin-G/streptomycin in a humidified 37°C incubator with 5% CO₂ (Reichl and Becker, 2012b). The media was changed every 2 days. Thereafter the cells were passaged 3-4 days post seeding (at 70-80% confluency) by washing with pre-warmed PBS followed by the addition of 1mL of trypsin-EDTA to the flask. The flask was then placed in an incubator for 5-10 min and observed under microscope to make sure cells were lifted before seeding in the new flask.

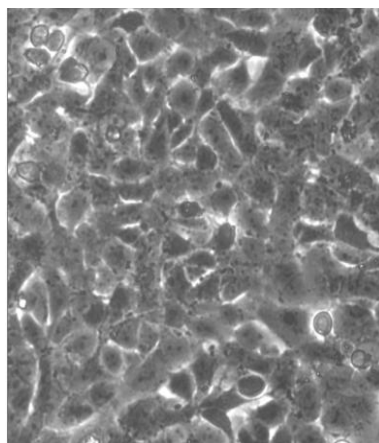


Figure 2-4: Morphology of RPMI 2650 cells

Light microscopic image (20 X) confirming the rounded and polygonal structures of the human nasal epithelial cells.

Cells were cryopreserved for further use by centrifugation at 1500 rpm for 10 min to obtain a cell pellet, followed by resuspension of the pellet in cryopreservation media (10% DMSO and 90% RPMI 2650 media). A 1mL volume of the cell suspension was aliquoted to the cryovials and stored overnight at -80°C in cell cooling box (Mr. Frosty, Nalgene®, Thermo Fisher Scientific, UK). After 24 h, cryovials were transferred to liquid nitrogen for long-term storage.

2.3.7.1. Human nasal epithelial airway cell culture model

To develop an *in-vitro* human nasal cell culture model, 6-well permeable inserts (ThinCert®) were used as a support for cell growth, with the addition of a matrix coating of 5µg/cm² of rat-tail collagen. Inserts were left to dry for 3-4 h in a laminar airflow hood before excess collagen was aspirated and inserts washed twice with PBS.

To assess the release and transport of AMT from formulations, an *in-vitro* nasal epithelial airway cell culture model was developed with RPMI-2650 cells seeded onto collagen-coated 6-well 0.4µm permeable inserts (ThinCerts™) at a seeding density of 4 x10⁵ cells/cm² (Bai *et al.*, 2008) (Reichl and Becker, 2012a) and grown for 14-days, with media replacement on alternative days. On days 10-14 an air-liquid interface (ALI) was initiated with the removal

of the media from the apical compartment producing the 'air-interface'. The integrity of the monolayer was determined by measuring the trans-epithelial electrical resistance (TEER) using an EVOM epithelial volttohmmeter (World Precision Instruments Inc.). TEER values for filter without cells (blank) were subtracted and values were calculated as per the surface area. TEER values were calculated as follows (Du et al., 2016):

$$\text{TEER } (\Omega \cdot \text{cm}^2) = (R_{\text{cell monolayer}} - R_{\text{blank filter}}) \times A$$

where A = surface area of the permeable insert (cm²), R_{cell monolayer} = resistance across cell monolayer permeable inserts and R_{blank filter} = resistance across permeable insert without cells. Control measurements were made using filters without cells (blank filter).

To confirm the formation of monolayer (Bai *et al.*, 2008) hence to further assess the formation of a suitable monolayer, lucifer yellow (LY) was used as a passive diffusion marker. LY was prepared in RPMI 2650 maintenance media without serum (termed serum free media (SFM)) and added to the apical chamber of the inserts to achieve a final concentration of 100µM with and LY-free SFM added to the basolateral chamber (1.5mL). The inserts were incubated at 37°C for 1 h. Thereafter, a sample of the basolateral media was then collected and quantified for LY permeation on a fluorescent plate reader at an excitation wavelength of 428nm and emission wavelength of 536nm using dual-scanning microplate spectrofluorometer (Spectra 70 Max Gemini XS, Molecular Devices, Sunnyvale, California). The percentage transport of LY across the permeable inserts were calculated as follows:

$$\% \text{ LY transport} = 100 \times \left(\frac{\text{RFU}_{\text{basolateral}}}{\text{RFU}_{\text{apical}}} \right)$$

where RFU_{basolateral} is the relative fluorescence units in the sample taken from basolateral compartment and RFU_{apical} is the relative fluorescence unit in the sample taken from the apical compartment.

The cut-off TEER values for an acceptable *in-vitro* model was set at 150 Ω.cm² (Bai *et al.*, 2008) (Reichl and Becker, 2012a) and LY transport of less than 1%

2.3.8. Porcine olfactory bulb neuroblastoma cell culture: OBGF400

To assess the compatibility between formulation and olfactory mucosa type cells, the porcine olfactory bulb neuroblastoma cell line OBGF400 was used as an *in-vitro* cell culture model of the olfactory neuronal pathway. OBGF400 cells are bipolar to multipolar in nature with prominent cell bodies and a distinctive nucleus and extending axonal structures confirm as neuronal cells (Figure 2-5). Currently, these are the only available immortalised neuronal cell line (Uebing-Czipura *et al.*, 2008).

OBGF400 were a kind gift from Dr. Gail Scherba (University of Illinois, USA) and were grown in DMEM/F-12 (Dulbecco's Modified Medium: Nutrient Mixture F12) supplemented with sodium bicarbonate, HEPES, Gentamicin (50µg/mL), Penicillin G/Streptomycin, Bovine calf serum in a humidified 37°C incubator with 5% CO₂. 25cm² flasks were used to grow the cells with 5mL media, which was changed every 2 days. At 80-90% confluency, the media was aspirated and cells were treated with Acutase[®] for 20-30 minutes for passaging.

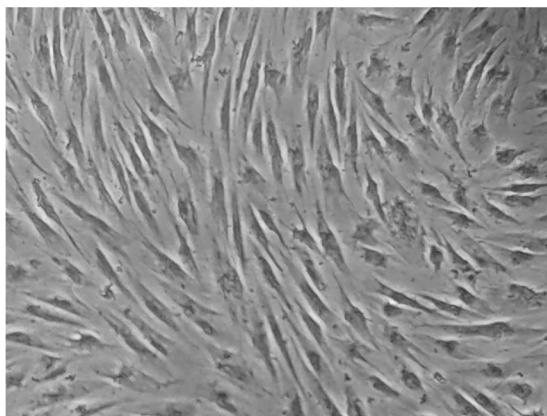


Figure 2-5: Morphology of OBG400 cells

Light microscopic image (20 X) indicating neuronal structures such as bi or multi polar processes, prominent cell body with distinctive nucleus.

To cryopreserve cells, 1mL maintenance media was added to the lifted cells and transferred to 15mL centrifuge tube. The cell suspension was then pelleted by centrifuging at 277 RCF (relative centrifugal force) for 7 minutes. After removal of the supernatant carefully the pellet was hand vortexed to disperse in the remaining fluid. Subsequently 0.5mL of cold (4°C) solution-I (1:1 maintenance media: calf serum) was added and gently hand vortexed. Finally, 0.5mL of cold (4°C) solution-II (1:4 DMSO: calf serum) was added in a drop wise fashion with hand vortexing after each addition.

A 1mL volume of the cell suspension was aliquoted to the cryovials and stored overnight at -80°C in cell cooling box (Mr. Frosty, Nalgene®, Thermo Fisher Scientific, UK). After 24 h, cryovials were transferred to liquid nitrogen for long-term storage.

2.3.9. Formulation cellular viability: 3-(4,5-Dimethylthiazol-2-yl)-2,5-Diphenyltetrazolium Bromide (MTT) assay

To assess the cellular toxicity of formulations towards nasal cell lines, an MTT cell viability assay was conducted with RPMI-2650 and OBG400 cells. Cells were suspended in 200µL medium and seeded at a density of 1×10^4 and 6×10^3 cells/well of a 96-well plate

respectively. After 24 hours the media was removed and replaced with 200µL of media containing either compound (AMT, curcumin or chysin) (0.01-50,000µM) or P127/mucoadhesive polymers (10-4000µg/mL) and incubated for 24 hours at 37°C in a 5% CO₂ air humidified environment. Subsequently 100µL of 0.5mg/mL MTT dissolved in PBS was added to each well and incubated at 37°C in an air humidified environment for 4 hours. Thereafter, the media was removed and 100µL of DMSO was added and the plates left to incubate for 15 minutes in the dark. The UV-absorbance of the formazan product was determined at 595nm. Each concentration was assayed in eight wells and run in three independent experiments and results expressed as percentage cytotoxicity relative to a control (0.5% DMSO).

2.3.10. AMT release and transport across an *in-vitro* human nasal epithelial cell culture model

Immediately prior to the start of the transport study, RPMI 2650 cells grown on permeable inserts were washed and fresh transport media (HBSS with 25mM HEPES) added to the apical and basolateral compartment of the wells and the cells left to acclimatise for 30 minutes in a humidified 37°C incubator. Thereafter the transport media was removed and 1mL of formulation were gently placed on top of the cell monolayer in the apical chamber and returned to the incubator for 5 minutes to allow the formulation to gel. Once gelled, fresh transport media was placed into the basolateral chamber and the transport study initiated. 250µL of the basolateral media was withdrawn at 5, 15, 30, 60, 120, 150 and 180 minutes and replaced with fresh pre-warmed transport media. Withdrawn samples were derivatised and AMT release quantified by HPLC analysis.

2.3.11. Nasal spray systems: droplet size distribution

To assess the potential *in-vivo* deposition characteristics of the proposed nasal formulation, a multi-dose pump spray delivery system was employed to characterise the formulation droplet size distribution using a laser diffraction technique. The Helos/Sympatec system was used

with an R3 lens (0.5-175µm). The nasal pump was vertically mounted 3cm away from the laser path and a vacuum source was mounted anterior to the pump system. The pump systems were pre-actuated prior to mounting, and actuated three times to detect the particle size distribution. Data was reported as volume diameters at 10%, 50% and 90% of the cumulative undersized volume distribution (Dv). Span was calculated as follows (Food and Administration, 2002):

$$\frac{Dv90 - Dv10}{Dv50}$$

2.3.12. Nasal spray system: human nasal cast deposition

To assess the potential *in-vivo* deposition characteristics of the proposed nasal formulation, a multi-dose pump spray delivery system was employed to assess the disposition of formulations into an anatomically correct transparent human nasal cast model (Koken Ltd, Japan). The inner surface of each nostril was evenly coated in a water-indicated dye (Kolorkut®, USA).

Formulation was loaded into a 5mL volume spray pump, which was pre-actuated 5 times prior to use. Thereafter a single spray (dose) was delivered into the nasal cast where the cast was fixed in an upright head position (Figure 2.6). The impact of spray angle (60-80°) and nostril insertion depth (5mm) on nasal deposition was analysed and captured images were subsequently processed through pixel quantification software to quantify the deposition patterns (Kundoor and Dalby, 2010). The depositions within the nasal cast was classified according to the predominate regions of deposition within the cast, i.e. lower nasal regions (nasal vestibule), the middle/upper nasal regions (turbinates) and the olfactory regions were assessed.

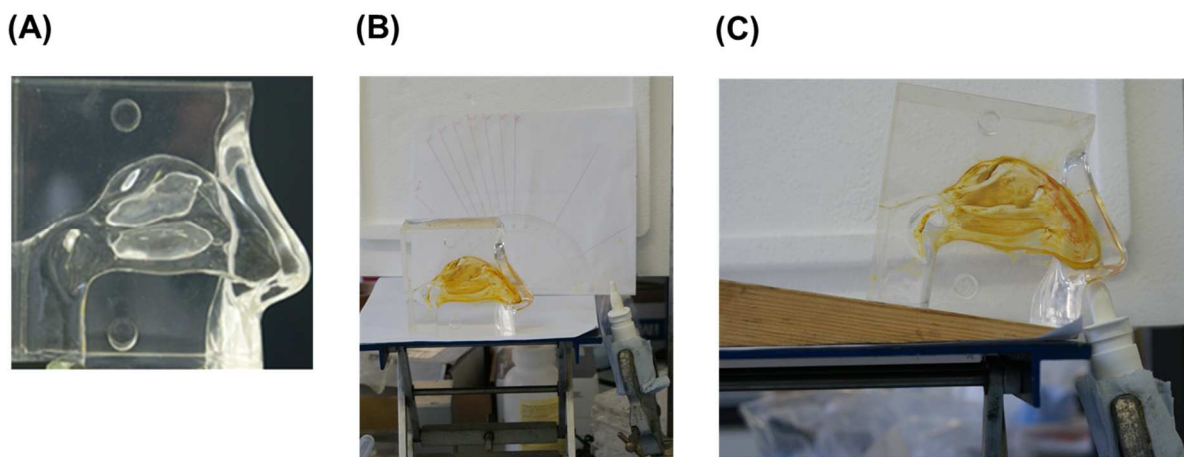


Figure 2-6: Assessment of nasal deposition in a human nasal cast model using a multidose nasal spray

A transparent human nasal cast (A) model was used to assess formulation deposition within the nasal cavity under conditions of different angles (60-90 °) (B) and nozzle insertion depths and anterior tilting of the head (C). To visualise and quantify regional deposition a water-indicating dye (Kolorkut®) was coated on the interior of the cast.

2.3.13. Statistical analysis

Unless otherwise stated, three independent experiments were carried out for each study. Statistical significance was evaluated by one-way ANOVA or paired two-tail Students t-test using GraphPad Prism version 6.00 for Windows (GraphPad Software, La Jolla California USA, www.graphpad.com). Unless otherwise states, data is reported as mean \pm standard deviation (SD). A significance level (P-value) of < 0.05 was considered as statistically significant.

2.4. Results

2.4.1. Formulation development and optimisation

2.4.1.1. Optimisation of thermoresponsive polymer content

Five preliminary formulations (F1-F5) containing 14-22% PF127 but without the addition of AMT or additives, were prepared in ultrapure water and assessed for the $T_{\text{sol-gel}}$ through visual methods. Formulations F2 and F3 (16 and 18% w/w PF127) demonstrated $T_{\text{sol-gel}}$ of 28 ± 1.3 and $25 \pm 1.5^{\circ}\text{C}$, closest to that of the nasal cavity (34°C) and were considered for further investigation (Table 2-1).

Table 2-1: Impact of PF127 on $T_{\text{sol-gel}}$, indicating the inverse relationship between concentration and $T_{\text{sol-gel}}$ in Pluronic only formulations.

Formulations	PF127 % w/w	$T_{\text{sol-gel}}$ $^{\circ}\text{C} \pm \text{SD}$
1	14	43 ± 1.1
2	16	28 ± 1.3
3	18	25 ± 1.5
4	20	23 ± 1.2
5	22	21 ± 1.3

Using CMC as the primary mucoadhesive to optimise formations, six further formulations with 18% PF127 and 2% CMC and AMT ranging from 0.5-1.5% were prepared (Table 2-2).

Table 2-2: Effect of addition of amantadine and excipients on gelation temperature

Formulations	CMC (% w/w)	Amantadine (% w/w)	BLK (% w/w)	MTB (% w/w)	T_{sol-gel} °C ± SD
F1	-	-	-	-	NG
F2	2	-	-	-	19 ± 1.6
F3	2	0.5	-	-	21 ± 1.5
F4	2	1.0	-	-	20.5 ± 1.0
F5	2	1.5	-	-	22 ± 0.4
F6	2	0.5	0.2	0.1	20.5 ± 1

All formulations contain 18% w/w PF127. CMC: Carboxymethyl cellulose, BLK: benzalkonium chloride; MTB: sodium metabisulfite; T_{sol-gel}: solution to gel transition temperature; NG: not gelled; SD: standard deviation. n=5.

However, formulations F2-F6 gelled at 21°C ± 1.5°C. Thereafter the concentration of PF127 was varied from 14-18% w/w and CMC concentration from 0.5-1.5% w/w. The addition of CMC lowered the T_{sol-gel} with increasing CMC concentration (Table 2-3) with only F9-10 demonstrating gelation from 25°C onwards and hence were selected for further optimisation.

Table 2-3: Effect of addition of CMC on gelation temperature

Formulation	PF127 (% w/w)	CMC (% w/w)	T_{sol-gel} °C ± SD
F7	14	0.5	>40
F8	14	2.0	>40
F9	16	0.5	27 ± 1.3
F10	16	2.0	25 ± 1.2
F11	18	0.5	23 ± 1.4
F12	18	1.0	22 ± 1.1
F13	18	1.5	21 ± 0.9

PF127: pluronic F127; CMC: carboxymethyl cellulose; T_{sol-gel}: solution to gel transition temperature; SD: standard deviation. n=5.

When PF127 concentrations were kept constant at 15% w/w with varying concentrations of CMC (0.5 to 1.5% w/w) and AMT (0.5 and 1.0% w/w), formulations with 1% w/w AMT did not demonstrate a gelation transition over the desired temperature range of 30-34°C (Table 2-4).

Table 2-4: Effect of addition of amantadine on gelation temperature

Formulation	CMC (% w/w)	AMT (% w/w)	T_{sol-gel} °C ± SD
F14	0.5	0.5	31 ±1.3
F15	0.5	1.0	>40
F16	1.0	0.5	32 ±1.5
F17	1.0	1.0	>40
F18	1.5	0.5	>40
F19	1.5	1.0	>40
F20	1.5	1.0	>40

All formulations contain 15% w/w PF127. CMC: carboxymethyl cellulose; T_{sol-gel}: solution to gel transition temperature; SD: standard deviation. n=5.

Further formulations increased PF127 concentrations in order to allow AMT content of 1% w/w per formulation (Table 2-5) with F23 demonstrated gelation close to the required nasal temperature.

Table 2-5: Effect of Increase in PF127 content on gelation temperature

Formulations	PF127 % (w/w)	CMC % (w/w)	T_{sol-gel} °C ± SD
F21	16	1	>35
F22	16	2	>35
F23	18	1	26 ±1.2
F24	18	2	26 ±1.6
F25	20	1	RT
F26	20	2	RT

All formulations contain 1% w/w AMT. CMC: carboxymethyl cellulose, RT- room temperature; T_{sol-gel}: solution to gel transition temperature; SD: standard deviation. n=5.

Increasing PF127 concentration from 16 to 17% w/w resulted in gelation at the target of 33°C ± 1.5°C (Table 2-6).

Table 2-6: Optimised formulation based on CMC as mucoadhesive

PF127 (%w/w)	CMC (% w/w)	AMT (% w/w)	BLK (% w/w)	MTB (% w/w)	D-sorb (% w/w)
17	1	1	0.1	0.1	0.5

PF127: pluronic F127; CMC: carboxymethyl cellulose; AMT: amantadine; BLK: benzalkonium chloride; MTB: sodium metabisulfite; D-sorb: D-sorbitol.

2.4.2. The impact of mucoadhesive polymers on formulation $T_{\text{sol-gel}}$

In order to compare the effect of different mucoadhesives on the overall performance of the formulations PEG 4K, PEG 12K and chitosan were incorporated into the optimised formulation (Table 2-7).

Table 2-7: Impact of mucoadhesive polymers on formulation gelation

Formulation	Composition (% w/w)	$T_{\text{sol-gel}}$ (°C ± SD)	pH
FCCM	1.00%	30°C ± 2	6.13 ± 0.15
FPEG 4K	1.00%	32°C ± 2	5.79 ± 0.21
FPEG 12K	1.00%	NG	5.86 ± 0.08
FCS 1	0.10%	31°C ± 1	5.52 ± 0.15
FCS 2	0.30%	NG	5.81 ± 0.21

All formulations included PF127 17%, amantadine 1%, BLK 0.1%, MTB 0.1%, D-Sorbitol 0.5%

FPEG 12K and FCS 2 (0.3% w/w chitosan) did not demonstrate gelation and were rejected. However, FCCM (1% w/w CMC), FPEG4K (1% w/w PEG 4000) and FCS 1 (0.1% w/w

chitosan) gelled beyond 30°C. Furthermore, the pH of these formulations was within 5.5-6.5 at preparation.

2.4.3. Formulation characterisation

2.4.3.1. Sol-gel transition ($T_{\text{sol-gel}}$) by rheology

To identify the appropriate rheological temperature ramp for associated studies, two different heating rates of 1°C/min and 5°C/min were utilised to optimise rheological studies using FCMC. Under these conditions the gelation phase commenced at 30°C \pm 0.7°C and completed at 34°C \pm 0.5°C at 1°C/min compared to 22.5°C \pm 0.5°C and completed at 27°C \pm 0.3°C when heated at the rate of 5°C/min (Figure 2- 7). A temperature ramp of 1°C/min was selected to further characterise all formulations.

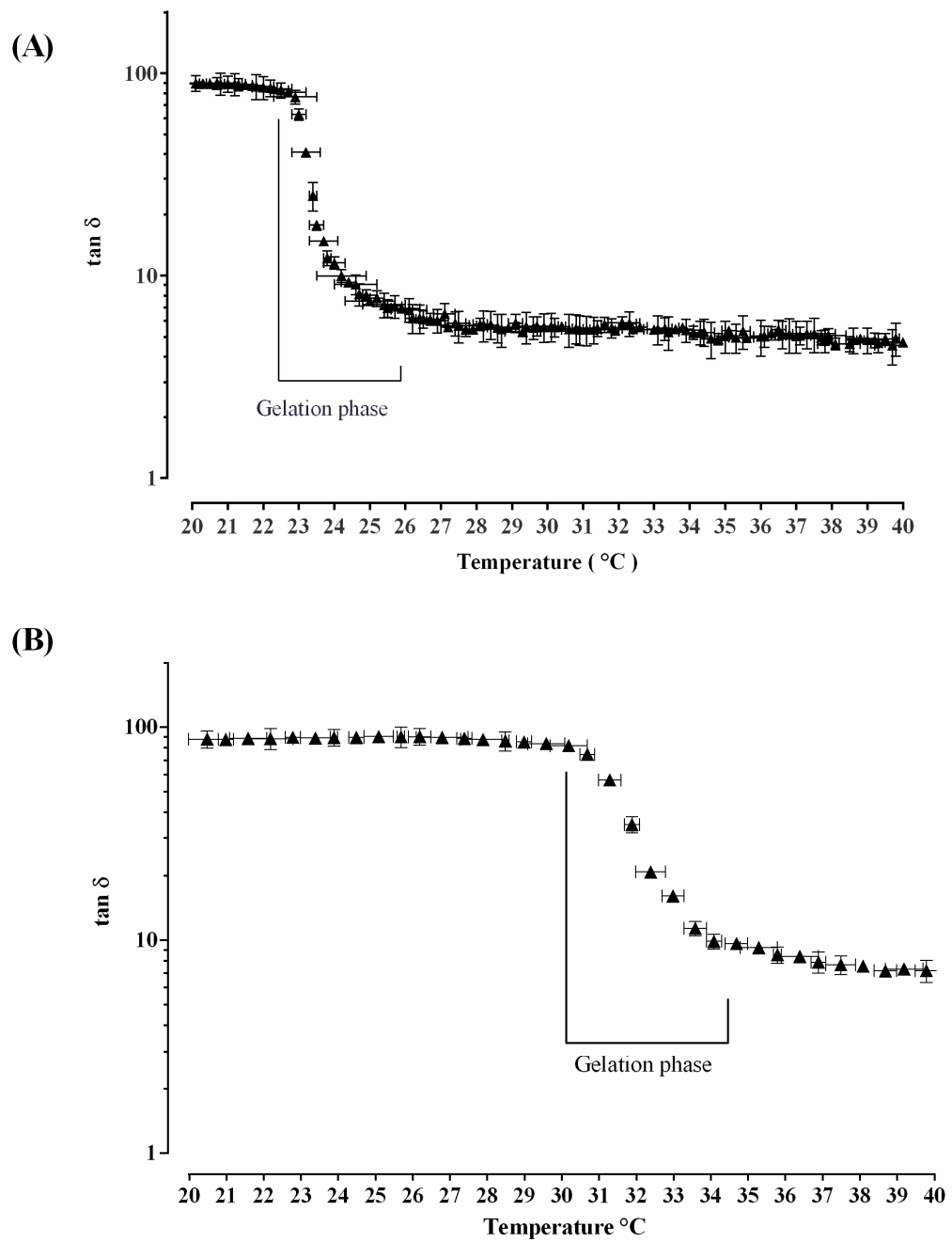


Figure 2-7: Impact of differing heating rates on FCMC temperature sweep properties

Rheological characterisation was assessed using FCMC as a model formulation with a heating rate of (A) 5°C/min and (B) 1°C/min. A sample volume of 1.26mL was used and the instrument setup in oscillatory mode within the linear viscoelastic range using parallel plate geometry with 40mm steel plates having a gap 1.0mm. Data represents mean \pm SD. n=4

All formulations demonstrated a gelation phenomenon, which initiated at approximately 26-28°C, and was preceded by the stable plateau region (Figure 2-8). FCS (Figure 2-8A) and FCMC (Figure 2-8C) demonstrated a complete profile with three distinct phases culminating in a stable gel formulation, whereas FPEG (Figure 2-8B) did not form a stable gel at the termination of the study (34°C).

The rate of gelation is also a key determinant of residency within the nasal cavity and this was assessed through a time-sweep analysis at a fixed temperature (34°C). FCMC demonstrated the quickest gelation of 28 ± 2 seconds (Figure 2-9C) which was followed by FCS (37 ± 3 seconds) (Figure 2-9A) and FPEG (> 60 seconds) (Figure 2-9B).

At nasal cavity temperature, a significant shear thinning behaviour was observed in all formulations, indicative of temperature-induced gel formation when compared to ambient temperatures (Figure 2.10), with viscosities for 34°C being statistically significantly different to those at 18°C ($P < 0.0001$). Furthermore, at 34°C no significant difference in viscosity was reported over the range of shear rate studied ($P=0.227$), however FPEG did however demonstrate a statistically significant lower viscosity compared to FCS and FCMC ($P < 0.01$).

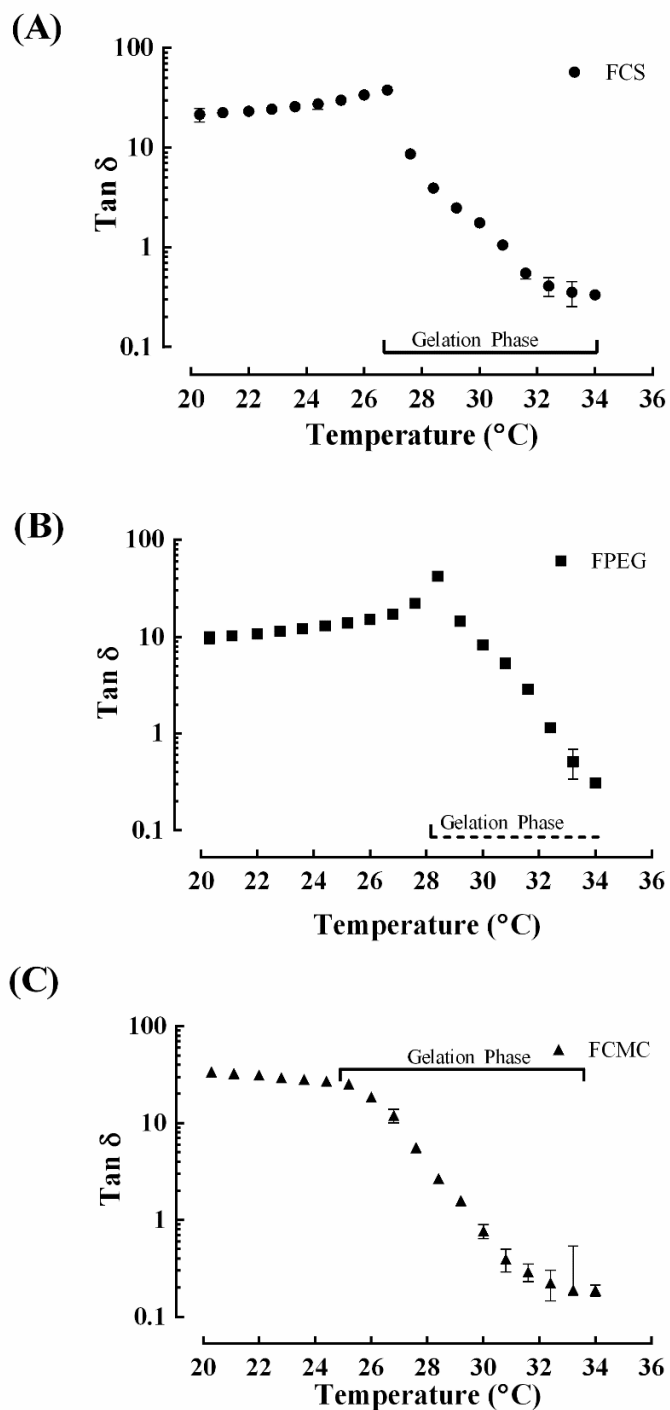


Figure 2-8: Temperature sweep of AMT containing formulations

Rheological analysis of AMT containing thermoresponsive gels. Figures A-C represent temperature sweep analysis for FCS, FPEG and FCMC using parallel plate geometry with 40mm steel plates having a gap 1.0mm. The approximate sample volume used was 1.26mL and the instrument was used in the oscillatory mode in the linear viscoelastic range. Data represents mean \pm SD. n=4

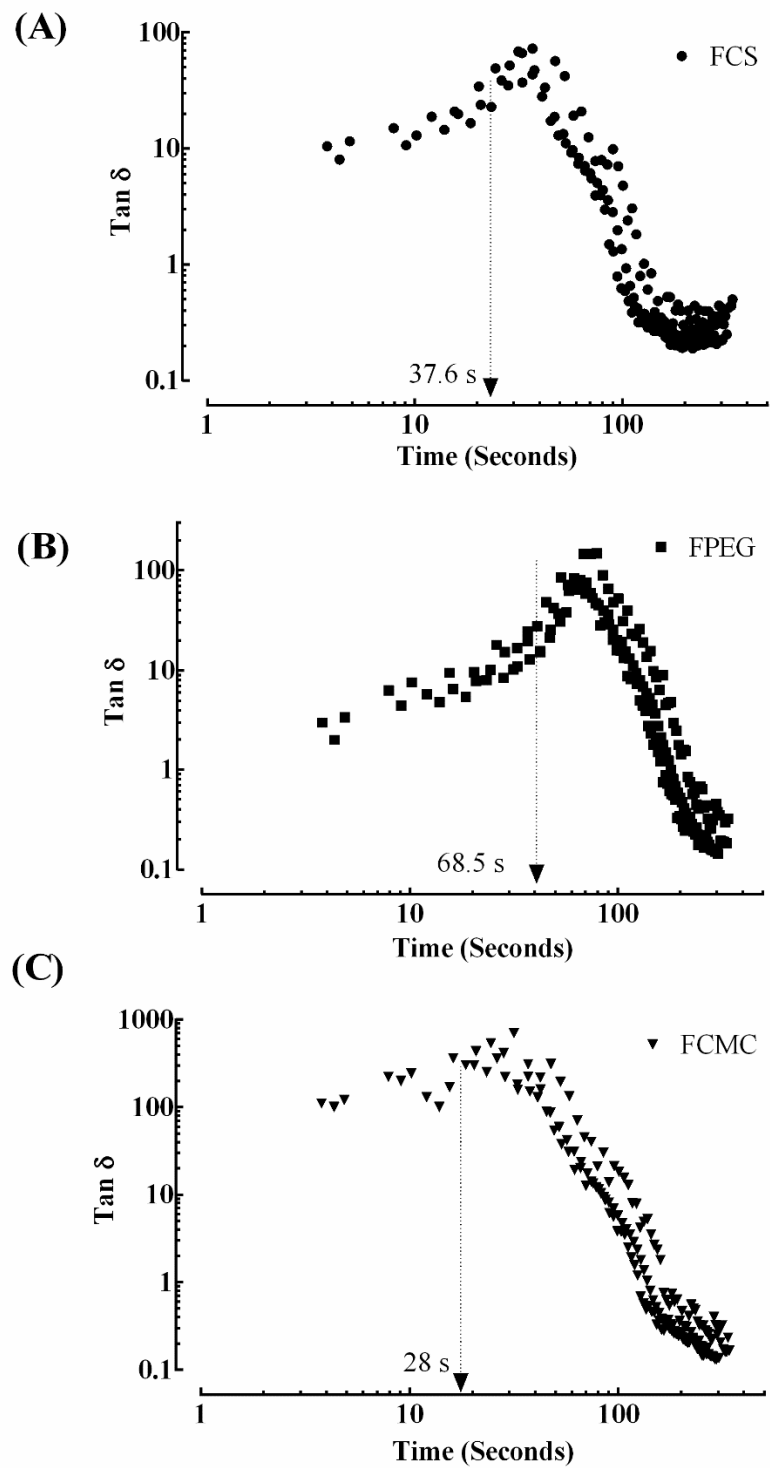


Figure 2-9: Time sweep of AMT containing formulations

Rheological analysis of AMT containing thermoresponsive gels. Figures A-C represent time sweep analysis at 34°C for FCS, FPEG and FCMC using parallel plate geometry with 40mm steel plates having a gap 1.0mm. The approximate sample volume used was 1.26mL and the instrument was used in the oscillatory mode in the linear viscoelastic range. Data represents mean \pm SD. n=4

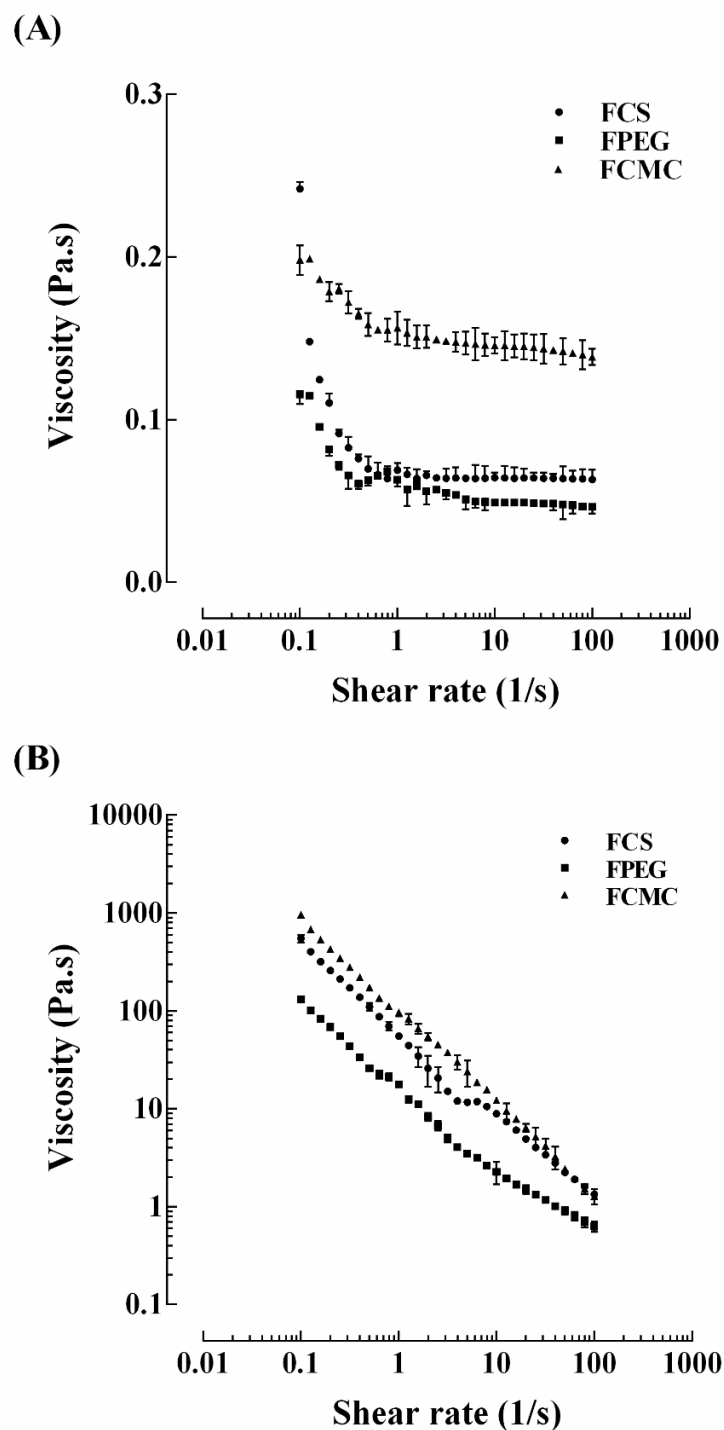


Figure 2-10: Steady shear behaviour of AMT containing formulations

Rheological shear viscosity analysis of the formulations (A) at ambient (18°C) and (B) at nasal cavity (34°C) temperature. Figures A-C represent steady shear analysis at 34°C for FCS, FPEG and FCMC using parallel plate geometry with 40mm steel plates having a gap 1.0mm. The approximate sample volume used was 1.26mL and the instrument was used in the oscillatory mode in the linear viscoelastic range. Data represents mean \pm SD. n=4

As the shear rate increased from 0.091 to 100 s⁻¹, the viscosity of the formulations dropped by 990-fold (FCMC), 409-fold (FCS) and 207-fold (FPEG) (Figure 2-10B). However, all formulations demonstrated Newtonian behaviour at nasal temperature compared to non-Newtonian (pseudoplastic) behaviour at ambient temperatures (Table 2-8), with significantly larger consistency coefficients (13-100 Pa.sⁿ) compared to those at ambient temperatures (0.06-0.157 Pa.sⁿ) (Table 2-8).

Furthmore as the shear rate at 34°C increased (Figure 2.10B), FCS viscosity started to decrease and it matched up with FCMC at the end of the test at shear rate 100.

Table 2-8: Power law rheological analysis of AMT at ambient and nasal temperatures

Formulation	Temperature (°C)	<i>K</i> (Pa.sⁿ)	<i>n</i>	Behaviour
FCMC	18	0.157	0.972	Non-Newtonian
FPEG	18	0.0545	0.9651	Non-Newtonian
FCS	18	0.0656	0.997	Non-Newtonian
FCMC	34	100.2	0.066	Newtonian
FPEG	34	13.59	0.3043	Newtonian
FCS	34	56.56	0.1762	Newtonian

m: Power-law consistency coefficient; *n*: Power-law index value

2.4.3.2. Assessment of formulation mucoadhesion: texture analysis

The results demonstrate that the required force for detachment of the mucin disc from the formulation FCMC was the greatest (48.3g ± 36.1g) followed by FPEG (36.6g ± 27.54g) and FCS (31.6g ± 7.6g) (Figure 2-11). However, a high degree of variability was noted in the experiment design and therefore no statistical significance between any of the formulations were identified.

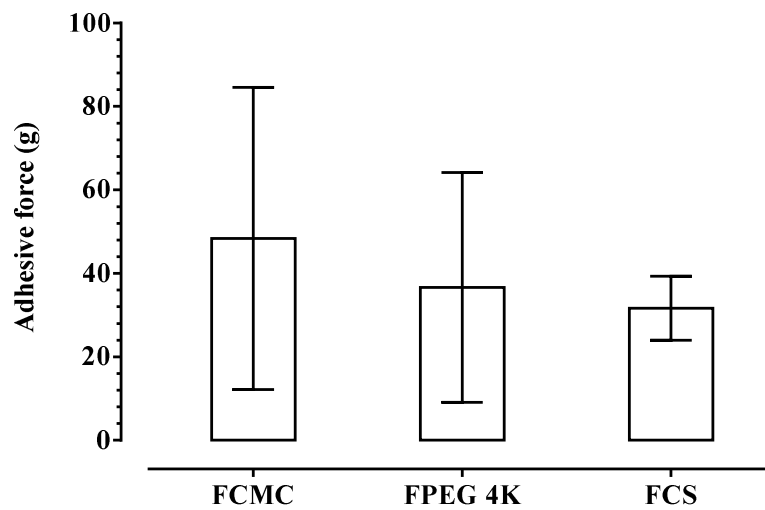


Figure 2-11: Assessment of formulation mucoadhesion through tensile strength measurements

Tensile strength of each optimised formulation was assessed through the interaction of the formulation with a mucin disc attached to a Brookfield's Texture analyser CT3 at 34°C. The force of detachment was measured with a detachment speed of 0.1mM/sec. FCMC: optimised caboxymethyl cellulose formulation; FPEG 4K: optimised PEG 4000 formulation; FCS: optimised chitosan formulation. Data represents mean ± SD. n=3.

2.4.3.3. Assessment of formulation mucoadhesion: displacement method

Mucoadhesion of the optimised formulations was further assessed using an inclined-plate method in the presence and absence of mucin as described by (Nakamura et al., 1999). In this test, mucoadhesion is assumed to have occurred if the displacement of the formulation in the absence of mucin is greater than in the presence of mucin (Nakamura *et al.*, 1999).

In the absence of mucin, statistically significant differences were observed in the displacement transfer between all optimised formulations ($P \leq 0.001$). With the inclusion of mucin, similar statistically significant differences were observed in the displacement transfer between all optimised formulations ($P \leq 0.001$) (Figure 2-12). Furthermore, all formulations demonstrated significant differences in the displacement transfer when comparing absence to the presence of mucin, indicating formulation mucoadhesion. The greatest displacement was observed with FPEG (absence of mucin: 9.5cm ± 0.05cm; presence of mucin: 5.7cm ± 0.19cm) with FCM demonstrating the least displacement (absence of mucin: 6.5cm ± 0.34cm; presence of mucin: 4.24cm ± 0.34cm) (Figure 2-12).

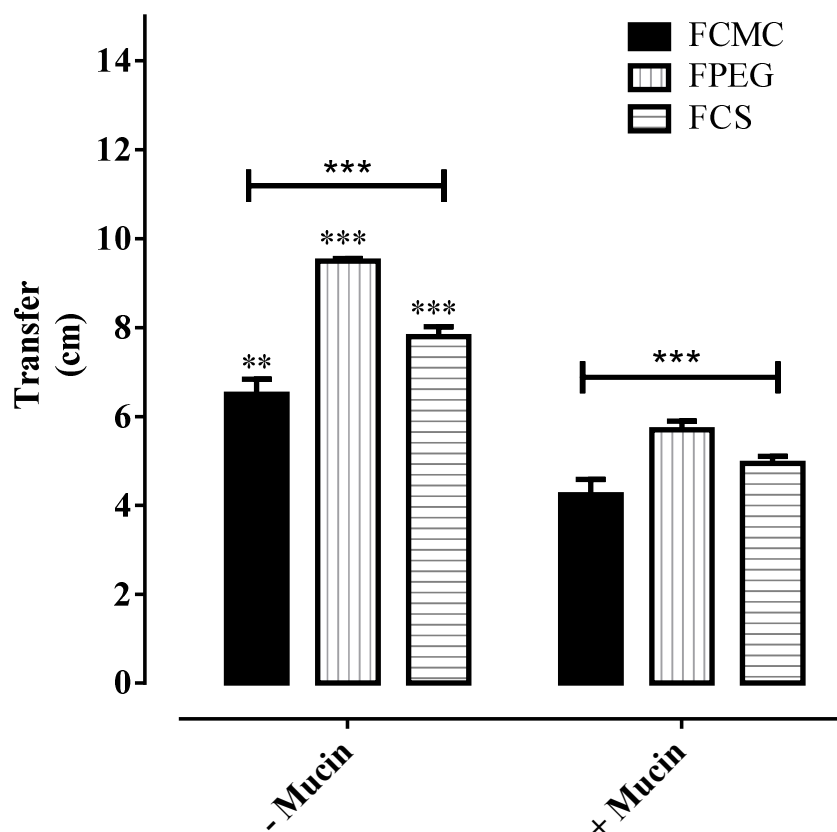


Figure 2-12: Assessment of formulation mucoadhesion through displacement measurements

Displacement transfer of optimised formulations in the absence and presence of mucin-containing agar gel plates. Mucoadhesion was assessed through application of a 250 μ L sample of each formulation when the plate was kept at a 45° angle in VWR orbital shaker maintained at 34°C. The displacement (cm) was used as a measure of the potential for adhesion. Data represents mean \pm SD. ** \leq P 0.01; *** \leq P 0.001. n=3.

2.4.3.4. Validation of a pre-column derivatisation method to detect AMT

The lack of chromophoric group makes the UV-detection of AMT difficult. However an approach developed by (Narola et al., 2010) for detecting memantine hydrochloride was adapted to detect AMT through pre-column derivatisation followed by HPLC-UV analysis.

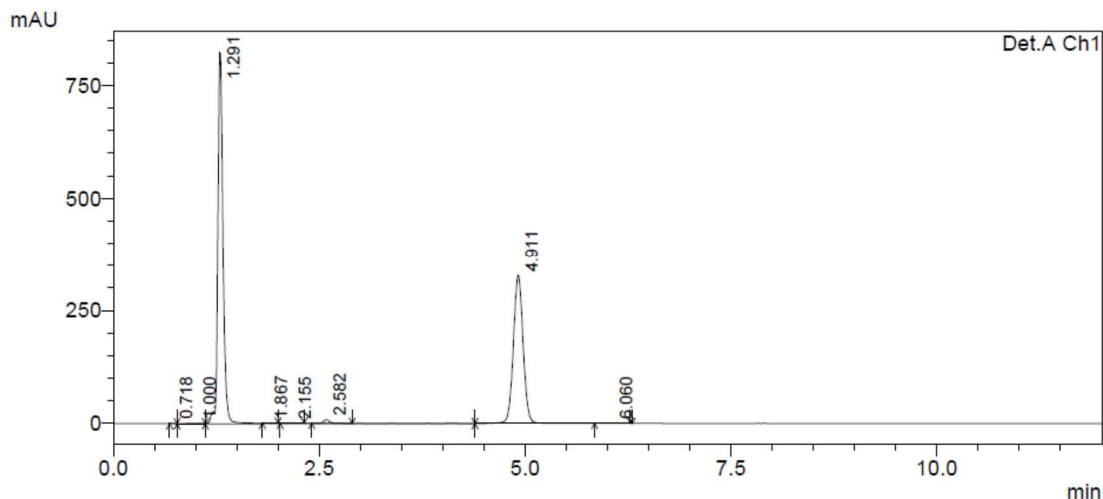


Figure 2-13: HPLC chromatogram of derivatised amantadine at retention time 4.911 min.

A Shimadzu HPLC system was used with a Phenomenex Luna C18 (150 × 4.6mm) 5µm column. The mobile phase consisted of premixed and degassed phosphate buffer:acetonitrile (20:80 v/v) which was filtered through 0.45µm membrane filter. The column was maintained at 30°C and volume of injection was 10µL. The flow rate was maintained at 2mL/minute with run time 12 minutes.

The pre-column derivatisation method developed was successfully used to detect AMT with a retention time of 4.9 minutes (Figure 2-13). System precision and method precision demonstrated RSD within acceptable limits of 1% and 2% respectively, indicating an acceptable level of precision of the analytical system.

System precision: six replicate injections of an identical standard AMT stock solution were injected into the HPLC and peak area calculated. The relative standard deviation (% RSD) for the six samples was not more than 1.0% indicating system precision is within acceptable limits as measured per individual run, each with its own identical standard AMT stock solution, with an overall RSD of 0.30% (Table 2-9).

Table 2-9: System precision assessment for AMT pre-column derivitisation method

Injection no.	Area counts ($\mu\text{V sec}$)			
	Run 1	Run 2	Run 3	Mean
1	2702580	2698550	2694502	2698544
2	2702812	2675784	2675811	2684802
3	2699283	2674899	2677574	2683919
4	2698179	2672313	2674985	2681826
5	2694163	2667233	2663766	2675054
6	2697227	2670255	2671056	2679513
Mean	2699041	2676506	2676282	2683943
SD	3306.0	11240.0	10193.3	7963.1
RSD (%)	0.12	0.42	0.38	0.30

System precision was assessed through 6 injection of the same AMT stock solution for each independent runs (3 runs in total). Mean and SD reported with percentage root-square deviation.

Method precision: six preparations of the same batch of samples were analysed for method precision with a resultant% RSD of less than 2.0% (Table 2-10) for all samples demonstrating method precision is within acceptable limits. Six replicate injections of the same batch sample of AMT solution were injected into the HPLC and peak area calculated and used to determine AMT content. The relative standard deviation (% RSD) for the six samples was not more than 2.0% indicating method precision is within acceptable limits and with an overall mean RSD for three independent runs of 0.72%.

Table 2-10: Method precision assessment for AMT pre-column derivitisation method

Injection no.	Assay (% w/w)			
	Run 1	Run 2	Run 3	Mean
1	101.10	99.90	101.25	100.75
2	100.50	100.10	103.25	101.28
3	100.30	98.99	100.78	100.02
4	99.50	100.58	99.12	99.73
5	98.90	101.10	98.25	99.42
6	100.60	99.12	99.23	99.65
Mean	100.15	99.97	100.31	100.14
SD	0.80	0.82	1.82	0.72
RSD (%)	0.80	0.82	1.81	0.72

Linearity of response: the linearity of precision for derivitised AMT was determined over a concentration range of 62.5 -1000µg/mL. A proportional response was evident versus the analytical concentration over the working concentration range with a r^2 of 0.9987 and linear equation of $y = 1354 \pm 9.07 \cdot x$ (Figure 2-14). The LOD was 2.8µg/mL, LOQ was 8.7µg/mL, and the signal to noise ratio was >10.

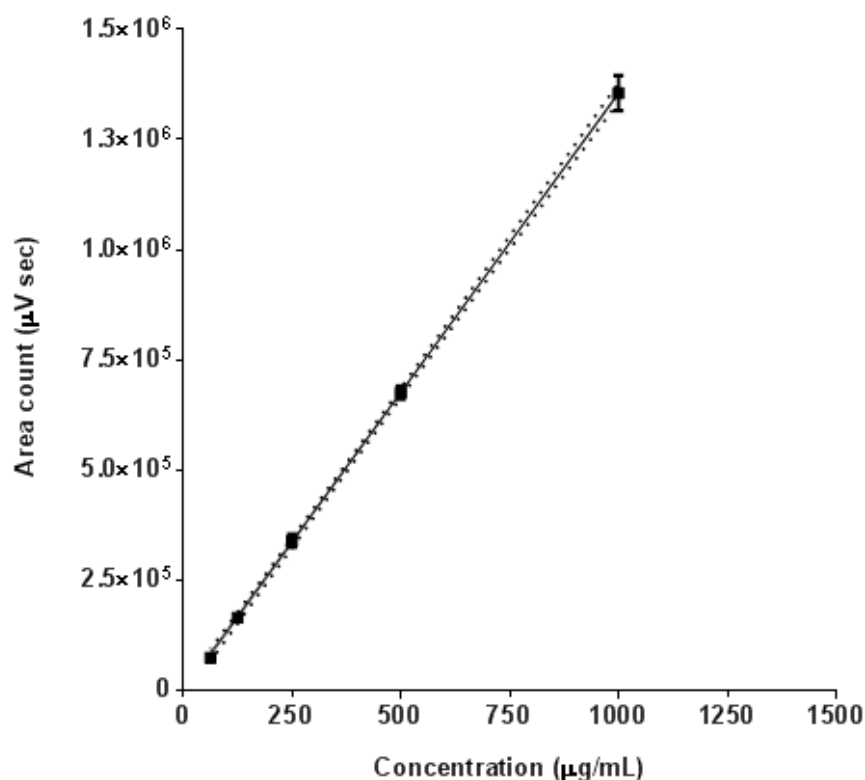


Figure 2-14: Linearity plot for a AMT pre-column derivatisation method

A RP-HPLC method was used with a Phenomenex Luna C18 (150 × 4.6mm) 5µm column. The mobile phase consisted of phosphate buffer:acetonitrile (20:80v/v). The column was maintained at 30°C and volume of injection was 10µL. The flow rate was maintained at 2ml/minute with run time 7 minutes. Data represents mean (solid line) ± SD (error bars). Dotted lines represent 95% confidence intervals for the best fit line. n=3.

2.4.3.5. Human nasal epithelial cell culture model: MTT assay

To investigate the toxicity of AMT and polymers used within the formulations, a cellular viability study was conducted using RPMI-2650. Cell viability was generally maintained for AMT up to 1mM, with an IC₅₀ of 4.6mM ± 0.05mM (Figure 2-15A) when exposed for 24 hours. For all polymers tested in RPMI 2650, no significant decrease in cellular viability was observed up to 4mg/mL (Figure 2-15B to E).

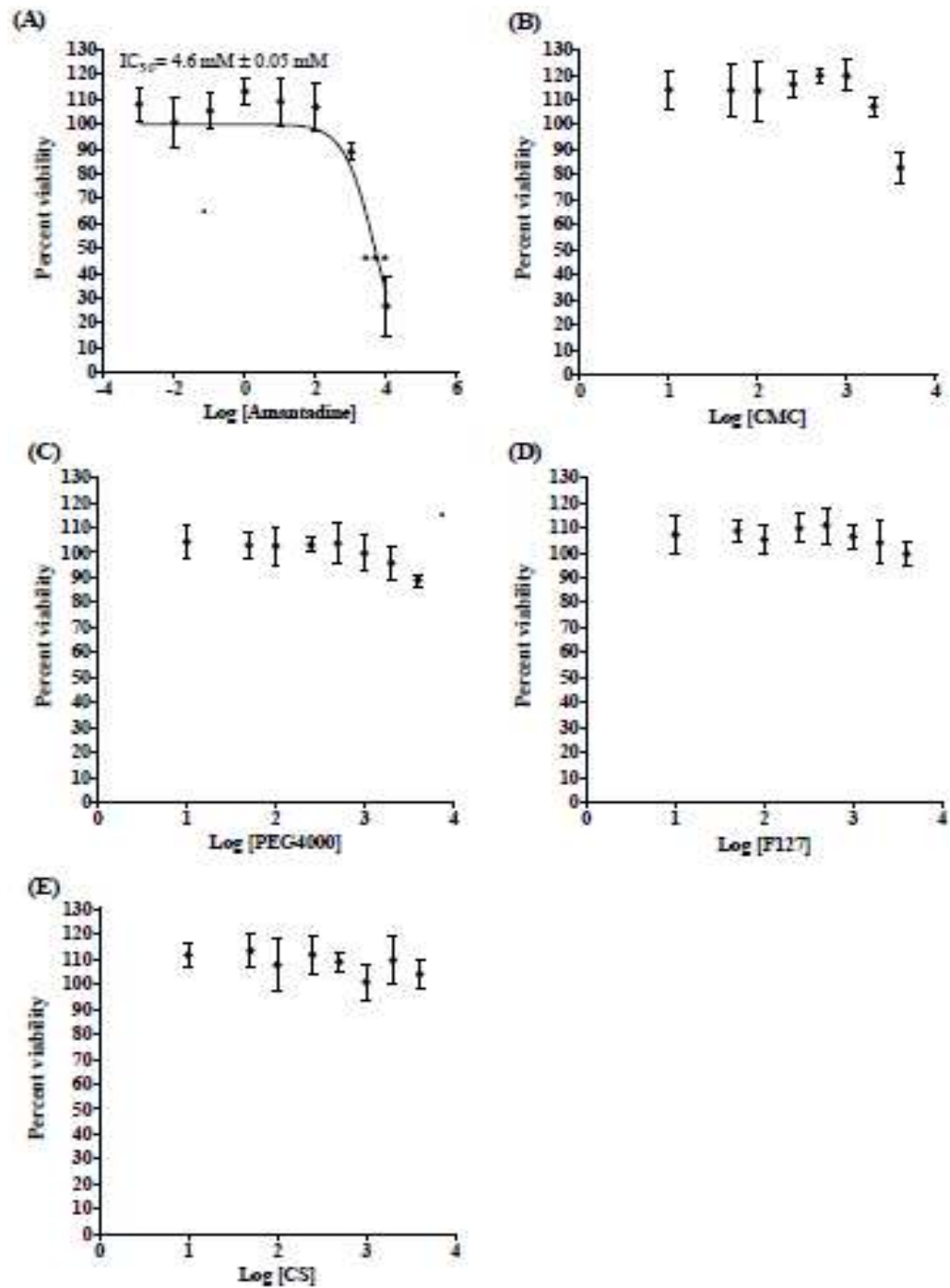


Figure 2-15: Cellular toxicity of amantadine (A), CMC (B), PEG4000 (C), F127 (D) and CS (E) on RPMI-2650 cells.

Cells were grown on a 96-well plate at a density of 20×10^3 cells per well and exposed to various concentrations of amantadine (0.0001 – 10000 μM) or polymer (10-4000 $\mu\text{g}/\text{mL}$). After 24 hour incubation 10 μL MTT in PBS (0.5mg/mL) added to each well & incubated for 4 hours. The MTT-formazan produced was solubilised in DMSO and quantified colorimetrically using spectrophotometer. The control cell (without drug) corresponded to a cell viability of 100%. Data is reported as mean \pm SD with up to 8 replicates per compound in at least 3 independent experiment.

2.4.3.6. Porcine olfactory bulb cell culture model: MTT assay

To investigate the toxicity of amantadine and polymers used within the formulations with olfactory neurones, the OBGF400 cell line was used as a surrogate for the olfactory nasal mucosa and olfactory neural pathways to assess the cellular viability study of cells in the presence of the formulation components. Cell viability was generally maintained for AMT and all polymers incorporated into the formulations across the concentration ranges studied with no significant decreases in cellular viability (Figure 2-16).

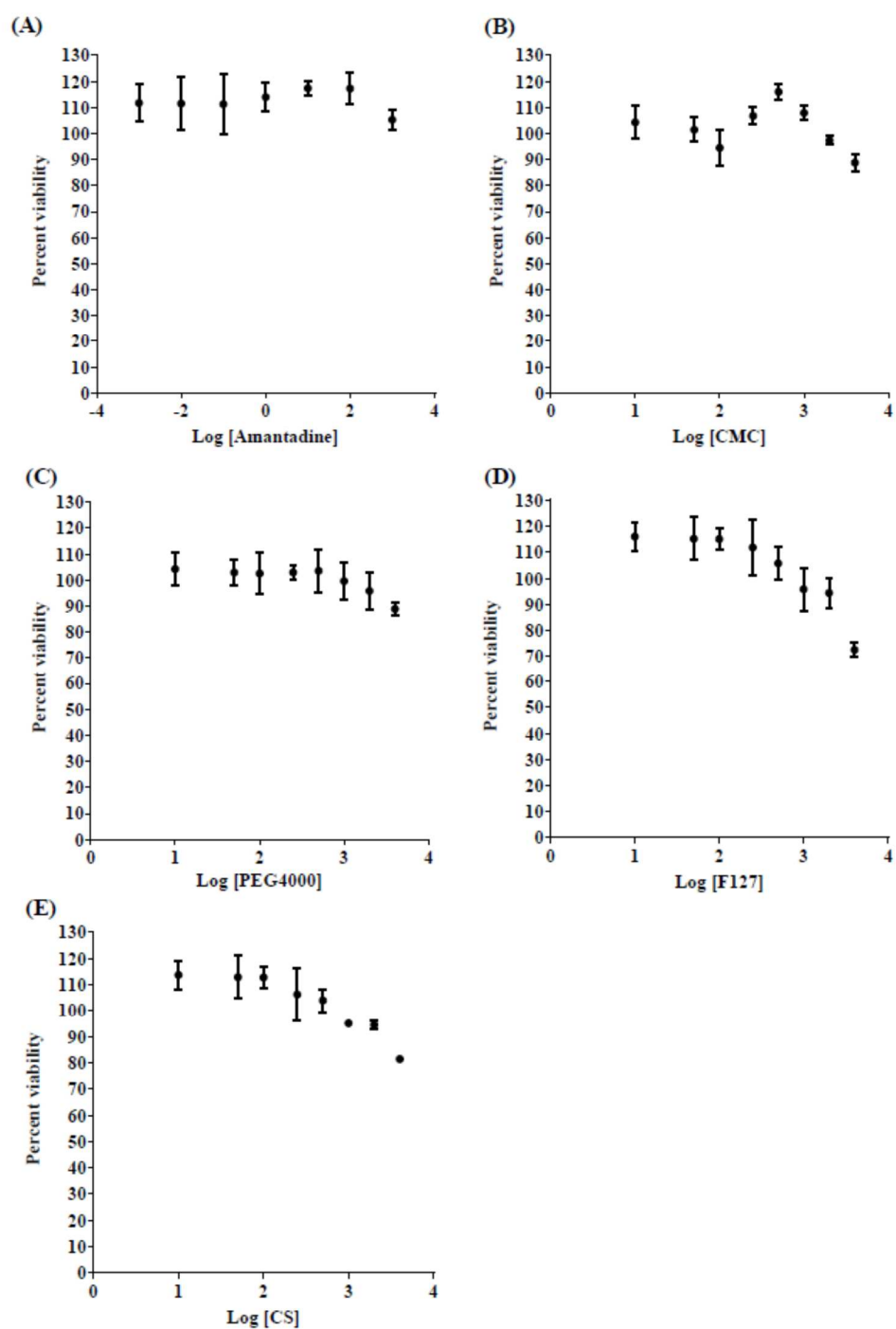


Figure 2-16: Cellular toxicity of amantadine (A), CMC (B), PEG4000 (C), F127 (D) and CS (E) on OBGF400.

Cells were grown on a 96-well plate at a density of 10×10^3 cells per well and exposed to various concentrations of amantadine (0.0001 – 10000 μ M) or polymer (10-4000 μ g/mL). After 24 hour incubation 100 μ L MTT in PBS (0.5mg/mL) added to each well & incubated for 4 hours. The MTT-formazan produced was solubilised in DMSO and quantified colorimetrically using spectrophotometer. The control cell (without drug) corresponded to a cell viability of 100%. Data is reported as mean \pm SD with up to 8 replicates per compound in at least 3 independent experiment.

2.4.3.7. The development of a human nasal epithelial airway cell culture model

RPMI 2650 cells were used to develop a permeable-insert based cell culture model of the human nasal epithelial using an ALI. RPMI 2650 cells were grown for 22 days with an ALI initiated on the 6th day post-seeding. The TEER was used as a measure of monolayer formation and rose steadily during the first 10 days post-seeding and reaching peak TEER over days 12-20 (126-140 $\Omega\cdot\text{cm}^2$) (Figure 2-17).

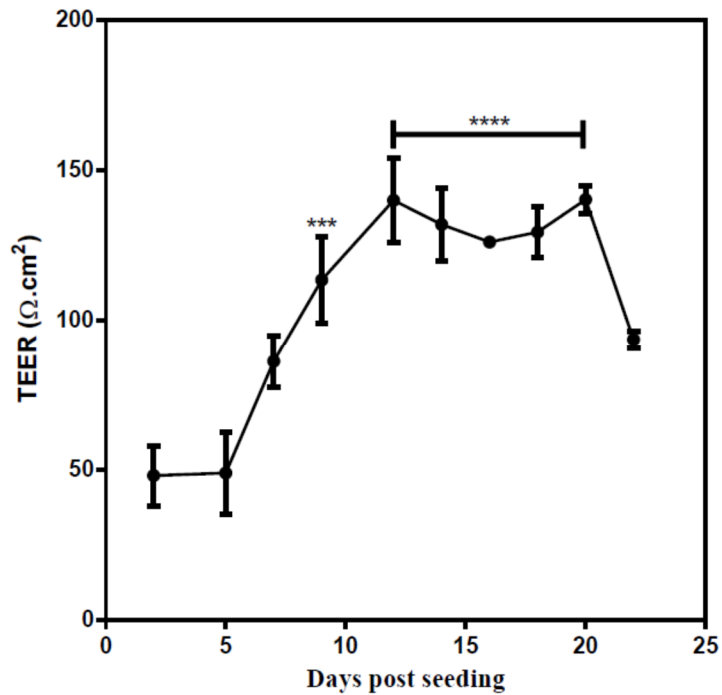


Figure 2-17: Monolayer resistance of RPMI 2650 cells grown on permeable inserts.

RPMI 2650 cells were seeded at a density of 4×10^5 cells/cm² onto collagen coated inserts and incubated at 37°C with 5% CO₂ in a humidified atmosphere. The media was replaced every other day and TEER values were measured with EVOM voltammeter up to 22 days. Statistical analysis compares TEER at day 2 to all other data points. *** $P \leq 0.001$ and **** $P \leq 0.001$. N=3.

2.4.3.8. Human nasal epithelial airway cell culture model: AMT transport

The *in-vitro* release of AMT alone and from formulations was further assessed in an *in-vitro* nasal epithelial airway cell culture model over 3-hours (Figure 2-18).

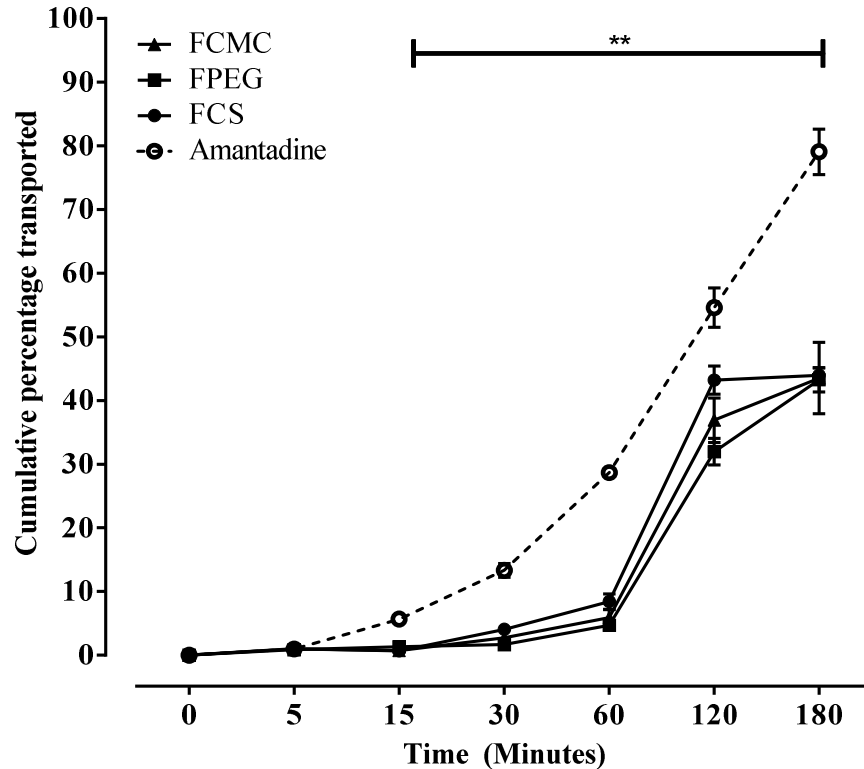


Figure 2-18: Release and transport of AMT from formulations

The transport of AMT was assessed across an *in-vitro* permeable insert cell culture model of the human nasal epithelia. N= 3, ** P ≤ 0.01

In all formulations a statistically significant ($P \leq 0.01$) mean release of 43-44% was observed over the duration of the transport study in comparison to that of AMT alone ($79\% \pm 3.58\%$) (Figure 2-18) when studied across RPMI 2650 monolayers. No significant difference in release was observed within the 3 optimised formulations.

2.4.4. Stability and AMT release from optimised formulations

To assess the stability of the optimised formulations, batches were prepared and stored in stability cabinets at 25°C/60 % RH and refrigerated (4°C) for 8 weeks, with sampling of drug at weekly intervals to assess gelation and release profiles. At preparation (week 0), all formulations demonstrated similar release profiles with Higuchi kinetics and Fickian-type diffusion (Table 2-11 and Figure 2-19). During the first week of storage at 4°C, all formulations demonstrated similar release profiles to week 0 (Figure 2-20). However, after 1-week storage at 25°C/60 % RH only FCS demonstrated a gelation transition and showed a similar release profile to week 0 (Figure 2-20), while FPEG and FCMC failed to gel at 34°C.

FCMC and FCS continued to show gelation phenomena over the 8-week study period when stored at 4°C but FPEG did not gel after the first week of storage at 4°C (Figure 2-21). Statistically significant differences ($P < 0.05$) in the release profile of FCMC and FCS were observed after 8-weeks storage at 4°C, typically resulting in slower release profiles (reduction in kH at week 8 compared to week 0) (Table 2-11). FCS continued to show gelation phenomena at 25°C/60 % RH at week 2 (Figure 2-22), but failed thereafter to gel.

In all cases, AMT release obeyed a Higuchi model, with a consistent release constant (kK : 1.2-1.5), although this was significantly reduced at 8-weeks (FCMC: 1.440 ± 0.150 to 1.224 ± 0.063 ; FCS: 1.319 ± 0.028 to 1.291 ± 0.043). Diffusion was modelled by the Korsmeyer-Peppas power law and generally demonstrated Fickian-type diffusion early on (except for FCS). By week 8 this had moved towards anomalous transport (Table 2-11), whereby drug diffusions and the polymer relaxation were contributing to the overall release kinetics.

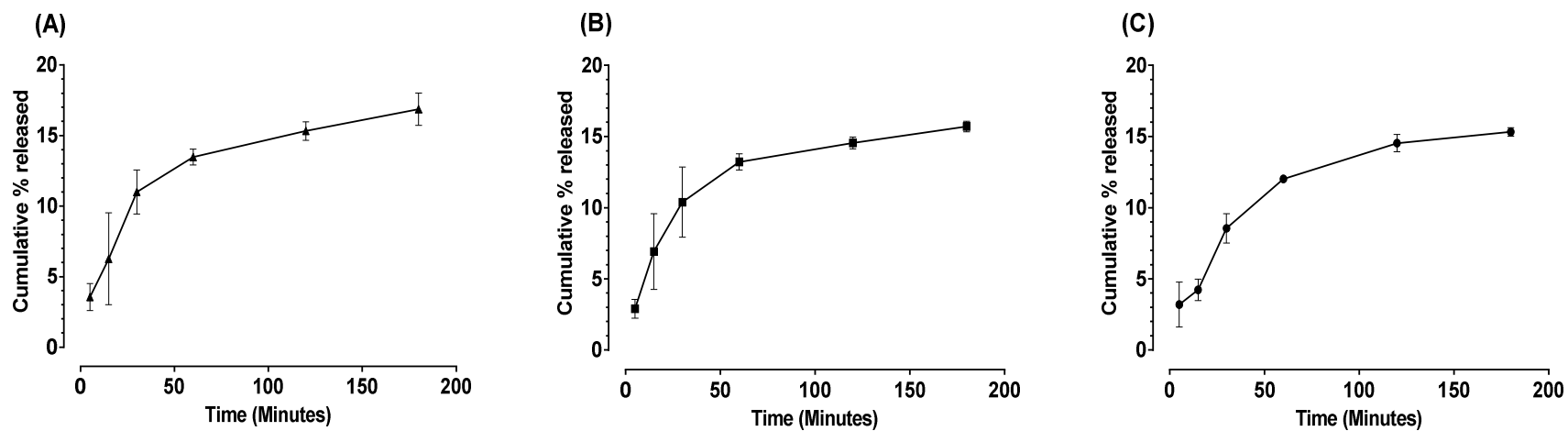


Figure 2-19: Amantadine cumulative % release for optimised formulations at week 0 and stored at 4°C, (A) FCMC; (B) FCS and (C) FPEG

Formulations were prepared and immediately assessed for drug release at a baseline (termed week 0). The stability of the formulation was assessed based on the gelation of a 250 μ L of sample of the formulation at 34°C with n 5 minutes, followed by assessment of the extent of drug release in ANE in a membrane less diffusion study over three hours and drug content by HPLC. Data represents mean \pm SD. n=3 independent batches.

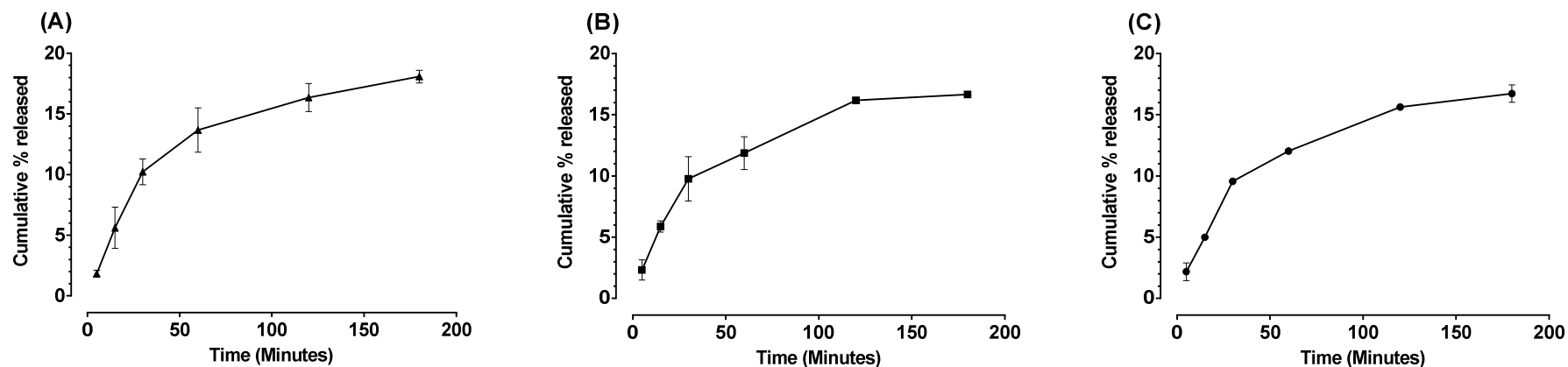


Figure 2-20: Amantadine cumulative % release for optimised formulations at week 1 and stored at 4°C, (A) FCMC; (B) FCS and (C) FPEG

Formulations were prepared and stored in a 4°C stability cabinet at preparation. A sample was withdrawn for assessment of drug release at 1 week post-formulating (termed week 1). The stability of the formulation was assessed based on the gelation of a 250 µL of sample of the formulation at 34°C within 5 minutes, followed by assessment of the extent of drug release in ANE in a membrane less diffusion study over three hours and drug content by HPLC. Data represents mean ± SD. n=3 independent batches.

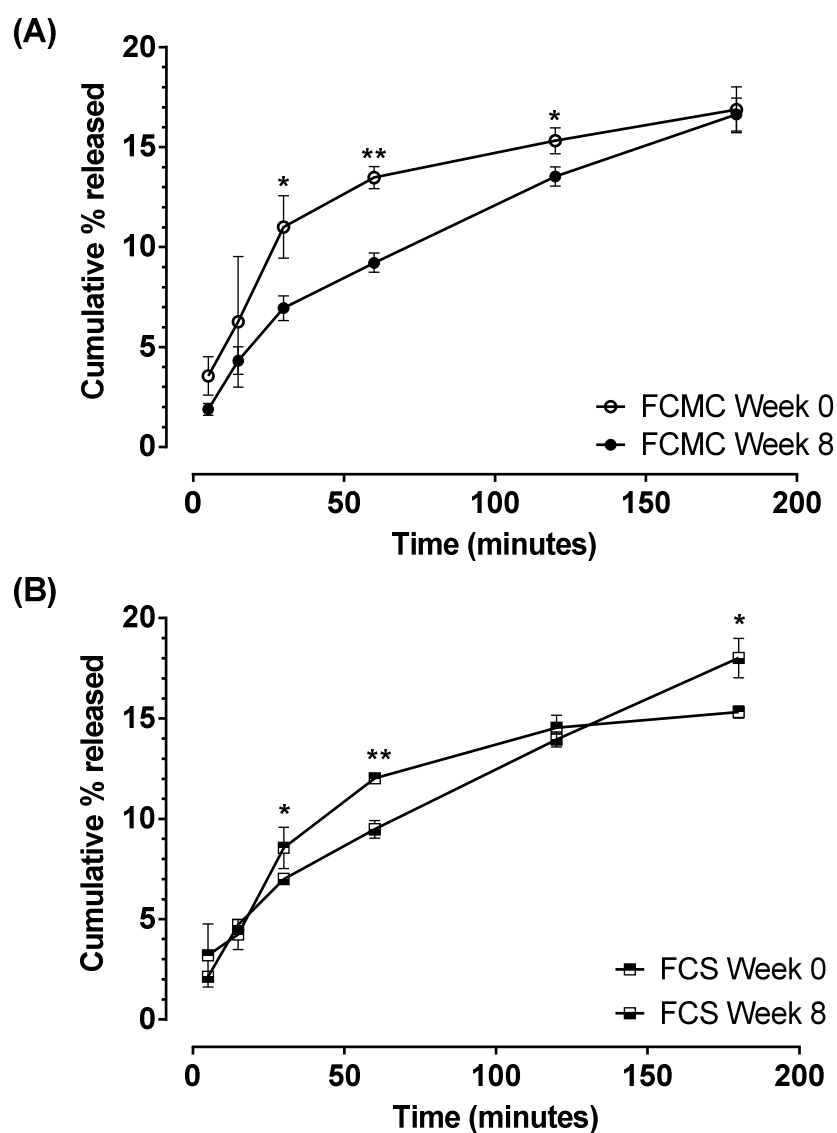


Figure 2-21: Amantadine cumulative % release for optimised formulations at week 8 and stored at 4°C, (A) FCMC; (B) FCS.

Formulations were prepared and stored in a 4°C stability cabinet at preparation. A sample was withdrawn for assessment of drug release at 8 weeks post-formulating (termed week 8) and compared to drug release at preparation (week 0). The stability of the formulation was assessed based on the gelation of a 250 µL of sample of the formulation at 34°C within 5 minutes, followed by assessment of the extent of drug release in ANE in a membrane less diffusion study over three hours and drug content by HPLC. Data represents mean ± SD. n=3 independent batches.

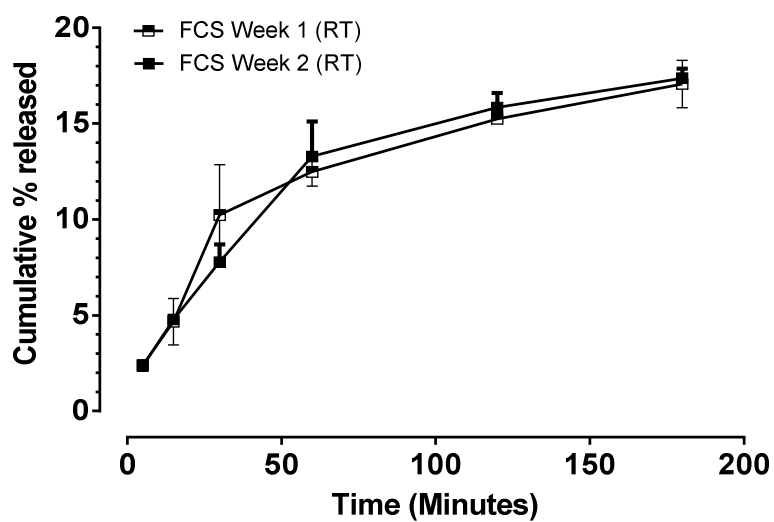


Figure 2-22: Amantadine cumulative % release for FCS at week 1 and 2 stored at 25°C.

Formulations were prepared and stored in a 25°C/60 % RH stability cabinet at preparation. A sample was withdrawn for assessment of drug release at 1 and 2 weeks post-formulating (termed week 1 and 2). The stability of the formulation was assessed based on the gelation of a 250 μ L of sample of the formulation at 34°C within 5 minutes, followed by assessment of the extent of drug release in ANE in a membrane less diffusion study over three hours and drug content by HPLC. Data represents mean \pm SD. n=3 independent batches.

Table 2-11: Drug release kinetics analysis of formulations stored at refrigerated (4°C) and ambient (25°C) temperature for up to 8 weeks.

	Week	Formulation	Higuchi	Korsmeyer-Peppas
4°C	0	FPMC	$kH = 1.440 \pm 0.150$	$kKP = 2.859 \pm 0.899 ; n = 0.391 \pm 0.051$
		FPEG	$kH = 1.372 \pm 0.084$	$kKP = 2.931 \pm 1.160 ; n = 0.352 \pm 0.076$
		FCS	$kH = 1.319 \pm 0.028$	$kKP = 2.888 \pm 0.632 ; n = 0.684 \pm 0.039$
	1	FPMC	$kH = 1.480 \pm 0.091$	$kKP = 2.004 \pm 0.027 ; n = 0.438 \pm 0.024$
		FPEG	$kH = 1.356 \pm 0.087$	$kKP = 2.012 \pm 0.032 ; n = 0.423 \pm 0.013$
		FCS	$kH = 1.485 \pm 0.119$	$kKP = 1.852 \pm 0.135 ; n = 0.433 \pm 0.019$
	8	FPMC	$kH = 1.224 \pm 0.063$	$kKP = 1.034 \pm 0.170 ; n = 0.538 \pm 0.024$
		FCS	$kH = 1.291 \pm 0.043$	$kKP = 1.011 \pm 0.092 ; n = 0.553 \pm 0.024$
	25°C	1	FCS	$kH = 1.385 \pm 0.097$
2		FCS	$kH = 1.394 \pm 0.108$	$kKP = 1.614 \pm 0.351 ; n = 0.474 \pm 0.042$

kH: Higuchi constant; kKP: Korsmeyer-Peppas constant; n= release exponent. Mean \pm SD.

2.4.5. Nasal spray systems: droplet size distribution

Prevention of pulmonary deposition of nasally administered spray formulations is extremely important to ensure residency within the nasal cavity. Droplet size distribution is key in determining the potential for pulmonary deposition ($< 2\mu\text{m}$) (Stuart, 1973, Hatch, 1961a), however the droplet size is often dictated by the design of the orifice of the actuator device used to deliver the spray plume.

All our formulations demonstrated a diameter in excess of the traditional cut-off of $5\mu\text{m}$. (Table 2-12) (Figure 2-23 to 2.25). FCS demonstrated a 10% fraction of $7.27\mu\text{m} \pm 0.28\mu\text{m}$ (Figure 2.24 Table 2-12) closet to the cut-off for pulmonary deposition, whereas both FCMC and FPEG were well above this. FCS also demonstrated the smallest diameter (VMD= $92.41\mu\text{m} \pm 1.72\mu\text{m}$). However, when considering the span of particle sizes, FCS was the broadest ($1.38 \pm 0.$) with both FCMC (Figure 2-25) and FPEG showing a smaller distribution spread (Table 2-12 Figure 2-23).

Table 2-12: Laser diffraction particle size analysis

	Diameter (μm)				
	Dv10	Dv50	Dv90	VMD	Span
FCS	7.27 ± 0.28	109.07 ± 3.42	157.77 ± 0.99	92.41 ± 1.72	1.38 ± 0.21
FCMC	39.81 ± 1.02	129.86 ± 0.29	167.39 ± 0.09	120.87 ± 0.59	0.98 ± 0.30
FPEG	43.93 ± 0.88	104.67 ± 1.88	150.95 ± 1.04	100.35 ± 1.53	1.02 ± 0.06

Dv10, Dv50 and Dv90: particle diameter corresponding to 10, 50 and 90% cumulative undersize particle size distribution; VMD: volume mean diameter; data is represented of mean \pm SD, n=6 replicate spray actuations *per* formulation

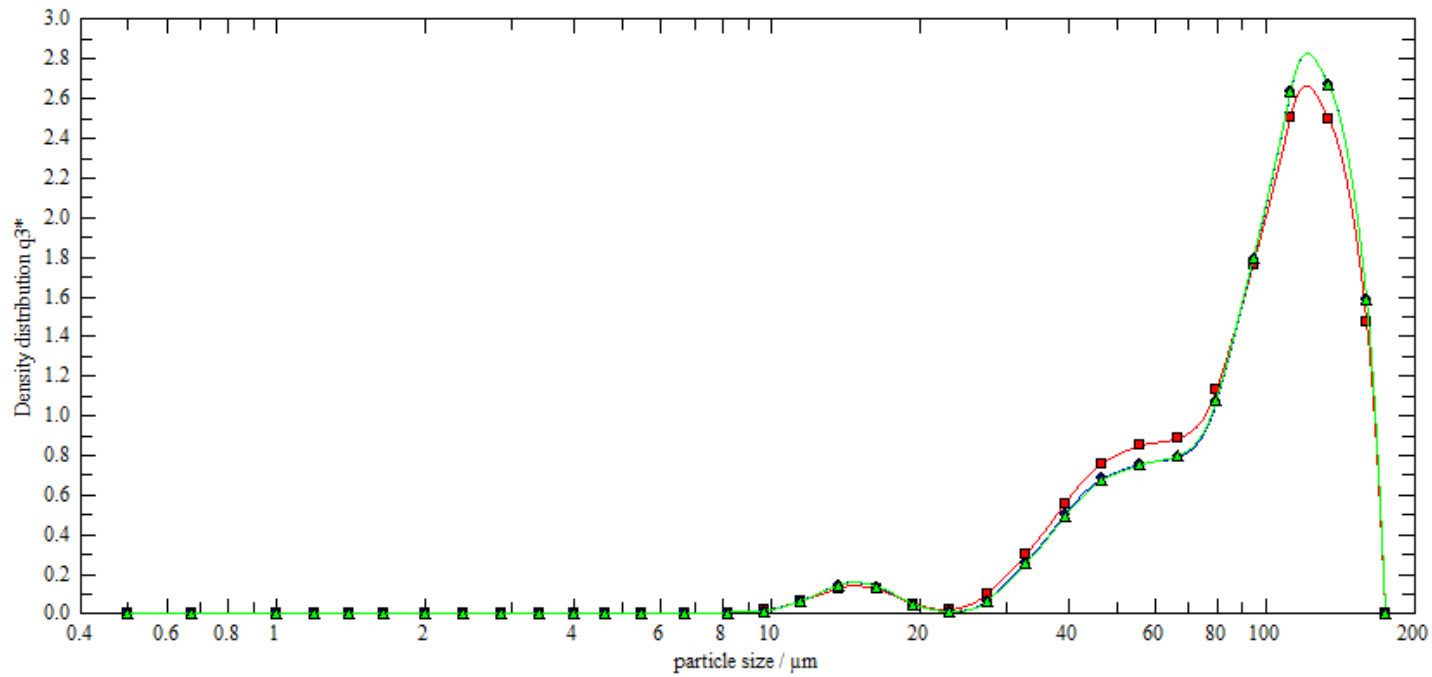


Figure 2-23: Nasal spray droplet size distribution graph for FPEG

The Helos/Sympatec system was used with an R3 lens (0.5-175 μm). The nasal pump was vertically mounted 3cm away from the laser path and a vacuum source was mounted anterior to the pump system. The pump systems were pre-actuated prior to mounting, and actuated three times to detect the particle size distribution. Data was reported as volume diameters at 10%, 50% and 90% of the cumulative undersized volumes.

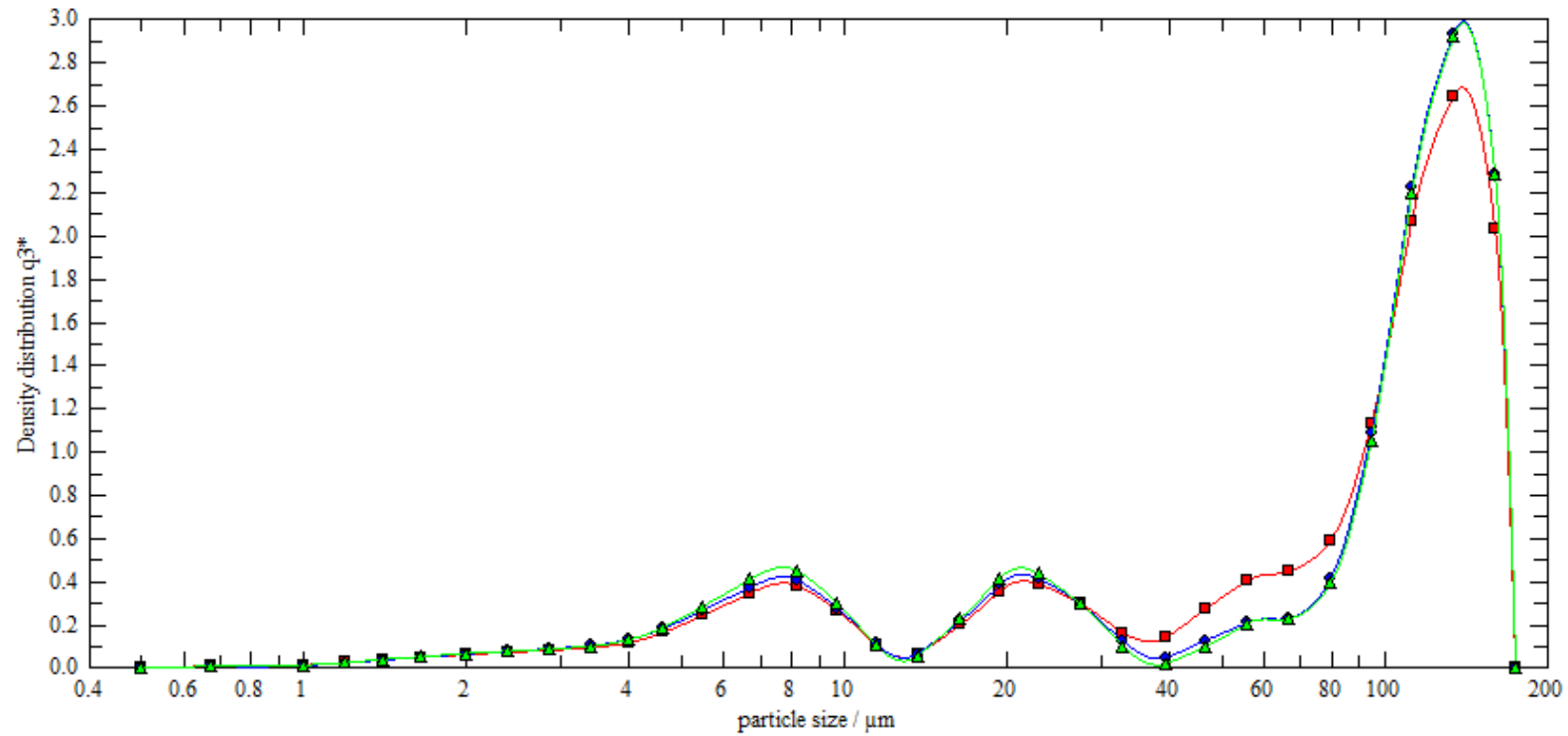


Figure 2-24: Nasal spray droplet size distribution graph for FCS.

The Helos/Sympatec system was used with an R3 lens (0.5-175μm). The nasal pump was vertically mounted 3cm away from the laser path and a vacuum source was mounted anterior to the pump system. The pump systems were pre-actuated prior to mounting, and actuated three times to detect the particle size distribution. Data was reported as volume diameters at 10%, 50% and 90% of the cumulative undersized volumes.

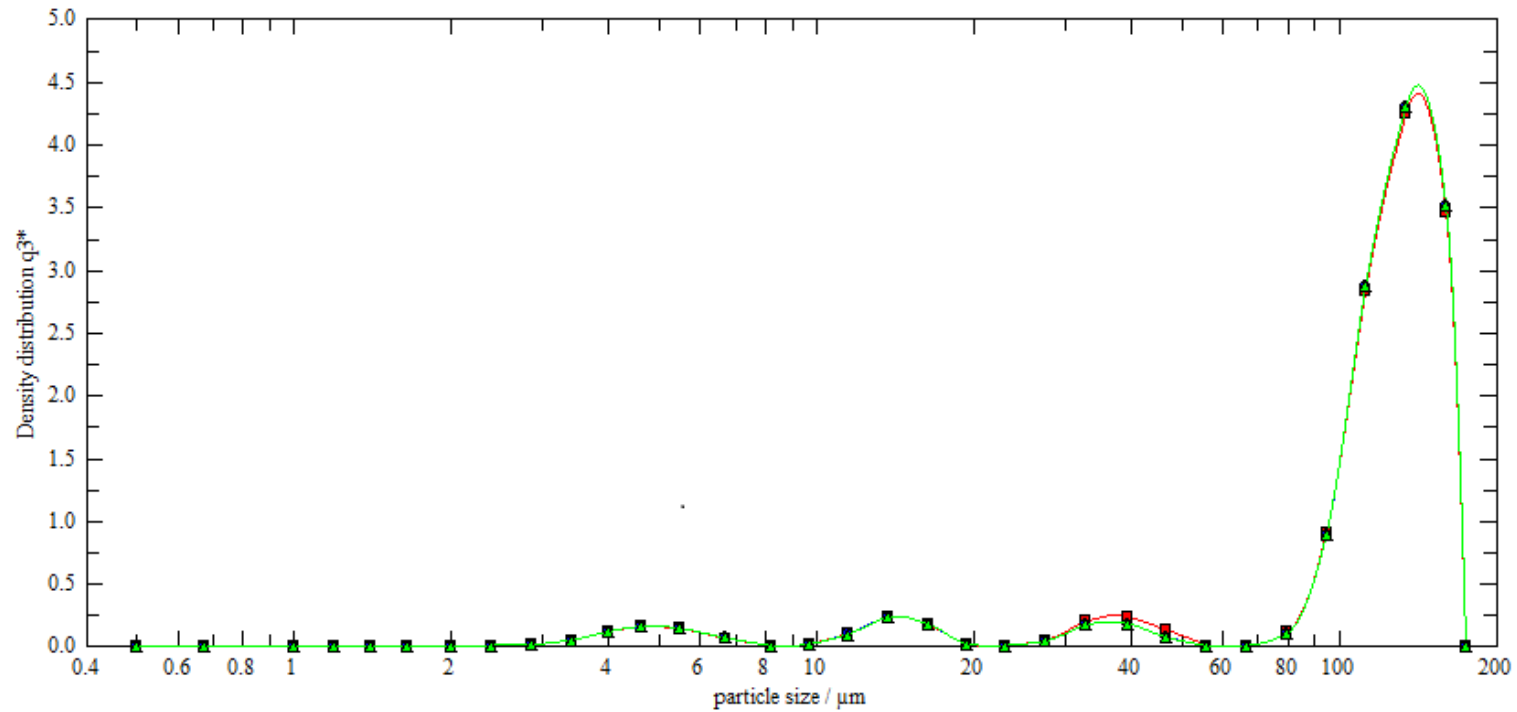


Figure 2-25: Nasal spray droplet size distribution graph for FCMC.

The Helos/Sympatec system was used with an R3 lens (0.5-175 μm). The nasal pump was vertically mounted 3cm away from the laser path and a vacuum source was mounted anterior to the pump system. The pump systems were pre-actuated prior to mounting, and actuated three times to detect the particle size distribution. Data was reported as volume diameters at 10%, 50% and 90% of the cumulative undersized volumes.

2.4.5.1. Nasal spray system: human nasal cast deposition

To assess the potential *in-vivo* application of formulations, the spray deposition within a human nasal cast model was assessed. The angle of spray administration was altered from 60-80° and the impact on deposition patterns assessed. For all formulations the administration angle had a significant effect on deposition, with an increased angle (80°) having a significantly pronounced localisation in the nasal vestibules and lower regions of the nasal cavity. In general, with an increasing angle of spray from 60° to 80°, the deposition for all formulations was more anterior in the nasal cavity.

For FCS the greatest level of olfactory deposition was recorded at 60° (0.7cm²) with spray at an angle of 80° leading to pronounced distribution in the nasal vestibules and middle-upper turbinates (Figure 2-27). Following insertion of the nozzle into the nasal orifice by 5mm, pronounced delivery on the olfactory region was noted at 60° (0.6cm²), which diminished as the angle of spray increased to 80° (0.15cm²) (Figure 2-27). When the nasal cast was tilted by 15° posterior, the deposition across all spray angles was generally localised to the middle-upper turbinates 4.0-4.6cm² with limited olfactory deposition (0.2-0.4cm²) (Figure 2-27).

For FCMC the greatest level of olfactory deposition was reported at 70° (0.25cm²) with spray at an angle of 80° leading to pronounced distribution in the nasal vestibules and middle-upper turbinates (Figure 2-28). Following insertion of the nozzle into the nasal orifice by 5mm, pronounced delivery on the olfactory region was noted at 60° (0.91cm²), which diminished as the angle of spray increased to 80° (0.09cm²) (Figure 2-28). When the nasal cast was tilted by 15° posterior, the deposition across all spray angles was generally localised to the middle-upper turbinates 4.3-4.6cm² with no olfactory deposition (Figure 2-28).

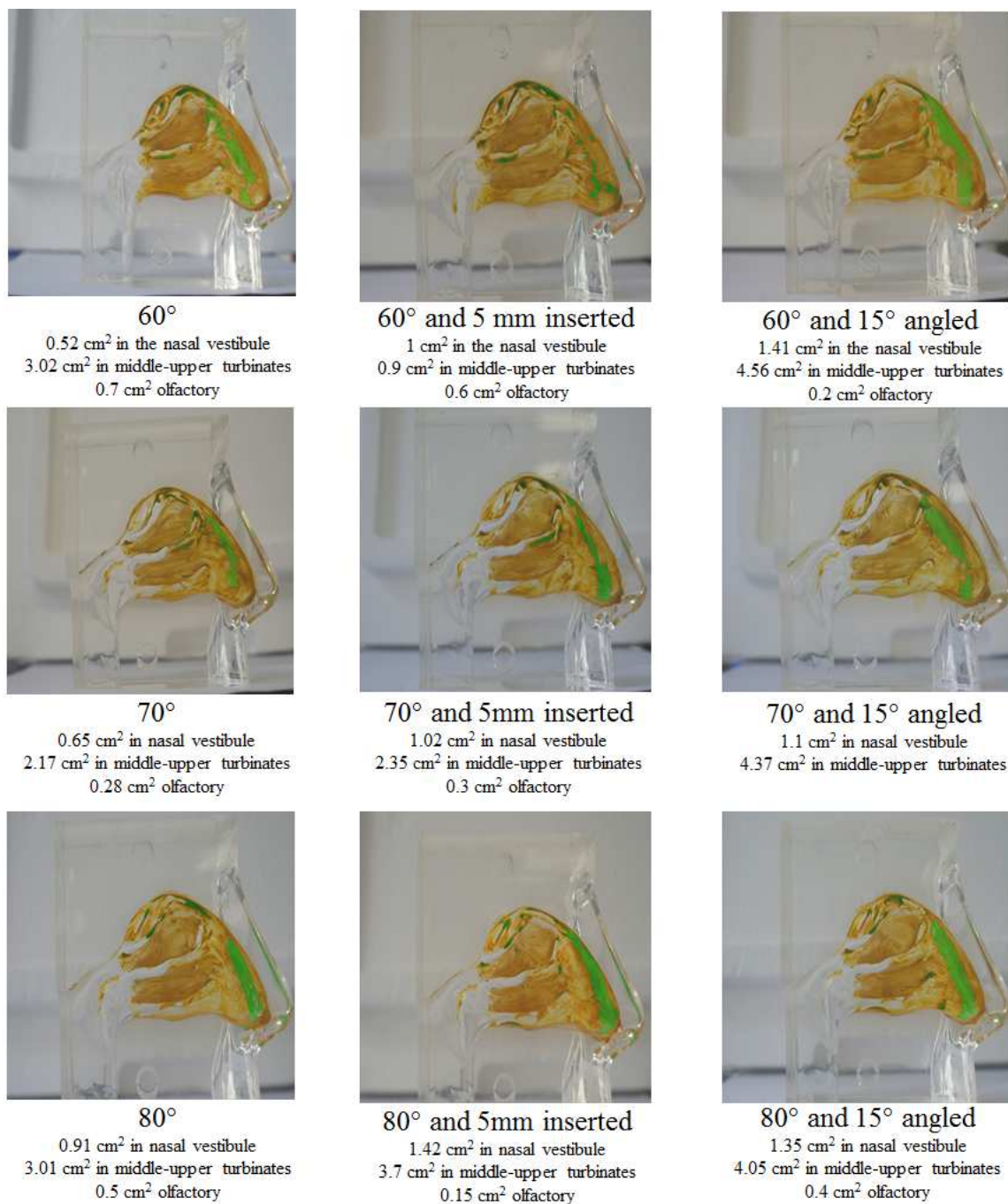


Figure 2-26: Representative nasal deposition patterns of FCS.

The inner surface of each nasal cavity was evenly coated in a water-indicated dye (Kolorkut®). Formulation was loaded into the spray pump, pre-actuated, before one dose was delivered into the nasal cast where the cast was fixed in an upright head position. Angles refer to nasal spray position relative to the horizontal plane (60, 70 or 80°), insertion of the spray orifice into the nostril (5mm) or with the nasal cast angled 15° forward. Green regions represent the deposition of the formulation.

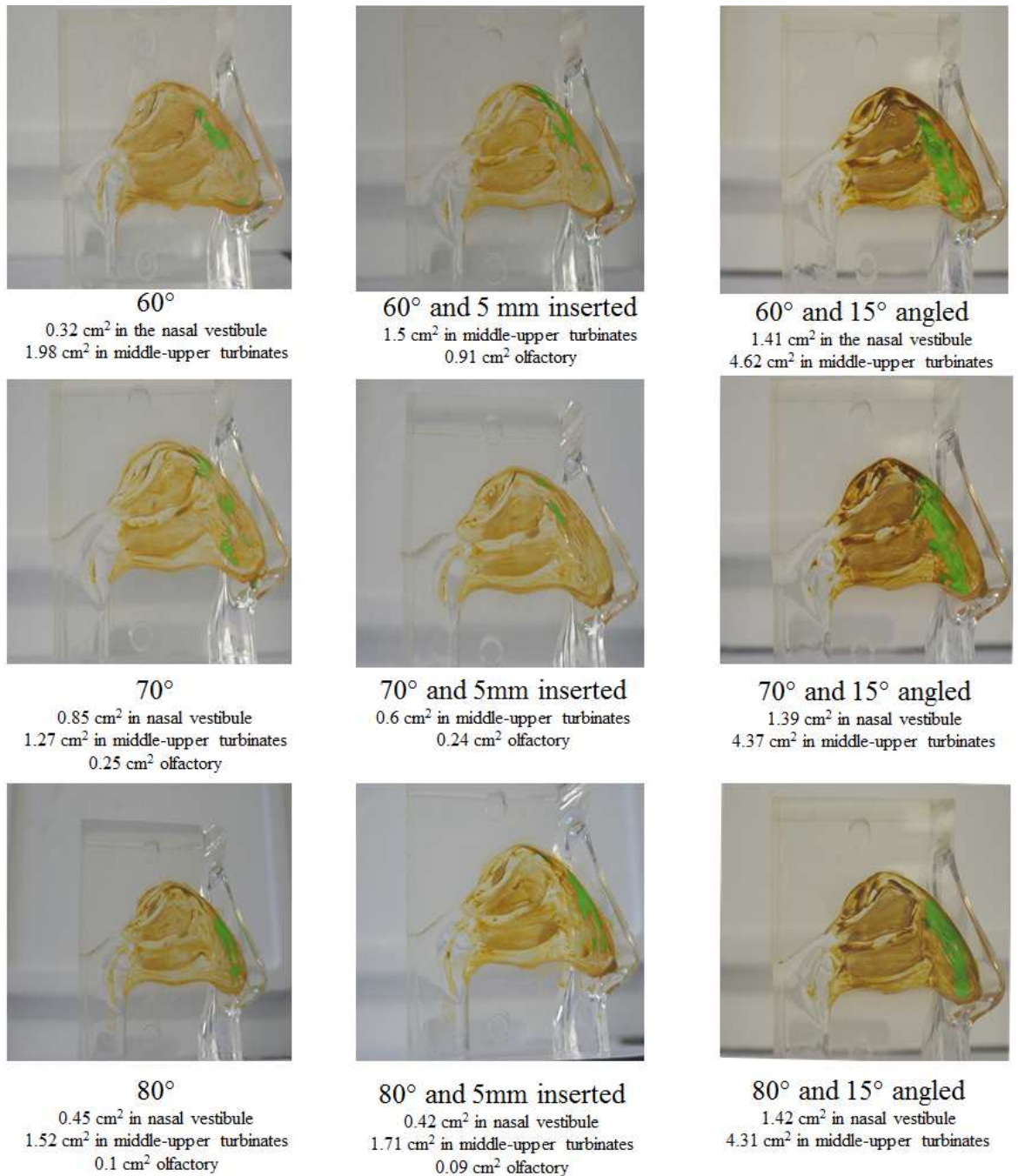


Figure 2-27: Representative nasal deposition patterns of FCMC.

The inner surface of each nasal cavity was evenly coated in a water-indicated dye (Kolorkut). Formulation was loaded into the spray pump, pre-actuated, before one dose was delivered into the nasal cast where the cast was fixed in an upright head position. Angles refer to nasal spray position relative to the horizontal plane (60, 70 or 80°), insertion of the spray orifice into the nostril (5mm) or with the nasal cast angled 15° forward. Green regions represent the deposition of the formulation.

2.5. Discussion

Drug delivery to the CNS is a major challenge due to the presence of the BBB, which acts as a significant physical and metabolic barrier for the transport of therapeutic agents into the wider CNS. The endothelial cells forming the cerebral capillaries of the BBB act as a physical barrier which limits the transport of molecules in and out of the brain and wider CNS (Pardridge, 2007b, Zlokovic, 2008). Age related CNS dementia-type disorders, such as Parkinson's disease (PD) and AD, are insidious progressive neurological disorders which affects over 1.5% of the population over 65-years of age (Foltynie *et al.*, 2004), with age-adjusted prevalence rates thought to be around 150 per 100,000 with a suggested mean onset in the 70's (Foltynie *et al.*, 2004).

One of the major complications of age associated CNS disorders is the emergence of dysphagia affecting the ability to ingest/swallow and is a thought to affect between 45-95% of PD patients (Foltynie *et al.*, 2004, Leopold and Kagel, 1997) and has significant implications for orally dosed therapeutics such as levodopa and other anti-Parkinsonian and anti-Alzheimer's disease therapeutics agents.

For PD specifically the occurrence of bradykinesia and morning akinesia is often associated with delayed gastric emptying following the oral administration of anti-Parkinsonian therapeutics. This is again confounded using dopaminergic and other concomitant medical interventions. At least 24% of PD patients are thought to suffer from gastroparesis, the delay in emptying of the stomach, which will inevitably impact upon clinical outcome of any orally administered medication.

There has been a recent shift in the approaches to deliver APIs to the brain and wider CNS with a view to overcoming the BBB and other CNS-barriers, specifically the intranasal route has been targeted to obtain systemic deposition as a practical alternative to oral and parenteral routes (Leonard *et al.*, 2007, Ikechukwu Ugwoke *et al.*, 2000).

The nasal cavity is divided into two symmetrical halves by a septum with each cavity subdivided into four areas namely vestibules, atrium, respiratory region and olfactory regions. With a surface area of 150cm², total volume of 15-20mL the nasal cavity provides an optimal absorption area for drugs into the systemic circulations which would inevitably enhance the bioavailability of the therapeutic agent, particularly those which demonstrate poor oral absorption (intestinal permeation) or significant first-pass metabolism (extra-hepatic and hepatic) (Bitter *et al.*, 2011, Illum, 2012).

Although originally exploited for the delivery of locally acting agents (allergic rhinitis, nasal polyps and sinusitis) the highly vascularised nature of the nasal cavity has provided a portal for systemic delivery of small molecules and biomolecules (Ozsoy *et al.*, 2009) (Zaki *et al.*, 2007b). This non-invasive route not only provides rapid onset of action, but often increased bioavailability in low doses as it bypasses the first pass metabolism (Pires *et al.*, 2009).

The olfactory region covers the uppermost part of the cavity covering approximately 2.5cm² in each cavity in humans. Although this area is about 3% of the nasal surface area (Gizurarson, 2012) since the olfactory neurons do not have the synapse between the receptive element and the afferent pathways, it presents itself as a direct route to the CNS (Wen, 2011) and is the only part of the CNS which is directly exposed to the outer environment (Illum, 2000).

The primary aim of this chapter was to develop and characterise thermoresponsive and mucoadhesive nasal gel systems, which have the potential to deliver the model anti-Parkinsonian drug amantadine (AMT) onto the nasal epithelia and at the olfactory mucosa. These studies consisted of screening a range of mucoadhesive polymers to identify the most potent mucoadhesive and characterise the rheological properties, mucoadhesive nature

and AMT release kinetics from optimised formulations. Furthermore, cellular toxicity studies were conducted to assess the compatibility between formulations and nasal epithelial (RPMI 2650) and olfactory bulb cells (OBGF400). This was then followed by assessing the stability of optimised formulations and assessing the deposition patterns within a human nasal cast model when delivered from multi dose nasal spray.

2.5.1. Development of thermosensitive mucoadhesive hydrogel formulations

A key function of the developed formulations is to delay the clearance from the nasal cavity through the formation of a mucoadhesive 'gel' at an ideal $T_{\text{sol-gel}}$ of 32-34°C (Lindemann *et al.*, 2001). Although a formulation may undergo gelation at a lower temperature, it would be difficult to prepare at ambient temperature and difficult to administer (Majithiya *et al.*, 2006). Hence our primary formulation selection criteria was based on a $T_{\text{sol-gel}}$ of between 25-34°C through a visual gelation test using dry block.

The initial formulation development considered only the thermoresponsive nature of the formulation and included only PF127. An increasing PF127 concentrations (14-20% w/w) lead to a proportional decrease in the $T_{\text{sol-gel}}$, with F1 (Table 2-1) (14% w/w PF127) resulting in the highest $T_{\text{sol-gel}}$ (43°C ± 1.1°C). The reason for this decrease in $T_{\text{sol-gel}}$ with increasing PF127 concentration has previously been reported and is related to the non-ionic PEO-PPO-PEO block copolymer composition and their interactions which form polymolecular aggregates (micelles) in solution (Nagarajan and Ganesh, 1996, Zhou and Chu, 1988, Wanka *et al.*, 1990, Mortensen and Brown, 1993, Mortensen and Pedersen, 1993) (Prudhomme *et al.*, 1996). This transition occurs as a critical micellisation concentration (CMC) where below the CMC very small particle sizes are reported with little micellisation. Above the CMC the micelle formation becomes appreciable and the micellar mass increase in a linear fashion with temperature (Pisal *et al.*, 2004).

At low temperatures, typically 4-8°C, a significant hydration layer surrounds the PF127 molecules and as the temperature is raised, the hydrophilic chains of the copolymer begin to become desolvated due to the rupture of the hydrogen bonds established between the water molecules and these chains. During this process, the balance is shifted towards the hydrophobic interactions which predominate amongst the polyoxypropylene domains, and leads to gel formation (Attwood *et al.*, 1985, Miller and Drabik, 1984).

Previous studies have reported a concentration range between 14-20% w/w PF127 as demonstrating a gelation process close to nasal temperature (Zaki *et al.*, 2007a, Shin *et al.*, 2013, Nie *et al.*, 2011, Majithiya *et al.*, 2006, Kumari *et al.*, 2012, Jones *et al.*, 2009, Bhandwalkar and Avachat, 2013). With the inclusion of additives (F1-F6) including CMC, AMT, BLK and MTB, the $T_{\text{sol-gel}}$ was generally lower ($21^{\circ}\text{C} \pm 1.5^{\circ}\text{C}$). As a final optimised formulation would require mucoadhesive polymers as additional excipients, the impact of these additives on $T_{\text{sol-gel}}$ is important to characterise.

The results from F1-F6 resulted in the decision to reduce the PF127 range to 14-18% w/w to increase the $T_{\text{sol-gel}}$ in combination with the existing additives however with a reduced concentration range of CMC (0.5-1.5% w/w) (F7-F13) (Table 2-3).

The impact of increasing the mucoadhesive CMC on $T_{\text{sol-gel}}$ was evident, resulting in a decrease in $T_{\text{sol-gel}}$ across all formulations. Furthermore, at fixed CMC concentration, increasing PF127 resulted in decrease in $T_{\text{sol-gel}}$, although F9 and F10 demonstrated gelation close to the nasal cavity temperature with a PF127 concentrations of 16% w/w. This was used as the basis to further develop the formulations with the addition of AMT but at lower PF127 concentrations (15% w/w) (Figure 2-4). The impact of increasing concentrations of AMT is again clearly evident in the way $T_{\text{sol-gel}}$ increases (e.g. F14: $31^{\circ}\text{C} \pm 1.3^{\circ}\text{C}$ and F15: $> 40^{\circ}\text{C}$). From this set of optimised formulations, it was decided to take F16 and F17 for further development but to adjust the PF127 concentration to allow a $T_{\text{sol-gel}}$ at nasal cavity

temperature while also incorporating higher AMT doses into the formulation (1% w/w). Therefore, the final batch of formulations comprised of 16-20% w/w PF127 and 1 or 2% w/w CMC with the inclusion of 1% w/w AMT (Table 2.5). From these studies it was noted that F22 and F23 resulted in a $T_{\text{sol-gel}}$ which was generally equally distributed around the nasal cavity temperature. It was also noted that the key driver for changes in $T_{\text{sol-gel}}$ was the PF127 concentration rather than CMC. The final optimised formulation was therefore a derivative of F22 and F23 and contained 17% w/w PF127 (Table 2.6) and resulted in gelation at $33^{\circ}\text{C} \pm 1.5^{\circ}\text{C}$.

Whilst the trend in altering PF127 concentrations has been previously reported, the impact of additives on $T_{\text{sol-gel}}$ is important to assess when developing and optimising thermoresponsive nasal gel formulations. (Vadnere et al., 1984) studied the effect of different additives on the gelation temperature of PF127 gels. They observed that NaCl, KCL, Na_2SO_4 lowered the $T_{\text{sol-gel}}$ whereas urea, alcohol and dodecyl sulphate increased it. They came to the conclusion that additives act by disrupting the hydration sphere surrounding the hydrophobic PF127 molecules. Furthermore, Schmaljohann (Schmaljohann, 2006) stated that all additives effect the solvent to some extent, for example addition of surfactants which are amphiphilic will adsorb to the polymer molecule and alter its hydrophilic/hydrophobic balance. This may result in shifting of $T_{\text{sol-gel}}$ to a greater extent or even abolish the phase transition entirely.

When considering the final optimised formulations, CMC, PEG4000 at 1% w/w and FCS at 0.1% w/w were deemed appropriate and demonstrated $T_{\text{sol-gel}}$ close to that of the nasal cavity with appropriate pH properties (5.5-6.5) (Sutto et al., 2004b). Chitosan at 0.3% w/w (FCS 2) did not gel and this may have been a result of the presence of acetic acid used to dissolve chitosan affecting the micelle formation by reducing hydrogen bonding formation (Cho *et al.*, 2011). PEFG 12,000 (FPEG 12K) also failed to gel. According to (Pandit and McGowan, 1998) the greater the molecular weight of the PEG the lower the concertation of PEG is required to

prevent the phase transition of P127. We observed similar phenomenon as PEG 12K could not form a gel whereas PEG 4K did when both were used in the same concentration. It has been proposed that the higher the molecular weight of PEG, the more they occupy a larger volume in the solution and therefore become more effective at disrupting the stability of F127 micellar aggregates, even at very low concentration (Malmsten and Lindman, 1993) (Pandit and McGowan, 1998).

The pH of our three optimised formulations was within the nasal pH range (Washington *et al.*, 2000) (Table 2.7). Although nasal pH ranges from 5.5 to 6.5, nasal mucosa has been shown to tolerate wide pH ranges from 3-10 (Pujara *et al.*, 1995). The prevention of mucocilliary clearance is one of the major hurdles in delivering drugs intranasally. Studies have demonstrated that decreasing the nasal pH below its normal pH range can also decrease the ciliary beat frequency (CBF). This process is thought to be regulated by the intracellular changes in alkalinisation (increase CBF) or acidification (reduces CBF) (Sutto *et al.*, 2004a, Seybold *et al.*, 1990). Thus formulations with lower pH's may act to attenuate the CBF and mucocilliary clearance within the nasal cavity to increase its residence time.

2.5.2. Rheological assessment of thermosensitive formulations

An assessment of the rheological changes in the formulation during transitions across temperature is important to ascertain important molecular-level information about this phase transition, that would otherwise be unavailable. However, it was also important that when assessing formulations using rheology that the three-dimensional gel structure was not damaged. Hence all rheological tests were performed in the linear visco-elastic region where the strain on the formulation is not destructive to the gel structure and the data will provide useful information on the intermolecular and interparticulate forces in the formulation (Korhonen *et al.*, 2000).

When assessing the properties of thermoresponsive gel-like systems, the storage/elasticity modulus (G') and the loss modulus (G'') are key metrics for describing the rheology of the

formulation. The elasticity modulus is an important metric in this regard and measures the energy stored and which is subsequently recovered for each cycle of deformation (Almdal *et al.*, 1993). It presents with lower values with reduced temperatures but significantly increases with an increase in temperature, and the point at which G' overtakes G'' indicates the initiation of the gelation phenomena (Chang *et al.*, 2002). To assess this phase transition, the ratio of G'' and G' (the loss tangent, $\tan \delta$) was used, and where a phase-transition occurs an abrupt change in $\tan \delta$ is observed with values of < 1 indicating a greater G' compared to G'' , indicative of gel formation. This phase transition is often associated with three distinct phases: (i) an initial stable liquid phase plateau at low temperatures; (ii) an abrupt transition phase during the gelation process; (iii) a late stage stable gel plateau.

During the rheological study, it was observed that gelation temperature also depends on the rate of heating. A similar phenomenon was observed by (Gradinaru *et al.*, 2012) when polyurethane based triblock copolymers were heated at 0.5°C/min and 1°C/min, where at a 1°C/min heating rate the gelation phase started at 30°C and the gelation was completed at 34°C (Neuhaus *et al.*, 2006).

Temperature sweep results (Figure 2-7) show that formulations FCMC and FCS both demonstrated gelation at the end of the test at 34°C, whereas FPEG was still in the gelation phase. (Pisal *et al.*, 2004) found that PEG increased the gelation temperature of PF127 gel. The study also showed that PEG narrows the gelation temperature, meaning formation and melting of the gel occurs over a short temperature range. FPEG demonstrated similar effects and on this basis FPEG was deemed as being an unsuitable candidate as its retention in the nasal cavity may be unsuitable.

It is important that the formulation gels as soon as it is in the cavity so that it doesn't get cleared by the mucociliary clearance mechanism. The results (Figure 2-8) show that FCMC and FCS were the quickest to start the gelation phase where as FPEG was twice slower than the other two.

From an interpretation of the Ostwald model, the gel structure can be changed as a result of any deformation induced changes in the gel particles, through changes in the alignment of the polymer chains and also any changes in the interactions between polymer chain segments and any side chains. Therefore, upon heating the values of n will be lower for stronger gels due to an increase in the noncovalent forces between neighbouring particles (Islam *et al.*, 2004).

It was also apparent that the presence of different mucoadhesives can significantly alter the behaviour of the formulations. For examples, the viscosity of FCMC was always higher than all other formulations and particularly at 34°C where there is an approximate 8-fold difference between FCMC and FPEG. Furthermore, the FCMC demonstrated a much lower n -value compared to FCS and FPEG (Table 2-8), suggesting a stronger gel formation at 34°C. This phase represents the gradual conversion into a highly viscous/solid state. During this phase the intricate hydrogen-binding network between the unimers of F127 and water molecules are disrupted and drives the formation of micelles, which further aggregate to form the physical gel-like structure (Kabanov *et al.*, 2002). On the basis of ^{13}C NMR studies (Pisal *et al.*, 2004) suggested that at high temperature, conformational changes in the methyl group of the polyoxypropylene within the hydrophilic micellar region and in the motion of the hydrophilic end chains takes place. This results in dehydration and end chain friction, which causes the gelation.

2.5.3. Evaluation of *in-vitro* mucoadhesion

Due to mucociliary clearance mechanisms in the nasal cavity, any material on the mucous layer without mucoadhesive properties will have a half-time no longer than 20 minutes (Illum, 2000) and hence highlights the importance of imparting mucoadhesive properties into nasal gel-type formulations.

Mucoadhesion is defined as “attractive interaction at the interface between a pharmaceutical dosage form and a mucosal membrane” (Khutoryanskiy, 2011b). The mechanism of mucoadhesion is not yet clearly understood, and there are several theories proposed by scientists. There is no particular technology developed specifically to measure mucoadhesion, most of the developed tests are built up on previously available techniques, and two types of *in-vitro* mucoadhesion tests have been predominated. The shear stress measurements were first applied to mucoadhesion in a Wilhelmy plate method as developed by Smart *et al* (Smart *et al.*, 1984, Smart and Kellaway, 1982). Tensile strength tests have also been developed (Ponchel *et al.*, 1987) and are widely used.

Our initial attempts at applying tensile strength measurements to assess mucoadhesion resulted in poorly differentiating and non-significant differences in tensile strength across formulations and the methods was deemed unreliable (Figure 2-11). We then adapted a method that had previously been described by (Mikos and Peppas, 1990) and (Nakamura *et al.*, 1999).

Our results demonstrated that FPEG resulted in the greatest degree of displacement (absence of mucin: 9.5cm ± 0.05cm; presence of mucin: 5.7cm ± 0.19cm) with FCS demonstrating the least displacement (absence of mucin: 6.5cm ± 0.34cm; presence of mucin: 4.24cm ± 0.34cm), with all formulations showing a statistically significant difference in displacement ($P < 0.001$) when compared to the absence of mucin. The results demonstrate the superiority of FCMC and FCS compared to FPEG and the fact that displacement is observed in the absence of mucin would indicate that the use of mucin is able to recover some of the mucoadhesive

properties of the mucoadhesive polymers included within the formulations, and although known to show less biophysical properties as compared to native mucin, this purified mucin has less batch-to-batch variation and hence provides better reproducibility in measuring mucoadhesiveness (Khutoryanskiy, 2011a).

Due to the nature of these tests it is often advised not to rely on single method to assess mucoadhesion (Hagerstrom and Edsman, 2003). Although both the tests show similar results the displacement transfer method was more reproducible, reliable and statistically significant. Furthermore Ivarsson and Wahlgren (Ivarsson and Wahlgren, 2012) demonstrated similar results with CMC-based formulations requiring a stronger detachment force than CS under tensile strength measurements, however they also noted that conflicting reports existing with different methods and support the previously reported by Hagerstrom and Edsman method (Hagerstrom and Edsman, 2003) for the need to avoid solely relying on a single method of mucoadhesion assessment.

It is believed that mucoadhesion occurs at micro level interactions between mucus and the mucoadhesive, however tensile strength measurements occur at a macro level and therefore may not represent the micro-level changes taking place during mucoadhesion (Smart, 1999). The mucoadhesive properties of polymers can be influenced by the polymer structure and functional groups and the most commonly used mucoadhesive polymers are composed of polar chemical functional groups such as hydroxyl ($-\text{OH}$), carboxyl ($-\text{COOH}$), amide ($-\text{NH}_2$), and sulfate ($-\text{SO}_4\text{H}$) groups which are able to interact with the mucin glycoproteins and capable of forming hydrogen bonds (Park and Robinson, 1987, Madsen *et al.*, 1998). Furthermore the charge of the polymer is important in governing the mucoadhesion with non-ionic polymers (such as PF127) demonstrated minimal mucoadhesion properties, with greater mucoadhesion often demonstrated with anionic polymers such as CMC (Peppas and Buri, 1985) and superior mucoadhesion with cationic polymers (such as chitosan), particularly at neutral pHs (Lehr *et al.*, 1992).

2.5.4. Cellular toxicity associated with formulation exposure

The compatibility and cellular toxicity of formulations components with the target tissue/cell type is an important process in determining the safety and efficacy of the formulations. At a cellular level the viability of cells can be assessed through a range of cellular toxicity studies. To our knowledge, no studies have demonstrated the cellular toxicity of the polymers incorporated into thermoresponsive mucoadhesives nasal gel systems against either human nasal epithelial systems (RPMI 2650) or olfactory neuronal cells (OBGF400). Our studies demonstrated that with RPMI 2650 cells the IC_{50} for AMT was relatively high, $4.6\text{mM} \pm 0.05\text{mM}$ (Figure 2-15) with no significant reduction in cellular viability with PF127, CS, CMC or FPEG. Similarly, no significant reduction in cellular viability was observed with AMT and all polymers investigated for OBG400 cells (Figure 2-16).

PF127 is a relatively safe and widely used thermoresponsive and biocompatible polymers and hence would be expected to possess minimal toxicities towards human tissues. A range of studies have also confirmed our results with Khattak *et al* reporting that a 0.1-5% w/w solution of PF127 demonstrated no cellular toxicity over a 5 day period in human liver carcinoma (HepG2) cells (Khattak *et al.*, 2005). (Gong *et al.*, 2009) demonstrated limited toxicity towards HEK293 cells from 0-1000 $\mu\text{g}/\text{mL}$ but with a reduction in cell viability at 2500 $\mu\text{g}/\text{mL}$ to $64 \pm 9\%$. Zhang *et al* (Zhang *et al.*, 2007) also demonstrated limited toxicity towards HEK293 cells at 1% w/w (10,000 $\mu\text{g}/\text{mL}$). (Brunet-Maheu *et al.*, 2009) demonstrated limited toxicity towards MG-63 osteoblast cells which was time dependant and decreased to 85% on day 2 of incubation with 20% w/w PF127. Yang *et al* (Yang *et al.*, 2012) demonstrated no significant toxicity of PEG4000 in Hela cells across a concentration range of 0.5-9mg/mL. Furthermore no cellular toxicity was reported in Caco-2 cells for concentration of PEG4000 of up to 4% w/w (Hodaei *et al.*, 2015). (Lin *et al.*, 2006a) developed a novel PEGylated amphiphilic copolymer of poly(δ -valerolactone) (PVL) with PEG4000 and reported no cellular toxicity over a PEG4000 concentration range of 0.001-0.1mg/mL.

CMC is a commonly used tablet disintegrant and has been granted GRAS status by the FDA (SCOGS, 1979) and is therefore considered to be relatively non-toxic. As a result, there are very few studies reporting the cellular viability data for CMC in the native polymer form (i.e. without formulation into a novel delivery system) with limited cytotoxicity associated with exposure to human corneal epithelial cells with cellular viability dropping to $80\% \pm 3\%$ following 24 hours of incubation (Lee *et al.*, 2015).

CS is a natural polysaccharide and is often used as a cellular scaffold in biomaterial and tissue engineering applications (Tchemtchoua *et al.*, 2011, Sun *et al.*, 2011, Martin-Lopez *et al.*, 2012, Lv *et al.*, 2011) and is therefore generally considered to be relatively safe to use when exposed to cell cultures.

Cellular toxicity studies have therefore confirmed that the formulation polymers studied do not adversely affect the viability of cell proliferation which concurs with their widespread use in pharmaceutical formulations and biomedical/tissue engineering systems. Furthermore, limited cellular toxicity was observed with MTT with an IC_{50} in the low milli-molar concentration range and therefore its use within the developed formulation would pose little cellular toxicity concerns.

2.5.5. AMT release and transport across a permeable insert model of the human nasal epithelia

Whilst the assessment of AMT release in non-cell based systems may give an indication of the kinetics of release, the impact of a physiological/cellular barrier is important to assessing the eventual delivery into the systemic circulation or CNS via cellular barrier.

We developed a permeable insert based model system of the human nasal epithelia using RPMI 2650 cells and assessed the transport of released AMT from formulations to better understand any potential changes in release patterns of AMT when interacting with a cellular

barrier. Furthermore, the lack of current immortalised olfactory mucosa cell lines makes it difficult to develop a viable model for the human olfactory epithelial mucosa barrier.

The growth of RPMI 2650 cells on permeable inserts resulted in an increase in the monolayer integrity, as judged by the TEER (Figure 2-17), with a statistically significant ($P \leq 0.0001$) difference in TEER values compared to day 2 post seeding observed during days 12-20, with a peak TEER value attained on day 12 ($139 \pm 14 \Omega \cdot \text{cm}^2$) (Figure 2-17). These results are in agreement with (Bai et al., 2008) who validated these results in their findings of western blot which showed presence of four tight junction proteins ZO-1, occludin, claudin-1 and E-cadherin considerably higher when maintained under ALI conditions.

The release of AMT from all formulations was delayed compared to the diffusion of AMT alone across the monolayer with release of 43-44% was observed over the duration of the transport study in comparison to that of AMT alone ($79\% \pm 3.58\%$) (Figure 2-18). The mechanism of drug release, as described by the Korsmeyer-Peppas power law, was modelled according to a super case-II effect ($n > 0.89$) where the sorption of solvent results in breaking of the polymer network (termed solvent crazing) (Alfrey *et al.*, 1966) as a result of the swelling of the gel within the vitreous nucleus and can be a result of crosslinking density (Oriente, 1995), drug loading (Davidson, 1986) and copolymer composition (Franson and Peppas, 1983). The super-case II diffusion of AMT from all gel systems was surprising, and therefore the release of AMT from the formulations is not clear as it is beyond the limits of the power law. It suggests that a rapid release of AMT occurred later in the experiment resulting in rapid relaxation governing/controlled transport of AMT from the polymer network (Hopfenberg, 1974) (Peppas and Khare, 1993). The ionic composition of the media, comprising a pH of 7.4, may have directly altered the state of ionization within the polymer gel network, compared with the pH of the ANE (pH 5.5) leading to an altered release profile, with the rapid release being a time-dependant reflection of the shift in equilibrium as the solvent (media) penetrates the polymer network (Long and Richman, 1960, Klech and Simonelli, 1989).

However, our results demonstrate viable release and transport of AMT across the nasal epithelial and hence confirm that the optimised formulations may be potentially viable formulation systems for the local delivery of AMT (and other APIs) to the nasal cavity resulting in delivery across the nasal epithelia.

2.5.6. Stability and release of AMT from optimised formulations

Whilst the gelation, rheology and release of AMT from freshly prepared formulations provides vital information to characterise these formulations, their stability and the impact of formulation instability on AMT release is important in understanding their potential applications clinically. Optimised formulations were stored at both refrigerated (4°C) and room temperature (25°C) conditions within controlled humidity cabinets for a duration of 8 weeks. At regular intervals of the stability study samples were withdrawn for assessment of AMT release kinetics.

The analysis of stability of the optimised formulations during prolonged storage demonstrated that both FCMC and FCS were relatively stable (in terms of AMT release kinetics) during a period of 8 weeks when stored in refrigerated conditions but FPEG failed to gel after the first week of storage at 4°C. Furthermore, the release kinetics for FCMC and FCS were associated with a slower release profile as a result of a reduction in kH at week 8 compared to week 0 (Week 0: FCMC: 1.440 ± 0.150 and FCS: $= 1.319 \pm 0.028$; Week 8: FCMC: 1.224 ± 0.063 and FCS: $kH = 1.291 \pm 0.043$) (Table 2-11) (Figure 2-19 and 2-21).

Formulations stored at 25°C generally failed to gel after 8 weeks of storage with FCS demonstrating a gelation transition and similar AMT release profile to week 0 (Figure 2-19 B) after the first week of storage and which continued to show gelation phenomena at 25°C/60 % RH at week 2 (Figure 2-22), but failed to gel thereafter.

The release kinetics generally followed Korsmeyer-Peppas power law kinetics and demonstrated Fickian-type diffusion early on (except for FCS). At the end of the study period

this had moved towards anomalous transport (Table 2-11), whereby drug diffusions and the polymer relaxation were contributing to the overall release kinetics.

The swellable nature of hydrogel systems involves a dissolution process which creates an erosion front within the polymer, the imbibing of water as a solvent, results in the relaxation of polymer chains and the dissolution of the drug particles and results in an almost tripartite phenome of diffusion, swelling and erosion. In Fickian-type diffusion (Case-I), the rate of solvent diffusion (R_D) is much slower compared to the rate at which polymer chains relax (R_R). For non-Fickian diffusion (Case II, Anomalous and Super Case II) the main differences lies with the R_D whereby for Case II $R_R \gg R_D$, for anomalous-type kinetics $R_D \approx R_R$ and for Super Case II $R_D \gg R_R$ (J, 1967, Lin *et al.*, 2005, Khare and Peppas, 1995, Klech, 1989). Initially, formulations demonstrated Fickian-type diffusion but the Korsmyer-Peppas exponent increased over the stability period to > 0.5 by week 8 moving towards anomalous transport. This would suggest that polymer relaxation (swelling/erosion) plays a critical role in the release of AMT at earlier stability time points. The mathematical description and modelling of the casual factors for anomalous transport is challenging, and is beyond the scope of this study however a number of detailed reviews have been published discussing this issue (De Kee *et al.*, 2005). The mass transport of AMT into the polymer network can be assumed to be comprised of 3 processes (Vrentas and Vrentas, 1998, Aminabhavi *et al.*, 1989), whereby the solvent (water) is absorbed onto the surface of the polymer. The solvent molecules may then enter the lattice network of the polymer, which causes a 'swelling' of the network and elongation. This elongation is then counter balanced by an elastic-restrictive force to oppose the swelling. Eventually a state of equilibrium is reached when both forces are balanced, these process can significantly alter the kinetics of drug diffusion through the polymer network and are highly influenced by time-scale associated structural changes in the polymer (Wu and Peppas, 1993, Thomas and Windle, 1982, Thomas and Windle, 1981, Thomas and Windle, 1980).

The move towards anomalous transport over 8 weeks may suggest at a polymer network time-associated effect (Crank, 1968, HJ, 1966), which becomes more apparent over the longer stability study. The equilibrium between swelling and elastic-restrictive force within the polymer may be associated with a time-dependent equilibrium, where equilibrium is not established immediately (Long and Richman, 1960).

Although the formulations are in liquid-phase during the stability storage period, the interactions between both mucoadhesive polymers and thermoresponsive polymers may influence eventual formulations of the polymer networks, altering the equilibrium processes and hence contributing towards the anomalous transport.

The lack of literature reports concerning of the stability of pluronic-based hydrogel was recently reported by (Grela et al., 2014) and they aimed to characterise the stability of PF127 over a range of temperatures during prolonged storage (up to 3 months). They noted that a stronger degradation of the formulation structure, as noted from $T_{\text{sol-gel}}$, viscosity and rheology assessment, was evident at elevated storage temperatures. However, storage of optimised formulations at refrigerated temperature would enhance the relative stability of the gelation phenomena and associated AMT release kinetics for prolonged periods of time.

2.5.7. Nasal spray system

The prevention of pulmonary deposition of any nasally administered formulations is key to ensuring the residency within the nasal cavity. The droplet size distribution is important in identifying the potential for pulmonary deposition ($< 2\mu\text{m}$) (Stuart, 1973, Hatch, 1961a), however the droplet size is often dictated by the design of the orifice of the actuator device used to deliver the spray plume. For ensuring retention of drug within the nasal passages, droplet sizes of in-excess of $5\mu\text{m}$ are recommended and represented our target cut-off (Stuart, 1973, Hatch, 1961b).

Our formulations all demonstrated a diameter in excess of the traditional cut-off of $5\mu\text{m}$. (Table 2-12). FCS demonstrated a 10% fraction of $7.27\mu\text{m} \pm 0.28\mu\text{m}$ (Table 2-12) closest to the cut-

off for pulmonary deposition, whereas both FCMC and FPEG were above this. FCS also demonstrated the smallest diameter (VMD= $92.41\mu\text{m} \pm 1.72\mu\text{m}$). However, when considering the span of particle sizes, FCS was the broadest (0.96 ± 0.30) with both FCMC and FPEG showing a smaller distribution spread (Table 2-12). A one-way ANOVA confirmed droplets VMD were significantly different across all formulations ($P < 0.0001$), suggesting that the incorporation of different mucoadhesive polymers contributed to the differing polymer sizes with FCS demonstrating the small resulting droplets ($92.41\mu\text{m} \pm 1.72\mu\text{m}$) and FCMC the largest ($120.87\mu\text{m} \pm 0.59\mu\text{m}$). When considering the viscosity of the polymers used in each formulation (Figure 2-10), CMC resulted in the most viscous formulations and this may have contributed to the larger particle sizes, with similar trends observed for CS and PEG.

To assess the potential *in-vivo* application of formulations, FCS and FCMC were taken forward to assess spray deposition within a human nasal cast model. The angle of spray administration was altered from 60-80° and the impact on deposition patterns assessed. For both formulations the administration angle had a significant effect on deposition, with an increased angle (80°) having a significantly pronounced localisation in the nasal vestibules and lower regions of the nasal cavity. For FCMC (Figure 2-28) this deposition area was significantly lower than that for FCS (Figure 2-27).

Spray angles of 60° and 70° lead to deposition of the formulation in the olfactory regions of the nasal cavity, highlighting the possibility for exploitation in nose-to-brain delivery of amantadine. FCS sprayed at an angle of 60° with insertion lead to olfactory deposition of 0.6-0.7cm². For FCMC a greater olfactory deposition of 0.91cm² was observed at 60° with insertion. Although the higher deposition for FCS may be a result of the smaller particle sizes for FCS ($92.41 \pm 1.72\mu\text{m}$) compared to $120.87 \pm 0.59\mu\text{m}$, the impact of nozzle insertion for FCMC may enhance delivery onto the olfactory regions (Figure 2-28). When considering the surface area of the human olfactory mucosa (2-10cm²) (Gross *et al.*, 1982), FCMC may be a viable candidate for

further development targeting nose-to-brain drug delivery (Badhan *et al.*, 2014). In both formulations, the impact of head position (15° posteriorly) was important in governing nasal depositions, leading to significantly higher deposition within the middle-upper regions of the cast irrespective of the insertion angle

The higher viscosity of FCMC compared to FCS resulted in significantly larger particle sizes ($P < 0.001$) for the optimal formulations and may have resulted in a more focussed (less disperse) spray plume resulting in more localised deposition patterns. In contrast, the lower viscosity of FCS, leading to small particles would lead to a wider plume and greater deposition in the nasal cavity (Kundoor and Dalby, 2011, Guo *et al.*, 2005).

2.6. Conclusion

The treatment of age-associated degenerative CNS disorders such as Parkinson's diseases (PD), poses particular difficulties in the design of appropriate drug delivery systems capable of overcoming the hindrances associated with dyskinesia and dystonia that are inherent in current pharmacological interventions for PD. Although reformulation of existing orally dosed formulations may provide some benefit, there is an inherent need to provide an alternative delivery routes for a range of CNS disorders which can both provide ease of clinical use but also to improve the bioavailability of the therapeutic.

The nasal mucosa fulfils this purpose in light of the large and vascularised route of access for drugs to the systemic circulation and can provide a relatively non-invasive approach to deliver drugs. A key concern of any nasal administered formulation is the residency of the formulation within the nasal cavity. Existing formulations are often associated with a nasal drip or 'run-off' effect which potentially diminish the bioavailability of nasal formulation. A novel development in this area has been the formulation of intelligent response based hydrogel nasal formulations which act to enhance residency within the nasal cavity (Schmolka, 1972b, Nazar et al., 2011, Wu et al., 2007, Alsarra et al., 2009, Li et al., 2010, Jeong et al., 2002, Agrawal et al., 2010, Li et al., 2014, Qian et al., 2014, Chen et al., 2013b, Nakamura et al., 1999, Ikechukwu Ugwoke et al., 1999, Zaki et al., 2007a, Hosny and Banjar, 2013, Basu and Maity, 2012).

This study has investigated the potential to administer the antiviral/antiparkinsonian drug through the nasal route using mucoadhesive and thermoresponsive hydrogel formulation systems. We have demonstrated that both CMC and CS can provide the requirements for mucoadhesion in these formulations, whilst also leading to a relatively stable formulation which can be targeted to deliver drug in specific regions of the nasal cavity dependant on administration angle and nozzle insertion depth. Furthermore, our results have indicated the potential for nose-to-brain delivery of amantadine, yielding a potentially novel avenue therapeutics delivery route to avoid the blood-brain barrier.

Chapter 3

**Development and
characterisation of mesoporous
nanoparticles for olfactory drug
delivery**

3.1. Introduction

The delivery of drugs and therapeutic agents to the CNS is hampered by the insidious nature of the BBB in restricting the entry of xenobiotics across into the brain and wider CNS (Abbott, 2005, Abbott *et al.*, 2010b, Abbott and Romero, 1996, Pardridge, 2007b). The BBB has evolved to essentially govern the permeability of drugs through its formation as a physical barrier formed by the endothelial and epithelial (Persidsky *et al.*, 2006) and as a result of the expression of membrane transporters and transcytotic vesicles. Furthermore, the physicochemical properties of compounds permeating across the BBB is a driving factor in its ability to distribute into the CNS.

Despite advances in neurosciences and drug delivery technologies, the targeting and delivery of therapeutics into the brain and CNS is still a limiting factor, with less than 1% of all CNS-targeted compounds showing activity against CNS disease states (Pardridge, 2005, Lipinski, 2000). This is despite many of these compounds possessing physicochemical properties that would normally predispose them to good membrane permeability (e.g, molecular weight < 500 and highly lipid soluble) (Pardridge, 2007c, Pardridge, 1998).

As an alternative to direct BBB penetration the olfactory mucosa has gained interest as a potential novel target site for CNS delivery. The olfactory region covers the uppermost part of the nasal cavity covering approximately 2.5-10cm² in humans (Gizurarson, 2012), is comprised of approximately 12 million olfactory receptor cells (Purves, 2007) and is the only part of the CNS which is directly exposed to the external environment (Illum, 2000, Pires *et al.*, 2009).

The olfactory nerve pathway provides a rapid and non-invasive route for CNS drug delivery. This is evident from studies carried out showing fluorescent traces associated with olfactory nerves as they traverse through cribriform plate, with highest drug concentrations observed in the olfactory bulb (OB), and the correlation between olfactory epithelium (OE) and OB (Lochhead and Thorne, 2012, Renner *et al.*, 2012).

Previously we demonstrated the development of a novel mucoadhesive-thermoresponsive nasal gel formulation for the delivery of the water soluble drug amantadine. However, with poorly soluble drugs, such formulation systems often requires mixed solvent systems with high solvent concentrations (Agrawal and Maheshwari, 2014).

To enhance the solubility of poorly soluble drugs, nanotechnology based formulation systems are often employed and have been developed as a concept for solubility enhancement for over 30 years (Poste *et al.*, 1976, Papahadjopoulos, 1988, Douglas *et al.*, 1987, Davis *et al.*, 1987, Poste and Kirsh, 1983). Considering that it has been estimated that approximately 40% of new active substrates are difficult to formulate due to poor water solubility (Lipinski, 2000, Lipinski, 2002),(Lee *et al.*, 2014), the application of nanoparticle technologies to improve solubility is gaining interest. Furthermore, the formulation of drug products into orally dosed tablet formulation can be problematic to the targeting the brain and CNS as a result of the limitations associated with the drug crossing the gastrointestinal barrier coupled with the BBB. Despite approaches to enhance the solubility to improve dissolution, limitations associated with bypassing the BBB may still exist.

A potentially novel class of compounds with widely cited biological activities, including cognitive effects, are flavonoids. These are polyphenolic compounds that are abundantly found in fruits and vegetables and have attracted attention due to their antioxidant activities. Over 6000 flavonoids have been reported to date and many have been reported to possess CNS indicating effects including the protection of neurons from neurotoxins and neuro-inflammation in degenerative disease status such as Dementias (Williams and Spencer, 2012, Solanki *et al.*, 2015, Shukitt-Hale, 2012, Mecocci *et al.*, 2014, Macready *et al.*, 2009, Cherniack, 2012, Blumberg *et al.*, 2014). Furthermore, an increasing body of clinical evidence is supporting the view that flavonoid impart a protective function towards dopamine neurons through prevention of oxidative damage and apoptosis (Mercer *et al.*, 2005, Meng *et al.*, 2009). Furthermore, a range of flavonoids have been reported to be capable of reducing the impact

of drug efflux transporter proteins, such as P-glycoprotein or BCRP, which are prominently expressed at BBB and significantly hinder CNS drug delivery and which have also been identified to be expressed at the olfactory mucosa (Kandimalla and Donovan, 2005). The localisation and expression at the olfactory mucosa may therefore provide a limiting factor for the directly delivery of substrates of P-glycoprotein or BCRP, mimicking aspects of the barrier function of the BBB.

Of the wide array of flavonoids/phytochemical based compounds reported, curcumin has been widely reported to impart a protective function from AD/PD in epidemiological studies in humans and in rodent models (Muthane *et al.*, 1998, Ganguli *et al.*, 2000, Alladi *et al.*, 2009, Mythri *et al.*, 2011). Curcumin, also known as diferuloylmethane or 1,7-bis (4-hydroxy-3-methoxyphenyl) -1,6-hepatadiene-3,5-dione, is a natural yellow coloured and low molecular weight polyphenol compound purified from the rhizome of the plant *Curcuma longa*. It is insoluble in water and hence it's therapeutic applications are limited due to its poor bioavailability when administered orally as a result of rapid glucuronidation in therapeutic and resultant poor tissue distribution (Ravindranath and Chandrasekhara, 1980, Pan *et al.*, 1999).

Phytochemical flavonoids are therefore a potently novel multi-faceted class of molecules which show potential for a range of CNS patho-physiologies (Katayama *et al.*, 2007, Breedveld *et al.*, 2006b, Allen *et al.*, 2002b, Ashida *et al.*, 2000, Pick *et al.*, 2011, Fleisher *et al.*, 2015, Zhang *et al.*, 2004, van Zanden *et al.*, 2007, Zhang *et al.*, 2005, Robey *et al.*, 2004, Ferrandiz and Alcaraz, 1991, Breedveld *et al.*, 2006a, Allen *et al.*, 2002a).

Recently, the application of nanoparticle technology to improve the solubility of curcumin has been reported and resulted in an increase in the pharmacokinetics and bioavailability (Gupta *et al.*, 2009, Gupta and Dixit, 2011b, Gupta and Dixit, 2011a, Krausz *et al.*, 2015). Among various type of nanoparticle based carrier system, mesoporous silica nanoparticles

offer various advantages, such as large surface area, porous surface with pores ranging from 2-50nm allows maximum drug loading, which can act as a drug reservoir and they are also biodegradable (Zhai *et al.*, 2012) whilst also being relatively stable in many harsh organic solvents (Stein *et al.*, 2000).

The focus of this chapter was to develop mesoporous silica nanoparticles as carrier systems for poorly soluble compounds such as phytochemicals, to both enhance their inherent solubility but to also to assess their compatibility as drug delivery systems for intranasal and olfactory drug delivery.

Another important member of the flavonoid family is chrysin, which also has shown neuroprotective activity (He *et al.*, 2012). Due to its wide variety of actions such as antioxidant, anti-inflammatory, anti-tumour, antihemolytic and anti-hypertensive and its abundance in plants makes it an attractive compound.

3.2. Aims and objectives

The aim of this chapter was to develop a mesoporous silica nanoparticle drug delivery system suitable for the loading of the water insoluble phytochemicals curcumin and chrysin.

To achieve these aims the overall objective were:

- To identify the appropriate nanoparticle size for olfactory uptake
- To synthesize and characterize a mesoporous nanoparticle system (MSNPs) within a tuneable size range
- To assess the cellular toxicity of MSNPs against olfactory derived cell culture models
- To assess the cellular toxicity of curcumin and chrysin against olfactory cell culture models
- To study the uptake of MSNPs into olfactory neurons
- To assess the loading capacity of MSNP towards curcumin and chrysin
- To assess the release of phytochemical-loaded MSNP

3.3. Materials and Methods

Eagle's Minimum Essential Medium (MEM), Dulbecco's Modified Eagle Medium: Nutrient Mixture F12 (DMEM-F12), Dulbecco's Phosphate buffered saline (PBS), L-glutamine 200mM, non-essential amino acids (NEAA), penicillin/streptomycin and trypsin-EDTA solution were obtained from PAA laboratories (Austria); foetal bovine serum (FBS) (Labtech, Essex, UK); potassium chloride, magnesium sulphate, calcium chloride, acetonitrile, orthophosphoric acid, acetic acid, ethanol, sodium hydroxide, and sodium chloride were obtained from Fisher Scientific (Loughborough, UK); acutase (Biolegend, UK); gentamycin, cetyl trimethylammonium bromide (CTAB), tetraethoxy orthosilicate (TEOS), MTT (3-(4, 5-dimethylthiazol-2-yl)-2, 5-diphenyl Tetrazolium bromide), trypan blue, dimethyl sulfoxide (DMSO), potassium phosphate, ammonium hydroxide, rhodamine 6G, FITC (fluorescein isothiocyanate), DAPI (4',6-diamidino-2-phenylindole), collagen, cell culture water, monobasic were obtained from Sigma-Aldrich (Dorset, UK).

3.3.1. Fluorescent bead uptake in porcine olfactory bulb neuroblastoma (OBGF400) cells

OBGF400 cells were cultured as described in section 2.3.9. Coverslips were sterilised in 70% ethanol for 30 min, dried in a laminar air hood and coated with $6\mu\text{g}/\text{cm}^2$ of a collagen prepared in sterile water from a 0.1% w/v (0.1M acetic acid) stock solution, with coating taking place in 12-well plates. Plates were left to dry in the laminar air flow for 2 hours. Excess collagen was then removed and coverslips washed with sterile water and left for drying. Thereafter cell suspensions of OBGF400 cells were seeded at a density of 1×10^5 cells/ cm^2 into wells of a 12 well plate containing the coated coverslips and left to adhere and proliferate to a confluency of approximately 70% in a 5% CO₂ humidified incubator. Fluorescent latex beads (carboxylate modified) of 100nm ($\lambda_{\text{ex}} \sim 491\text{nm}$; $\lambda_{\text{em}} \sim 521\text{nm}$) and 500nm ($\lambda_{\text{ex}} 487\text{nm}$; $\lambda_{\text{em}} 530\text{nm}$) were dispersed into HEPES (25mM) buffered HBSS at a concentration of 0.1% v/v and sonicated for 10 minutes in a water-bath sonicator prior to the addition into wells. Coverslips were incubated for 2 hours in a 5% CO₂ humidified incubator before being washed with ice cold

HEPES (25mM) buffered HBSS and fixed with 4% w/v paraformaldehyde for 30 minutes in the dark. The coverslips were then mounted onto glass slides with mounting media containing DAPI. The localisation of the latex beads was analysed using an upright confocal microscope (Leica SP5 TCS II MP) and visualised with a 40x oil immersion objective. All images were acquired using an argon laser at 494nm to visualise FITC and a helium laser to visualise DAPI at 461nm.

3.3.2. Preparation of mesoporous nanoparticles (MSNP)

A desirable mesoporous nanoparticle system is the one which offers large surface area, high pore volume, and tuneable size. However the dispersity of the MSNPs is highly dependent on the methods employed for template removal and particle collection (Wu *et al.*, 2013). To therefore identify an appropriate method to develop size controlled MSNPs three published methods were considered and formed MSNP were characterised by size and morphology before selecting a suitable method for subsequent studies.

3.3.2.1. Synthesis of MSNPs: template removal by calcination (Gul-MSNP)

This method is based upon a published study by Gulfam and Chung and is termed the 'Gul- method' (Gul-MSNP) (Gulfam and Chung, 2014). To a reaction volume, 10mL ethanol, 20mL diethyl ether and 0.8mL ammonium hydroxide were dissolved in 70mL distilled water. 500mg CTAB was introduced in this emulsion system and the mixture was vigorously stirred at 600rpm. After 30 min, 2.5mL TEOS was rapidly added into the system and the mixture was vigorously stirred at 600rpm for 4h. The white precipitate was collected by filtration and subsequently washed with distilled water before being dried at 60°C for 24h. The CTAB template was removed by vigorously stirring the particles in a mixture containing 15mL HCl and 120mL ethyl alcohol at 70°C for 24h. The formed nanoparticles were further calcinated at 600°C for 12h. Thereafter the bare mesoporous silica nanoparticles were washed several times with distilled water and ethyl alcohol before being air dried at 80°C. These were termed 'Gul-MSNP'.

3.3.2.2. Synthesis of MSNPs: charged template approach (Pro-2-MSNPs)

This method is based upon a published study by (Nooney et al., 2002) and is termed the 'Pro-2 method' forming 'Pro-2-MSNPs'. This method involves the homogeneous synthesis using a charged template and is associated with a water/ethanol solvent washing approach. Briefly, 138g of ethanol and 162g of deionized water were combined and the resultant pH adjusted to 11.7 with the addition of 11.6mL of ammonium hydroxide (29wt % NH₃ in water). 0.274g of CTAB was then added with rapid stirring at room temperature. Subsequently after 5 min, 1.39mL of TEOS was added with the solution turning slightly turbid indicating hydrolysis. After 2 hours the suspension was filtered.

3.3.2.3. Synthesis of MSNPs: template removal by refluxing (Fan-MSNPs)

This method is based upon a published study by (Fan et al., 2011) and is termed the 'Fan method' formulating 'Fan-MSNPs'. In this method 1.0g of CTAB (2.74mmol) was dissolved in 480mL distilled water. Thereafter 3.5mL of aqueous sodium hydroxide solution (2M) was added and the temperature of the mixture was raised to 80°C. 5mL TEOS (22.4mmol) was then introduced drop wise into the reaction mixture whilst stirring vigorously for two hours until a white precipitate was formed. The precipitate was then filtered and washed with distilled water and methanol and dried under vacuum. The surfactant template (CTAB) was removed by refluxing 1.5g of the synthesized silica particles with 1.5mL of HCL (37.2% w/v) and 150mL methanol for 6 hours. The product was washed extensively with distilled water and methanol. The surfactant free silica particles were placed under high vacuum with heating at 60°C to remove the remaining solvent from the mesopores.

3.3.3. Assessment of MSNP particle size distribution and zeta-potential (ζ)

The size and zeta potential (ζ) of MSNPs were determined using dynamic light scattering techniques through the use of a NanoBrook 90 Plus Zeta (Brookaven Instruments Corporation). 100 μ L of 1mg/mL sonicated MSNPs suspension was added to 3mL ultrapure water, vortexed and used to measure the particles size. The mean diameter was obtained

from 3 runs of 3 minutes. The polydispersity index (PDI) was used to indicate the particle size distribution in within the sample. The zeta potential is an indicator for charge present on the surface of nanoparticles, which is responsible for the stability of formulation and interaction with cellular membranes. The zeta potential of nanoparticles is measured using the principle of electrophoretic mobility under an electric field. The average of 3 readings (each reading = 30 runs) was reported. The temperature was maintained at 25°C during the measurements.

3.3.4. Scanning electron microscopy (SEM) based assessment of the morphology of MSNP

Samples of MSNP were mounted on 12mm aluminium pin stubs with 12mm carbon tabs and coated with 15nm of gold. The powders were imaged at 5 kV with a 150pA beam in high vacuum due to beam damage to the samples at higher kV's. The nanoparticles were imaged at 10kV with a 100pA beam also in high vacuum. The SEM used was Carl Zeiss EVO LS 15. The gold coater used was a Quorum QR105S.

3.3.5. Porosity assessments using nitrogen adsorption/desorption isotherm analysis

The specific surface areas of the blank MSNPs was analyzed using the Brunauer–Emmet–Teller (BET) method (Brunauer *et al.*, 1938) using a Quantchrome NOVA (Quantchrom, Finland). The analysis was based on the amount of Nitrogen (N₂) gas adsorbed at various partial pressures (P/P₀) between 0.05 and 0.3. Before N₂ adsorption, samples were under vacuum at a temperature of 100°C. The nitrogen molecular cross sectional area (0.162nm²) was used to determine the surface area. The pore size distribution and total pore volume was determined by using density functional theory (DFT) method. All calculations were software automated (Quantchrome NOVWIN, Quantchrom, Finland).

3.3.6. Thermogravimetric analysis (TGA) of MSNP

Thermal stability analysis of the functionalized silica was performed by thermogravimetric analysis (TGA) using a Pyris 1 TGA (Perkin Elmer) instrument. 3mg of MSNP materials were analyzed under nitrogen purge with a starting temperature of 35°C and 10°C/min ramp rate to

800°C. The corresponding carbon, hydrogen and nitrogen elemental analysis was performed using LECO CHN-2000 elemental analyzer under flowing oxygen.

3.3.7. Loading of fluorescein isothiocyanate (FITC) and targeted to OBG400

FITC loaded MSNP (FITC-MSNP) were prepared using a slightly modified method proposed by (Fan et al., 2011). 100mg of MSNP were refluxed with 8mL toluene and 100µL of 3-aminopropyltriethoxysilane for 20 hours to form amine-functionalised MSNPs. 150mg of these functionalised MSNPs were reacted under an argon atmosphere with 1.75mg of FITC (0.009mmol) 5µL of triethylamine (TEA) and 10mL of anhydrous dimethylformamide (DMF). The mixture was stirred at room temperature for 24h followed by centrifuging and washing twice at 8000rpm for 8 mins with DMF, diethyl ether and methanol. Finally, to remove the remaining solvent from the FITC-MSN particles were subjected to high vacuum at 60°C.

To assess the release of FITC from FITC-MSNP, 1mg/mL FITC-MSNP was dispersed in PBS (154mM PBS pH 7.4), briefly sonicated and placed in a shaking incubator maintained at 37°C and 100rpm. Samples were withdrawn at set time intervals and the volume replaced with an equal volume of pre-warmed release medium. The release of FITC was assessed through fluorescence measurements using a dual-scanning microplate spectrofluorometer (Spectra Max Gemini XS, molecular devices, Sunnyvale, California) at an excitation wavelength of 470nm and emission wavelength of 520nm.

For intracellular tracking in OBG400 cells, FITC-MSNP were dispersed into HEPES (25mM) buffered HBSS at a concentration of 50µg/mL prior to the addition into wells of a 12 well plate containing collagen coated coverslips and incubated for 2 hours in a 5% CO₂ humidified incubator. Thereafter the coverslips were washed with ice cold HEPES (25mM) buffered HBSS and fixed with 4% w/v paraformaldehyde for 30 minutes in the dark. The coverslips were then mounted onto glass slides with mounting media containing DAPI. The localisation of the latex beads was analysed using an upright confocal microscope (Leica SP5

TCS II MP) and visualised with a 40x oil immersion objective. All images were acquired using an argon laser at 494nm to visualise FITC and a helium laser to visualise DAPI at 461nm.

3.3.8. Differential scanning calorimetry (DSC)

Heating curves of curcumin, chrysin, blank MSNPs and loaded MSNPs were obtained using differential scanning calorimeter (DSC Q200, TA instruments, Delaware). Samples were weighed and 2-5mg were loaded into a non-hermetically crimped aluminium pan and heated under a nitrogen purge at the rate 50mL/min. Samples were heated from 30 to 350°C at the heating rate 10°C/min under nitrogen. The data was analysed using Universal Analysis 2000 software V4.5A TA instruments.

3.3.9. Fourier transform infrared (FT-IR)

The loading of phytochemicals was additionally confirmed by using FT-IR techniques for the bare MSNPs, and drug Loaded MSNPs. FT-IR absorbance was collected using a FT-IR spectrophotometer (Thermo Scientific, USA) over the spectral range of 550-4000cm⁻¹.

3.3.10. HPLC analytical detection of curcumin

The detection of curcumin was based on an adapted method previously reported by (Li et al., 2009). An Agilent 1200 Series (Waldbronn, Germany) equipped with a multiple wavelength detector (MWD) and a Phenomenex Luna C18 (150 × 4.6mm) 5µm column was used for RP-HPLC. The mobile phase was prepared using ACN:5% acetic acid in a ratio of 45: 55 (v/v). Mobile phases were filtered through 0.45µm filter and sonicated before use. The flow rate was maintained at 0.8mL/min with a 15 minutes run time and injection volume of 20µL, while column temperature was mainlined at ambient temperature. Calibration curves were constructed using standard solutions of known concentrations from 5 to 50µg/mL. The software used for data collection, analysis and control of the system was ChemStation Version 1.24 SP1. The UV detection of curcumin was measured at 420nm.

3.3.11. HPLC method for chrysin

An RP-HPLC method was used to quantify chrysin (Zaveri *et al.*, 2008). The same HPLC system described above was used to analyse chrysin samples. The mobile phase comprised of water:methanol:acetonitrile:phosphoric acid in a ratio of 60:30:38:1 (v/v). Mobile phases were filtered through 0.45µm filter and sonicated before use. The flow rate was maintained at 1.0mL/min with 17 minutes run time and the injection volume was 10µL while column temperature was kept at ambient temperatures. Calibration curves were constructed using standard solutions of known concentrations from 0.78 to 10000µg/mL. The UV detection of chrysin was measured at 262nm.

3.3.12. Toxicity of MSNP towards olfactory cells

To assess the cellular toxicity of MSNP towards olfactory cells, the OBG400 cell line was used as model systems for the olfactory mucosa. Cells were seeded into 96-well plates at a density of 1×10^4 cells per well (see section 2.3.10). Cells were subsequently exposed to 10-1000µg/mL Fan-MSNPs for 24 hours at 37°C in a 5 % CO₂ air humidified environment and cellular toxicity was assessed using a MTT cytotoxicity assay (see section 2.3.11). The UV-absorbance of the formazan product was measured on a multi-plate reader (Bio-Rad laboratories, Hercules, CA) using 570nm as a test wavelength and 600nm as a reference wavelength. The mean of the blank UV-absorbance was subtracted from the UV-absorbance of each controls and samples and percentage viability was calculated. The percentage of cellular viability was calculated as follows (Zhang *et al.*, 2010):

$$\% \text{ cell viability} = \frac{\text{absorbance of sample}}{\text{absorbance of control}} * 100$$

The IC₅₀ was subsequently calculated using a sigmoidal dose response function within the Graphpad Prism version 5.0 (GraphPad Software, Inc. USA). Each concentration was assayed in eight wells and run in three independent experiments and results expressed as percentage cytotoxicity relative to a control (0.5% DMSO).

3.3.13. Cellular toxicity of phytochemicals

The cellular toxicity of curcumin and chrysin were also assessed using OBG400 cells at a concentration range of 0.01-50,000 μ M, as described above. Each concentration was assayed in eight wells and run in three independent experiments and results expressed as percentage cytotoxicity relative to a control (0.5% DMSO). The cell viability was calculated by comparing the absorbance of phytochemical or drug treated well to that of control well.

3.3.14. Phytochemical loading of MSNP Drug loading

Loading of chrysin: 20mg/mL chrysin was dissolved in the DMF and in a separate vial 20mg/mL of MSNPs were dispersed in DMF and bath sonicated for 15 minutes. A volume of 1mL from each vial was combined and resulting in a final concentration of 10mg/mL of both chrysin and MSNP. The glass vial was sealed and covered with foil, sonicated for 15 minutes in water sonicating bath and left for stirring at 100rpm at room temperature. After 24 hours the vial contents was filtered through a 0.22 μ m cellulosic white membrane filter (MSI Micron Separations Inc., USA). The filtrate was collected to determine loading and this approach was termed the 'wet' approach.

The loaded nanoparticles collected on the filter paper were dried under high vacuum for 2 days, washed with PBS to remove superficially adsorbed chrysin on the surface and loading was assessed through TGA. This approach was termed the 'dry' approach. Chrysin loaded Fan-MSNP were termed 'Chry-MSNP'.

Loading of Curcumin: 20mg/mL curcumin was dissolved in a 30:70 mixture acetone:ethanol and processed as described above. Curcumin loaded Fan-MSNP were termed 'Curc-MSNP'.

The confirmation of phytochemical loading was determined using HPLC-UV, DSC and TGA analysis. For the 'wet' method, an entrapment efficiency (EE) was calculated based on the following formula (Mohseni et al., 2015):

$$EE (\%) = \frac{\text{Drug added} - \text{Free "unentrapped drug"}}{\text{Drug added}} \times 100$$

For the 'dry' method, a loading content (LC) was calculated from the difference between the final weight loss for Fan-MSNP and Phytochemical-MSNP at the end of the heating cycle and derived from data obtain from TGA analysis.

3.3.15. Live cell imaging: Cell-IQ®

To assess the morphological alterations in cellular structures when exposed to Fan-MSNP, curcumin loaded MSNP (Curc-MSNP) and chrysin loaded MSNP (Chry-MSNP), live cell imaging of OBG400 was conducted over a 40-hour period in an oxygen, CO₂ and humidity controlled phase contrast imaging systems (CellIQ®, Chip-Man Technologies, Tampere, Finland). OBG400 cells were seeded into wells of a 6-well plate at a density of 5x10⁵ cells/well and allowed to adhere and proliferate to 70% confluence. Subsequently wells were washed with warm HEPES (25mM) buffered HBSS, followed by the addition of 50-150µg/mL of Fan-MSNP, Curc-MSNP and Chry-MSNP dispersed in maintenance media for 40 hours with images captured within a defined window within each well every 15 minutes using live-cell imaging and presented as images.

3.3.16. *In-vitro* drug release studies

To assess the *in-vitro* release of curcumin and chrysin from MSNPs, studies were performed in PBS (154mM pH 7.4) containing 0.1% Tween 80. Phytochemical loaded MSNP, 2mg, were dispersed into 2mL of release medium, briefly sonicated and placed in a shaking incubator maintained at 37°C and 100rpm. Samples were withdrawn at set time intervals and the volume replaced with an equal volume of pre-warmed release medium. The release of

phytochemicals was assessed through HPLC-UV methods. Throughout the release studies Tween 80 was used to maintain sink conditions and also to dissolve curcumin in the release medium (Yallapu *et al.*, 2010). The results were calculated in terms of cumulative release (%w/w) relative to actual entrapped weight of curcumin or chrysin in the MSNPs. To assess the impact of pH on drug release, release studies were also conducted at pH 5.5 (average nasal pH).

3.3.17. Incorporation of Fan-MSNPs into thermoresponsive nasal gel systems

In an attempt to ascertain whether the thermoresponsive nasal gel systems can act as viable bulk carriers for MSNP, final optimised formulations: FCMC, FCS and FPEG (Chapter 2), were formulated with the replacement of AMT with Fan-MSNPs at concentrations of 0.2, 0.4 and 1% w/v. Rheological assessments of the gelation trend and temperature stability were conducted as described in section 2.3.3.

3.3.18. Statistical analysis

Unless otherwise stated, three independent experiments were carried out for each study. Statistical significance was evaluated by one-way ANOVA or paired two-tail Students t-test using GraphPad Prism version 6.00 for Windows (GraphPad Software, La Jolla California USA, www.graphpad.com). Unless otherwise stated, data is reported as mean \pm standard deviation (SD). A significance level (P-value) of < 0.05 was considered as statistically significant.

3.4. Results

3.4.1. Fluorescent bead uptake

The cellular uptake of nano-sized fluorescent latex beads (100nm and 500nm) was assessed using confocal microscopy to determine the optimal cut-off for MSNP size. For 100nm sized latex beads the cellular localisation of the beads is evident, particularly in the membrane regions and cytoplasm (Figure 3-1). For the 500nm sized latex beads a x63 magnification was used to enlarge isolated OBG400 cells with membrane localisation and partial cytoplasmic trapping observed (Figure 3-1).

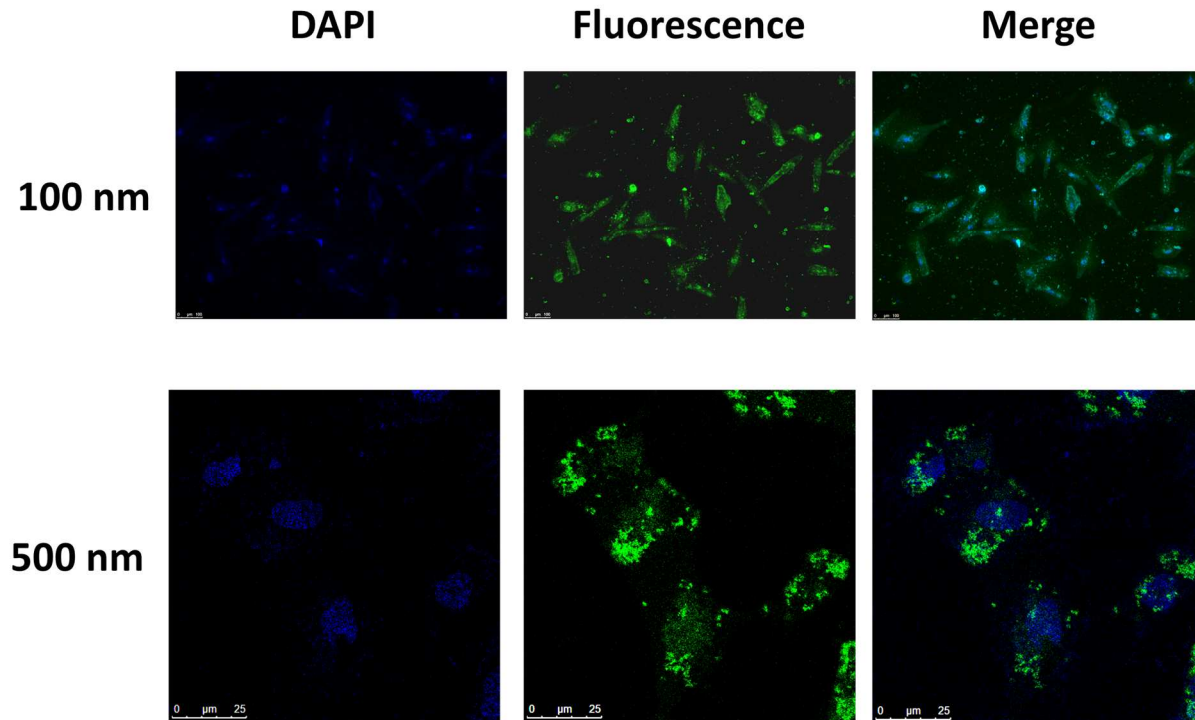


Figure 3-1: Cellular uptake of fluorescent latex beads in OBGF400

A concentration of 0.1 % v/v of latex beads (100nm and 500nm) were dispersed into HEPES (25mM) buffered HBSS prior to the addition into wells containing OBGF400 cells grown on collagen coated coverslips. Beads were incubated for 2 hours before the coverslip were washed, fixed and mounted onto coverslips with mounting media. Confocal microscopy was used to visualize the cellular localisation of beads with a 40x (100nm) or 63x (500nm) oil immersion objective. All images were acquired using an argon laser at 494 nm to visualise the beads and a helium laser to visualise DAPI at 461nm.

3.4.2. Synthesis and characterisation of MSNP

To develop MSNP, three reported methods were utilised to identify an appropriate method leading to optimal nanoparticles of less than 500nm. The three approaches differed primarily in the method of template removal. The assessment of final MSNP size for each method employed identified the 'Fan-method' as resulting the smallest nanoparticle size with a narrow PDI and stable negative zeta potential (Table 3-1).

Table 3-1: Particle size and zeta-potential of different MSNPs

Method	Particle size (nm)	Zeta potential (ζ) (mV)	PDI
Gul-MSNP	275 \pm 8.1	-20 \pm 0.98	0.23 \pm 0.08
Pro-2-MSNP	465 \pm 10	-18.25 \pm 1.18	0.25 \pm 0.1
Fan-MSNP	216.5 \pm 2.1	-23.9 \pm 0.4	0.13 \pm 0.02

Data is presented as mean \pm SD; n=3 and from 3 separate batches.

3.4.2.1. Scanning electron microscopy based assessment of the morphology of MSNP

To confirm the particle size and polydispersity of the formulated MSNP, SEM imaging was used to assess the morphological structure of MSNP produced from each method.

Gul-MSNP: the nanoparticles developed from the 'Gul-method' demonstrate some uniform spherical porous morphologies (Figure 3-2A), however the irregularity in spherical structures was evident (Figure 3-2B). Furthermore, the application of sonication to enhance dispersion and reduce PDI, resulted in the disruption/damage of the mesoporous nature of the silica spheres (Figure 3-21C and D).

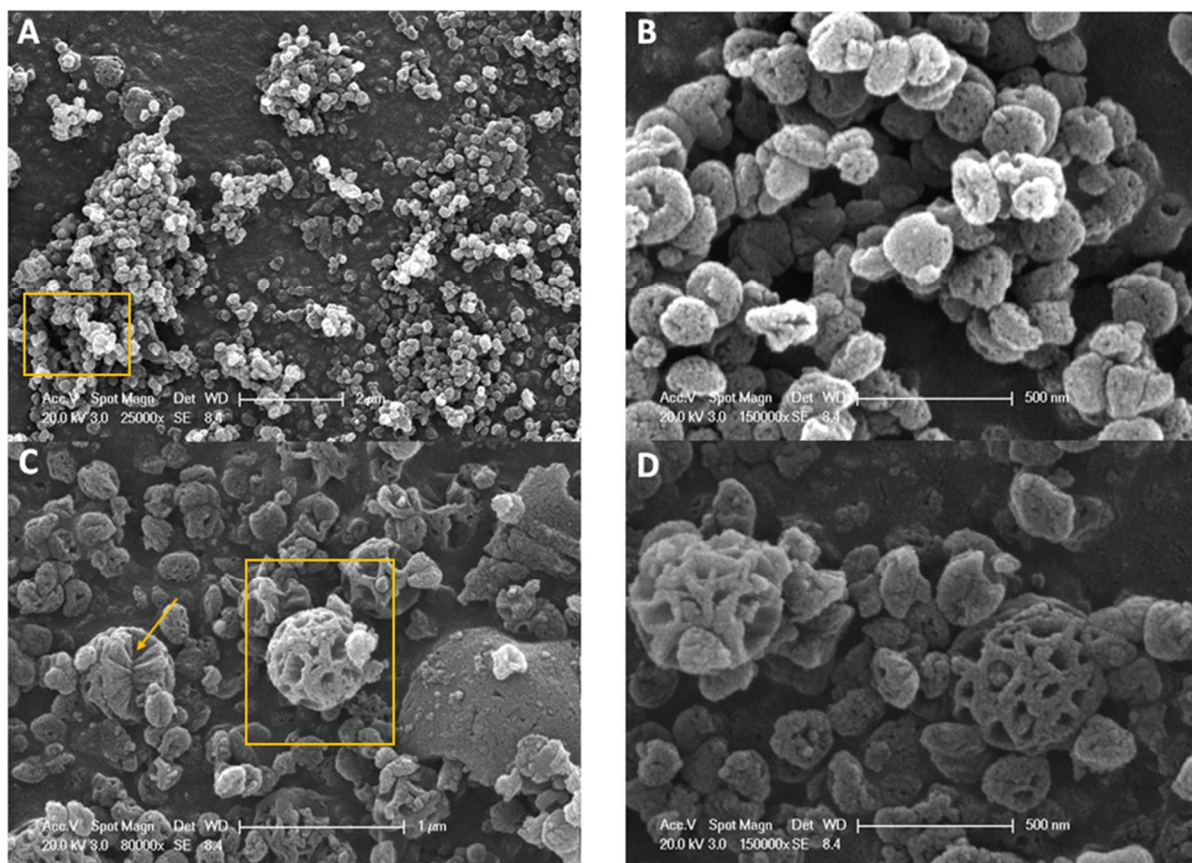


Figure 3-2: Scanning electron micrograph of Gul-MSNPs

(A) Base magnification of 25000x with yellow box highlighting region of interest (ROI); (B) 150000x magnification of ROI from (A); (C) Region of interest at magnification of 80000x with ruptured MSNP indicated by the yellow arrow and individual MSNP ROI highlighted; (D) 150000x magnification of ROI from (C). Samples were mounted on 12mm aluminium pin stubs with 12mm carbon tabs and coated with 15nm of gold. The powders were imaged at 5kV with a 150pA beam in high vacuum due to beam damage to the samples at higher kV's. The nano-particles were imaged at 10kV with a 100pA beam also in high vacuum. The SEM used was Carl Zeiss EVO LS 15. The gold coater used was a Quorum QR105S.

Pro-2-MSNP: the nanoparticles developed from the ‘Pro-2-method’ demonstrated relatively uniform smooth particles with ordered mesoporous morphologies (Figure 3-3), however the irregularity in spherical structures was evident (Figure 3-3B). The starburst nature of the morphology is also evident, extending from the centre of the nanoparticle to the surface.

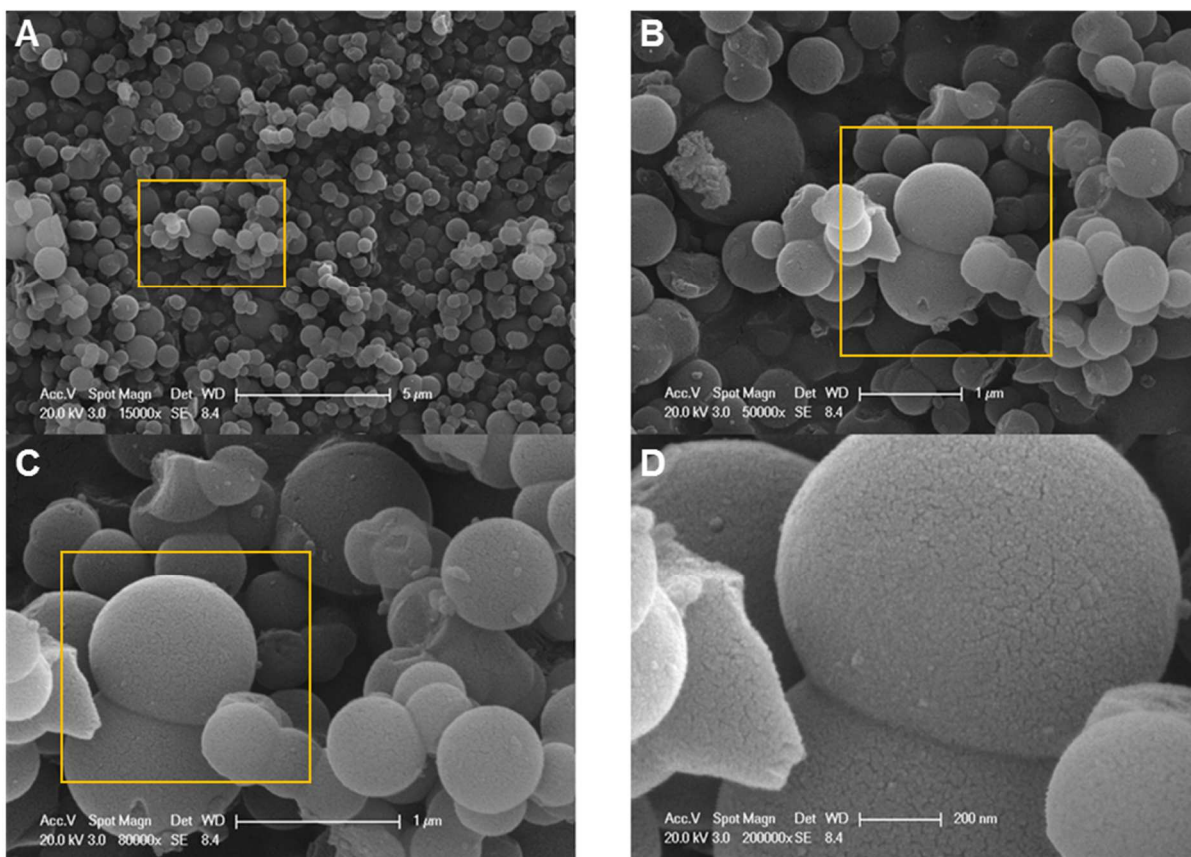


Figure 3-3: Scanning electron micrograph of Pro 2 MSNP

(A) Base magnification of 15000x with yellow box highlighting region of interest (ROI); (B) 50000x magnification of ROI from (A) with a further ROI highlighted; (C) 80000x magnification of ROI from (C) with new region of interested highlighted by the yellow square; (D) 200000x magnification of ROI highlighted from (C)..The samples were mounted on 12mm aluminium pin stubs with 12mm carbon tabs and coated with 15nm of gold. The powders were imaged at 5kV with a 150pA beam in high vacuum due to beam damage to the samples at higher kV's. The nanoparticles were imaged at 10kV with a 100pA beam also in high vacuum. The SEM used was Carl Zeiss EVO LS 15. The gold coater used was a Quorum QR105S.

Fan-MSNPs: the nanoparticles developed from the 'Fan-method' demonstrated significantly more uniform particle distribution of similar sizes and relatively uniform smooth particles with (Figure 3-4) and particle sizes of approximately 200nm. (Figure 3-4C), confirming the suitability of the 'Fan-method' to develop MSNP.

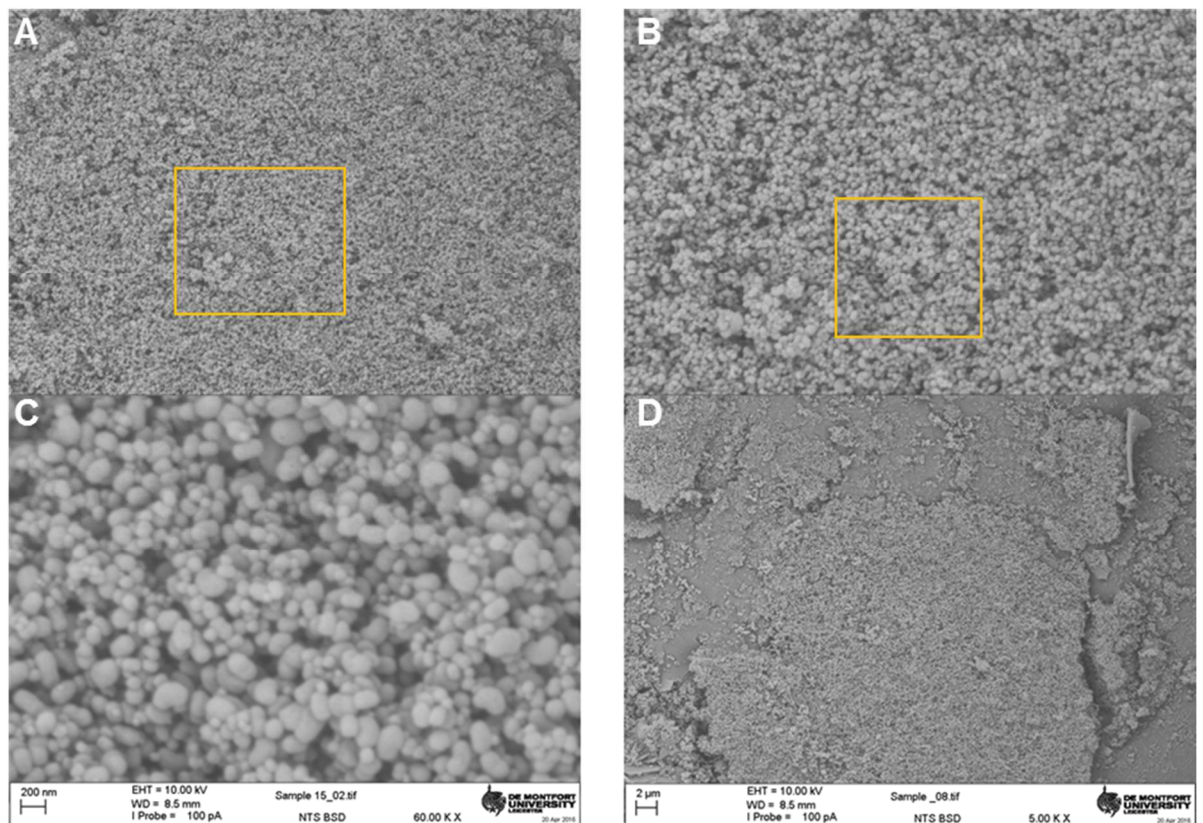


Figure 3-4: Scanning electron micrograph of Fan-MSNP

(A) Region of interest (ROI); (B) Magnification of ROI from (A); (C) 60000x magnification of ROI from (B); (D) 5000x magnification of detection grid. The samples were mounted on 12mm aluminium pin stubs with 12mm carbon tabs and coated with 15nm of gold. The powders were imaged at 5kV with a 150pA beam in high vacuum due to beam damage to the samples at higher kV's. The nano-particles were imaged at 10kV with a 100pA beam also in high vacuum. The SEM used was Carl Zeiss EVO LS 15. The gold coater used was a Quorum QR105S.

3.4.2.2. Surface porosity of MSNP using nitrogen adsorption-desorption studies

To determine the porosity of the Fan-MSNP and ascertain the pore volume and density, nitrogen adsorption/desorption isotherms were generated. The isotherm generated contains a distinct hysteresis phenomenon which occurs due to capillary condensation at a relative pressure (P/P_0) in the range of 0.2-0.4 and confirms the mesoporous nature of the particles (Table 3-2 and Figure 3-5).

Furthermore, this data confirms the honey comb structure of Fan-MSNP with a large surface area $987.67 \pm 3.38 \text{ m}^2/\text{g}$ and the DFT method confirms that the average pore size of $1.93 \pm 0.01 \text{ nm}$ (Figure 3-6 and 3-7) with total pore volume $0.95 \pm 0.004 \text{ cc/g}$ (Table 3-2).

Table 3-2: Nitrogen adsorption desorption data for Fan-MSNP

Batch	1	2	3	Mean (\pm SD)
Specific surface area (m^2/g)	988.76	990.38	983.88	987.67 ± 3.38
Average pore size (nm)	1.93	1.94	1.93	1.93 ± 0.01
Total pore volume (cc/g)	0.95	0.96	0.95	0.95 ± 0.004

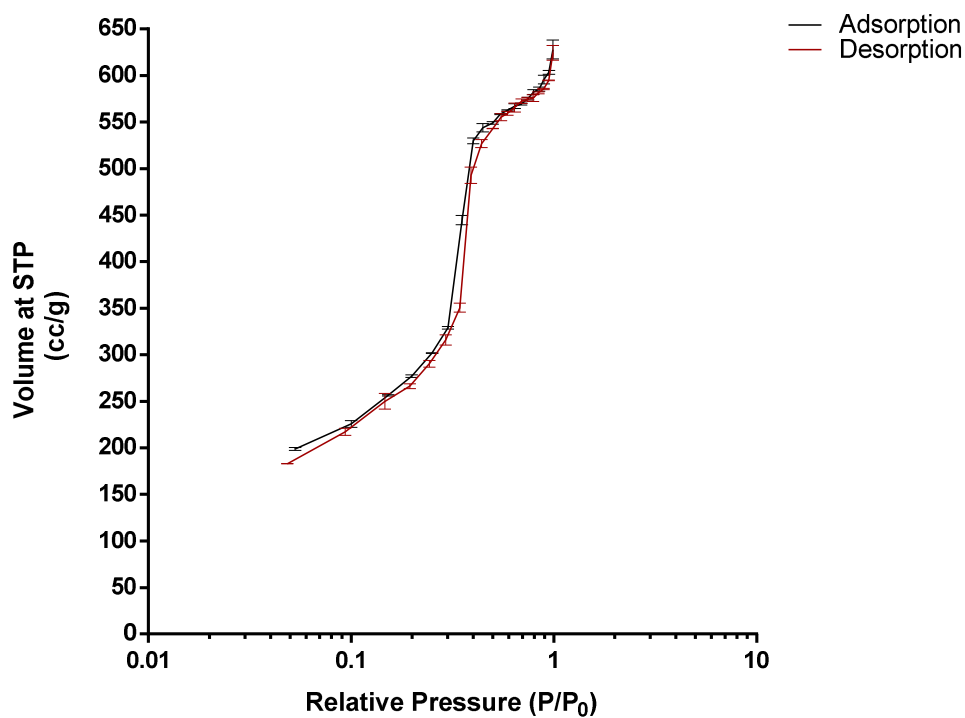


Figure 3-5: Nitrogen adsorption/desorption isotherms of Fan-MSNP.

STP: standard temperature and pressure.

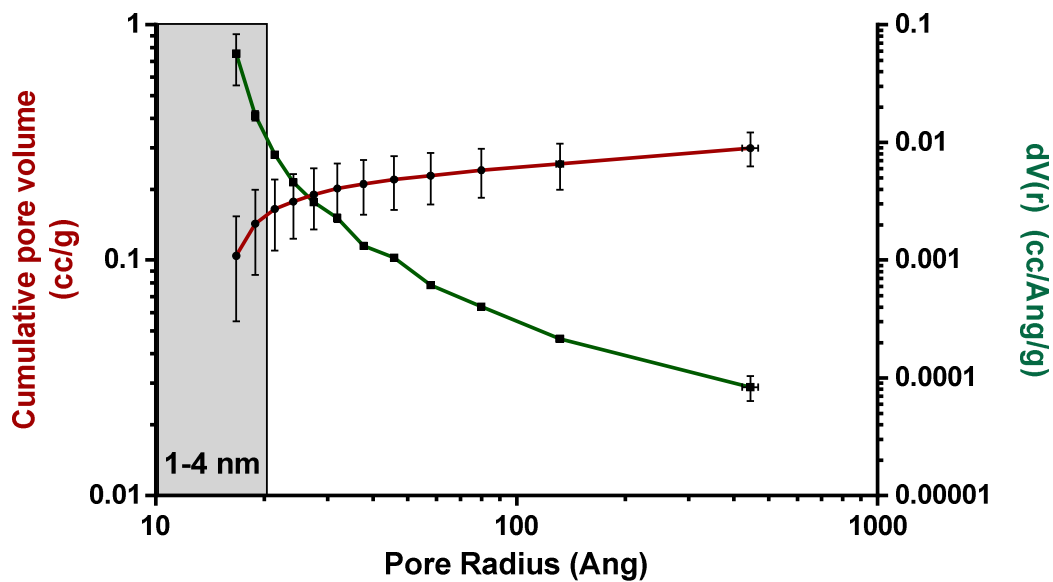


Figure 3-6: BJH pore radius distribution of Fan-MSNP.

The Barrett Joyner-Halenda pore sizes (\AA : Ang) were calculated based on assessment of the cumulative pore volume (y-axis) (red line) with the region corresponding to a pore diameter of 1-4nm indicated by the shaded box.

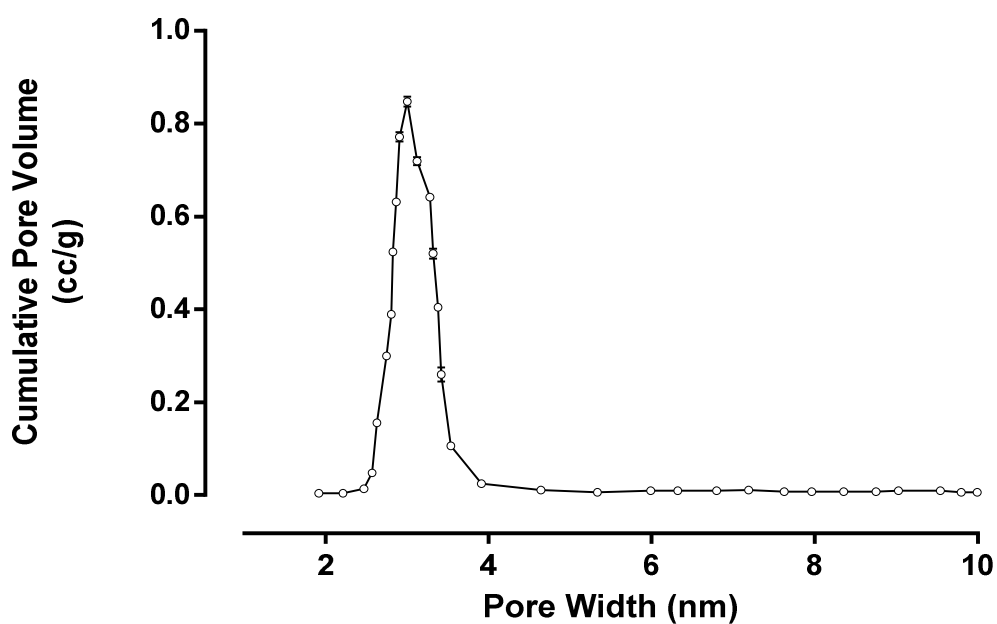


Figure 3-7: BJH pore width distribution of Fan-MSNPs.

The pore width (nm) were calculated based on assessment of the cumulative pore volume.

3.4.2.3. FTIR assessment of MSNP

The mesoporous nature of the particles can also be confirmed by characteristic vibrational bands in the FTIR spectra (Wanyika *et al.*, 2011). In Fan-MSNPs (Figure 3-8) bands at 795, 960 and 1633 cm^{-1} were due to SiO-H symmetrical stretching, Si-OH bending and SiO-H bending respectively. The strong band at 1057 cm^{-1} is attributed to Si-O-Si stretching vibrations, whereas the broad band at 3421 cm^{-1} is due to stretching vibration of the Si-OH group.

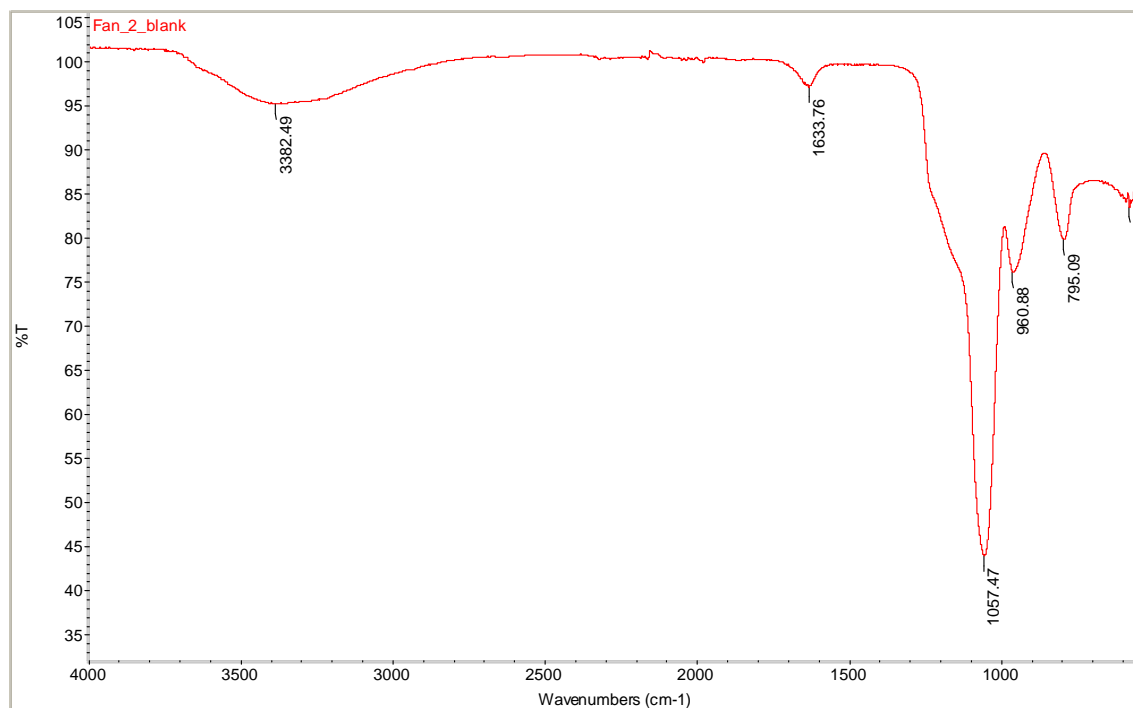


Figure 3-8: FT-IR spectra of Fan-MSNP.

A samples (2mg) of dried Fan-MSNP was loaded onto the diamond detection grid the FT-IR spectrophotometer and the IR spectra determined over the spectral range of 550-4000cm⁻¹ and reported as percentage transmittance (%T).

Template removal from the mesoporous nanoparticles can be confirmed from the FTIR data (Figure 3-9) four peaks can be observed in 550, 1500, 2900 and 3000cm⁻¹ before CTAB removal. These peaks were eliminated after refluxing with EtOH-HCl.

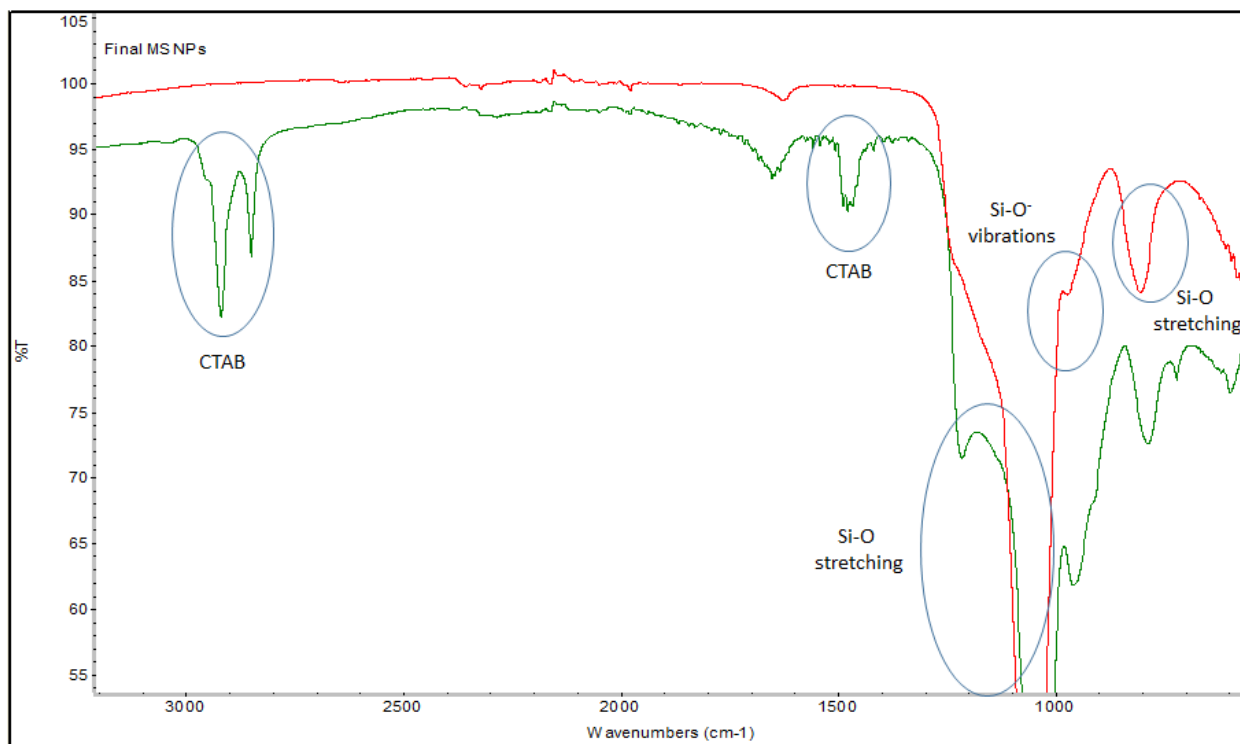


Figure 3-9: FT-IR spectra of Fan-MSNPs prior to CTAB removal (green) and immediately after CTAB removal (red).

The spectra indicate that due to presence of CH, CH₂ and CH₃ groups in CTAB molecule structure, four peaks can be observed in 550, 1500, 2900 and 3000cm⁻¹ before CTAB removal.

3.4.3. FITC loading of MSNPs for cellular uptake studies

The loading of MSNP with FITC was confirmed through FT-IR approaches. FITC was loaded passively into functionalised MSNPs by reacting amino group and isothiocyanate (Fan *et al.*, 2011). Loading of FITC dye can be confirmed by FT-IR, where a band the absorbed amide group was observed at 1550 and 1640 cm^{-1} and a band at 1583 cm^{-1} corresponding to benzene ring of FITC (Figure 3-10).

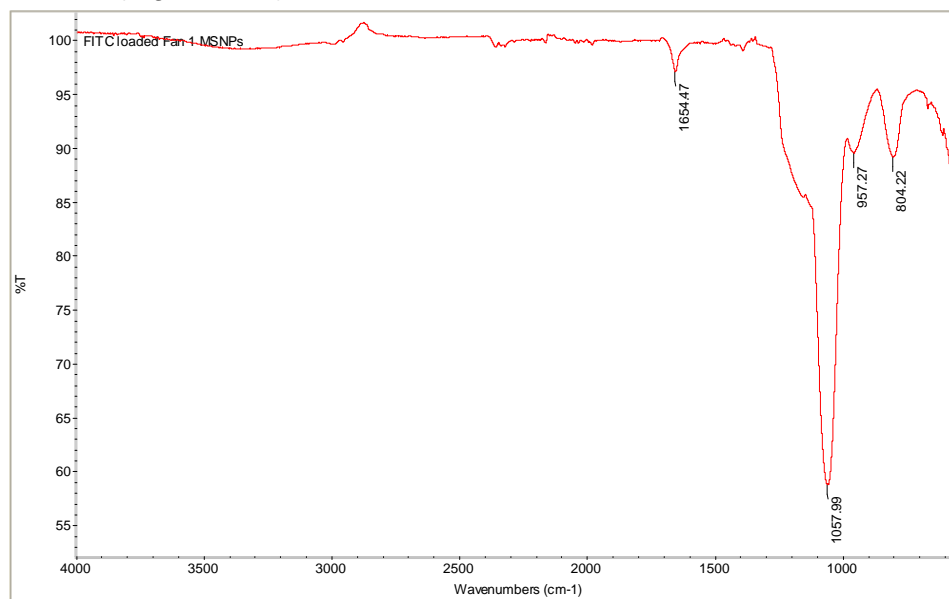


Figure 3-10: FT-IR spectra of FITC-MSNPs

A sample (2mg) of dried FITC-MSNPs was loaded onto the diamond detection grid the FT-IR spectrophotometer and the IR spectra determined over the spectral range of 550-4000 cm^{-1} and reported as percentage transmittance (%T).

3.4.4. FITC release from Fan-MSNPs

The loading of FITC into Fan-MSNPs resulted in a % EE of $48 \pm 2.3\%$. The release of FITC was subsequently assessed in PBS (pH 7.4). Following a 2-hour incubation $4.8 \pm 0.19\%$ was released from FITC-Fan-MSNPs (Figure 3-11).

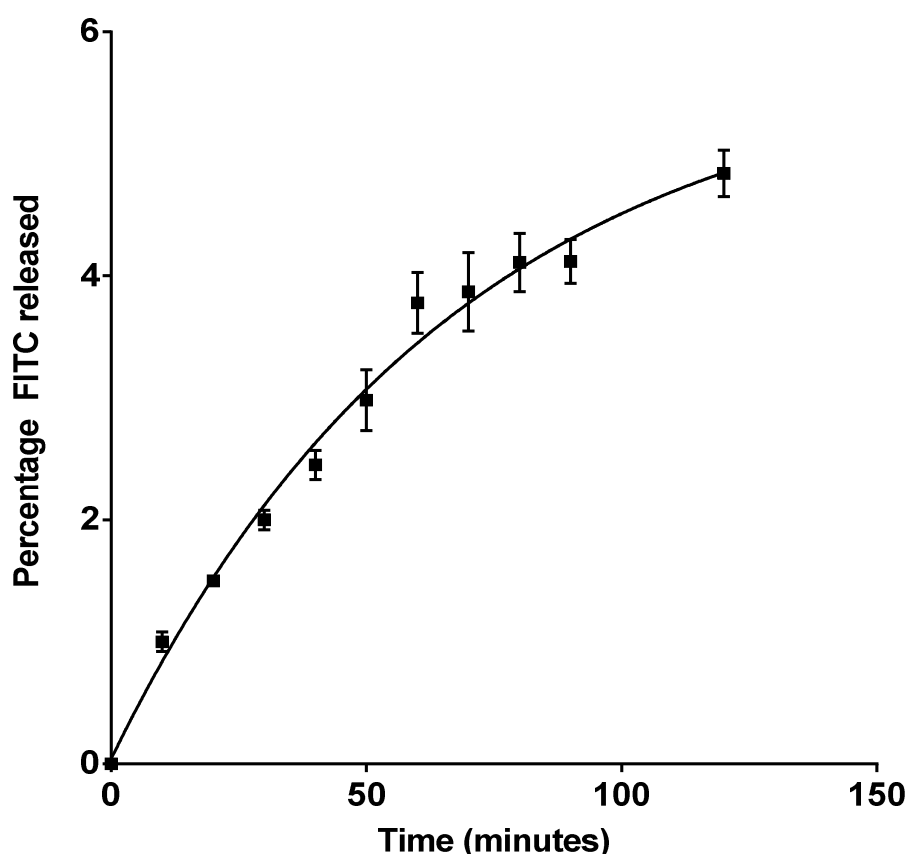


Figure 3-11: Release of FITC from FITC-MSNPs.

150mg of MSNPs were reacted under an argon atmosphere with 1.75mg of FITC (0.009mmol) 5 μ l of triethylamine (TEA) and 10ml of anhydrous dimethylformamide (DMF). The mixture was stirred at room temperature for 24h followed by centrifuging and washing twice at 8000RPM for 8 mins with DMF, diethyl ether and methanol. To remove the remaining solvent from the FITC-MSN particles were subjected to heating at 60 $^{\circ}$ C under vacuum. The release was assessed in PBS (pH 7.4) and quantified using a SpectraMax fluorescent microplate reader at an λ_{ex} : 490nm and λ_{em} : 517nm. N=3.

3.4.5. Cellular uptake of FITC-Fan-MSNPs

FITC-Fan-MSNPs were subsequently incubated for 2-hours with OBG400 cells seeded onto collagen-coated coverslips and the cellular localisation of FITC-Fan-MSNPs was determined using confocal microscopy and z-stack image processing. Single stage confocal imaging demonstrated generalised cellular location, with the presence of FITC-Fan-MSNPs within the cellular membrane and cytoplasm (Figure 3-12). However, to further discern the exact localisation within the cell, a z-stack multistage image capture was initiated to capture FITC-Fan-MSNPs fluorescence through the z-dimension of the cell.

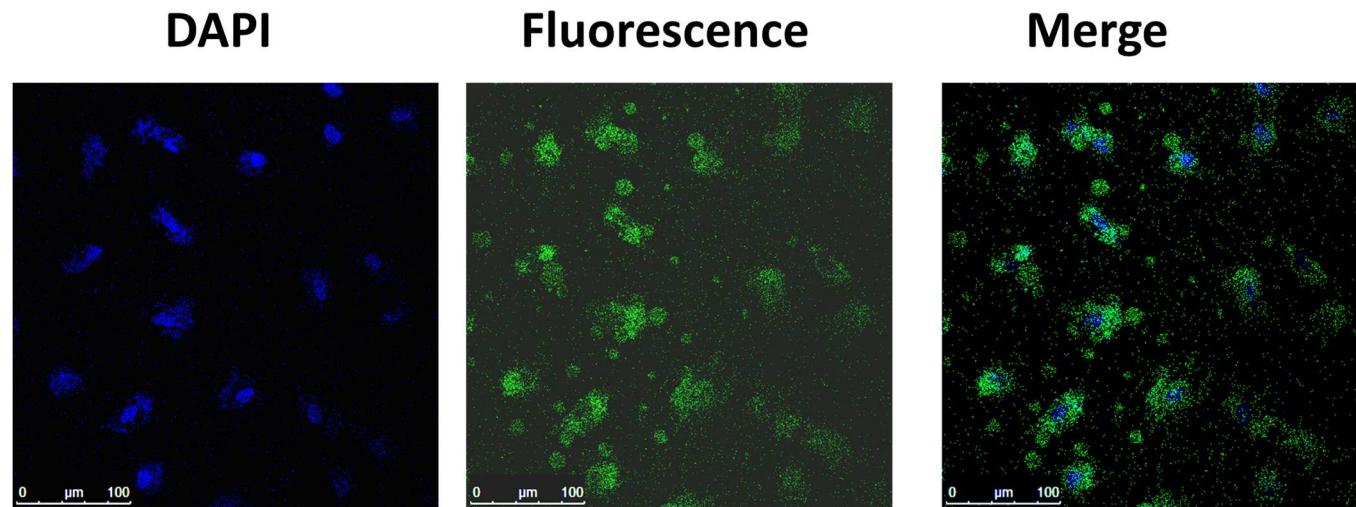


Figure 3-12: Cellular localisation of FITC-MSNPs

50 μ g/mL FITC-MSNPs were resuspended in HEPES (25mM) buffered HBSS prior to the addition into wells of a 12 well plate containing collagen coated OBG400 coverslips. FITC-MSNPs were incubated with coverslips for 2 hours before being thoroughly washed, and fixed with 4%w/v paraformaldehyde for 30 minutes in the dark. The coverslips were then mounted onto glass slides with mounting media containing 4',6-diamidino-2-phenylindole (DAPI). The localisation of the latex beads was analysed using an upright confocal microscope (Leica SP5 TCS II MP) and visualised with a 40x oil immersion objective. All images were acquired using an argon laser at 494nm to visualise FITC and a helium laser to visualise DAPI at 461nm.

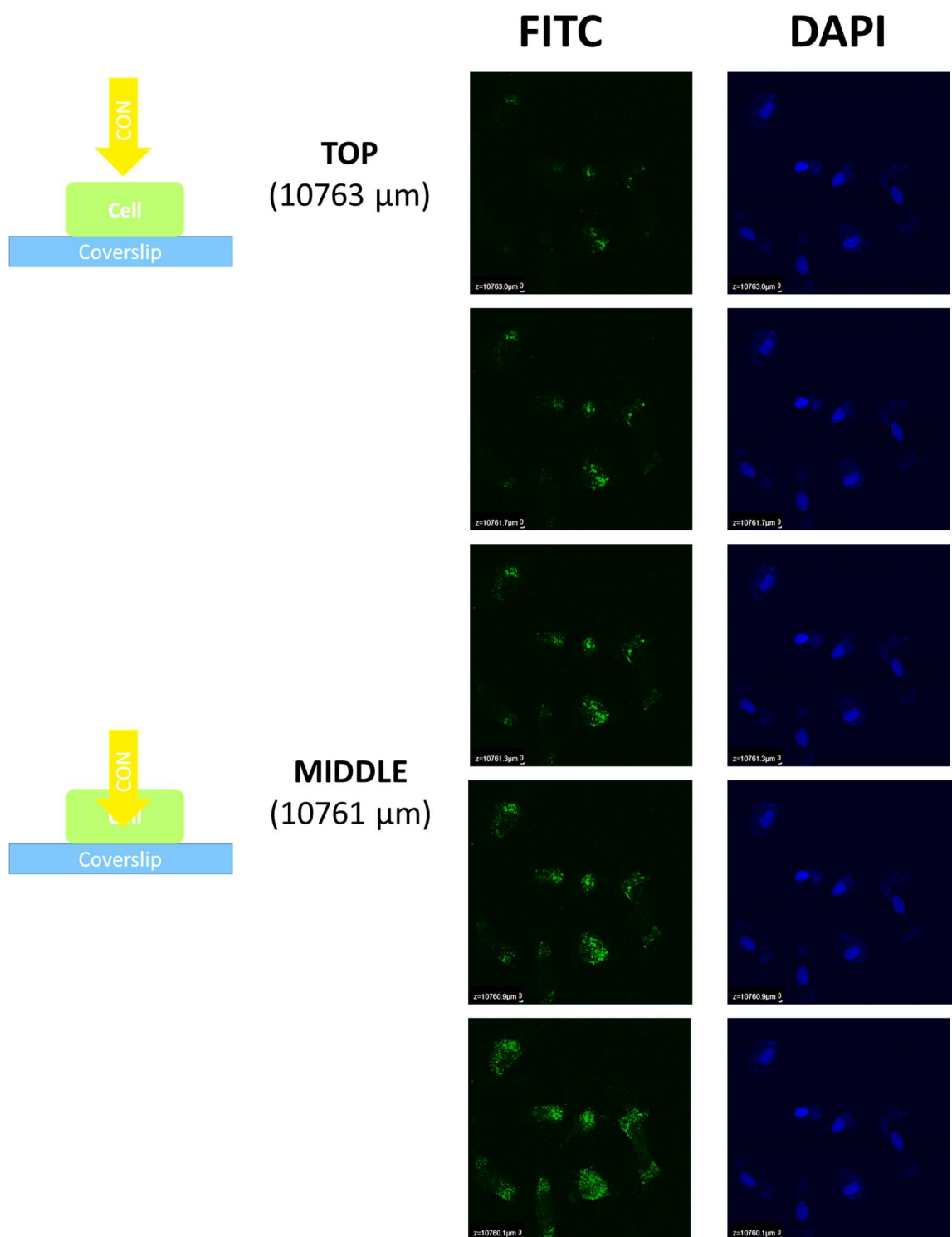


Figure 3-13: z-dimension cellular localisation of FITC-MSNP (stage 1)

FITC-MSNP previously incubated with OBG400 cells for 2 hours were further subjected to a *z-stack* analysis with the lens (CON) positioned above the cell layer (10763 μm) and lowered through the cells to the bottom of the cell layer (10758.4 μm). Images were captured of FITC (green) and DAPI (blue) through the *z-dimension*.

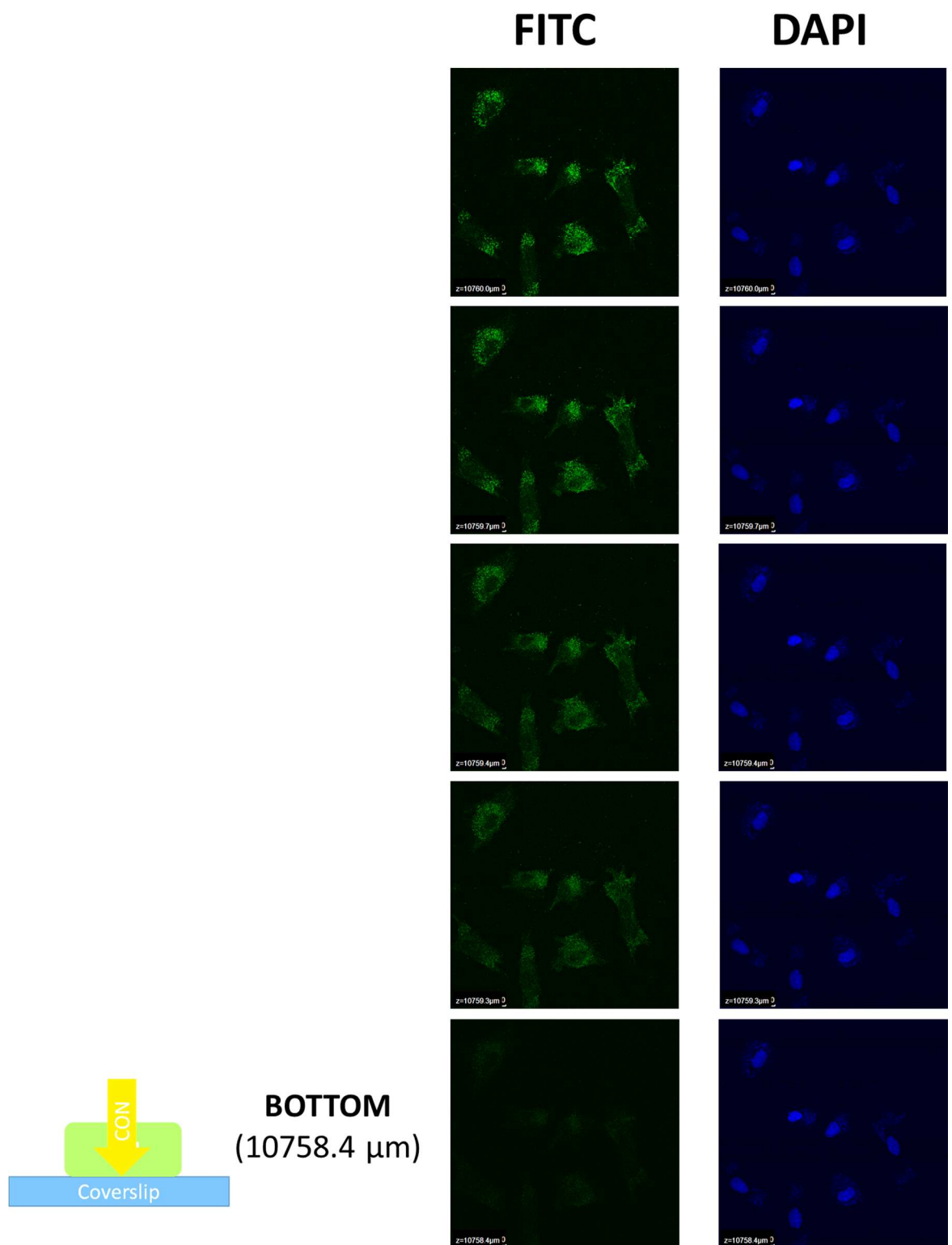


Figure 3-14: z-dimension cellular localisation of FITC-MSNP (stage 2)

FITC-MSNP previously incubated with OBG400 cells for 2 hours were further subjected to a *z-stack* analysis with the lens positioned above the cell layer (10763μm) and lowered through the cells to the bottom of the cell layer (10758.4μm). Images were captured of FITC (green) and DAPI (blue) through the *z-dimension*.

The confocal stage was set at the upper-most boundary of the OBG400 cells and the stage moved down towards the coverslip with images captured over a z-dimension of approximately 5 μ m. At the onset of the z-stack analysis, FITC-Fan-MSNP is localised on the exterior of the cell boundary and potentially on the surface of the cells (10763 μ m). As the stage progresses, the localisation of FITC-Fan-MSNP increases with clear demarked zones of cytoplasmic localisation near the 'mid-to-bottom' regions of the cells (Figure 3-13 and 3-14).

3.4.6. Phytochemical loading of Fan-MSNP

The loading of curcumin into MSNP was confirmed through FT-IR analysis. The characteristic IR absorption frequencies in the spectral range of 550-4000 cm^{-1} were measured for free curcumin and Curc-MSNPs. The interaction between MSNPs and curcumin after being loading was also analysed using FTIR.

Curcumin spectra shows a sharp peak at 3507 and 3293 cm^{-1} corresponding to -OH group vibrations without and with intermolecular hydrogen bonding respectively. However, in case of Curc-MSNPs instead of these two peaks only one new broad peak at 3430 cm^{-1} was observed which confirms the intermolecular hydrogen bonding isolated silanol and enolic hydroxyl group. The peak at 1620 cm^{-1} was observed due to stretching vibrations of C=O bond (Figure 3-15).

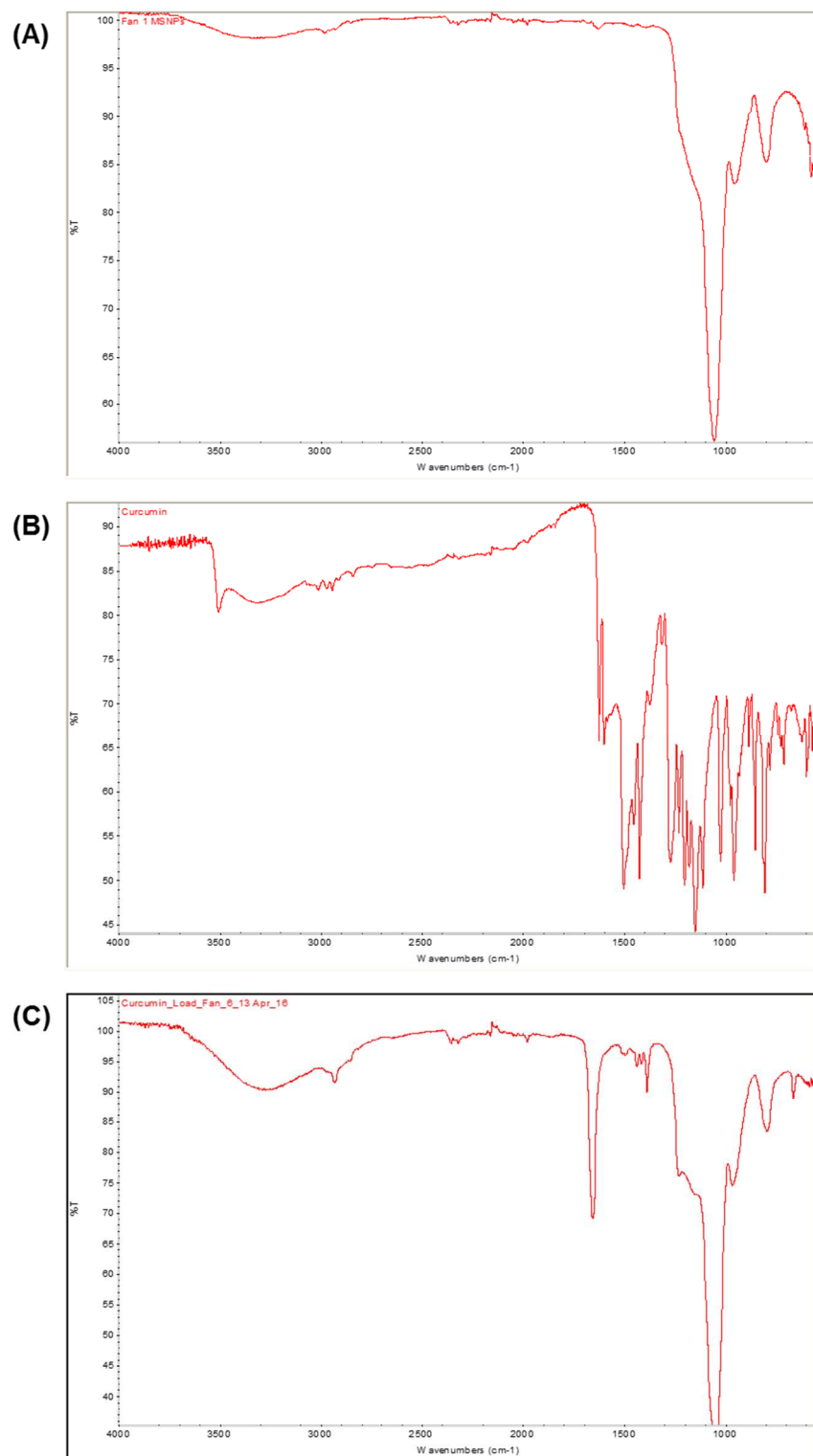


Figure 3-15: FTIR spectra of (A) Fan-MSNP; (B) and (C) Curc-MSNP

10mg of curcumin or MSNP were placed on the diamond probe of a Thermo Scientific FT-IR spectrophotometer and the IR spectrum analysed over the spectral range of 550-4000cm⁻¹ and reported as the percentage transmittance (%T).

To further characterise the loading of curcumin into Fan-MSNP, DSC thermographs were analysed for blank and loaded MSNP. The thermographs of pure curcumin show characteristic single melting endothermic peak at 176°C (Figure 3- 16). However, the DSC thermographs for Curc-MSNPs show no characteristic melting point for curcumin at 176°C.

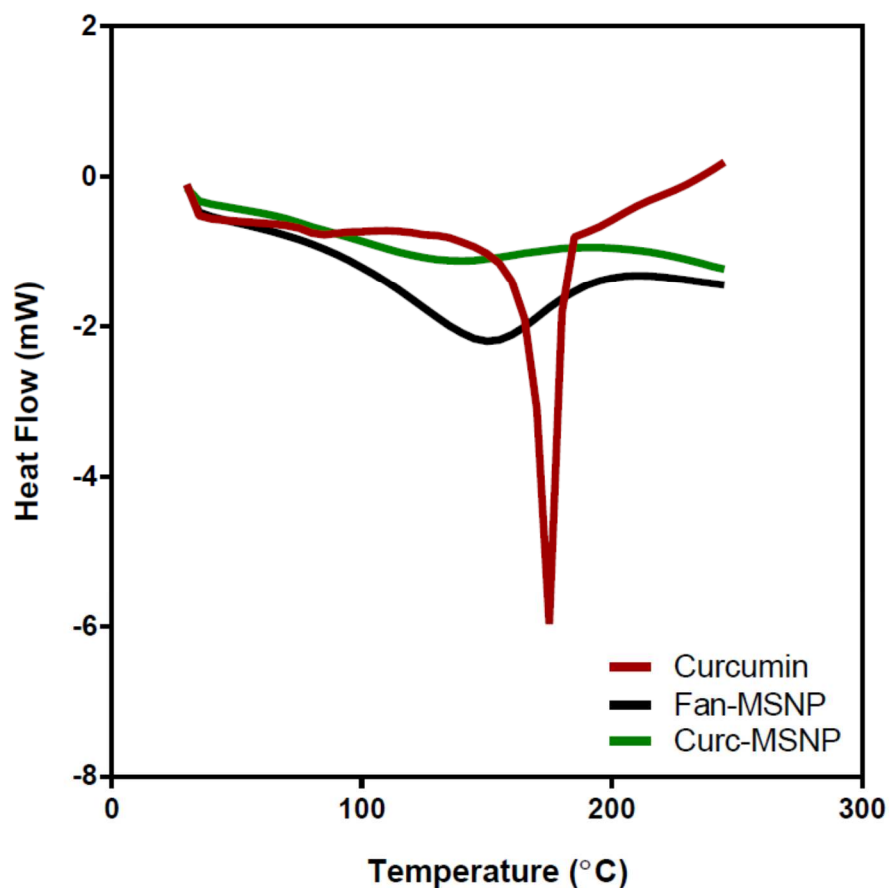


Figure 3-16: DSC thermographs of curcumin, Fan-MSNP and Curc-MSNP

2-5mg of samples were weighed and placed on the sample pan with quantified determined over a heating range of 30-250°C, at the rate of 10°C/min and under nitrogen purge of 50mL/min.

The TGA results show that the total weight loss of the Fan-MSNPs at the end of the run was $22.16 \pm 1.12\%$ compared to the blank MSNPs, $7.21 \pm 0.45\%$ with a calculated LC of $14.95 \pm 0.67\%$ and which corresponds to the calculated EE of $12.34 \pm 1.28\%$ for the 'wet method' (Figure 3.17).

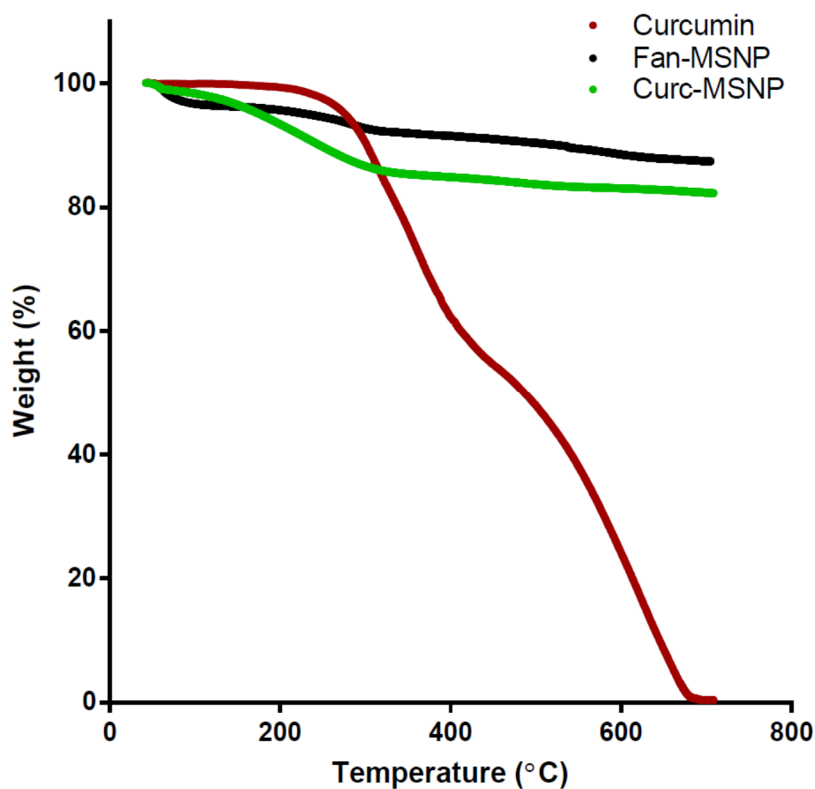


Figure 3-17: TGA thermograms of curcumin, Fan-MSNPs and Curc-MSNPs.

2-5mg of samples were weighed and placed on the sample pan with weight loss quantified determined over a heating range of 50-700°C, at the rate of 10°C/min and under nitrogen and air purge.

Curc-MSNP were further characterise for changes in particle size and zeta potential compared to blank MSNP. The hydrodynamic mean diameter of Fan-MSNPs size increased from $216.8 \pm 2.1\text{nm}$ to $263.51 \pm 8.3\text{nm}$ after loading with curcumin ($P \leq 0.01$) with a statistically significant increase in the PDI from 0.13 ± 0.02 to 0.26 ± 0.05 ($P \leq 0.05$) (Figure 3-18).

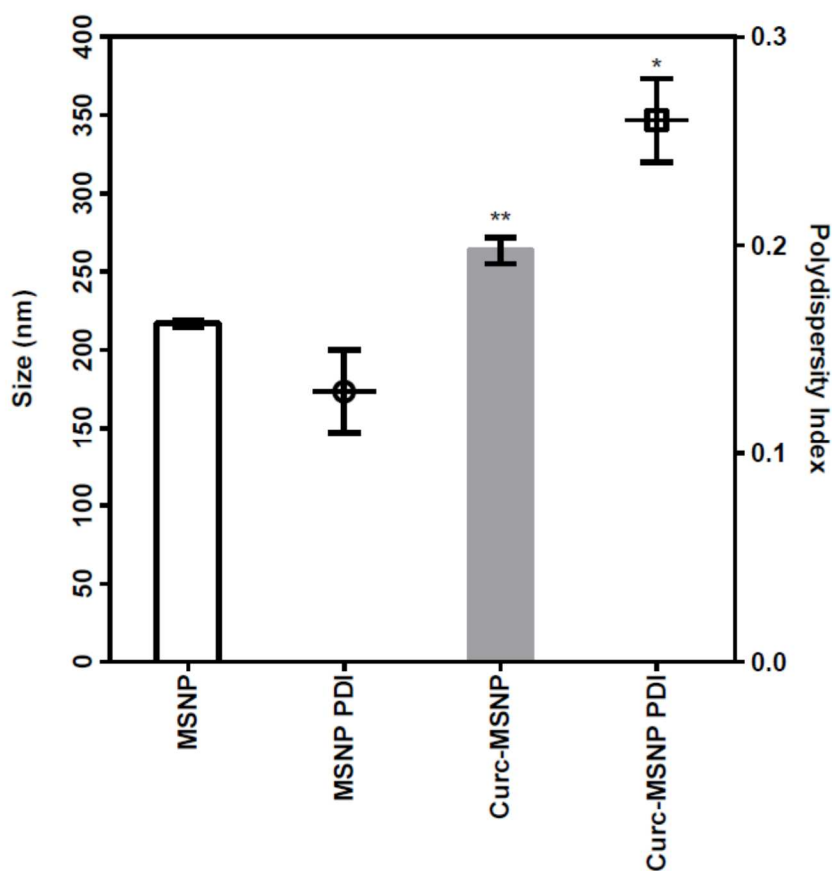


Figure 3-18: Fan-MSNP size and PDI before and after loading with curcumin

100 μL of 1mg/mL sonicated Fan-MSNP or Curc-MSNP suspensions were diluted in 3mL ultrapure water, vortexed and analysed through dynamic light scattering techniques using NanoBrook 90 Plus Zeta (Brookhaven Instruments Corporation) to assess the particles size (mean diameter) and polydispersity index (PDI). Statistical significance tested between unloaded and loaded MSNP. * $P \leq 0.05$, ** $P \leq 0.01$.

Following loaded with curcumin, the zeta potential of the Curc-MSNP decreased from $-23.9 \pm 0.4\text{mV}$ to $-16.9 \pm 0.9\text{mV}$ ($P \leq 0.01$) (Figure 3-19).

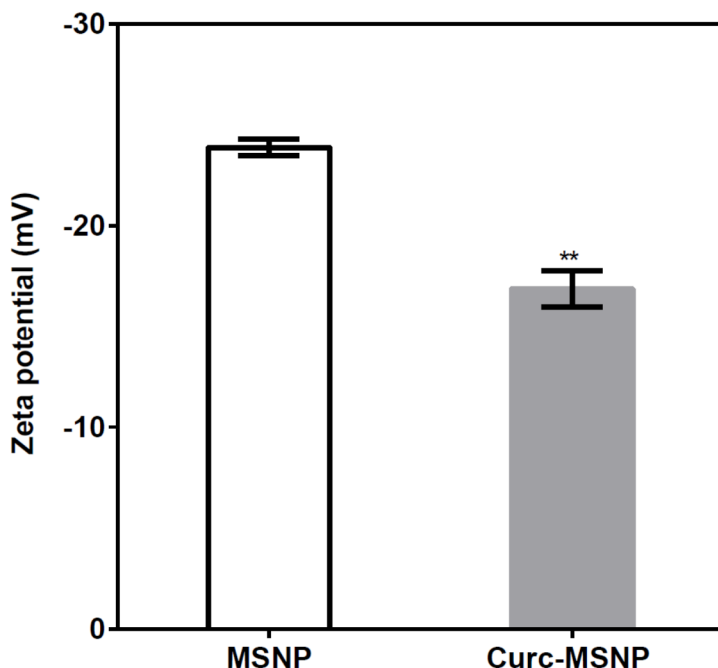


Figure 3-19: Fan-MSNP zeta potential before and after loading of flavonoid curcumin

100 μL of 1mg/mL sonicated Fan-MSNP or Curc-MSNP suspensions were diluted in 3ml ultrapure water, vortexed and analysed through dynamic light scattering techniques using NanoBrook 90 Plus Zeta (Brookhaven Instruments Corporation) to assess the sample zeta potential. * $P \leq 0.05$, ** $P \leq 0.01$.

The loading of chrysin into Fan-MSNP was confirmed using FT-IR analysis. The characteristic IR absorption frequencies in the spectral range of $550\text{-}4000\text{cm}^{-1}$ were measured for free chrysin and Chry-MSNP. the FT-IR spectrum of chrysin, shows the carbonyl group vibrations coupled with the double band in the γ -benzopyrone ring at 1655cm^{-1} and absorption bands at 1612 , 1577 and 1450cm^{-1} related to carbon vibration in benzene and γ -pyrone rings (valance vibrations $\text{C}=\text{C}$) can be observed in Figure 3-20.

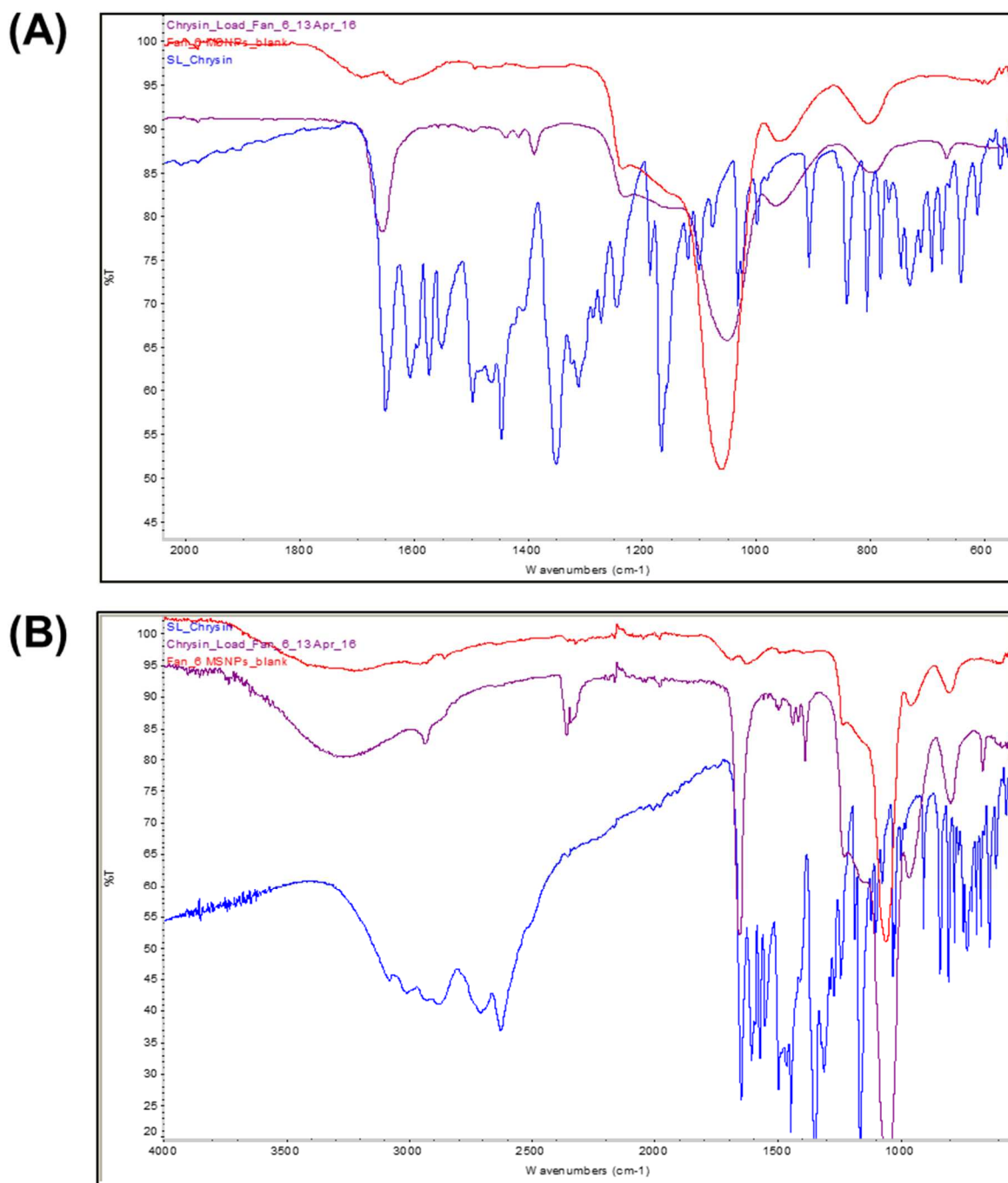


Figure 3-20: FTIR spectra of chrysin, blank MSNPs and Chry-MSNPs

Samples were analysed using Thermo Scientific FT-IR spectrophotometer in the spectral range of: (A) 1800-4000 cm^{-1} and (B) 550-1850 cm^{-1} for chrysin (blue), Fan-MSNPs (red) and Curc-MSNPs (purple).

To further characterise the loading of chrysin into Fan-MSNP, DSC thermographs were analysed for blank and loaded MSNP. The thermographs of pure chrysin show characteristic melting point depression at 286°C (Figure 3-21). However, the DSC thermographs for Curc-MSNP show no characteristic melting point for chrysin at 286°C.

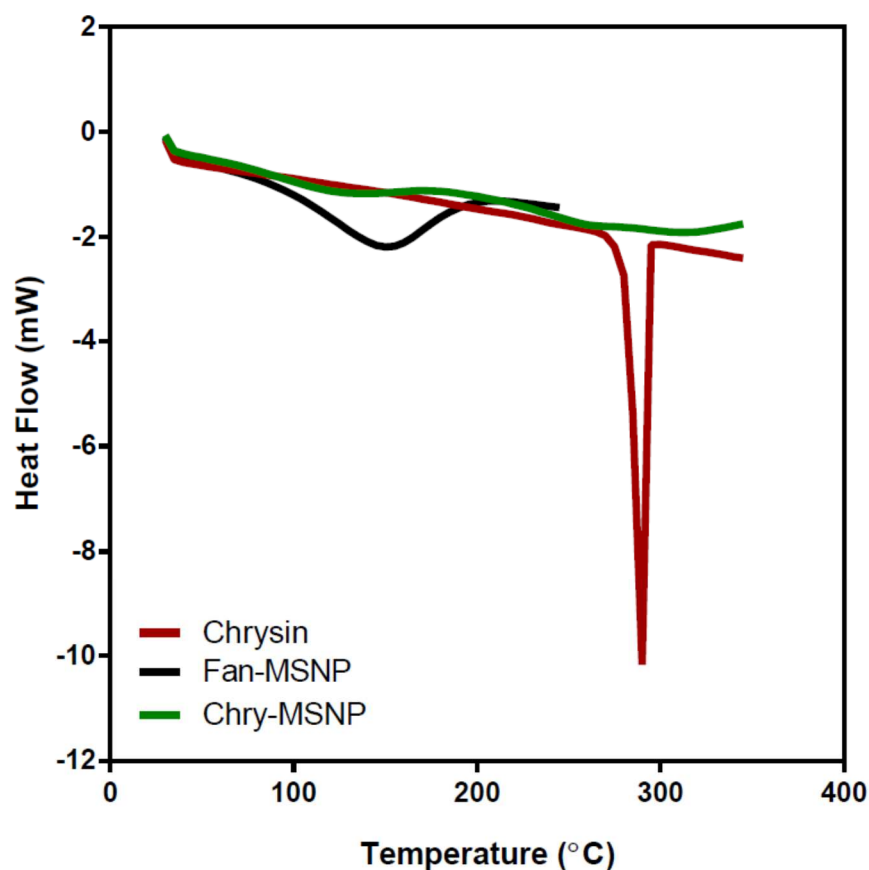


Figure 3-21: DSC thermographs of chrysin, Fan-MSNP and Chry-MSNP

2-5mg of samples were weighed and placed on the sample pan with the weight loss quantified determined over a heating range of 30-250°C, at the rate of 10°C/min and under nitrogen purge of 50mL/min.

The TGA results show that the total weight loss of the Fan-MSNPs at the end of the run was $21.07 \pm 0.75\%$ compared to the blank MSNPs, $9.58 \pm 1.94\%$ with a calculated LC of $11.49 \pm 1.19\%$ and which corresponds to the calculated EE of $12.34 \pm 1.28\%$ for the 'wet method' (Figure 3-22).

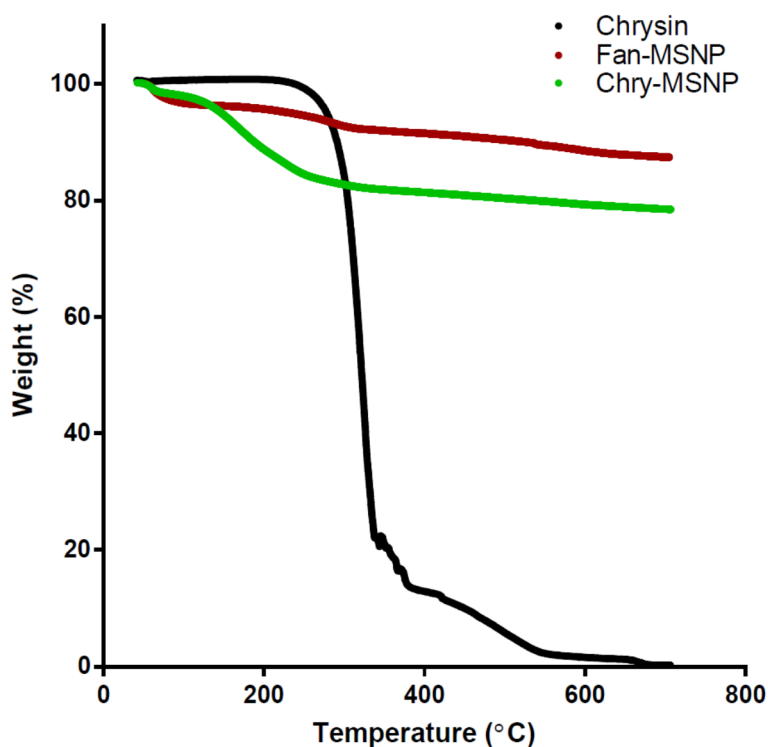


Figure 3-22: TGA thermograms of chrysin, Fan-MSNPs and Chry-MSNPs.

2-5 mg of samples were weighed and placed on the sample pan with weight loss quantified determined over a heating range of 50-700°C, at the rate of 10°C/min and under nitrogen and air purge.

Chry-MSNPs were further characterised for changes in particle size and zeta potential compared to blank MSNP. The hydrodynamic mean diameter of Fan-MSNPs size increased from $216.8 \pm 2.1\text{nm}$ to $283.5 \pm 8.3\text{nm}$ after loading with chrysin ($P \leq 0.01$) with a statistically significant increase in the PDI from 0.13 ± 0.02 to 0.31 ± 0.11 ($P \leq 0.05$) (Figure 3-23).

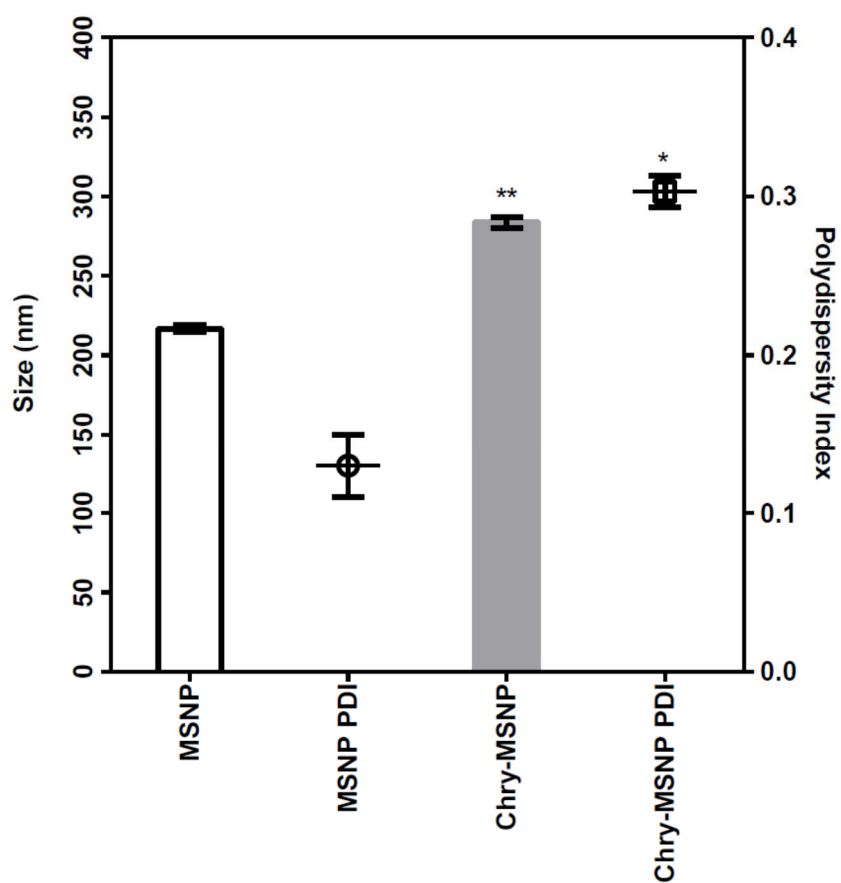


Figure 3-23: Fan-MSNP size and PDI before and after loading with chrysin

100 μ L of 1mg/mL sonicated Fan-MSNP or Chry-MSNP suspensions were diluted in 3ml ultrapure water, vortexed and analysed through dynamic light scattering techniques using NanoBrook 90 Plus Zeta (Brookhaven Instruments Corporation) to assess the particles size (mean diameter) and polydispersity index (PDI). Statistical significance tested between unloaded and loaded MSNP. * $P \leq 0.05$, ** $P \leq 0.01$.

Furthermore, the zeta potential of the Chry-MSNPs decreased $-23.9 \pm 0.4\text{mV}$ to $-30.8 \pm 0.3\text{mV}$ ($P \leq 0.01$) (Figure 3-24).

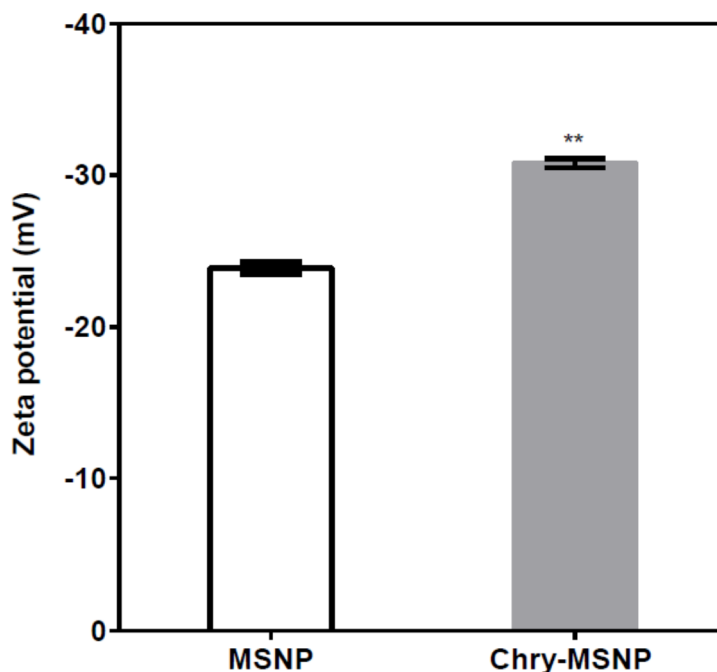


Figure 3-24: Zeta potential before and after loading of flavonoid chrysin

100 μL of 1 mg/ml sonicated MSNPs suspension was diluted in 1.5ml ultrapure water, vortexed and used to measure the zeta potential. The mean diameter and PDI was obtained from 3 runs of 3 minutes by dynamic light scattering technique using NanoBrook 90 Plus Zeta (Brookhaven Instruments Corporation). ** $P \leq 0.01$.

3.4.7. HPLC-UV detection of curcumin

The HPLC-UV method was developed and successfully validated to detect curcumin with a retention time of 13.3 minutes for the majority constituent peak with minor peaks at 11.09 and 12.15 minutes for the minor constituents of curcumin (Figure 3-25). System precision and method precision demonstrated RSD within acceptable limits of 1% and 2% respectively, indicating an acceptable level of precision of the analytical system.

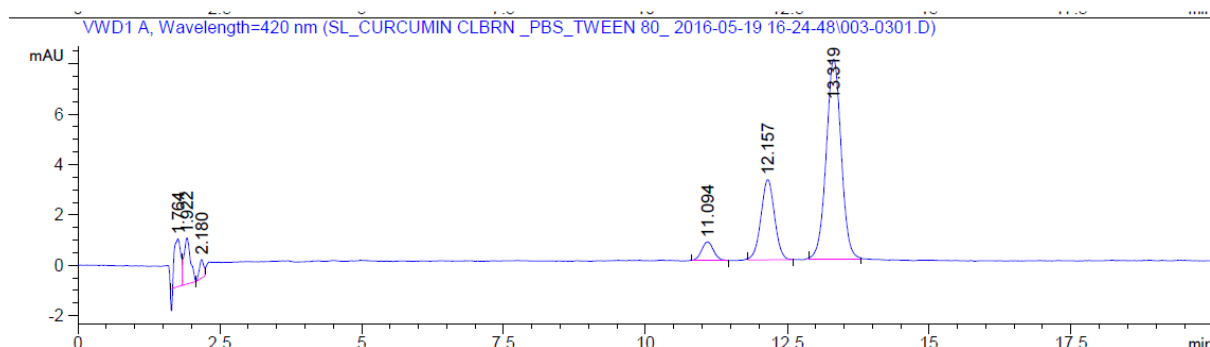


Figure 3-25: HPLC chromatogram of curcumin

Curcumin was detected using an Agilent 1200 Series (Waldbronn, Germany) equipped with a multiple wavelength detector (VWD) and a Phenomenex Luna C18 (150 × 4.6mm) 5µm column was used for RP-HPLC. Mobile phase was made up of ACN:5% acetic acid in a ratio of 45:55 (v/v). Mobile phases were filtered through 0.45µm filter and sonicated before use. The flow rate was maintained at 0.8ml/min with 15 minutes run time and the injection volume was 20µL while column temperature was kept at ambient with a UV-detection wavelength of 420nm.

System precision: six replicate injections of an identical standard curcumin stock solution were injected into the HPLC and peak area calculated. The relative standard deviation (%RSD) for the six samples was not more than 1.0% indicating system precision is within acceptable limits as measured per individual run, each with its own identical standard curcumin stock solution, with an overall RSD of 0.54% (Table 3-3). The LOD was 2.1µg/mL, LOQ was 7.1µg/mL and the signal to noise ratio was >10.

Table 3-3: System precision assessment for curcumin HPLC-UV detection

Injection no.	Area counts ($\mu\text{V sec}$)			Mean
	Run 1	Run 2	Run 3	
1	2546	2495	2415	
2	2562	2518	2447	
3	2542	2491	2451	
4	2532	2481	2454	
5	2544	2493	2465	
6	2545	2494	2467	
Mean	2545.17	2495.47	2449.83	2496.82
SD	9.68	12.11	18.79	13.52
RSD (%)	0.38	0.49	0.77	0.54

System precision was assessed through 6 injection of the same curcumin stock solution for each independent runs (3 runs in total). Mean and SD reported with percentage root-square deviation.

Method precision: six preparations of the same batch of samples were analysed for method precision with a resultant %RSD of less than 2.0% (Table 3-4) for all samples demonstrating method precision is within acceptable limits with an overall %RSD of 1.08%.

Table 3-4: Method precision assessment for curcumin

Injection no.	Assay (% w/w)			
	Run 1	Run 2	Run 3	
1	99.08	98.09	101.81	
2	98.49	99.75	101.20	
3	99.23	100.49	101.00	
4	97.51	101.47	100.20	
5	99.24	97.69	99.59	
6	99.87	97.60	101.30	
Mean	98.90	99.18	100.85	99.64
SD	0.81206281	1.62413	0.80999	1.08
RSD (%)	0.82106994	1.63754	0.80316	1.08

Linearity of response: the linearity of precision for curcumin was determined over a concentration range of 78 -10000 μ g/mL. A proportional response was evident versus the analytical concentration over the working concentration range with a r^2 of 0.998 and linear equation of $y = 700.3 \pm 0.82 \cdot x$ (Figure 3-26).

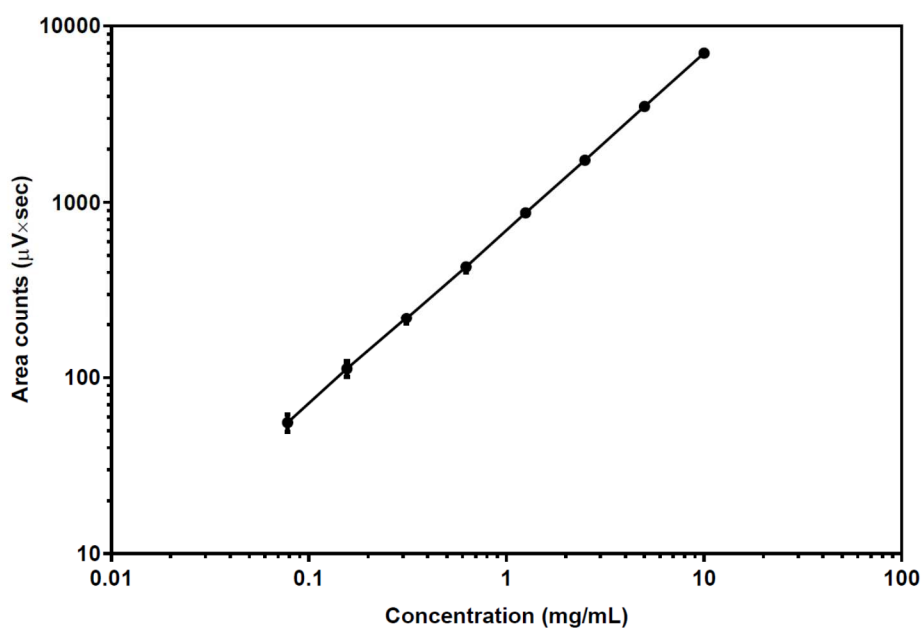


Figure 3-26: Linearity plot for curcumin

A HPLC-UV method was developed to assess the linearity of detection over a concentration range of 78 - 10000µg/mL. Data represents mean (solid line) \pm SD (error bars). n=3.

3.4.8. HPLC-UV detection of chrysin

The HPLC-UV method was developed and validated used to detect chrysin with a retention time of 11.78 minutes (Figure 3-27). System precision and method precision demonstrated RSD within acceptable limits of 1% and 2% respectively, indicating an acceptable level of precision of the analytical system.

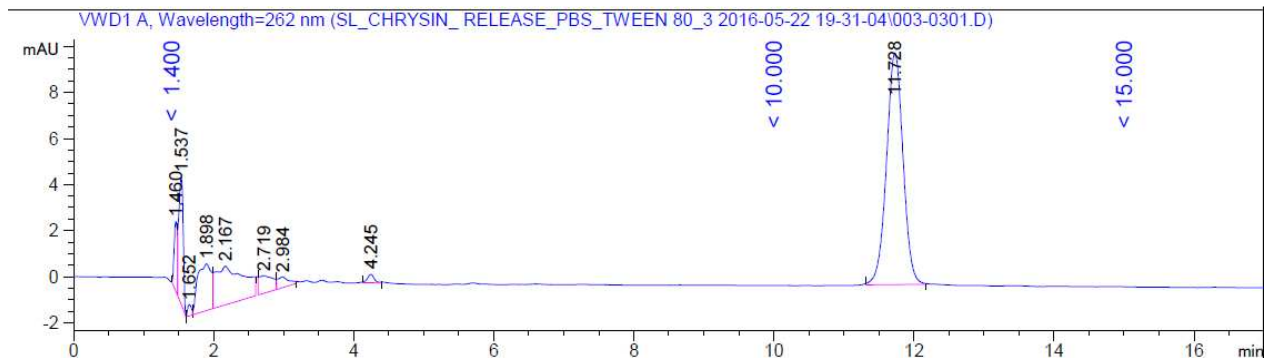


Figure 3-27: Chrysin HPLC chromatogram

Chrysin was detected using a Phenomenex Luna C18 (150 × 4.6mm) 5µm column through RP-HPLC. The mobile phase consisted of water:methanol:acetonitrile:phosphoric acid in a ratio of 60:30:38:1(v/v). Mobile phases were filtered through 0.45µM filter and sonicated prior to use. The flow rate was maintained at 1.0mlmin⁻¹ with an injection volume of 10µL. The UV detection of chrysin was measured at 262nm.

System precision: six replicate injections of an identical standard chrysin stock solution were injected into the HPLC and peak area calculated. The relative standard deviation (%RSD) for the six samples was not more than 1.0% indicating system precision is within acceptable limits as measured per individual run, each with its own identical standard chrysin stock solution, with an overall RSD of 0.27% (Table 3-5).

Table 3-5: System precision assessment for chrysin HPLC-UV detection

Injection no.	Area counts ($\mu\text{V sec}$)			Mean
	Run 1	Run 2	Run 3	
1	843	854	849	
2	842	855	851	
3	841	851	848	
4	843	850	852	
5	844	857	850	
6	842	855	843	
Mean	842.50	853.67	848.83	848.33
SD	1.05	2.66	3.19	2.29
RSD (%)	0.12	0.31	0.38	0.27

System precision was assessed through 6 injections of the same chrysin stock solution for each independent runs (3 runs in total). Mean and SD reported with percentage root-square deviation

Method precision: six preparations of the same batch of samples were analysed for method precision with a %RSD of less than 2.0% (Table 3-6) for all samples demonstrating method precision is within acceptable limits with an overall %RSD of 1.79%.

Table 3-6: Method precision assessment for chrysin

Injection no.	Assay (% w/w)			Mean
	Run 1	Run 2	Run 3	
1	102.12	98.19	102.12	
2	99.87	99.65	101.48	
3	98.99	102.36	100.56	
4	98.17	97.25	99.65	
5	97.69	98.11	98.57	
6	101.23	98.67	97.25	
Mean	99.67833333	99.0383	99.9383	99.55
SD	1.738302812	1.80681	1.82787	1.79
RSD (%)	1.743912397	1.82436	1.82899	1.79

Linearity of response: the linearity of precision for chrysin was determined over a concentration range of 78 -10000µg/mL. A proportional response was evident versus the analytical concentration over the working concentration range with a r^2 of 0.998 and linear equation of $y = 3220.3 \pm 1.35 \cdot x$ (Figure 3-28).

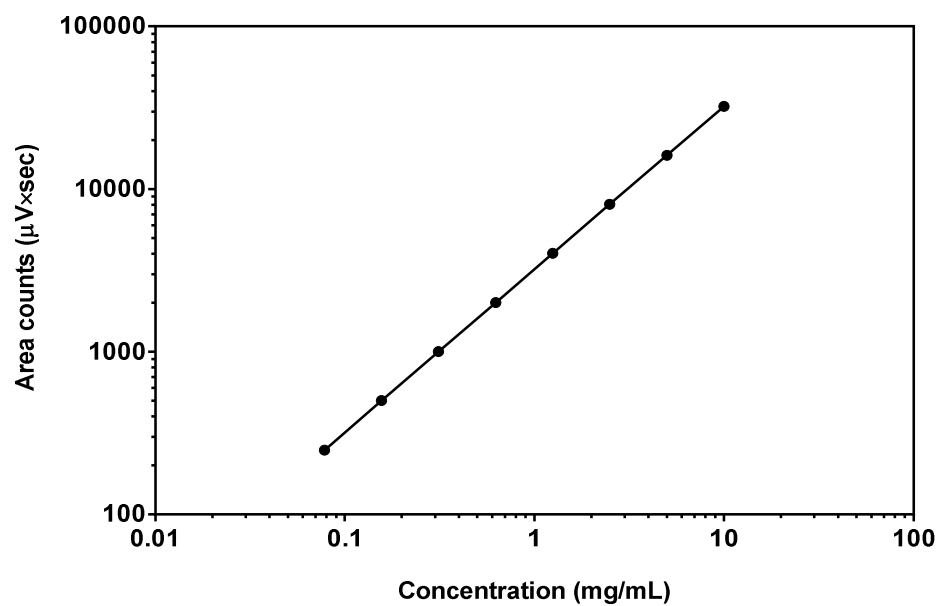


Figure 3-28: Linearity plot for chrysin

A HPLC-UV method was developed to assess the linearity of detection over a concentration range of 78 - 25000µg/mL. Data represents mean (solid line) \pm SD (error bars). n=3.

3.4.9. Cytotoxicity study

To investigate the toxicity of MSNP, curcumin and chrysin towards OBG400 cells a cell viability assay was conducted with phytochemicals/MSNP exposed to OBG400 for 24 hours. For Fan-MSNP, cell viability was generally maintained across the concentration range of 10-100 μ g/mL (Figure 3-29), with a statistically significant ($P \leq 0.01$) decrease in viability from 100 μ g/mL onwards.

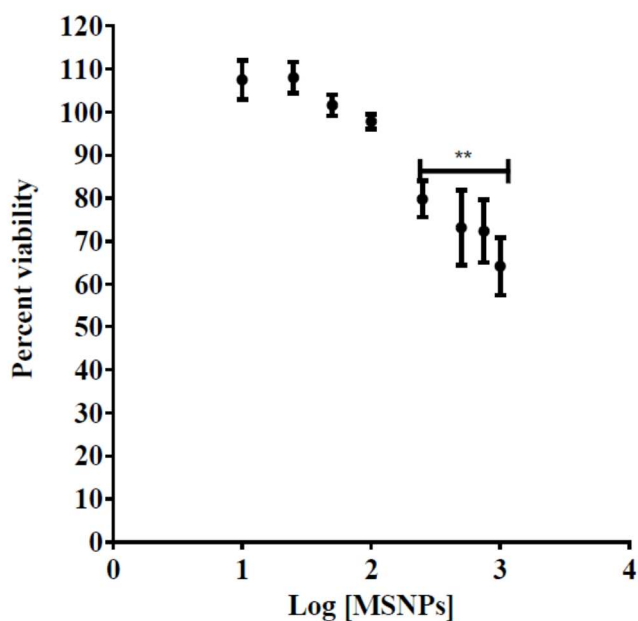


Figure 3-29: Cellular toxicity of Fan-MSNPs on OBG400 cells.

Cells were grown on a 96-well plate at a density of 10×10^3 cells per well and exposed to various concentrations of Fan-MSNP (10 – 1000 μ g/mL). After 24 hour incubation 100 μ L MTT in PBS (0.5mg/mL) added to each well & incubated for 4 hours. The MTT-formazan produced was solubilised in DMSO and quantified colorimetrically using a UV-spectrophotometer at 570nm. The control cell (without drug) corresponded to a cell viability of 100%. Data is reported as mean \pm SD with up to 8 replicates per compound in at least 3 independent experiment. ** $P \leq 0.01$.

For curcumin (Figure 3-30) and chrysin (Figure 3-31), cell viability was maintained across the concentration range of 0.001-10 μ M and an IC_{50} of $33 \pm 0.18\mu$ M was determined for curcumin. For chrysin at 100 μ M, a statistically significant ($P \leq 0.01$) decrease in cell viability was observed ($58.2 \pm 8.5\%$)

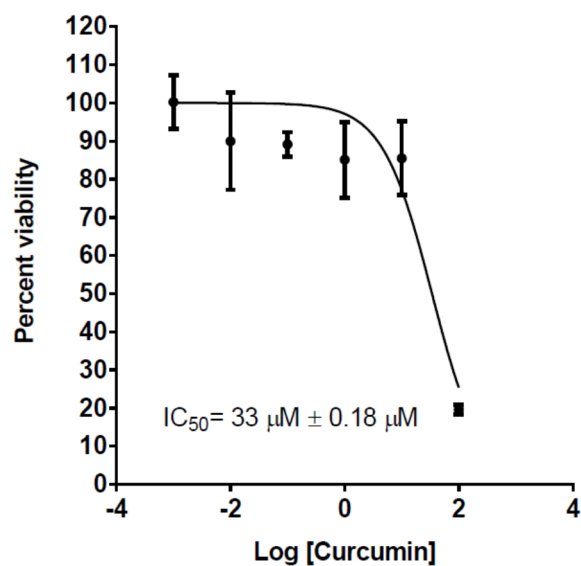


Figure 3-30: Cellular toxicity of curcumin on OBG400 cells

Cells were grown on a 96-well plate at a density of 10×10^3 cells per well and exposed to various concentrations of curcumin (10 – 1000 μ g/mL). After 24 hour incubation 100 μ L MTT in PBS (0.5mg/mL) added to each well & incubated for 4 hours. The MTT-formazan produced was solubilised in DMSO and quantified colorimetrically using a UV-spectrophotometer at 570nm. The control cell (without drug) corresponded to a cell viability of 100%. Data is reported as mean \pm SD with up to 8 replicates per compound in at least 3 independent experiment.

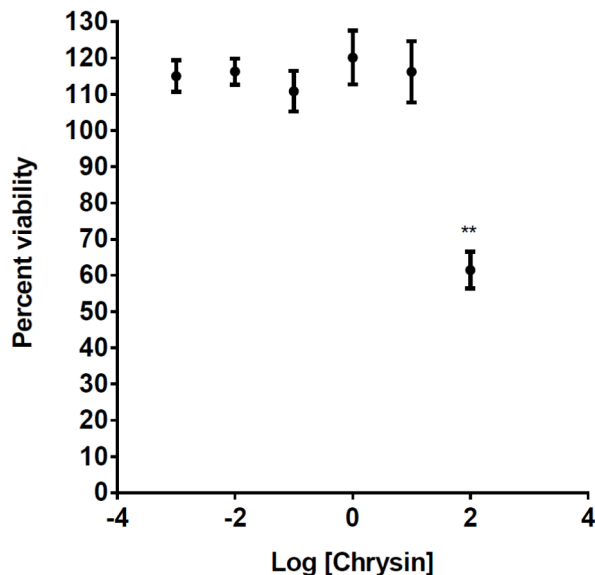


Figure 3-31: Cellular toxicity of chrysin on OBG400 cells.

Cells were grown on a 96-well plate at a density of 5×10^3 cells per well and exposed to various concentrations of chrysin (10 – 1000 μ g/mL). After 24 hour incubation 100 μ L MTT in PBS (0.5mg/mL) added to each well & incubated for 4 hours. The MTT-formazan produced was solubilised in DMSO and quantified colorimetrically using a UV-spectrophotometer at 570nm. The control cell (without drug) corresponded to a cell viability of 100%. Data is reported as mean \pm SD with up to 8 replicates per compound in at least 3 independent experiment. ** $P \leq 0.01$.

3.4.10. Cellular toxicity of MSNP: live-cell time-lapse phase-contrast microscopy

To assess the morphological alteration of cellular structures when exposed to Fan-MSNP, Curc-MSNP and Chry-MSNP, a gas and humidity controlled phase contrast imaging study was conducted using the CellIQ® imaging system. OBG400 cells, grown in wells of a 6-well plates, were exposed to 50-150µg/mL of Fan-MSNP, Curc-MSNP and Chry-MSNP for 40 hours with images captures within a defined window within each well every 15 minutes using live-cell imaging.

The impact of Fan-MSNP on cell viability/proliferation at 150µg/mL demonstrate a clear impact on the viability and proliferation of OBG400 over 40 hours resulting in a reduction in the cell morphological volume and cell death. This effect was diminished at a concentration of 50µg/mL, where cell morphology was maintained throughout the incubation period (Figure 3-32)

With Chry-MSNP, a similar impact on cell viability was noted at 150µg/mL. However, at 50µg/mL cell morphology was seen to change associated with the apoptosis of some cells (Figure 3-33). For Curc-MSNP, cell morphology was noted to alter at 150µg/mL leading to an increase in cell death over time, however at 50µg/mL cell viability was not affected and proliferation of cells was noted (Figure 3-34).

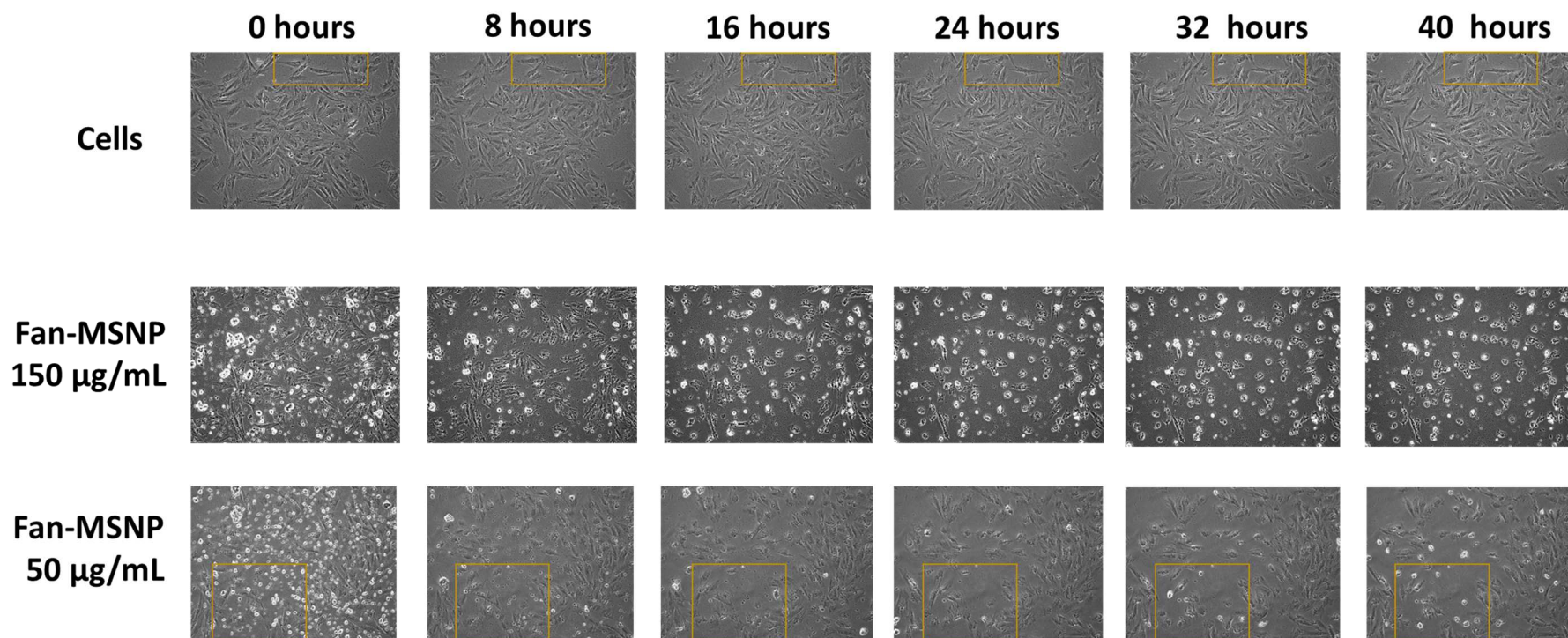


Figure 3-32: Cell-IQ live cell imaging of OBG400 cells (top) and Fan-MSNP at 150µg/mL (middle) and 50µg/mL (bottom).

OBGF400 cells were seeded at a density of 5×10^4 cells/well in a 6-well plates. Following the addition of Fan-MSNP or flavonoids loaded MSNP, the lens was positioned within fixed regions of interest within each well and images taken every 15 minutes over 40 hours, with the plate maintained in a 5% CO₂ and 37°C controlled environment. Regions of interests depicted changes in cell morphology are illustrated by the yellow boxes.

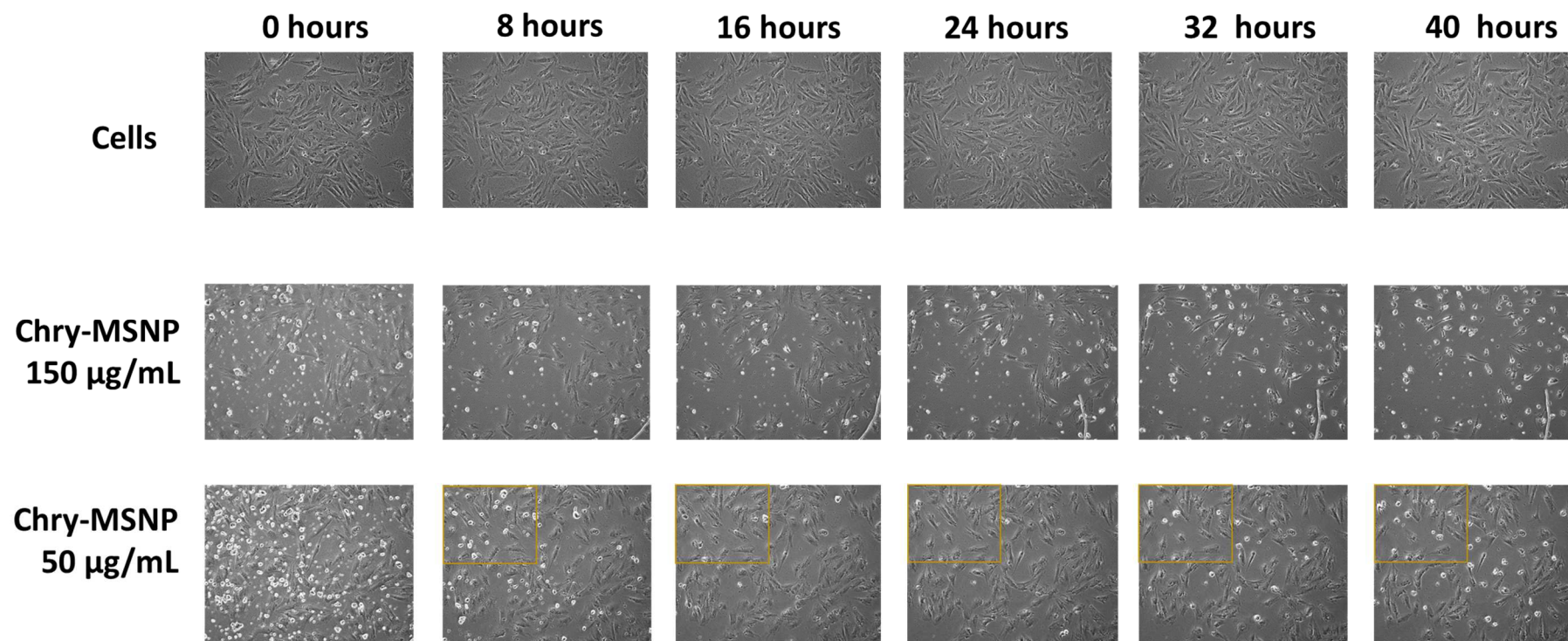


Figure 3-33: Cell-IQ live cell imaging of OBG400 cells (top) and Chry-MSNP at 150µg/mL (middle) and 50µg/mL (bottom).

OBGF400 cells were seeded at a density of 5×10^4 cells/well in a 6-well plates. Following the addition of Fan-MSNP or flavonoids loaded MSNP, the lens was positioned within fixed regions of interest within each well and images taken every 15 minutes over 40 hours, with the plate maintained in a 5% CO₂ and 37°C controlled environment. Regions of interests depicted changes in cell morphology are illustrated by the yellow boxes.

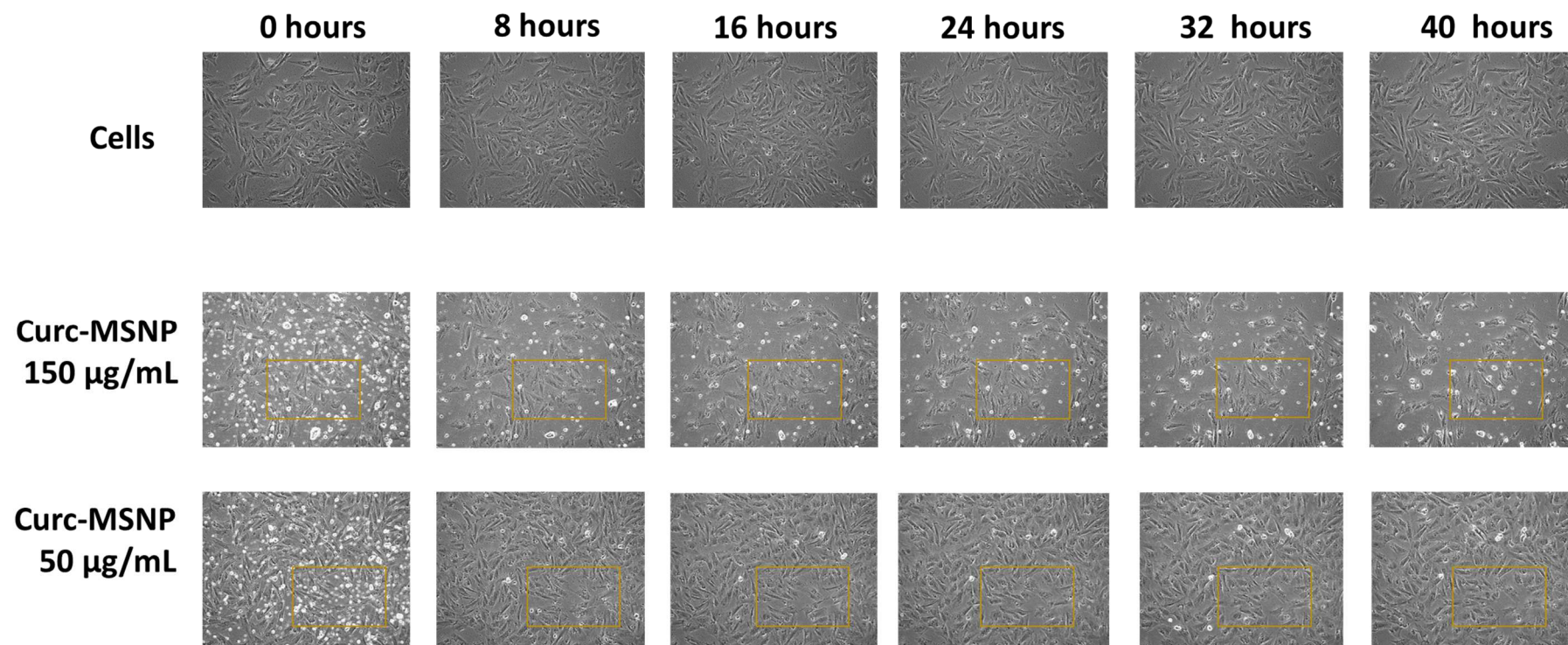


Figure 3-34: Cell-IQ live cell imaging of OBG400 cells (top), Curc-MSNP at 150µg/mL (middle) and 50µg/mL (bottom).

OBGF400 cells were seeded at a density of 5×10^4 cells/well in a 6-well plates. Following the addition of Fan-MSNP or flavonoids loaded MSNP, the lens was positioned within fixed regions of interest within each well and images taken every 15 minutes over 40 hours, with the plate maintained in a 5% CO₂ and 37°C controlled environment. Regions of interests depicted changes in cell morphology are illustrated by the yellow boxes.

3.4.11. Drug release study from the mesoporous silica nanoparticles

The release of curcumin from Curc-MSNP was assessed over 24 hours and demonstrated a pH sensitive release phenomena. A burst effect was also evident after 1 hour with 12% and 16.6% released at pH 7.4 and pH 5.5 respectively (Figure 3-35). Release at pH 7.4 was slower than that at pH 5.5, with $16.1 \pm 1.6\%$ released at 24 hours ($P \leq 0.001$). At pH 5.5 release increased over 24 hours to $53.2\% \pm 2.2\%$ ($P \leq 0.001$). However, no significant increase in curcumin release was observed from 1 hour to 24 hours.

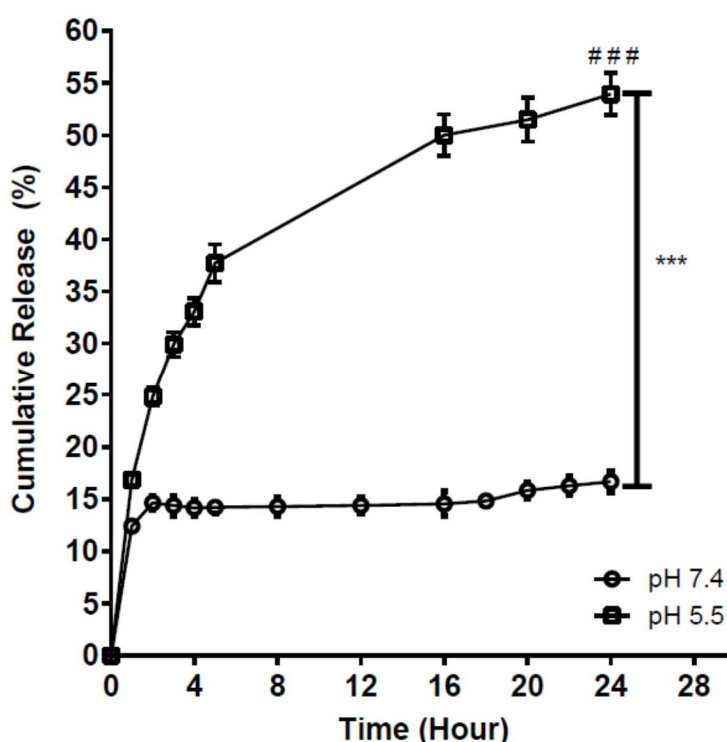


Figure 3-35: Cumulative percentage release of curcumin from Curc-MSNP.

The *in vitro* release of curcumin was performed in 154mM PBS pH 7.4 and pH 5.5 containing 0.1% Tween 80. 1mg/mL of Curc-MSNP were dispersed into 2ml of release medium, briefly sonicated and placed in a shaking incubator maintained at 37°C and 100 rpm. Samples were withdrawn at set time intervals and the volume replaced with an equal volume of pre-warmed release medium. Release was assessed through HPLC-UV methods. N=3. # # # indicates statistical comparison between the final time point (24 hours) and the first time point for (1 hour) for pH 5.5 with a $P \leq 0.001$. *** indicates statistical comparison between the final time point (24 hours) between pH 5.5 and 7.4 with a $P \leq 0.001$

The release of chrysin from Chry-MSNP was assessed over 24 hours and also demonstrated a pH sensitive release phenomena. A burst effect was evident after 1 hour with $3.2 \pm 1.2\%$ and $7.1 \pm 1.6\%$ released at pH 7.4 and pH 5.5 respectively (Figure 3-36). Release at pH 5.5 was slower than that for pH 7.4 ($P \leq 0.001$), with $9.4 \pm 0.6\%$ and $16.8 \pm 0.8\%$ at 24 hours respectively. However statistically significant differences ($P \leq 0.001$) were also observed between 1 hour and 24 hours release at each pH studied.

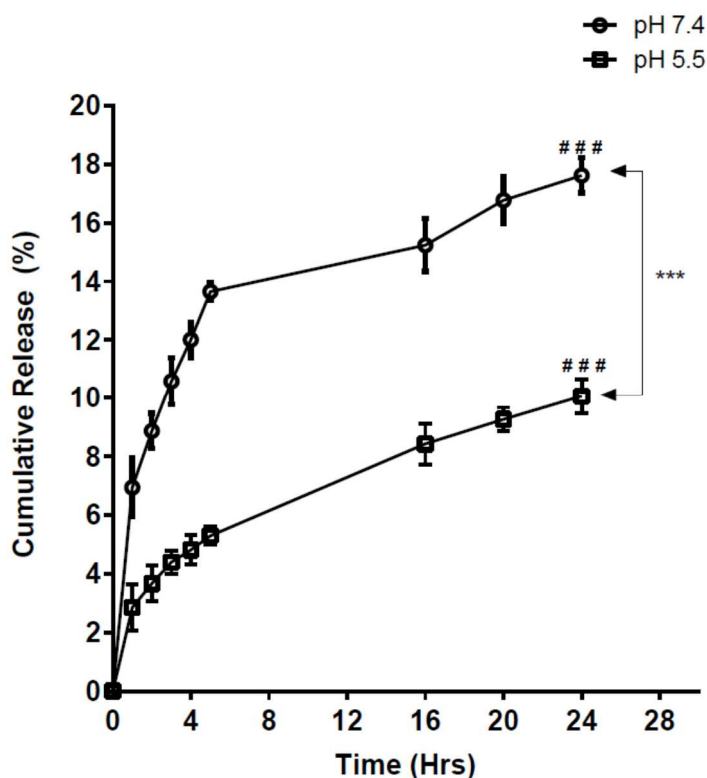


Figure 3-36: Cumulative percentage release of chrysin from Chry-MSNP

The *in vitro* release of chrysin was performed in 154mM PBS pH 7.4 and pH 5.5 containing 0.1 % Tween 80. 1mg/mL of Chry-MSNP were dispersed into 2ml of release medium, briefly sonicated and placed in a shaking incubator maintained at 37°C and 100 rpm. Samples were withdrawn at set time intervals and the volume replaced with an equal volume of pre-warmed release medium. Release was assessed through HPLC-UV methods. N=3. # # # indicates statistical comparison between the final time point (24 hours) and the first time point for (1 hour) for pH 5.5 and pH 7.4 with a $P \leq 0.001$. *** indicates statistical comparison between the final time point (24 hours) between pH 5.5 and 7.4 with a $P \leq 0.001$

3.4.12. Incorporation of Fan-MSNP into thermoresponsive nasal gel

In order to deliver Fan-MSNP, a carrier systems was required to contain Fan-MSNP and to allow delivery at the olfactory mucosa. Thermoresponsive nasal gels described in Chapter 2 were adapted by the direct replacement of AMT with 0.2%, 0.4% and 1% w/w Fan-MSNP.

All formulations demonstrated a tri-region gelation phenomenon, preceded by a stable plateau region and culminating in a stable gel formulation (Figure 3-37 to 3-39). Furthermore, a general trend of a decrease in the initiation temperature of gelation with increasing Fan-MSP (0.2%, 0.4% and 1% w/w) was noted: MSNP-FCMS: $25.8 \pm 0.05^{\circ}\text{C}$, $22.1 \pm 0.08^{\circ}\text{C}$ and $21.7 \pm 0.03^{\circ}\text{C}$; MSNP-FCS: $25.4 \pm 0.07^{\circ}\text{C}$, $25.1 \pm 0.08^{\circ}\text{C}$ and $20.1 \pm 0.09^{\circ}\text{C}$; MSNP-FPEG: $25.4 \pm 0.07^{\circ}\text{C}$, $25.1 \pm 0.08^{\circ}\text{C}$ and $20.1 \pm 0.09^{\circ}\text{C}$.

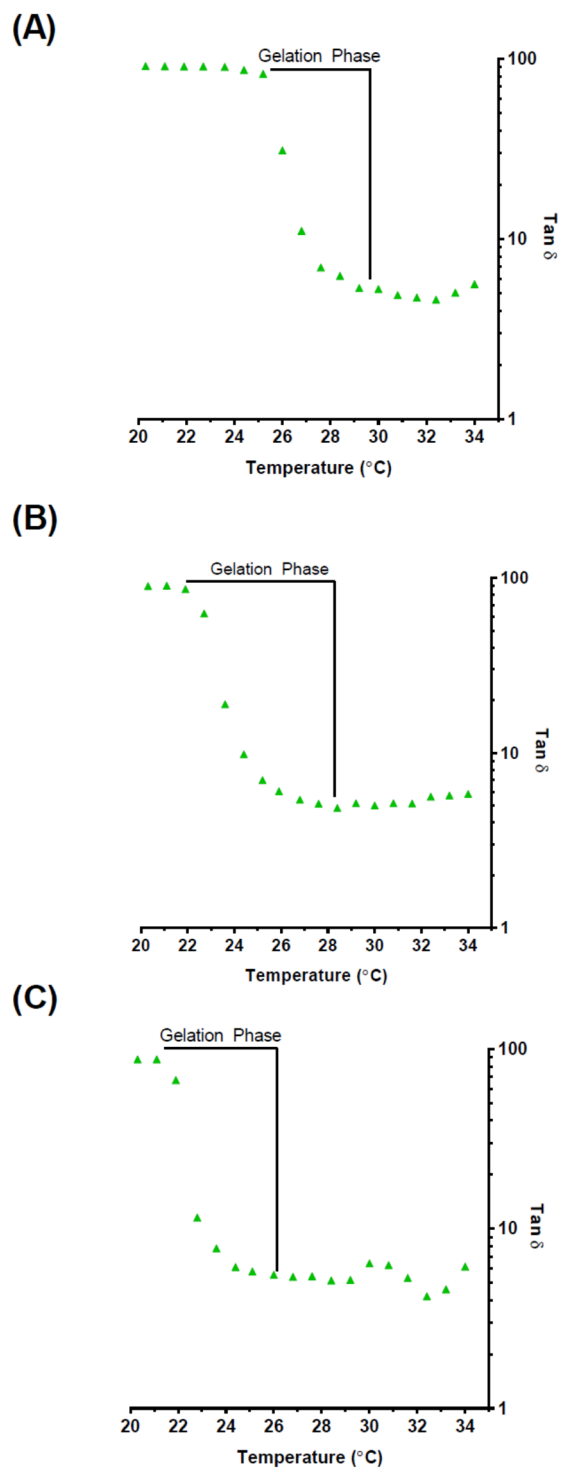


Figure 3-37: Temperature sweep of FCMC following incorporation of Fan-MSNP

Rheological analysis of FCMC following the incorporate of Fan-MSNP at a concentration of (A) 0.2% w/w; (B) 0.4% w/w and (C) 1% w/w. Fan-MSNP were used in place of AMT. Temperature sweep analysis was conducted using parallel plate geometry with 40mm steel plates having a gap 1.0mm. The approximate sample volume used was 1.26ml and the instrument was used in the oscillatory mode in the linear viscoelastic range. Data represents mean \pm SD. N=3

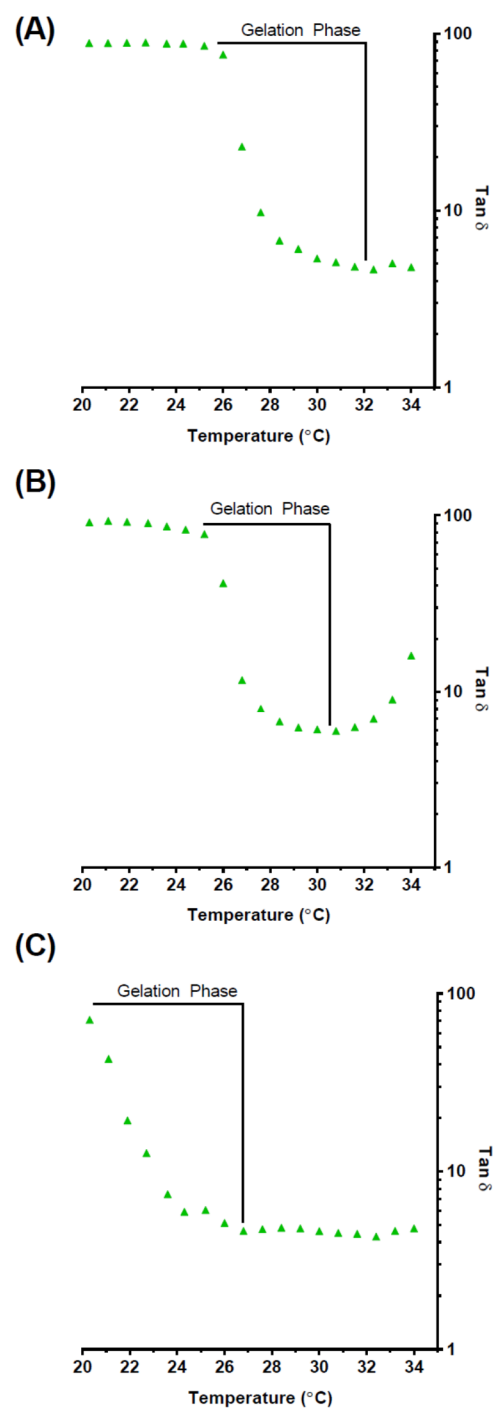


Figure 3-38: Temperature sweep of FCS following Incorporation of Fan-MSNP.

Rheological analysis of FCS following the incorporate of Fan-MSNP at a concentration of (A) 0.2% w/w; (B) 0.4% w/w and (C) 1% w/w. Fan-MSNP were used in place of AMT. Temperature sweep analysis was conducted using parallel plate geometry with 40mM steel plates having a gap 1.0mM. The approximate sample volume used was 1.26ml and the instrument was used in the oscillatory mode in the linear viscoelastic range. Data represents mean \pm SD. N=3

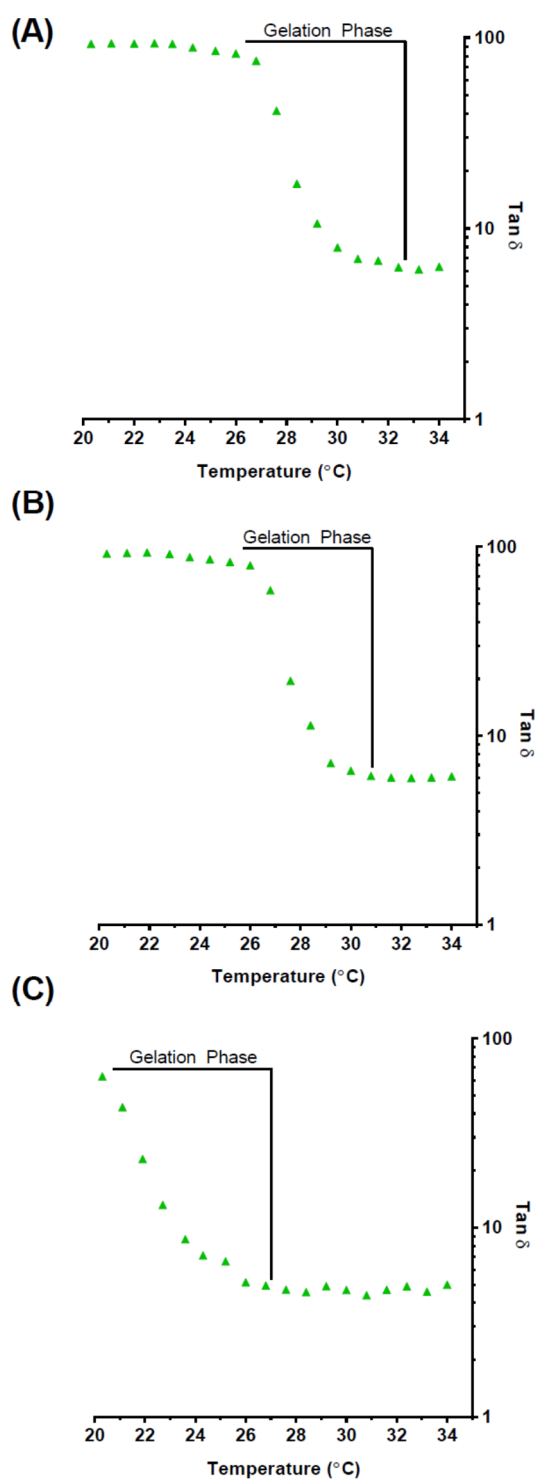


Figure 3-39: Temperature sweep of FPEG following Incorporation of Fan-MSNP

Rheological analysis of FPEG following the incorporate of Fan-MSNP at a concentration of (A) 0.2% w/w; (B) 0.4% w/w and (C) 1% w/w. Fan-MSNP were used in place of AMT. Temperature sweep analysis was conducted using parallel plate geometry with 40mM steel plates having a gap 1.0mM. The approximate sample volume used was 1.26ml and the instrument was used in the oscillatory mode in the linear viscoelastic range. Data represents mean \pm SD. N=3

To confirm gelation, the shear thinning behavior of the gel was assessed at ambient and nasal cavity temperatures. Sheer thinning behavior for all Fan-MSNP gel systems was noted with significant differences ($P < 0.0001$) when comparing ambient temperatures to 34°C across all Fan-MSNP loaded. A significant difference ($P < 0.05$) in sheer thinning behavior was noted at 1 % w/w at ambient and 34°C compared to 0.2 and 0.4 % w/w Fan-MSNP. (Figure 3-40).

For Fan-MSNP incorporated into FCS (Figure 3-41) and FPEG (Figure 3-42), similar observations were noted as for FCMS, however at 34°C no significant differences were noted between the Fan-MSNP concentrations.

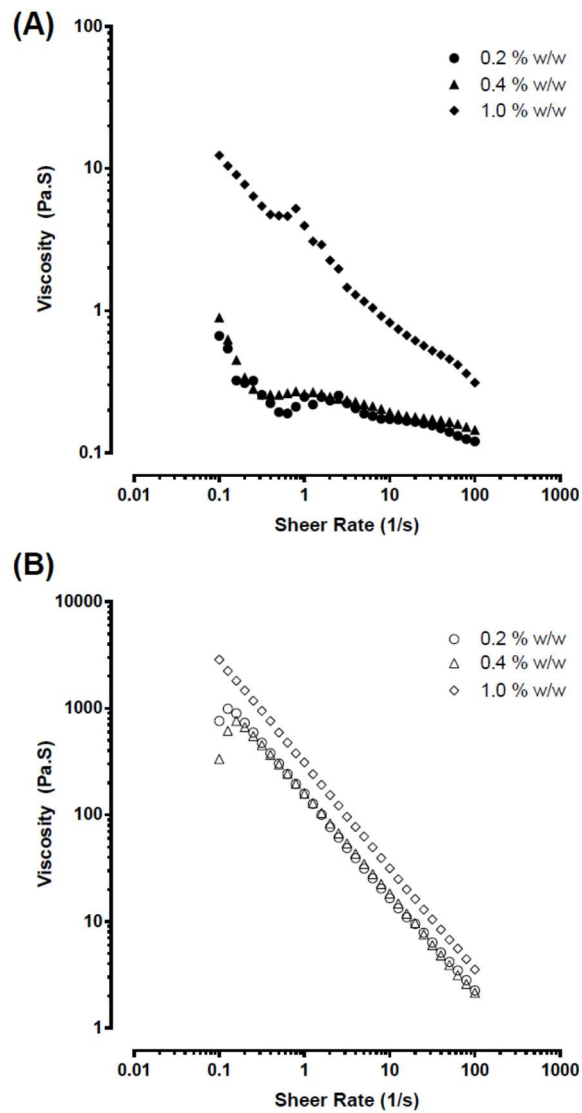


Figure 3-40: Steady shear behaviour of FCMC incorporating Fan-MSNP.

Rheological shear viscosity analysis of the FCMC at: (A) ambient (18°C) and (B) nasal cavity (34°C) temperatures was assessed using parallel plate geometry with 40mm steel plates having a gap 1.0mm. Concentration of 0.2, 0.4 and 1% w/w was used in formulations. The approximate sample volume used was 1.26ml and the instrument was used in the oscillatory mode in the linear viscoelastic range. Data represents mean \pm SD. n=4

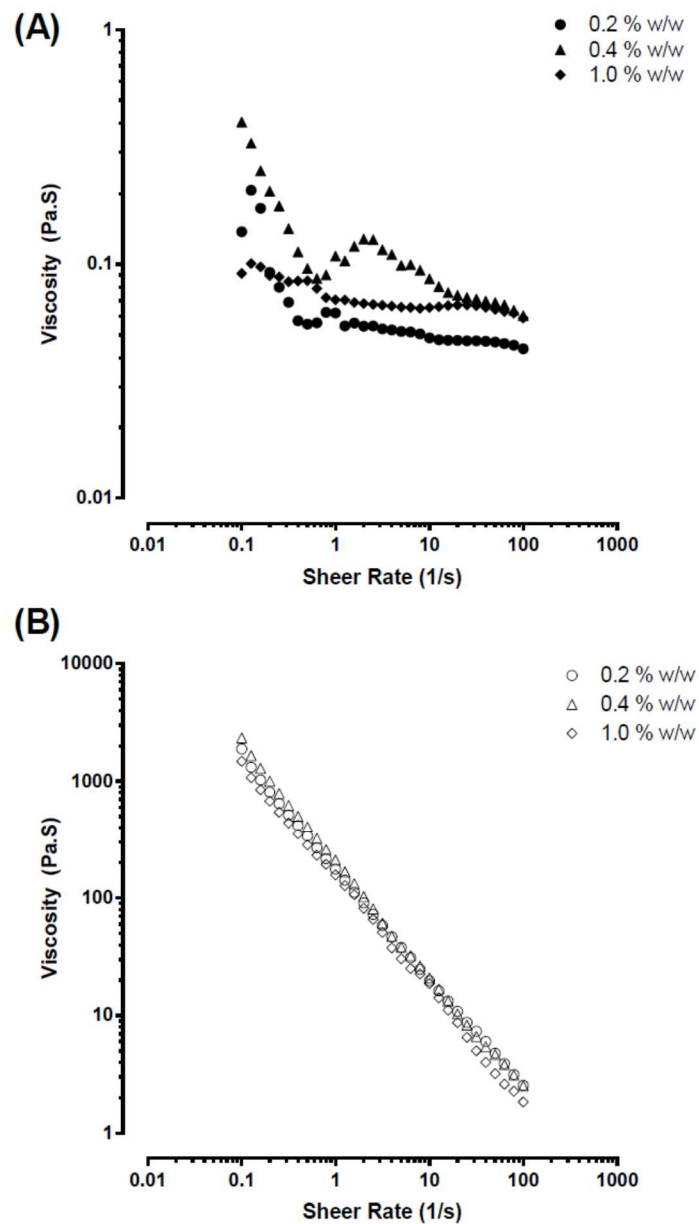


Figure 3-41: Steady shear behaviour of FCS incorporating Fan-MSNP.

Rheological shear viscosity analysis of the FCS at: (A) ambient (18°C) and (B) nasal cavity (34°C) temperatures was assessed using parallel plate geometry with 40mM steel plates having a gap 1.0mM. Concentration of 0.2, 0.4 and 1% w/w was used in formulations. The approximate sample volume used was 1.26ml and the instrument was used in the oscillatory mode in the linear viscoelastic range. Data represents mean \pm SD. n=4

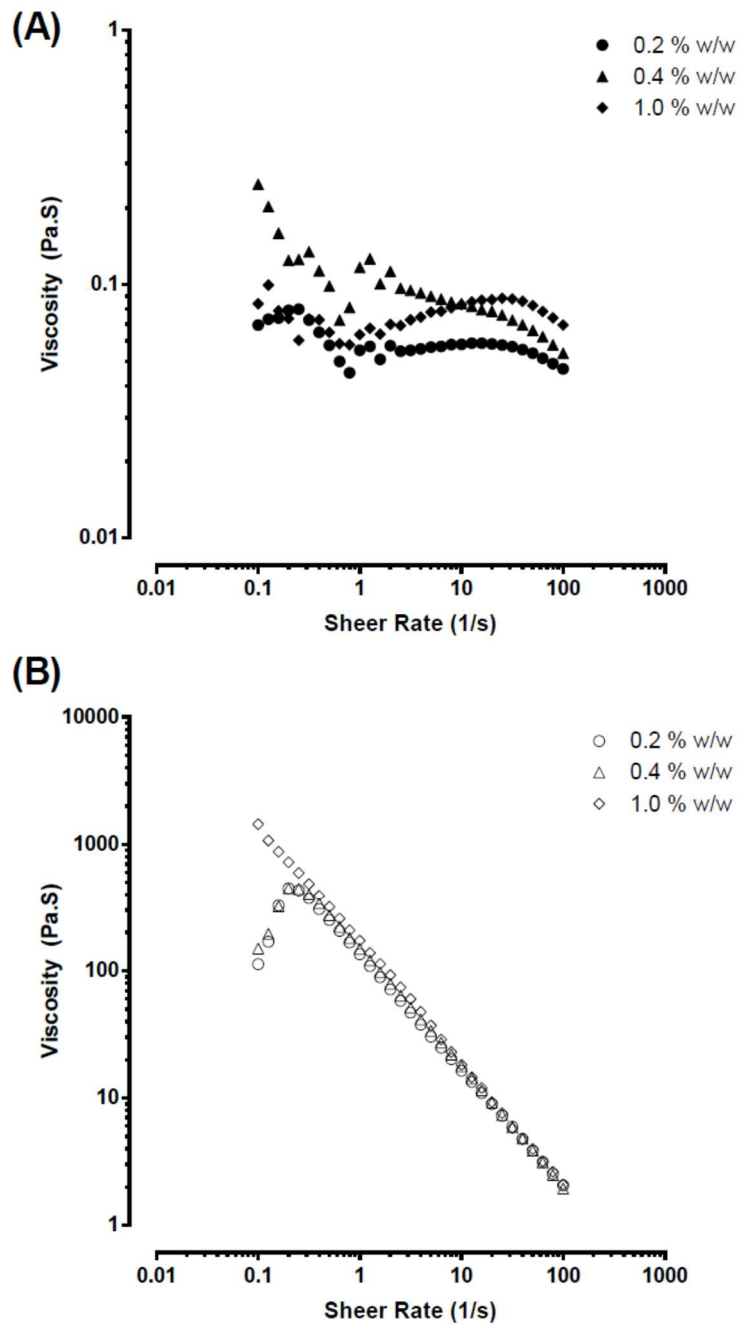


Figure 3-42: Steady shear behaviour of FPEG incorporating of Fan-MSNP.

Rheological shear viscosity analysis of the FPEG at: (A) ambient (18°C) and (B) nasal cavity (34°C) temperatures was assessed using parallel plate geometry with 40mm steel plates having a gap 1.0mm. Concentration of 0.2, 0.4 and 1% w/w was used in formulations. The approximate sample volume used was 1.26ml and the instrument was used in the oscillatory mode in the linear viscoelastic range. Data represents mean \pm SD. n=4

3.5. Discussion

Age related neurological disorders such as Parkinson's disease (PD) and Alzheimer's disease (AD), are insidious progressive neurological disorders which affects over 1.5% of the population over 65-years of age (Foltynie *et al.*, 2004). Current approaches to CNS drug delivery are often hampered by poor targeting and drug delivery to the BBB. Furthermore, the solubility of the drug may limit its formulation scope and impact upon the systemic bioavailability which drives CNS concentrations.

An alternative approach to the delivery of drugs to the brain and wider CNS often focus on solubility improvements and enhancements in targeted delivery. For drugs that are systemically administered, nanoparticles are widely employed as carrier delivery systems to improve the solubility and, following surface modification, targeting vehicles which are capable of targeting the CNS. Of the wide variety of NP systems that have been employed for CNS targeting, a recently developed mesoporous material based on silica has gained interested due to its tuneable particle radius and porosity.

In Chapter 2 we discussed approaches to the formulation of a water-soluble drug. Chapter 3 moves forwards to address the approaches required to formulate and deliver poorly soluble compounds through the development and use of mesoporous silica nanoparticles. For the purposes of selection of an appropriate compound, the phytochemicals chrysin and curcumin were selected based on their ability to modulate a range of CNS pharmacological targets and reported beneficial effects to CNS development/repair in part, due to their anti-oxidant properties. Furthermore, both are relatively poorly soluble and present as model candidates for poorly soluble APIs with the potential for significant clinical benefits if targeted and delivered to the CNS.

MSNP were utilised as a delivery vehicle within which chrysin and curcumin were entrapped, characterised and finally assessed for minimal cytotoxicity effects and intracellular uptake in the porcine olfactory bulb cell line OBGF400. MSNP are ideal drug delivery candidates and contain pore sizes ranging from 2-50nm and was first identified as MCM-41 superfamily or orders mesoporous silica materials(Kresge *et al.*, 1992a). Furthermore, MSN are synthesised through a temple-directed approach in the presence of a supramolecular surfactant that acts as a template to direct the structure the mesoporous nature of the material (Kresge *et al.*, 1992a, Cai *et al.*, 1999). The advantages of MSN are that they offer a large surface area/pore volume for drug loading within pore channels (Hu *et al.*, 2011, Vallet-Regi *et al.*, 2001) alongside the opportunity to adjust the pore size (Sun *et al.*, 2013, Hu *et al.*, 2012). Furthermore they possess limited toxicity profiles (Zhang *et al.*, 2012, Hudson *et al.*, 2008) and offer the opportunity to be used in bioimaging processes (Kim *et al.*, 2008, Wu *et al.*, 2011).

3.5.1. Target MSNP size range for olfactory uptake

A target goal for our studies are to demonstrate uptake of MSNP into olfactory bulb neuronal cells. To assess this process fluorescent latex beads of 100nm and 500nm size ranges were selected to allow cellular imaging of the intracellular localisation of beads, providing some insight into appropriate size ranges for viable cellular uptake.

100nm latex beads provided a broader and more uniform uptake into OBGF400 cells (Figure 3-1) when compared to 500nm latex beads. However, cellular uptake of both sizes of beads were detected using confocal microscopy and suggest MNSP formulation over this size range would be appropriate for olfactory uptake.

Although the use of fluorescent latex beads as retrograde transport markers for neuronal pathways is not new (Katz *et al.*, 1984, Persson and Gatzinsky, 1993, Katz and Iarovici, 1990), the application to olfactory bulb neuronal cells is novel and indicates the potential for nano-sized material to penetrate into this class of cells.

3.5.2. Formulation of MSNP

Having determined the optimal size range for olfactory neuronal cell uptake (100-500nm), MSNP were formulated according to the methods described by Fan *et al* (Fan *et al.*, 2011), (Gulfam and Chung, 2014) and by (Nooney *et al.*, 2002). With all of these approaches, MSNP are formulated use templating methods (hard templating and soft templating). The template removal determines the hollow interior of the MSNP. During the formation it is the CTAB that is responsible for the formation of the shell and TEOS determines the hollow interior of the MSNPs (Hao *et al.*, 2015). The three approaches we selected were part of a hard templating method but differed in the methods utilised to remove the template, Gul-MSNP were prepared using a calcination step with, exposure of the formed solid nanomaterial in an air-fired furnace at high temperatures to remove template, whereas Fan-MSNP were prepared with a solvent refluxing approach to remove template.

The smallest sized MSP were formulated using the 'Fan method' (Fan *et al.*, 2011), resulting in particles of 216.5 ± 2.1 nm with a narrow PDI of 0.13 ± 0.02 with the 'Pro-2 method' resulting in the largest sized particles of 465 ± 10 nm with a larger PDI of 0.25 ± 0.1 .

Gul-MSNP were of a similar size to that reported by (Gulfam and Chung, 2014), 225 ± 7.2 nm. On the other hand Fan *et al* reported particle sizes slight smaller than ours, approximately 180-185nm. Nevertheless, the outcome for both Gul-MSNP and Fan-MSNP resulted in a particle size similar to that reported by the original researchers and with a target particles size (100-500nm) with a narrow PDI. For the Pro-2-MSNP, our particle sizes were larger than those reported by Nooney *et al* (2002), 190nm. Because of the poorer sizes of the Pro-2-MSNP method, this method was discarded in favour of Gul-MSNP or Fan-MSNP.

To confirm the morphology of the formed MSNP, samples were analysed using SEM in order to assess the formation of spherical-shaped nanoparticles with hierarchical pores on the surface. Gul-MSNP demonstrated a less uniform spread of nanoparticle structures (Figure 3-2A and B). However, the presence of mesopores are visible in the overall pore structure (Figure

3-2C) however a broader size distribution of particles is evident (Figure 3-2D) along with presence of ruptured/poorly formed pores (Figure 3-2D). The formation of mesoporous nanoparticles resulted in the particles being packed closely and the process of drying directly from the liquid environment results in significant shrinkage due to Si-O-Si bond formation between adjacent nanoparticles. This irreversible shrinkage may result in the loss of the characteristic mesoporous nature (Liong *et al.*, 2008). This is clearly reflected in the SEM images (Figure 3-2) where Gul-MSNPs shows agglomerates and do not appear as uniform. Furthermore, the broader size range and PDI supports the notion of poorer consistency within and across batch formations of Gul-MSNPs.

The 'Pro-2 method' also resulted in spheroidal type mesoporous morphology, but the pore formation on the formed nanoparticles were too small to detect and the overall spread of particle sizes would suggest they are formed with a diameter of greater than 400nm, confirming the observations from DLS analysis.

Fan-MSNPs resulted in a more uniform distribution of formed MSNPs with a consistent spherical morphology and particle size of ~ 200nm, corresponding with the results from the DLS approaches. In case of the Fan method, MSNPs were formed by hydrolysis and condensation of tetraethoxysilane in a dilute aqueous environment using a cationic template (CTAB) and a catalyst NaOH (Fan *et al.*, 2011) through extraction in boiling solvents. This method would prevent the agglomeration of MSNPs seen using the Gul-method and hence is preferred over calcination as template removal method.

3.5.3. Surface porosity and pore size determination

Unlike non-porous nanoparticles, porous nanoparticles required further characterisation to assess pore density, pore diameters and surface area properties. Surface area is routinely assessed through nitrogen adsorption-desorption isotherms and calculated with Brunauer-Emmett-Teller (BET) theory (Barrett *et al.*, 1951) using isotherm adsorption data at P/P₀.

The total surface area, $987.67 \pm 3.38 \text{ m}^2/\text{g}$, was larger than that reported by Fan *et al* ($803.2 \text{ m}^2/\text{g}$). Furthermore, Fan-MSNP demonstrated a micro/meso sized pore diameter of $1.93 \pm 0.01 \text{ nm}$, smaller than that reported by Fan *et al* (3.7 nm). However the features of Fan-MSNP would clarify it as a high surface area narrow pore diameter nanoparticle, similar to other reported values for similar MSNP (He *et al.*, 2010, Wu *et al.*, 2016). Although we were unable to utilise TEM to assess the exact structural morphology, MCM-41 type mesoporous nanomaterial is hexagonal in shape and possess similarly high surface area and narrow pore diameters and Fan-MSNP may possibly be categorised under this type of mesoporous nanomaterial (Slowing *et al.*, 2006).

Furthermore, the nitrogen absorption-desorption isotherms identify the characterise hysteresis-type loop associated with capillary (pore) condensation at $P/P_0 > \approx 0.2$. The hysteresis loop can be classified as a H1 loop, which is often associated with porous materials exhibiting a narrow distribution of relatively uniform (cylindrical-like) pores.

The overall distribution of the pore radius was confirmed through BJH analysis and demonstrated a narrow pore radius relative to the cumulative pore volume with the majority of the radius distribution, $dV(r)$, located $<20\text{-}30 \text{ \AA}$ ($< 10 \text{ nm}$). Furthermore, the pore width distribution confirmed a pore with distribution of $< 4 \text{ nm}$. Similarly, (Fan *et al.*, 2011) demonstrated a H1 loop profile with a similar pore diameter distribution. Pore size is important for controlling the release kinetics of drug from the pore, with larger pore sizes often resulting in a higher rate of drug release (He and Shi, 2011).

3.5.4. FT-IR assessment of Fan-MSNP

Having confirmed the formation of mesoporous nanoparticles, FT-IR spectroscopy was utilised to confirm the removal of the template from the silica material, key in the formation of the porous structure. CTAB surfactant is identified by the presence of bands at approximately 2924 , 2855 , and 1478 cm^{-1} which correspond to C-H vibrations of the surfactant molecules.

These are highlighted in Figure 3-9 and, following template removal, are absent from the MSNP demonstrating complete removal of the template surfactant. Furthermore, the band at 1068cm^{-1} and a band at 795cm^{-1} , can be assigned to internal and external asymmetric Si-O stretching modes, and at 965cm^{-1} to the stretching vibrations of the surface Si-O⁻ groups (Huo et al., 2014),(Zhao et al., 1997),(Salonen et al., 1997).

Having confirmed the formation of surfactant free Fan-MSNP, we next passively loaded FITC into Fan-MSNP with a view to develop a cellular imaging tracer to assess cellular uptake of Fan-MSNP. Loaded FITC-MSNP demonstrated a distinct band at 1654cm^{-1} which is thought to be related to the amide group (Kotsuchibashi *et al.*, 2013), and the benzene ring of FITC at 1583cm^{-1} (Zhang *et al.*, 2015).

3.5.5. FITC loading and release in Fan-MSNP

Passive loading resulted in an EE of $48 \pm 2.3\%$ and the release of FITC was assessed in PBS (pH 7.4) media. The duration of the release study was set at 2 hours, primarily as a result of the short exposure-time expected with nasally delivered formulation coupled with the limited duration with which cell cultures can proliferate in the absence of growth media. Minimal FITC was identified as having been released from FITC-MSNP, $4.8 \pm 0.19\%$, over a 2-hour period suggesting the relative stability of the FITC molecule within the MSNP structure.

3.5.6. FITC-MSNP cellular uptake

Having confirmed the minimal leakage of FITC, FITC-MSNP were incubated with OBG400 to assess the cellular uptake of dye-doped FITC-MSNP. Following a 2-hour incubation with the cells, FITC-MSNPs were identified using confocal microscopy with cytoplasmic accumulation of FITC-MSNP, confirming the successful uptake into OBG400. A similar report of interaction after 2-hours (i.e. acute exposure) was reported by Huang *et al* (Huang *et al.*, 2010) using A375 human melanoma cells to study the effect of shape of the MSNPs on the cell internalisation.

To further ascertain the cellular localisation, a z-dimension confocal imaging sweep was conducted from the upper limit of the cell layer to the lower limit of the cell layer, a distance of 4.6µm, with multiple images taken as the objective transferred along the z-scale. The z-stack confirmed the strong localisation within the cytoplasm of OBGF400 cells. The fluorescent latex beads study identified the optimal size range for cellular uptake of nanoparticles into OBGF400 cells and the size of Fan-MSNP was located within this range, and the cellular localisation concurred with the confocal imaging identified with both 100nm and 500nm latex beads. Furthermore, Fan-MSNP were prepared without calcination and it has been demonstrated that the calcination process yields more hydrophobic MSNP which can hinder cellular uptake (He *et al.*, 2009), further confirming the rationale to not consider Gul-MSNP.

This highly unspecific but efficient internalisation of MSNPs is believed to be partially because of their strong affinity for clathrin-coated vesicles due to their siliceous composition, and unique hexagonal exterior and internal hexagonal mesopores (Huang *et al.*, 2005). It has been also observed that MSNPs enter the cytoplasm by escaping the endolysosomal entrapment. This endosome escaping is also known as “proton sponge” effect (Boussif *et al.*, 1995).

3.5.7. Phytochemical loading into Fan-MSNP

Having successfully developed Fan-MSNP and confirmed both its mesoporous nature, but also its ability to undergo cellular uptake with a fluorescent cargo molecule, the phytochemicals curcumin and chrysin were used as candidate poorly soluble compounds and potential viable payloads of CNS pharmacological target sites (Chearwae *et al.*, 2006, Choudhury *et al.*, 2013, Gupta *et al.*, 2009, Monroy *et al.*, 2013, Mythri *et al.*, 2011, Zbarsky *et al.*, 2005) (Yao *et al.*, 2014, Xiao *et al.*, 2014, Souza *et al.*, 2015, Santos *et al.*, 2015, Nabavi *et al.*, 2015, Jia *et al.*, 2015).

For Curc-MSNP using FTIR we were able to identify a broad peak at 3420cm^{-1} confirming the intermolecular hydrogen bonding in isolated silanol and enolic hydroxyl groups and a peak at 1620cm^{-1} due to stretching vibrations of C=O bond (Jambhrunkar et al., 2014),(Khan et al., 2015). Having detected the IR spectra of curcumin within the Curc-MSNP, the thermal behaviour of Curc-MSNP was determined using differential scanning calorimetry. For curcumin a single characteristic single melting endothermic peak at 176°C was observed which was absent in Curc-MSNP confirming the washing step in the 'dry method' has removed residual curcumin adsorbed onto the surface of the MSNPs and secondly that the loaded curcumin is in the amorphous form.

Thereafter TGA was utilised to assess the weight loss associated with Curc-MSNP as direct methods for measuring loading content (LC) (TGA detection), $14.95 \pm 0.67\%$, which corresponded to a calculated EE of $12.34 \pm 1.28\%$ for the 'wet method' (HPLC-UV detection). Finally, confirmation of loading was confirmed through the change in particle size, $216.8 \pm 2.1\text{nm}$ to $263.51 \pm 8.3\text{nm}$ after loading with curcumin ($P \leq 0.01$), with a statistically significant increase in the PDI from 0.13 ± 0.02 to 0.26 ± 0.05 ($P \leq 0.05$). This increase in particle size and PDI has been previously reported after loading curcumin in their mesoporous nanoparticles (Kim et al., 2015),(Jambhrunkar et al., 2014). Furthermore the decrease in zeta potential following loading, from $-23.9 \pm 0. \text{mV}$ to $-16.9 \pm 0.9\text{mV}$ ($P \leq 0.01$), has previously been reported, however the polarity of the resultant charge is a function of the pH of the media that the zeta potential is measured in, with reports that a lower pH media often leads to more positive zeta potential with loading (Lee *et al.*, 2008, Chung *et al.*, 2007, DeMuth *et al.*, 2011, Farghali *et al.*, 2016).

For Chry-MSNP we were able to identify the γ -benzopyrone ring at 1655cm^{-1} and absorption bands at 1612, 1577 and 1450cm^{-1} related to carbon vibration in benzene and γ -pyrone rings (valance vibrations C=C) (Group, 2005). Having detected the IR spectra of chrysin within the Chry-MSNP, the thermal behaviour of Chry-MSNP was determined using

differential scanning calorimetry. As with curcumin, a single melting endothermic peak at 286°C was observed which was absent in Chry-MSNP, a gain confirming the washing step in the 'dry method' has removed residual chrysin adsorbed onto the surface of the MSNPs and secondly that the loaded chrysin is in the amorphous form. Thereafter TGA was utilised to assess the weight loss associated with Chry-MSNP as direct methods to measuring loading content (LC) (TGA detection), $11.49 \pm 1.19\%$, which corresponded to a calculated EE of $12.34 \pm 1.28\%$ for the 'wet method' (HPLC-UV detection).

Finally, loading was confirmed through the change in particle size, $216.8 \pm 2.1\text{nm}$ to $283.5 \pm 8.3\text{nm}$ after loading with chrysin ($P \leq 0.01$), with a statistically significant increase in the PDI from 0.13 ± 0.02 to 0.31 ± 0.05 ($P \leq 0.05$). Following loading a decrease in zeta potential, from $-23.9 \pm 0.4\text{mV}$ to $-30.8 \pm 0.3\text{mV}$ ($P \leq 0.01$) was noted.

However reports from other chrysin loaded nanoparticle systems indicate a negative zeta potential in the range we detected (Wang *et al.*, 2015, Sathishkumar *et al.*, 2015). Traditionally the zeta potential has been considered an important element for cellular interaction, with positively charged NP being favoured over negatively charged NP due to the negative charge of a cell membrane (Cooper, 2000). That said, a number of reports have identified that the zeta potential is less of an issue for MSNP due to their highly mesoporous nature (Taebnia *et al.*, 2015) (Huang *et al.*, 2014). Furthermore the endosome escaping, "proton sponge" effect (Boussif *et al.*, 1995), may explain the ability of Fan-MSNP to undergo internalisation, considering negative charge, without any specific ligands for receptor mediated endocytosis.

The application of DSC is important in giving an insight into the physical state of the drug molecule in the carrier system and its interaction with the carrier itself. It is also important to identify if the loaded drug is present in a crystalline or amorphous form, which will directly determine its solubility. With mesoporous materials, the localisation of drug into the pores of the MSNP will exist as either a crystalline form, showing characteristic melting point depression of the drug, or in the amorphous form where no characteristic melting point will be seen in the

thermogram (Salonen *et al.*, 2005b). The thermographs for both curcumin and chrysin confirmed the amorphous form was present and has been reported elsewhere (Yallapu *et al.*, 2010) (Chen *et al.*, 2013a).

With TGA analysis some weight loss at low temperature may have been attributed to adsorbed water whereas the weight loss at higher temperatures can be attributed to loss of surface silanol groups. However, no significant weight loss was evident during the study and this implies Fan-MSNP were thermally stable (Wanyika *et al.*, 2011). In the case of both chrysin and curcumin, the loaded nanoparticles demonstrated no characteristic melting point depression confirming the amorphous nature of the loaded phytochemical and confirming negligible drug adsorbed (Salonen *et al.*, 2005a).

The relatively low loading of phytochemicals into MSNP may be relative to the zeta potential charge of the nanoparticle, with studies reporting increased drug loading by altering the surface charge of the MSNP to increase drug loaded (Yoncheva *et al.*, 2016, Ma'mani *et al.*, 2014).

3.5.8. HPLC-UV detection of phytochemicals

HPLC-UV approaches for the detection of curcumin and chrysin were based on previously published methods and resulted in successful detection of both phytochemicals, with both methods demonstrating system precision and method precision across the range of concentration studied.

The chromatogram for curcumin (Figure 3-25) demonstrated the three consistent curcuminoids peaks associated with commercially available curcumin with the greatest peak, namely curcumin (~80%), being used for analytical purposes rather than the smaller demethoxycurcumin (~ 17%) and bisdemethoxycurcumin (~ 3%) peaks (Govindarajan, 1980) (Figure 3-43).

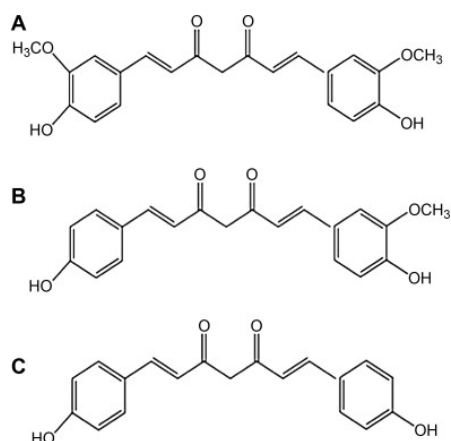


Figure 3-43: Chemical structures of (A) curcumin, (B) demethoxycurcumin and (C) and bisdemethoxycurcumin.

3.5.9. Cellular toxicity of MSNP

The target cell of Fan-MSNP are the cells of the olfactory system. In order to assess the compatibility between Fan-MSNP, curcumin and chrysin with olfactory cells a cellular toxicity assay was conducted using OBGF400 cells. Fan-MSN demonstrated cellular viability over 10-100µg/mL for 24 hours but concentration in excess of this results in a statistically significant ($P \leq 0.01$) decrease in viability. Reports of toxicity of MSNP with olfactory cells have not been reported by others but contradictory reports comment on relationships between the particle size and cellular toxicity, which appears to be cell line specific. For example, smaller-sized silica nanoparticles induced severe cellular damage in lung cancer cells, myocardial cells, and human endothelial cells (Napierska *et al.*, 2009, Ye *et al.*, 2010, Lin *et al.*, 2006b) and this was thought to be related to the fact that smaller nanoparticles have larger ratio of surface area to weight and therefore potentially more contact with the cells to induce damage (Oberdörster *et al.*, 2005, Kipen and Laskin, 2005, Nel *et al.*, 2006). However others have reported that larger silica nanoparticles are more cytotoxic than smaller particles on human hepatoma cells (Lu *et al.*, 2011).

All MTT assays were conducted in cell culture media containing serum. A possible explanation for the conflicting reports in cellular toxicity associated with MSNP (and NP more generally) may be associated with a protein corona that is formed on the surface of silica

nanoparticles that may alter the cytotoxic potential of the nanoparticles when in contact with serum proteins from tissue culture media (Barrett *et al.*, 1999, Cedervall *et al.*, 2007) .

For curcumin we reported an IC_{50} of $33 \pm 0.18\mu\text{M}$ and a statistically significant ($P \leq 0.01$) decrease in cell viability (to $58.2 \pm 8.5\%$) for chrysin at $100\mu\text{M}$ (Figure 3-33 and 3-31). No other reports are available of the cellular toxicity of curcumin or chrysin with OBGF400 cells, however others have reported similar IC_{50} in CNS related cell lines (porcine brain microvascular endothelial cells PBMEC/C1-2: $63 \pm 1.2\mu\text{M}$) (Kaur, 2016). Similar IC_{50} values have been reported for curcumin, $15.2\mu\text{M}$ and $16.4\mu\text{M}$ against A2780CP and MDA-MB-231 cells respectively (Yallapu *et al.*, 2010). Mukerjee and Vishwanatha (Boddupalli *et al.*, 2010) found the IC_{50} of curcumin loaded PLGA nanoparticle was $31\mu\text{M}$ for PWR 1E cells as compared to $37\mu\text{M}$ of free curcumin

Any foreign particle to be taken up by the cell is dependent upon many factors such as size, charge, affinity etc. It has been reported that nanoparticles smaller than 100nm could cause unspecific cellular uptake and cytotoxicity (Yu *et al.*, 2009). Silica nanoparticles in the size range of 50-300nm are capable of inducing endocytosis (Mayor and Pagano, 2007) without causing any cytotoxicity and they have been reported to possess high affinity to many phospholipids present on the surface of the cell, which may even induce pinocytosis (Slowing *et al.*, 2008b).

To evaluate the impact of long-term exposure of MSNP on OBGF400 cells, live cell imaging over 40 hours was conducted using the CellIQ® imaging system. This system captures phase contrast images of cells or regions of wells at pre-defined time-periods during a study. Cells were exposed to increasing concentrations of Fan-MSNP, Curc-MSNP and Chry-MSNP.

The impact of higher concentration of Fan-MSNP was clearly evident, resulting in alteration in the morphology of cells and a reduction/halting of proliferation over the 40-hour period with observable changes in cell viability over the first 16 hours. However, at lower concentrations,

this effect was minimal and cells were generally viable after 40 hours of incubation, and concurring with the concentration dependant trends results reported by the MTT cytotoxicity assay. (Chen *et al.*, 2014) compared the toxicity of MSNPs and gold nanoparticle capped

MSNPs on HeLa cells by MTT assay. Both the types showed no toxicity up to 100µg/mL when exposed up to 48 hours. MTT assay involving Saos-2 cells showed no toxicity up to 0.6mg/mL of mesoporous nanoparticles (Alvarez *et al.*, 2015). In another study Huang *et al.* (Huang *et al.*, 2010) performed an MTT assay on A375 human melanoma cells using spherical, short rod and long rod shaped bare MSNPs with a length 100, 240 & 450nm respectively. None of the MSNPs in the concentration range 0.0625mg/mL to 1mg/mL showed any statistically significant toxicity.

Chry-MSNPs and Curc-MSNPs also demonstrated a similar concentration dependant trend in changes in cellular morphology, interestingly cell viability decreased during the study time for the 50µg/mL Chry-MSNPs whereas proliferation of cells was noted with 50µg/mL Curc-MSNPs. The CellIQ® imaging technology has allowed the visual analysis of changes in cellular morphology and support the observations obtained from the MTT cellular toxicity studies.

3.5.10. Phytochemical release from MSNP

3.5.10.1. Curcumin

The release of curcumin from mesoporous nanoparticles followed a pH dependence, with greater release after 24 hours at pH 5.5, 53.2% ± 2.2%, compared to pH 7.4, 16.1 ± 1.6% ($P \leq 0.001$). This significant differences in release rates at different pH is important as the release in the nasal cavity (pH 5.5) is likely to be more rapid. Furthermore, it has been reported that curcumin is relatively unstable at pH 7.4 compared to more acidic pH, which may explain the lack of increase in cumulative release from 1 hour to 24 hours (~1.8%) compared to the ~36% increase in cumulative release at pH 5.5 at 24 hours (Wang *et al.*, 1997, Tonnesen and Karlsen, 1985, Kunnumakkara *et al.*, 2008). The degradation has been reported to be complex

but at a pH < 1, curcumin exists in the protonated form (H_4A^+), with increasing pH the neutral form (H_3A) predominates. Furthermore stability in acidic conditions is likely due to its conjugated diene structure which becomes gradually destroyed as the proton is removed during the dissociation of the phenolic groups within the structure of curcumin (H_2A^- , HA^{2-} and A^{3-}) which occurs at higher pHs and is likely the cause of curcumin being significantly more prone to degradation (Figure 3-44) (Lee et al., 2013),(Tonnesen and Karlsen, 1985).

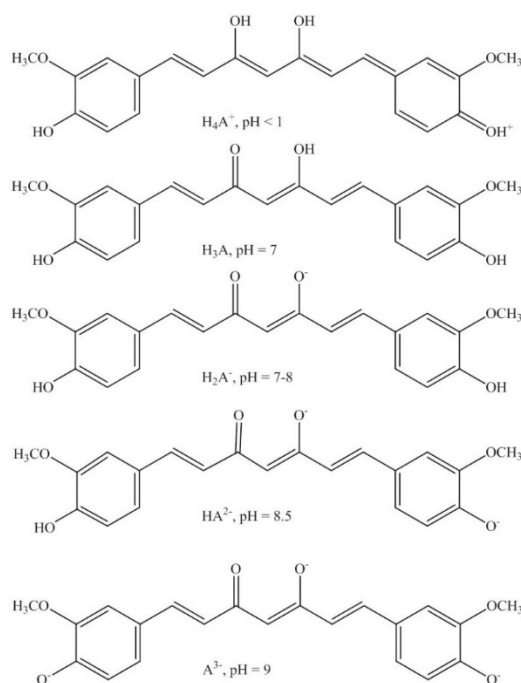


Figure 3-44: Curcumin degradation products
Degradation forms of curcumin at different pH (Lee *et al.*, 2013).

An analysis of the HPLC chromatograms for curcumin at 1 hour and 24 hour also confirms differences in peak ratios suggesting degradation of curcumin at pH 7.4 rather than pH 5.5 (see Figure 3.45 and 3.46).

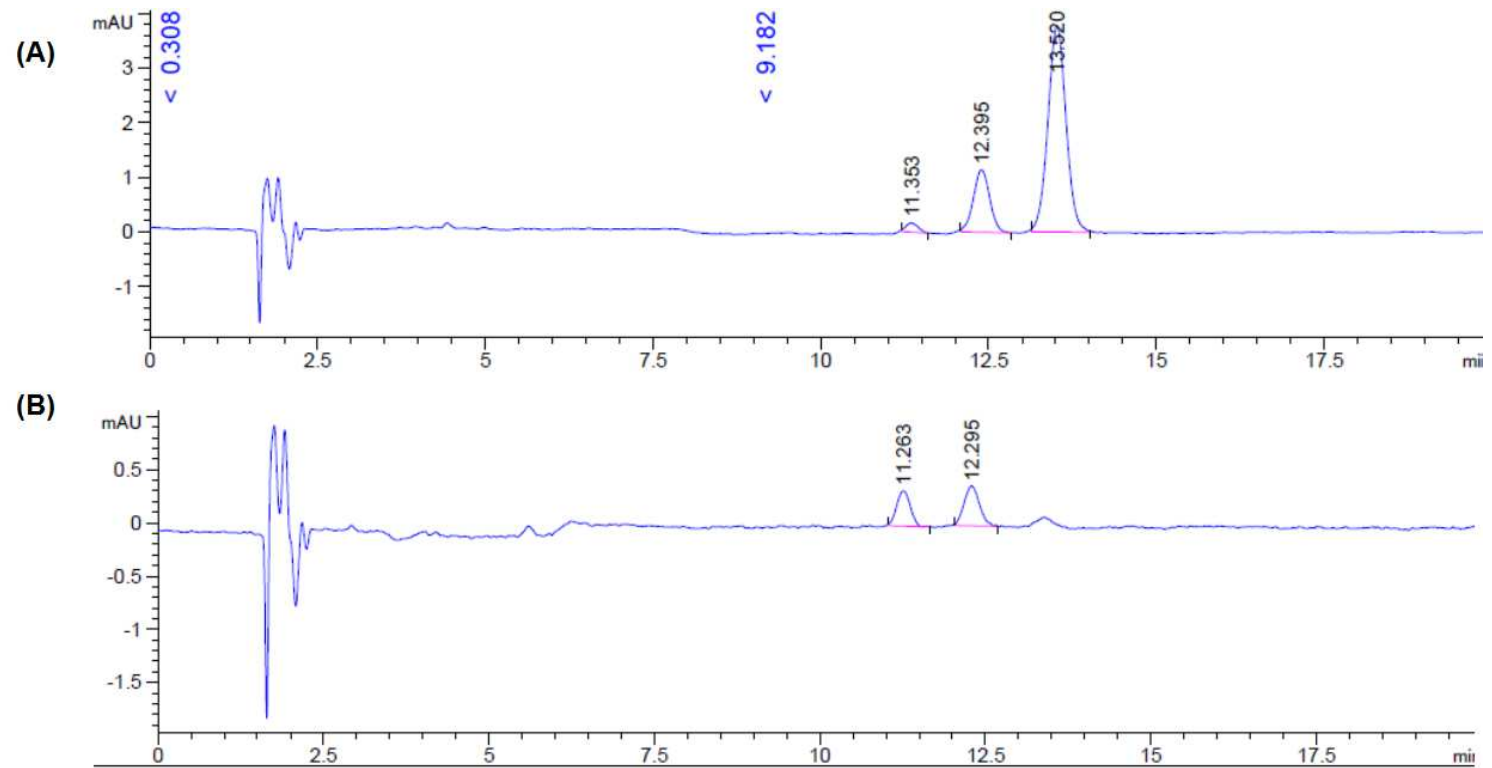


Figure 3-45: HPLC-UV chromatogram of curcumin at pH 7.4.

HPLC chromatograms illustrate peak separation/identification for 1 hour (A) and 24 hour (B) release samples. Retention time is indicated above peaks.

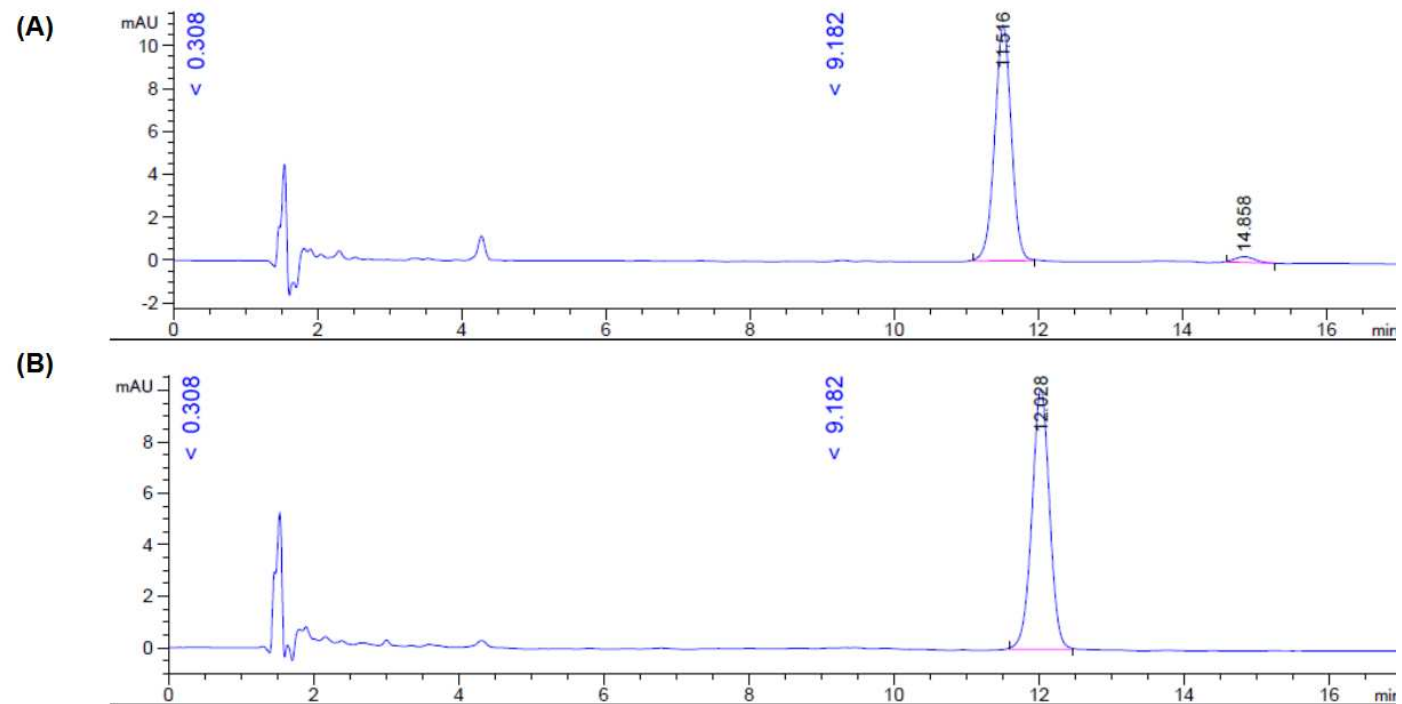


Figure 3-46: HPLC-UV chromatogram of curcumin at pH 5.5.

HPLC chromatograms illustrate peak separation/identification for 1 hour (A) and 24 hour (B) release samples. Retention time is indicated above peaks.

3.5.10.2. Chrysin

Chrysin demonstrated the opposite trend with increased release at pH 7.4 compared with 5.5, $16.8 \pm 0.8\%$ and $9.4 \pm 0.6\%$ respectively, after 24 hours. In both cases the cumulative release over the study period increases significantly ($P \leq 0.001$ for 1 hour versus 24 hours). Furthermore, the release profile for both phytochemicals demonstrated a burst effect at early time points and this pattern has also been reported elsewhere (Anitha et al., 2011, Zou et al., 2013, Yin et al., 2013). This may be a result of the rapid dissolution of the loaded phytochemicals closer to the exterior of the pores with slower penetration of solvent into the pores as a result of the micro/meso size pores of $< 2\text{nm}$ (Horcajada *et al.*, 2004).

Therefore at nasal pH (~ 5.5) both curcumin and chrysin loaded MSNP would be expected to be relatively stable at physiological pHs and undergo release from the MSNP.

3.5.11. Incorporation of Fan-MSNP into the thermoresponsive nasal gel

The delivery of poorly soluble compounds often requires the intervention of formulation scientists to enhance solubility. A novel approach for this can be found in the application of NP technologies as carrier entities for such compounds. Phytochemicals are inherently poorly soluble and have been the focus on many approaches to enhance solubility through incorporation into NP. However, to ensure residency of the NP within the olfactory region of the nasal cavity required its 'forced retention' at the olfactory mucosa. In Chapter 2 we explored the formulation and development of a potentially novel drug delivery system for AMT. To assess the compatibility between MSNP and thermoresponsive nasal gel, Fan-MSNP were incorporated into FCMC, FCS and FPEG and the gelation phenomena analysed using rheological processes. In this approach we replaced AMT with 0.2%, 0.4% and 1% w/w Fan-MSNP.

All formulations demonstrated a tri-region gelation phenomenon, preceded by a stable plateau region and culminating in a stable gel formulation and generally demonstrated a

decrease in the initiation temperature of gelation with increasing Fan-MSNP concentrations (Figure 3-37 to 3-39).

A recent study by Dorraj and Moghimi (2015) demonstrated that the direct incorporation of SLN into thermoresponsive gels increased the gelation temperature. In our studies the 1%w/w concentration corresponded to the AMT content within gels and our results contradict this observation. The fact that all formulations maintained the general tri-phasic trend suggests that there were no gross changes in the gel structure, however the resultant alteration in the initiation of the gelation phase may be a result of a disturbance in the micellar packing and entanglements of PF127 (Kim *et al.*, 2002, Nie *et al.*, 2011).

Furthermore, shear-thinning behaviour at 34°C compared to ambient conditions confirmed that gelation had occurred, as a result of the significantly higher viscosity reading at 34°C compared to ambient conditions (Figure 3-40). Interestingly, for FCMC the incorporation of 1% w/w Fan-MSNP resulted in a significantly different, more viscous gel structure as noted by the increased viscosity compared to the lower concentrations.

Therefore, the inclusion of MSNP into carrier systems such as thermoresponsive gel systems may pose as a viable and single delivery approach to deliver the poorly soluble drug to the olfactory mucosa, giving the benefit of targeted delivery onto the olfactory mucosa through physical manipulation of spray deposition angles

3.6. Conclusion

Phytochemicals possess a range of beneficial pharmacological properties that act directly on neurodegenerative pathways alongside negating the action of drug efflux transporters expressed at the BBB and other CNS barrier sites. However, their clinical use is often limited by poor solubility.

In this chapter, we have demonstrated the successful development of mesoporous silica nanoparticles, which are capable of acting as a viable delivery system to encapsulate phytochemicals. Furthermore, we demonstrated the successful cellular uptake of MSNP with limited cellular toxicity, making MSNP a viable candidate for olfactory targeting of loaded drugs.

Chapter 4

Adaptation of a pMDI spray device for targeted delivery onto the olfactory mucosa: a feasibility study

4.1. Introduction

In previous chapters we have explored the application of thermoresponsive nasal gels (Chapter 2) and nanoparticles (Chapter 3) as potential formulation systems which could be used to deliver a drug to the olfactory mucosa. However, the feasibility of adapting current existing technologies for olfactory mucosa delivery of drugs may provide an alternative route of delivery which may benefit certain compounds.

This chapter focuses on a feasibility design study to explore whether existing pressurised metered dose inhaler (pMDI) technologies can be adapted to delivery an API onto the olfactory mucosa and forms the **partial basis for work conducted through collaboration with 3M®**.

The application of pMDI formulation technologies for aerosol delivery to the lungs, allows for the selective delivery of drugs to the target tissue with minimal side effects. Furthermore, as delivery is targeted, lower doses are often employed to achieve optimal therapeutics outcome (Dalby and Suman, 2003, Hess, 2005). The era of pMDI devices began in the mid-1950s with the development of the Medihaler-Epi by 3M-Riker (Grossman, 1994, Anderson, 2005) with the market for pMDI devices having developed extensively for inhaler drug formulations.

The pMDI system comprises of the API dissolved directly into a propellant (HFA 134a or 224 or, if solubility limitations exist, formulation with a co-solvent (e.g. ethanol) (Figure 4-1). The high vapour pressure of the propellant coupled with the reduced particle sizes of the API (often pre-processed through particle size reduction techniques) often leads to an eventual spray size distribution which is small (Polli *et al.*, 1969, Newman, 2005). The formulation is housed, under pressure, within the canister and the metering value determines the overall spray volume (~60-100µL/actuation). Furthermore, the final particle size is often determined by

the nozzle orifice, with narrow nozzles resulting in a spray cone angled spray mist deposition larger quantities on the mouthpiece (Polli *et al.*, 1969, Newman, 2005).



Figure 4-1: A pressured metered dose inhaler (Lavorini, 2013).

The application of pMDI technologies to the area of nasal drug delivery has been limited primarily to the local treatment allergic rhinitis conditions (Djupesland, 2013). Furthermore, for nose-to-brain delivery, technologies have recently been developed, e.g. ArhcerFish® N2B (www.mysticpharmaceuticals.com), ViaNase® (www.kurvetech.com), POD (<http://impelnp.com/>), although there are not current marketed products based on these inhaler technologies. The direct delivery of an API targeting CNS delivery through a pMDI system would benefit medical emergencies such as status epilepticus, where repetitive or recurrent seizures can be fatal due to the long duration of seizures (Wolfe and Macfarlane, 2006).

Benzodiazepines such as diazepam, lorazepam, midazolam and clonazepam are first choice pharmacological treatment options in these conditions (Manno, 2011). The critical point in treating such conditions is the speed with which the medications can be delivered to the systemic circulation and then to the brain to control the seizures and protect the CNS. Outside of the hospital setting, the transmucosal route of delivery is the fastest alternative to intravenous injection. However intranasal delivery of benzodiazepines can be a faster way to control the seizures in the pre-hospital setting (Wermeling, 2009). Similar concerns have been raised by (Wolfe and Macfarlane, 2006) regarding paediatric status epilepticus where rectal diazepam is commonly used route of delivery which is not only expensive but also ineffective. They suggested that intranasal delivery of midazolam is much better alternative because of its rapid availability into blood and CSF.

4.2. Aims and objectives

The aim of this study was to assess the feasibility of developing a diazepam pMDI formulation using a custom fabricated intranasal actuator device, and to assess stability, administration orientations and air flow rates on the localisation of spray droplets onto the olfactory region of a human silicon nasal cast model.

The objectives were to:

- Determine solubility of diazepam in ethanol alone and ethanol HFA134a-mixture
- Assess the stability of these mixtures at elevated temperature and humidity
- Assess the spray pattern and required angle of spray using brilliant blue dye.
- Assess the deposition of diazepam onto the olfactory mucosa region
- Assess the cellular toxicity of diazepam in the olfactory bulb cell line OBGF400

4.3. Materials and Methods

4.3.1. Materials

Dulbecco's Modified Medium: Nutrient Mixture F12 (DMEM-F12), Dulbecco's Phosphate buffered saline (PBS), L-glutamine 200mM, penicillin/streptomycin and trypsin-EDTA solution were obtained from PAA laboratories (Austria); foetal bovine serum (FBS) (Labtech, Essex, UK); brilliant blue dye, acetonitrile, orthophosphoric acid, ethanol, methanol, brilliant blue dye (BB), potassium hydrogen phosphate were obtained from Fisher Scientific (Loughborough, UK); acutase (Biolegend, UK); gentamycin, (3-(4, 5-dimethylthiazol-2-yl)-2, 5-diphenyl Tetrazolium bromide) MTT, trypan blue and dimethyl sulfoxide (DMSO) were obtained from Sigma-Aldrich (Dorset, UK). Diazepam RS was obtained from F.I.S. (Vicenza, Italy)

4.3.2. Assessment of diazepam solubility in ethanol

To assess the maximum solubility of diazepam in ethanol, 2mg of diazepam was weighted in a clear glass vial followed by the addition of 1mL ethanol. The vial was sonicated and visually assessed for the complete dissolution of particles. The quantity of diazepam was increased by the further addition of 2mg followed by sonication and repeated until a precipitate remained.

4.3.3. Assessment of diazepam solubility in propellant

To assess the solubility of diazepam in the propellant HFA134a, diazepam was solubilised first in ethanol 5% w/w and 10% w/w (of total final canister volume) in clear PET vials and subsequently filled with propellant using a semi-automatic aerosol filler (Pamasol, Switzerland) (Table 4-1).

Table 4-1: pMDI canister composition

Ethanol % w/w	Mass (g)			Concentration
	<i>Empty</i>	<i>Filled</i>	<i>HFA134a</i>	(mg/mL)
5	18.4 ± 0.16	8.71 ± 0.03	8.15 ± 0.14	2.45 ± 0.04
10	18.80 ± 0.16	8.71 ± 0.007	8.73 ± 0.14	2.29 ± 0.038

Mean ± SD; n=12

Solution quality was visually assessed immediately after manufacture and frequently thereafter for 3 weeks for crystal growth, precipitation or immiscible layers (phase separation).

4.3.4. HPLC-UV detection of diazepam

A modified reverse phase HPLC-UV method was used to quantify diazepam (Rouini *et al.*, 2008). An Agilent 1200 Series (Waldbronn, Germany) equipped with a variable wavelength detector (VWD) and a Phenomenex Luna C18 (150 × 4.6mm) 5µm column was used for RP-HPLC. The mobile phase consisted of 10mM phosphate buffer (pH 2.5):methanol:acetonitrile (63:10:27 v/v) and was filtered through a 0.45µM filter and sonicated prior to use. The flow rate was maintained at 2.0mL/min with 20 minutes run time and an injection volume of 10µL. Calibration curves were constructed using standard solutions of known concentrations from 7.8 to 1000µg/mL. The software used for data collection, analysis and control of the system was ChemStation Version 1.24 SP1. The UV detection of diazepam was measured at 230nm.

4.3.5. Canister stability studies

Pre-coated 16mL pMDI canisters were provided by 3M with matching 63µL valves. Canisters were filled with the optimal diazepam formulation and stored valve up, in a humidity cabinet (Firlabo, Finland) at 40°C/75% relative humidity. The stability of the formulations within the canisters was assayed based through spray content analysis assay following 3 months of storage. Briefly, a dosage unit sampling apparatus (DUSA) (Copley Scientific, USA), was assembled and attached to a flow-through air-flow system set at 10 L/min. To actuate the

canisters, a custom designed 3M prototype nasal pMDI actuator, termed the 'Aardvark' system, was provided by 3M and consisted of a 60 μ m nozzle orifice (Figure 4-2).



Figure 4-2: The 3M fabricated nasal pMDI actuator (termed the 'Aardvark' system).

At the end of the third month of storage, diazepam canisters were combined with the pMDI actuator and a single spray actuated into the DUSA. 5mL of ethanol was subsequently added and the unit shaken for 1 minute before 1mL of the ethanol sample was analysed by HPLC-UV to quantify diazepam content.

4.3.6. Nasal pMDI spray: droplet size distribution

To assess the potential *in-vivo* deposition characteristics of the proposed nasal pMDI formulation, the spray droplet size was characterised using a laser diffraction technique. The Helos/Sympatec system was used with an R3 lens (0.5-175 μ m). The nasal spray was vertically mounted 3cm away from the laser path and a vacuum source was mounted anterior to the pump system. The spray systems were pre-actuated prior to mounting, and actuated three times to detect the particle size distribution.

Data was reported as volume diameters at 10%, 50% and 90% of the cumulative undersized volume distribution (D_v). Span was calculated as:

$$\frac{D_{v90} - D_{v10}}{D_{v50}}$$

4.3.7. Nasal pMDI spray deposition within a nasal cast model: brilliant blue visualisation

To visually assess the deposition of spray patterns within a human nasal cast, brilliant blue dye was hand milled in a mortice and pestle for 30 minutes with circular motions, prior to being passed through a 20 μ m sieve. 3.6mg of this reduced particle size was weighed and dissolved in 360mg of ethanol. 50mg of this solution was weighed and transferred into an aluminium canister before being filled with propellant and sonicated prior to use. The final concentration of the dye was maintained at 0.07mg/g. The nasal cast was coated with an opaque acrylic nitrocellulose layer and allowed to dry. The pMDI nozzle was angled at 30, 40 and 50° to the plane (Figure 4-3) and one spray actuated into the nasal cast.

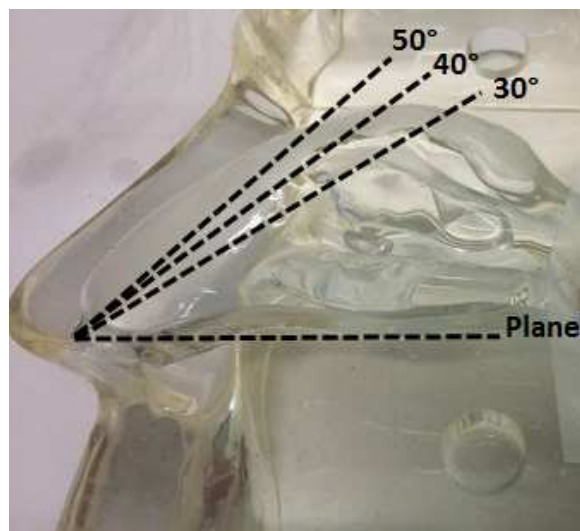


Figure 4-3: Spray angle used within the nasal pMDI actuators.

Furthermore, the impact of nozzle dimensions on depositions was assessed with a 'short' and 'long' nozzle attachment (Table 4-2 and Figure 4-4)

Table 4-2: Dimensions of nozzle attachments

	Dimensions (mm)		
	Length	Width	Orifice
Short	30	5.6	2.23
Long	36	3.7	1.21

Width refers to the largest width at the attachment point to the actuator

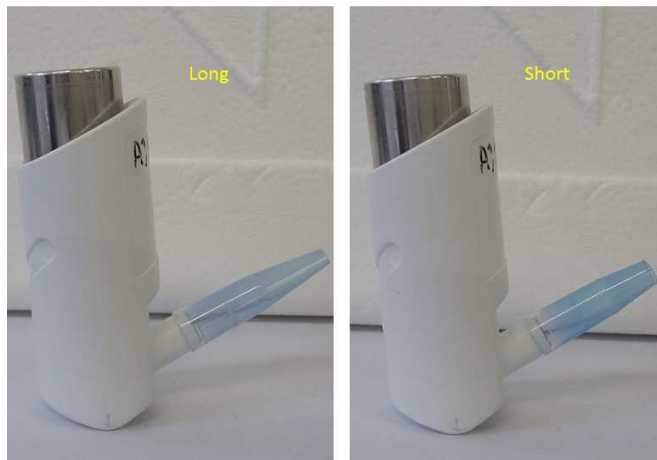


Figure 4-4: Nozzle attachments

Two attachments different in length and aperture were used to study the deposition pattern in the nasal cast.

Deposition patterns were assessed under the application of an airflow to mimic gentle inhalation (10L/min) and rapid inhalation (30L/min) (Foo *et al.*, 2007) following attachment of the nasal cast to a flow controller unit (Copley Scientific, UK).

4.3.8. Nasal pMDI spray deposition within a nasal cast model: diazepam localisation

To evaluate this adopted spray device for olfactory drug delivery of diazepam, the nasal pMDI system was actuated 3 times prior to spraying 1 dose into the uncoated nasal cast model with optimal spray angle and air-flow as determined from the BB deposition studies. The upper flat region of the nasal cast representing the approximate olfactory region in the human nasal cavity was washed twice with 100µL ethanol, collected and the deposition of diazepam on the olfactory region quantified by HPLC-UV approaches.

4.3.9. Cellular toxicity of diazepam

To assess the cellular toxicity of diazepam towards nasal cell lines, an MTT cell viability assay was conducted with OBG400 cells. Cells were suspended in 200µL medium and seeded at a density of 6×10^3 per well of a 96-well plate. After 24 hours the media was removed and replaced with 200µL of media containing DZP (0.001-10,000µM) and incubated for 24 hours at 37°C in a 5 % CO₂ air humidified environment. Subsequently 20µL of 5mg/mL MTT dissolved in PBS was added to each well and incubated at 37°C in an air humidified environment for 4 hours. Thereafter, the media was removed and 100µL of DMSO was added and the plates left to incubate for 15 minutes in the dark. The UV-absorbance of the formazan product was determined at 595nm in a microplate reader (BIO-RAD). Each concentration was assayed in eight wells and run in three independent experiments and results expressed as percentage cytotoxicity relative to a control (0.5% DMSO).

4.4. Results

4.4.1. Assessment of diazepam solubility in ethanol

The solubility of diazepam in ethanol was confirmed as 36mg/mL (45.6mg/g of ethanol assuming a density of 0.789 g/ml).

4.4.2. Assessment of diazepam solubility in propellant

To assess the solubility and stability of diazepam when dispersed in HFA134a, diazepam was dissolved in 5% w/w and 10% w/w ethanol followed by filling with propellant and storage in stability cabinets at 40°C/75% RH for three weeks. During the three-week test period, no visual crystal growth, precipitation or immiscible layers were observed for 5% w/w or 10% w/w in either formulation (Figure 4-5)

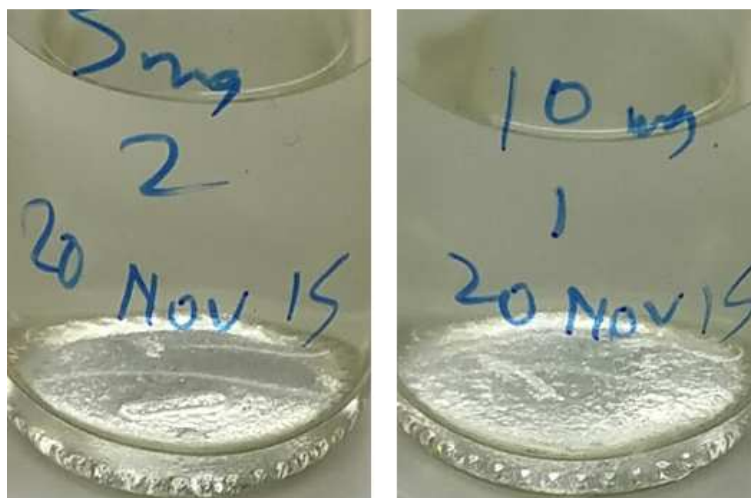


Figure 4-5: Stability of diazepam formulated in 5% or 10% w/w ethanol and HF134a following 3-week storage. Glass vials were prepared with diazepam dissolved in 5% or 10% w/w ethanol. Vials were stored at 40°C/75% RH for three weeks.

4.4.3. HPLC-UV detection of diazepam

The HPLC-UV method was developed and successfully used to detect diazepam with a retention time of 13.95 minutes (Figure 4-6). System precision and method precision demonstrated RSD within acceptable limits of 1% and 2% respectively, indicating an acceptable level of precision of the analytical system.



Figure 4-6: Diazepam HPLC chromatogram.

Diazepam was detected using an Agilent 1200 Series (Waldbronn, Germany) equipped with a variable wavelength detector (VWD) and a Phenomenex Luna C18 (150 × 4.6mm) 5µm column was used for RP-HPLC. Mobile phase was made up of 10mM phosphate buffer (pH 2.5):methanol:acetonitrile (63:10:27, v/v). Mobile phase was filtered through 0.45µM filter and sonicated before use. The flow rate was maintained at 2.0ml/min with 20 minutes run time and the injection volume was 10µL while column temperature was ambient with a UV-detection wavelength of 230nm.

System precision: six replicate injections of an identical standard diazepam stock solution were injected into the HPLC and peak area calculated. The relative standard deviation (%RSD) for the six samples was not more than 1.0% indicating system precision is within acceptable limits as measured per individual run, each with its own identical standard diazepam stock solution, with an overall RSD of 0.45% (Table 4-3).

Table 4-3: System precision assessment for diazepam

Injection no.	Area counts ($\mu\text{V sec}$)			Mean
	1	2	3	
1	3000	3045	3000	
2	3025	3041	3012	
3	3012	3025	3013	
4	3008	3018	3027	
5	3015	3009	3036	
6	3018	3012	3045	
Mean	3013	3025	3022.17	3020.06
SD	8.58	15.03	16.82	13.48
RSD (%)	0.28	0.50	0.56	0.45

System precision was assessed through 6 injections of the same diazepam stock solution for each independent runs (3 runs in total). Mean and SD reported with percentage root-square deviation

Method precision: six preparations of the same batch of samples were analysed for method precision with a resultant %RSD of less than 2.0% (Table 4-4) for all samples demonstrating method precision is within acceptable limits with an overall %RSD of 1.09%.

Table 4-4: Method precision assessment for diazepam

Injection no.	Assay (% w/w)			
	Run 1	Run 2	Run 3	
1	101.25	100.12	97.56	
2	99.58	99.78	102.17	
3	100.08	99.05	103.36	
4	101.23	98.98	100.98	
5	99.87	102.12	103.12	
6	98.67	101.89	101.11	
Mean	100.11	100.32	101.38	100.61
SD	1.00	1.37	2.12	1.50
RSD (%)	0.82	1.64	0.80	1.09

Linearity of response: the linearity of precision for diazepam was determined over a concentration range of 78 -10000 μ g/mL. A proportional response was evident versus the analytical concentration over the working concentration range with a r^2 of 0.999 and linear equation of $y = 2288.7 \pm 1.1 \cdot x$ (Figure 4-7).

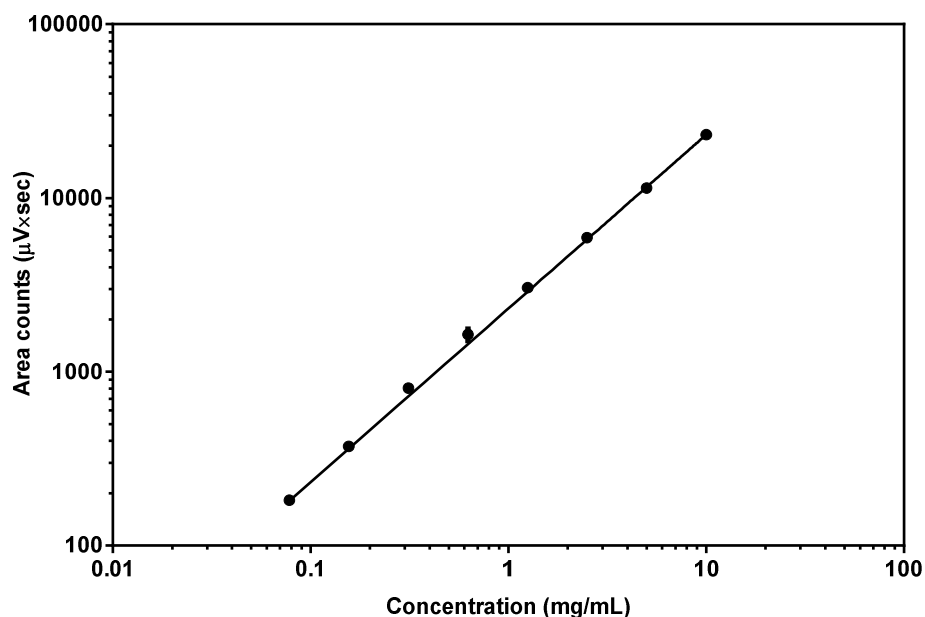


Figure 4-7: Linearity plot for diazepam.

A HPLC-UV method was developed to assess the linearity of detection over a concentration range of 78 - 10000µg/mL. Data represents mean (solid line) ± SD (error bars). n=3.

4.4.4. Canister stability studies

Canisters were prepared and stored in stability cabinet at 40°C/75% RH for three months. At the end of the 3-month period, the canisters were removed from the cabinet, shaken and actuated 10 times into waste prior to a single unit sprayed into a DUSA. At preparation the content assay for 5% and 10% w/w ethanol canisters were determined to be 0.187 ± 0.005 mg/mL and 0.178 ± 0.025 mg/mL respectively. At the end of the storage period the assay content was 0.169 ± 0.008 and 0.159 ± 0.01 mg/mL for the 5% and 10% w/w ethanol canisters, and were not significantly different to the starting canister content assay (Figure 4-8). The LOD was 1.1µg/mL, LOQ was 4.3µg/mL and the signal to noise ratio was >10.

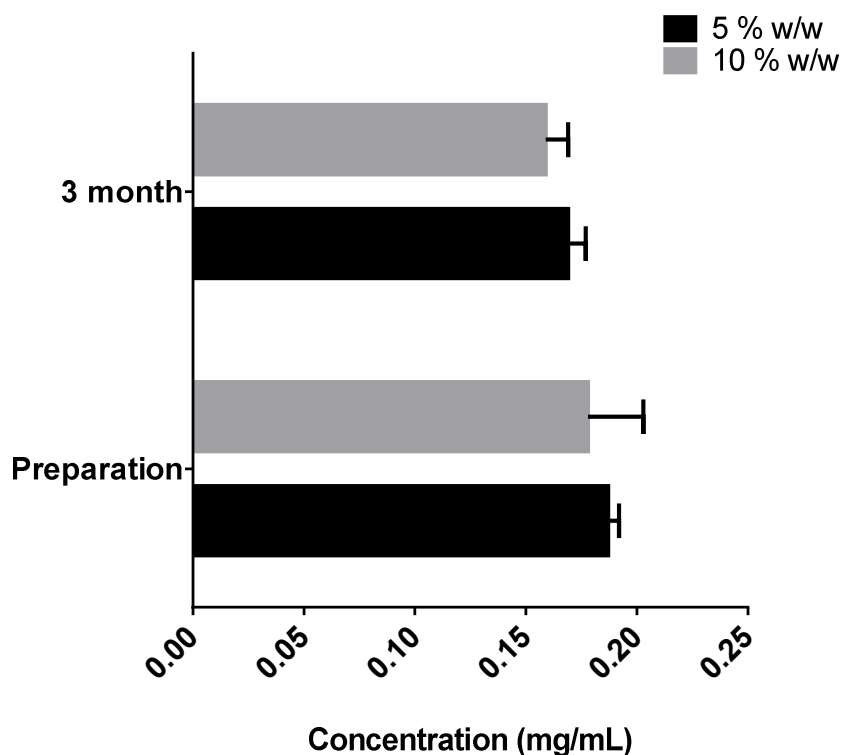


Figure 4-8: Diazepam content assay of 5 and 10% w/w ethanol canisters.

Canisters were prepared and stored in a stability cabinet at 40°C/75% RH for three months. Thereafter a single spray of the canister content was actuated into a DUSA, washed with ethanol and the recovered diazepam assayed using HPLC-UV.

4.4.5. Nasal pMDI spray: droplet size distribution

The 5% w/w diazepam formulation was prepared and attached to the 3M ‘Aardvark’ actuator. Droplet size distribution was assessed using laser diffraction techniques. The VMD (d_{v50}) for the propellant alone was $18.89 \pm 1.07 \mu\text{m}$ with a significantly larger droplet size for BB of $45.11 \pm 1.89 \mu\text{m}$, $P \leq 0.001$ (Figure 4-9). The VMD for diazepam was similar to that of the propellant, $19.25 \pm 0.25 \mu\text{m}$. The relative span of diazepam was similar to that of propellant alone (3.2 ± 0.12), however the span was significantly smaller ($P \leq 0.001$) for BB, 1.43 ± 0.09 .

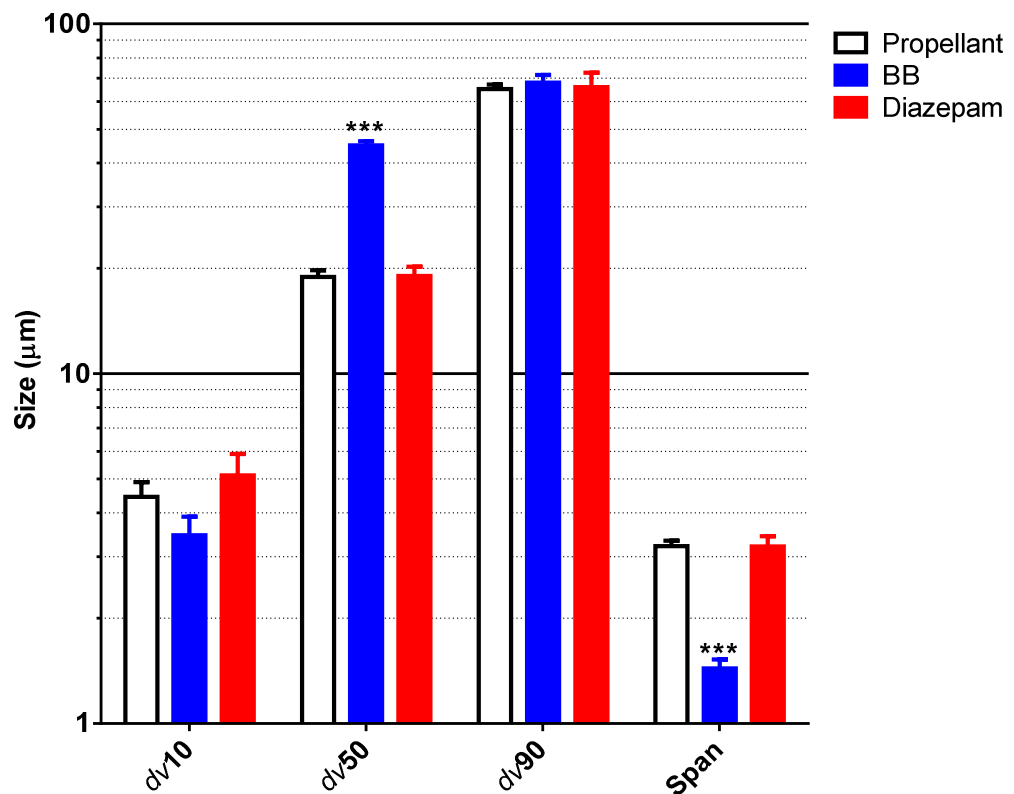


Figure 4-9: Spray particle size distribution.

Spray Particle size distribution for canisters filled with propellant alone (white bars), brilliant blue dye (BB, blue bars) and diazepam (red bars). Dv10, Dv50 and Dv90: particle diameter corresponding to 10, 50 and 90% cumulative undersize particle size distribution; data is represented of mean \pm SD, n=6 replicate spray actuations *per* formulation

4.4.6. Nasal pMDI spray deposition within a nasal cast model: brilliant blue visualisation

To assess the distribution of the plume following deposition into the nasal cavity, brilliant blue (BB) dye was used as a visual indicator and incorporated into the pMDI system. The deposition as assessed under static and dynamic air flow. Under static air flow, a narrow angle orientation (30°) nozzle results in more posterior deposition within the nasal cast, with deposition increasing more towards to the olfactory region as the angle increased to 40° and 50° (Figure 4-10 A)

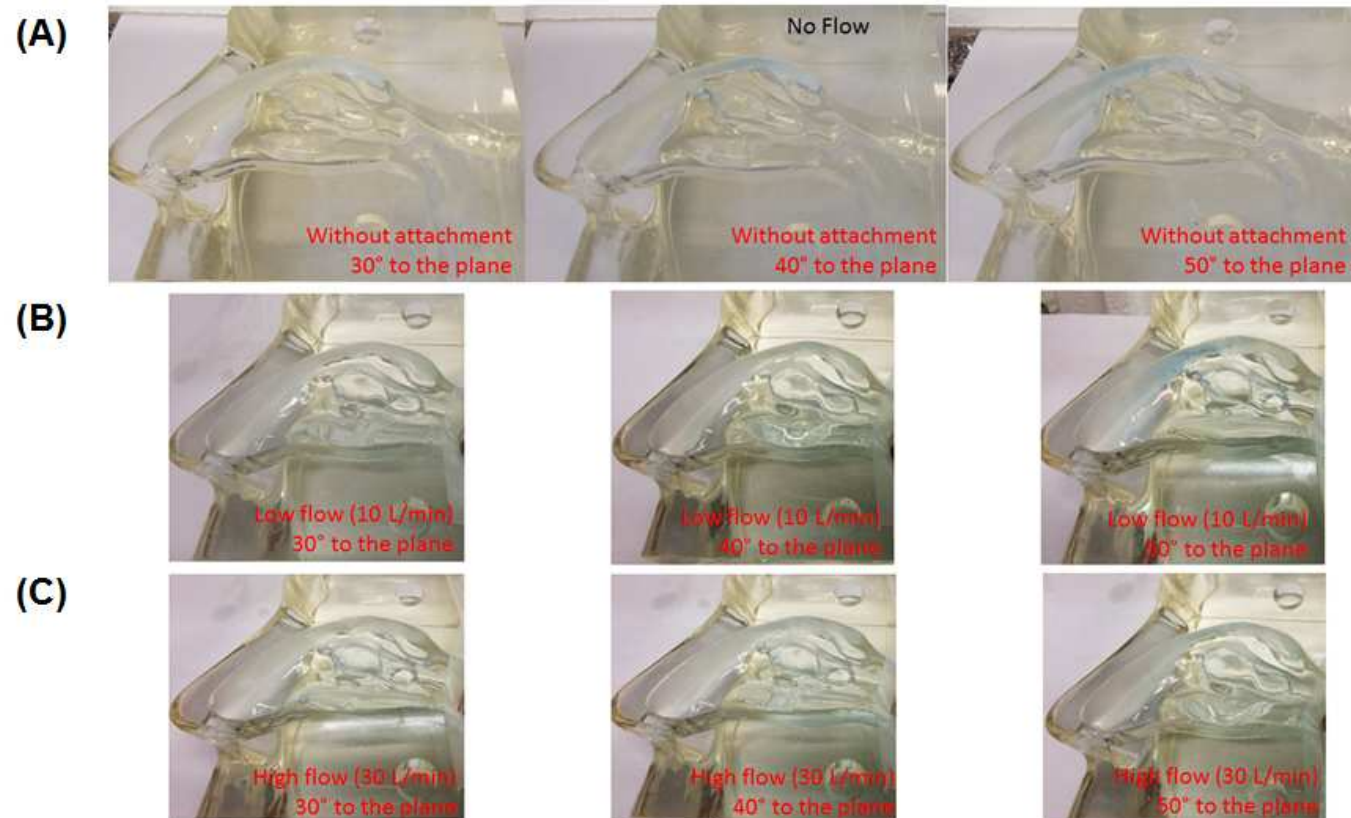


Figure 4-10: Nasal cast deposition of BB pMDI under static and dynamic airflow.

Brilliant blue (BB) canisters were prepared and actuated into a nasal cast model under static (A), low (10L/min) (B) and high (30 L/min) (C) air-flow and at 30,40 and 50° to the plane. The deposition of BB was visually assessed.

(A)



(B)

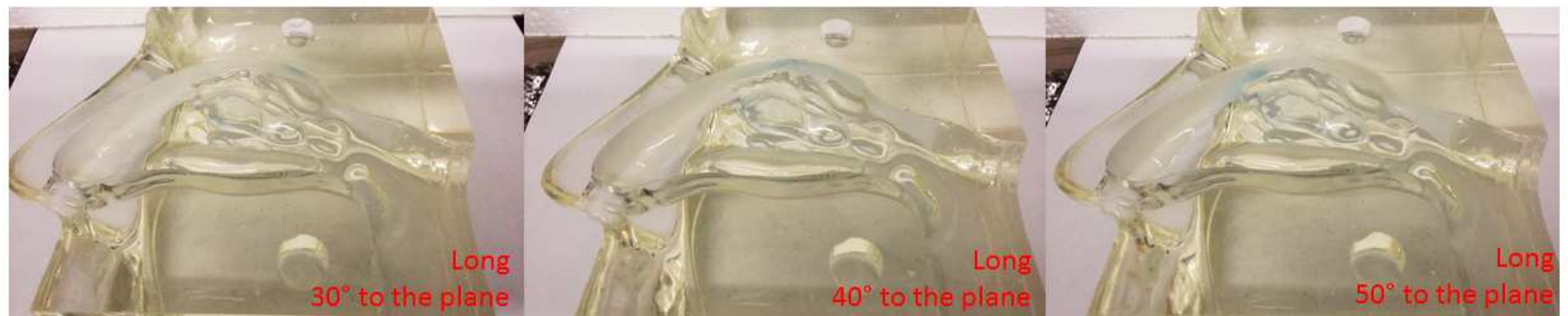


Figure 4-11: Nasal cast deposition of BB pMDI under static air flow and with the 'short' and 'long' nozzle attachments.

Brilliant blue (BB) canisters were prepared and actuated into a nasal cast model using a short (A) and long (B) nozzle attachment angled at 30,40 and 50° to the plane. The deposition of BB was visually assessed.

Under conditions of low flow, the deposition followed a similar pattern with a greater distribution within the nasal vestibule, particularly at 40° (Figure 4-10B). Under high flow, the distribution within the nasal cast was generally diffuse, with no specific localisation in the olfactory region regardless of the spray angle adopted (Figure 4-10C). With the inclusion of the short or long nozzle attachment (Figure 4-11A and B), spray deposition patterns generally followed a similar trend to that without the use of the attachments (Figure 4-10A). However, the localisation within the nasal cavity was less pronounced when using the attachments compared to the absence of the attachments, however the intensity of localisation (as assessed by the visual density of colour) was increased on the olfactory regions for the long attachment at 40° and 50°.

4.4.7. Diazepam deposition in a nasal cast model

To assess the deposition of diazepam from 5% w/w ethanol canisters, a single actuation of prepared canisters was deposition within the nasal cast at an angle of 40° using static, low and high airflows but with no attachments. The deposition of diazepam in the olfactory regions quantified by HPLC-UV. The overall deposition within the olfactory region under static airflow as 6.45% ± 0.12% with low flow resulting in a similar deposition of 6.78% ± 0.58%. However, under high flow, the olfactory deposition was significantly smaller 3.15% ± 0.8% (P < 0.01) (Figure 4-12).

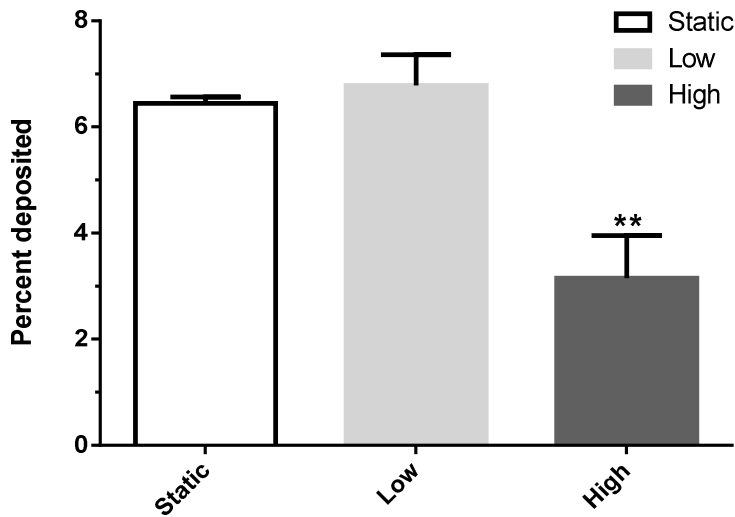


Figure 4-12: Olfactory deposition of diazepam.

Diazepam was dissolved in 5% w/w followed by the addition of the propellant HFA134a. A single actuation was administered into the nasal cast at an angle of 40° and under static, low and high air flow. Data represents mean ± SD. N=4 replicate sprays from 2 batches. ** P ≤ 0.01.

4.4.8. Cellular toxicity of diazepam

To investigate the toxicity of diazepam towards OBGF400 cells, a cell viability assay was conducted with diazepam exposed to OBGF400 for 24 hours over a concentration range of 0.001-1000 μ M. Cell viability was generally maintained over a concentration of 0.001-100 μ M with a calculated IC_{50} of $213.2 \pm 0.15\mu$ M (Figure 4-13).

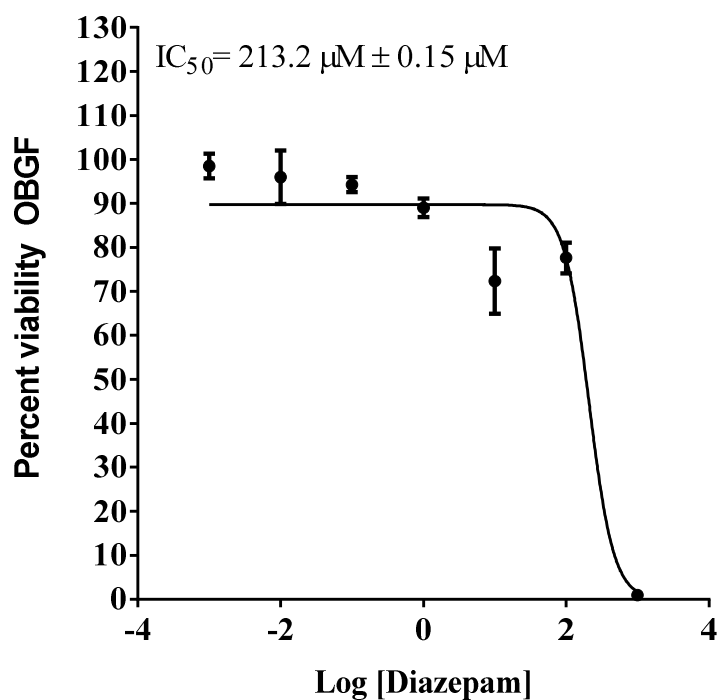


Figure 4-13: Cellular toxicity of diazepam on OBGF400 cells.

Cells were grown on a 96-well plate at a density of 5×10^3 cells per well and exposed to various concentrations of diazepam (0.001 – 1000 μ M). After 24 hour incubation 20 μ L MTT in PBS (5mg/mL) added to each well & incubated for 4 hours. The MTT-formazan produced was solubilised in DMSO and quantified colorimetrically using a UV-spectrophotometer at 570nm. The control cell (without drug) corresponded to a cell viability of 100%. Data is reported as mean \pm SD with up to 8 replicates per compound in at least 3 independent experiment. .

4.5. Discussion

The BBB provides an insidious barrier to the effective delivery of drugs to the brain (Abbott, 2005, Abbott *et al.*, 2010b, Abbott and Romero, 1996, Pardridge, 2007b). Interest in the nose-to-brain (olfactory transfer) routes as a mechanism to bypass the BBB has recently gained attention with an increasing larger body of evidence in human volunteer studies to demonstrate the validity of this transfer route. Despite this increase in interest in the olfactory mucosa as a potential target site for therapeutic delivery to attain brain penetration, no clinical translation of a direct nose-to-brain device exists. However, recently a number of medical device manufacturers have developed viable adaptation of traditional pulmonary pMDI actuators to allow targeted nose-to-brain drug delivery, e.g. ArhcerFish® N2B (www.mysticpharmaceuticals.com), ViaNase® (www.kurvetech.com), POD (<http://impelnp.com/>).

The application of nose-to-brain delivery would benefit therapeutic conditions requiring rapid clinical interventions such as epilepsy, where the duration of seizures could be life threatening and where administration of the therapeutic would likely not be conducted by the patient themselves. The use of benzodiazepine therapy is widespread for seizures and the speed of delivery is important in reverse the seizures episodes. However, the lack of apparent nasal deliver systems provides a novel therapeutic target group to exploit for nose-to-brain delivery and has been demonstrated for midazolam through nasal (systemic) delivery approaches (O'Regan *et al.*, 1996, Mahmoudian and Zadeh, 2004, Mittal *et al.*, 2006).

This chapter is presented as a short feasibility study to explore the use of a novel nasal pMDI actuator system termed 'Aardvark' and developed by 3M® for the purposes of olfactory drug delivery.

To formulate a diazepam pMDI system, the identification of a suitable solvent and its miscibility with the propellant HFA134a was required. The solubility of diazepam in ethanol, a common solvent system incorporating into pMDI systems to aid drug solubility, was found to be 36.36mg/mL and provided a suitably high concentration, considering most pMDI systems required smaller doses administered due to their targeted effect and the maximum recommended dose of diazepam for status epilepticus, 30mg (Sirven and Waterhouse, 2003).

The filling of the canister vials with a mixture of HFA134a and ethanol (5 and 10% w/w) with diazepam, also resulted in no formation of crystal growth or precipitates over a 3 week period, indicating the suitability of ethanol as a co-solvent and the stability of the final formation. Ethanol is fully miscible with HFA134a but can impact upon the vapour pressure and hence the aerosol respirable fraction as well as inducing crystal growth of drug particles (Byron and Patton, 1994, Williams lii and Liu, 1999), however this was not observed with our studies. The confirmation of the final canister composition was then followed on by assessment of the long-term stability, in terms of content assays, on diazepam within the formulated canisters. It was found that both 5 and 10% w/w canisters maintained the stability of diazepam over the month period with no significant degradation of diazepam (Figure 4-8).

To ensure the lack of pulmonary deposition following nasally administration of a drug formulations, the droplet size distribution is key in determining the potential for pulmonary deposition and it is usually accepted that a VMD of $< 5\mu\text{m}$ (Stuart, 1973, Hatch, 1961a) will lead to significant pulmonary deposition. Having confirmed the stability of diazepam within the canisters when stored over 3 months, we next assessed the droplet size distribution from the actuators (Figure 4-9). The dispersion of a drug into the propellant increased the eventual droplet size, and the inclusion of both BB (for visual indication of deposition) and diazepam results in an increase in size distribution fraction (Figure 4-9). The d_{v10} , indicating the fraction of which the spray volume is made up of droplets of equal or less diameters, is an important

measure of the fine particle fraction having the potential for pulmonary disposition. In all three formulation development the d_{v10} was generally larger than the traditional cut-off for pulmonary delivery 3-5 μm vs 2 μm . Furthermore, the VMD (d_{v50}) was similar between the propellant alone and the final diazepam formulation (Figure 4-9). The relative span between formulation was similar expect for BB, which demonstrated significantly smaller span and hence narrower particle size distribution. This may be a result of the extensive milling of the BB granules, which was not required with diazepam. Furthermore, the median droplet size (d_{v50}) was similar to that reports elsewhere for optimal nasal depositions (Newman *et al.*, 1988, Foo *et al.*, 2007). As a pMDI system is actuated, the formulation exits the spray orifice and becomes broken down into atomized droplets containing a proportion of each excipient used within the formulation, and when formulated with a drug, the droplets will also contain an identical proportion of drug. The propellant is designed to rapidly evaporates and results in an intermediate droplet that consist of the co-solvent (any further non-volatile excipients) and the drug. Furthermore, as the co-solvent evaporate the residual particles contain the non-volatile elements (i.e. drug) of the initial spray, which deposits at the target site. It is important to note that these residual particles are often significantly smaller than their initial droplets following actuation (Sheth *et al.*, 2015).

Having demonstrated the suitability of a final diazepam formulation along with appropriate droplet size distribution, we next assessed the important administration properties to ensure olfactory delivery using BB formulation as a visual indicator for olfactory deposition. Static, low and high air flows were used to simulate application with differing levels of inhalation (Foo *et al.*, 2007) (Figure 4-10). It was demonstrated that optimal olfactory deposition was achieved under static (Figure 4-10A) and low flow (Figure 4-10B) when the spray was administrated at an angle of 40° or 50°. The impact of air-flow is important as the administration of nasal spray systems is often associated with a natural 'inhalation' activity which can significantly alter the

particle distribution through the air flow (Kimbell *et al.*, 2007). Indeed, when comparing low to high flow (Figure 4-10C), the dispersion of the droplets is evident by the lack of any homogenous blue deposition regions.

Nasal pMDI systems, unless specifically designed for olfactory delivery, will often come associated with a nozzle that has not been defined to provide localised olfactory delivery, *in lieu* of a wider spray plume angle and hence more wide spread nasal delivery. To investigate this, we adapted the 'Aardvark' actuator to include an attachment that would better angle the spray plume (Figure 4-11). Although the attachments provided some 'focussing' of droplets within the olfactory region, the narrowing of the orifice may have resulted in impaction of the spray plume on the sides of the attachment preventing complete delivery of the actuated dose into the nasal cast. However, existing nose-to-brain devices often employ such attachment, presumably to enhance the targeting of the spray plume towards the olfactory mucosa, e.g. Optinose (Optinose US Inc, USA) (<http://www.optinose.com/>).

As the attachments resulted in reduced olfactory targeting, the deposition of diazepam to the olfactory region was assessed at 40° in the absence of any attachments. Static and low air flows gave similar depositions within the olfactory regions (6.4-6.8%) (Figure 4-12), with a significantly reduced deposition, $3.15\% \pm 0.8\%$ ($P < 0.01$), under high air flow (Figure 4-12). Indeed, both the plume angle (not determined in this study) and administration angle have previously been reported as critical parameters for effective nasal deposition with decreasing turbinate deposition with increasing administration angle (Foo *et al.*, 2007).

The deposition onto the olfactory mucosa was relatively low, however it has previously been demonstrated that $\leq 5\%$ (Foo *et al.*, 2007) of any nasal administered formulation will reach the olfactory mucosa, and coupled with the smaller area within the human nasal cavity (3-10% of the total nasal surface area (Morrison and Costanzo, 1990b)), it is important to consider the

potency of the selected compound towards target receptors. With non-efficient olfactory targeting, the choice of API must be associated with knowledge of it being a potent chemical, whereby minimal levels of deposition onto the olfactory mucosa would provide sufficient delivery to ensure a positive response at the target site within the CNS.

The compatibility of the diazepam content within the spray system with OBG400 cells was further assessed through a cellular viability assay. Cell viability was maintained over a broad concentration range of 0.001-100 μ M with an IC₅₀ of 213.2 \pm 0.15 μ M (Figure 4-13). The total canister content of diazepam was approximately 2.2-2.5mg/mL, equating to approximately 10mM. However, the content assay from a single actuation provides details of the actual total nasal deposition, 0.15-0.20mg/mL equating to approximately a 10-fold lower molar concentration (1mM). Furthermore, deposition of diazepam was reported to be approximately 6-8%, therefore the expected olfactory mucosa exposure would be 60-80 μ M, and therefore would not be toxic to the olfactory cells.

4.6. Conclusion

In conclusion, this short study has demonstrated the potential to adapt existing pulmonary pMDI formulations systems to develop a novel olfactory-targeting nasal pMDI system. Diazepam was selected as a model candidate based on its potency and relatively ease to formulate (i.e. solubility in ethanol). Furthermore, the use of a nasal cast model has aided in identifying the spray administration angles to obtain optimal olfactory deposition and the potential lack of any toxicity with the administered dose that would deposit on the olfactory mucosa.

Chapter 5

Conclusion

5. Conclusions

The overall aim of this work was to evaluate possible formulation approaches that would be exploitable to overcome the physiological barriers present in the nasal cavity to deliver therapeutics directly to the brain. To consider this challenge, we investigate three potential formulation systems (i) thermoresponsive mucoadhesion nasal gels sprays; (ii) mesoporous silica nanoparticles and (iii) nasal pMDI devices.

Chapter 2 focussed on the development of a simple but effective formulation for water-soluble drugs, with the anti-Parkinsonian drug amantadine selected as our model candidate. Hence each formulation was subjected for assessment based on gelation time, rheological properties, mucoadhesiveness, drug release, spray deposition in a nasal cast model, droplet size characterisation, toxicity and storage stability. We identified FCS and FPEG as optimal formulation systems with the slowest drug release from FPEG and the greatest from FCS. A key obstacle for intranasally administered drugs is the retention time within the nasal cavity, and the inclusion of both a thermosensitive and mucoadhesive polymer would improve the residence time of the formulation in the nasal cavity and thereby increasing the window for drug absorption across the nasal and olfactory mucosa. Since gelation time and mucoadhesion was crucial for residency, different mucoadhesives were analysed for their impact on the efficiency of the formulations. It was also important to evaluate these formulations for their overall efficiency in delivering the drug. Whilst we did not utilise *in-vivo* or *ex-vivo* approaches to assess mucoadhesion, the measurement of mucoadhesion was conducted by both tensile strength measurement using texture analysis and an inclined agar mucin gel ramp was used for evaluation. This was not only very simple method, but was also more reproducible and hence reliable than tensile strength measurement. The results demonstrate the superiority of FCMC and FCS compared to FPEG. Out of the formulations we studied, overall the formulation

FCS stood out among the others because it was not only stable for the longest period but also showed better mucoadhesive properties and release profile.

An eight-week stability study demonstrated that none of the formulations were stable at room temperature but were stable under refrigerated conditions, and hence these formulations could be developed as drops or in the form of liquid spray when stored under these conditions. Furthermore, our optimal formulations were screened for their cellular toxicity towards nasal epithelial and olfactory mucosa cells and demonstrated no significant cellular toxicity, demonstrating their compatibility *in-vivo*. With a well-designed spray system, targeting the olfactory region will be more efficient. Hence formulations were also analysed using a spray device for their droplet size, and spray pattern in the nasal cast. All the formulations showed particle sizes greater than 5µm, as required to avoid entry into the lungs and the nasal cast results showed that FCMC covered the highest olfactory region (0.91cm²), and furthermore the use of the nasal cast allowed for a semi-mechanistic understanding of the administration techniques required to achieve optimal olfactory delivery.

To address the delivery of poorly soluble drugs, Chapter 3 focussed on the development of mesoporous silica nanoparticles as carrier systems for curcumin and chrysin, two poorly soluble phytochemicals with a range of CNS cellular and molecular target sites. MSNP were selected due to their highly porosity and ability to enhance the solubility of loading molecules. MSNP were synthesized using three published different methods and compared on the basis of their morphological properties. We identified that Fan-MSNP had better PDI and smaller size (~216nm) as compared to the other methods. BET surface analysis confirmed that the obtained nanoparticles were mesoporous/microporous in nature. Cellular uptake of FITC loaded fan-MSNPs in OBGF400 cells confirmed the compatibility of these nano-systems for the intranasal route. Curcumin and chrysin were chosen to load in these system. Loading efficient for both curcumin and chrysin were between 12-15% and confirmed through HPLC,

TGA and FTIR approaches with DSC analysis confirming that the loaded curcumin and chrysin were in amorphous form. Release studies conducted at pH 5.5 and pH 7.4 demonstrated more significant release for curcumin at pH 5.5. Furthermore MSNP were generally non-toxic to OBG400 cells over 10-100µg/mL for 24 hours. These results were also supported by the images obtained by live cell imaging Cell IQ. Thermosensitive gels can be a possible vehicle for these MSNPs in the nasal cavity hence we incorporated bare MSNP in the gels we optimised in the Chapter 1, and observed no significant rheological changes apart from a slight reduction in the initiation of gelation, as compared to the original formulations and suggesting that thermoresponsive gels may provide a suitable carrier for MSNP. Lastly, we also evaluated the feasibility of adapting pulmonary pMDI delivery devices for the targeted olfactory delivery of diazepam in collaboration with 3M™. A stability study was conducted where diazepam was dissolved in ethanol and filled with HFA 134a kept at 40°C/75% relative humidity for 3 weeks. After confirming the stability of the formulation in the glass vials, these formulations were filled in 3M™ canisters and stability (diazepam content assay) assessed over a 3 month duration studied, which resulted in no significant decrease in diazepam content over 3 months in the prepared pMDI canisters. Using the 3M™ nasal actuator, the deposition of the spray plume with a nasal cast model was assessed through the formulation of canisters containing brilliant blue dye as a visual indicator of deposition and the optimal administration techniques determined. The resultant assessment of diazepam deposition onto the olfactory mucosa was quantified as 5-6% of total dose from a single actuation of the canister. Furthermore, the use of an actuator nozzle attachment demonstrated a more focussed targeting of the spray plume onto the olfactory mucosa, however it resulted in the significant deposition of the spray plume onto the internal walls of the attachment. As some existing N2B pMDI system utilise extended actuator nozzles, further work is warranted on the design of an appropriate actuator nozzle attachment which would limit internal spray plume deposition and enhance the targeting ability onto the olfactory mucosa.

A clear challenge in targeting the olfactory mucosa is the correct administration angles of the device. Using both a nasal gel and pMDI system, this was still challenging, and therefore N2B delivery would, at present, be more appropriate for highly potent APIs where the deposition of < 10% of the administered dose would result in a clinically significant response.

References:

- ABBOTT, N. J. 2005. Dynamics of CNS barriers: evolution, differentiation, and modulation. *Cell Mol Neurobiol*, 25, 5-23.
- ABBOTT, N. J., PATABENDIGE, A. A., DOLMAN, D. E., YUSOF, S. R. & BEGLEY, D. J. 2010a. Structure and function of the blood-brain barrier. *Neurobiol Dis*, 37, 13-25.
- ABBOTT, N. J., PATABENDIGE, A. A. K., DOLMAN, D. E. M., YUSOF, S. R. & BEGLEY, D. J. 2010b. Structure and function of the blood-brain barrier. *Neurobiology of Disease*, 37, 13-25.
- ABBOTT, N. J. & ROMERO, I. A. 1996. Transporting therapeutics across the blood-brain barrier. *Molecular Medicine Today*, 2, 106-113.
- AGRAWAL, A. & MAHESHWARI, R. 2014. Formulation development and evaluation of in situ nasal gel of poorly water soluble drug using mixed solvency concept. *Asian Journal of Pharmaceutics (AJP): Free full text articles from Asian J Pharm*, 5.
- AGRAWAL, A. K., GUPTA, P. N., KHANNA, A., SHARMA, R. K., CHANDRAWANSHI, H. K., GUPTA, N., PATIL, U. K. & YADAV, S. K. 2010. Development and characterization of in situ gel system for nasal insulin delivery. *Pharmazie*, 65, 188-93.
- ALAM, M. I., BABOOTA, S., AHUJA, A., ALI, M., ALI, J., SAHNI, J. K. & BHATNAGAR, A. 2014. Pharmacoscintigraphic evaluation of potential of lipid nanocarriers for nose-to-brain delivery of antidepressant drug. *Int J Pharm*, 470, 99-106.
- ALFREY, T., GURNEE, E. F. & LLOYD, W. G. 1966. Diffusion in glassy polymers. *Journal of Polymer Science Part C: Polymer Symposia*, 12, 249-261.
- ALLADI, P. A., MAHADEVAN, A., YASHA, T. C., RAJU, T. R., SHANKAR, S. K. & MUTHANE, U. 2009. Absence of age-related changes in nigral dopaminergic neurons of Asian Indians: relevance to lower incidence of Parkinson's disease. *Neuroscience*, 159, 236-45.
- ALLEN, J. D., VAN LOEVEZIJN, A., LAKHAI, J. M., VAN DER VALK, M., VAN TELLINGEN, O., REID, G., SCHELLENS, J. H., KOOMEN, G. J. & SCHINKEL, A. H. 2002a. Potent and specific inhibition of the breast cancer resistance protein multidrug transporter in vitro and in mouse intestine by a novel analogue of fumitremorgin C. *Mol Cancer Ther*, 1, 417-25.
- ALLEN, J. D., VAN LOEVEZIJN, A., LAKHAI, J. M., VAN DER VALK, M., VAN TELLINGEN, O., REID, G., SCHELLENS, J. H. M., KOOMEN, G. J. & SCHINKEL, A. H. 2002b. Potent and Specific Inhibition of the Breast Cancer Resistance Protein Multidrug Transporter in Vitro and in Mouse Intestine by a Novel Analogue of Fumitremorgin C 1 This work was supported in part by grant NKI 97-1433 from the Dutch Cancer Society (to AHS). Synthesis investigations by A. v. L. and GJ. K. were supported by the Netherlands Research Council for Chemical Sciences (NWO/CW) and the Netherlands Technology Foundation (STW). 1. *Molecular Cancer Therapeutics*, 1, 417-425.
- ALMDAL, K., DYRE, J., HVIDT, S. & KRAMER, O. 1993. Towards a phenomenological definition of the term 'gel'. *Polymer Gels and Networks*, 1, 5-17.
- ALSARRA, I. A., HAMED, A. Y., MAHROUS, G. M., EL MAGHRABY, G. M., AL-ROBAYAN, A. A. & ALANAZI, F. K. 2009. Mucoadhesive polymeric hydrogels for nasal delivery of acyclovir. *Drug Dev Ind Pharm*, 35, 352-62.
- ALVAREZ, G. S., ECHAZU, M. I. A., OLIVETTI, C. E. & DESIMONE, M. F. 2015. Synthesis and Characterization of Ibandronate-Loaded Silica Nanoparticles and Collagen Nanocomposites. *Current Pharmaceutical Biotechnology*, 16, 661-667.
- AMBRUS, R., KOCBEK, P., KRISTL, J., SIBANC, R., RAJKO, R. & SZABO-REVESZ, P. 2009. Investigation of preparation parameters to improve the dissolution of poorly water-soluble meloxicam. *Int J Pharm*, 381, 153-9.
- AMINABHAVI, T. M., AITHAL, U. S. & SHUKLA, S. S. 1989. Molecular transport of organic liquids through polymer films. *Journal of Macromolecular Science, Part C*, 29, 319-363.
- ANDERSON, P. J. 2005. History of aerosol therapy: liquid nebulization to MDIs to DPIs. *Respir Care*, 50, 1139-50.

- ANITHA, A., DEEPAGAN, V. G., DIVYA RANI, V. V., MENON, D., NAIR, S. V. & JAYAKUMAR, R. 2011. Preparation, characterization, in vitro drug release and biological studies of curcumin loaded dextran sulphate–chitosan nanoparticles. *Carbohydrate Polymers*, 84, 1158-1164.
- ARTS, I. C. W., VAN DE PUTTE, B. & HOLLMAN, P. C. H. 2000. Catechin contents of foods commonly consumed in The Netherlands. 2. Tea, wine, fruit juices, and chocolate milk. *Journal of Agricultural and Food Chemistry*, 48, 1752-1757.
- ASHIDA, H., FUKUDA, I., YAMASHITA, T. & KANAZAWA, K. 2000. Flavones and flavonols at dietary levels inhibit a transformation of aryl hydrocarbon receptor induced by dioxin. *FEBS Lett*, 476, 213-7.
- ATTWOOD, D., COLLETT, J. H. & TAIT, C. J. 1985. The micellar properties of the poly(oxyethylene) - poly(oxypropylene) copolymer Pluronic F127 in water and electrolyte solution. *International Journal of Pharmaceutics*, 26, 25-33.
- AUNGST, B. J., ROGERS, N. J. & SHEFTER, E. 1988. Comparison of nasal, rectal, buccal, sublingual and intramuscular insulin efficacy and the effects of a bile salt absorption promoter. *J Pharmacol Exp Ther*, 244, 23-7.
- BADHAN, R. K., KAUR, M., LUNGARE, S. & OBUOBI, S. 2014. Improving brain drug targeting through exploitation of the nose-to-brain route: a physiological and pharmacokinetic perspective. *Curr Drug Deliv*, 11, 458-71.
- BAHRAMI, G. & MOHAMMADI, B. 2007. Determination of clarithromycin in human serum by high-performance liquid chromatography after pre-column derivatization with 9-fluorenylmethyl chloroformate: application to a bioequivalence study. *J Chromatogr B Analyt Technol Biomed Life Sci*, 850, 417-22.
- BAI, S., YANG, T., ABBRUSCATO, T. J. & AHSAN, F. 2008. Evaluation of human nasal RPMI 2650 cells grown at an air-liquid interface as a model for nasal drug transport studies. *J Pharm Sci*, 97, 1165-78.
- BAKER, H., GENTER, M.B. 2003. The Olfactory System and the Nasal Mucosa as Portals of Entry of Viruses, Drugs, and Other Exogenous Agents into the Brain. *Handbook of olfaction and gustation*. 2nd ed. New York: Marcel Dekker.
- BAKER, H. & SPENCER, R. F. 1986. Transneuronal transport of peroxidase-conjugated wheat germ agglutinin (WGA-HRP) from the olfactory epithelium to the brain of the adult rat. *Exp Brain Res*, 63, 461-73.
- BALIN, B. J., BROADWELL, R. D., SALCMAN, M. & EL-KALLINY, M. 1986. Avenues for entry of peripherally administered protein to the central nervous system in mouse, rat, and squirrel monkey. *J Comp Neurol*, 251, 260-80.
- BARRETT, E. G., JOHNSTON, C., OBERDÖRSTER, G. & FINKELSTEIN, J. N. 1999. Silica binds serum proteins resulting in a shift of the dose-response for silica-induced chemokine expression in an alveolar type II cell line. *Toxicology and applied pharmacology*, 161, 111-122.
- BARRETT, E. P., JOYNER, L. G. & HALENDA, P. P. 1951. The Determination of Pore Volume and Area Distributions in Porous Substances. I. Computations from Nitrogen Isotherms. *Journal of the American Chemical Society*, 73, 373-380.
- BASU, S. & BANDYOPADHYAY, A. K. 2010. Development and characterization of mucoadhesive in situ nasal gel of midazolam prepared with Ficus carica mucilage. *AAPS PharmSciTech*, 11, 1223-31.
- BASU, S. & MAITY, S. 2012. Preparation and characterisation of mucoadhesive nasal gel of venlafaxine hydrochloride for treatment of anxiety disorders. *Indian J Pharm Sci*, 74, 428-33.
- BAUER, M., KARCH, R., NEUMANN, F., WAGNER, C. C., KLETTER, K., MULLER, M., LOSCHER, W., ZEITLINGER, M. & LANGER, O. 2010. Assessment of regional differences in tariquidar-induced P-glycoprotein modulation at the human blood-brain barrier. *J Cereb Blood Flow Metab*, 30, 510-5.
- BETTINI, R., COLOMBO, P., MASSIMO, G., CATELLANI, P. L. & VITALI, T. 1994. Swelling and drug release in hydrogel matrices: polymer viscosity and matrix porosity effects. *European Journal of Pharmaceutical Sciences*, 2, 213-219.
- BHANDWALKAR, M. J. & AVACHAT, A. M. 2013. Thermoreversible Nasal In situ Gel of Venlafaxine Hydrochloride: Formulation, Characterization, and Pharmacodynamic Evaluation. *Aaps Pharmscitech*, 14, 101-110.
- BITTER, C., SUTER-ZIMMERMANN, K. & SURBER, C. 2011. Nasal drug delivery in humans. *Curr Probl Dermatol*, 40, 20-35.
- BLUMBERG, J. B., DING, E. L., DIXON, R., PASINETTI, G. M. & VILLARREAL, F. 2014. The science of cocoa flavanols: bioavailability, emerging evidence, and proposed mechanisms. *Adv Nutr*, 5, 547-9.

- BODDUPALLI, B. M., MOHAMMED, Z. N., NATH, R. A. & BANJI, D. 2010. Mucoadhesive drug delivery system: An overview. *J Adv Pharm Technol Res*, 1, 381-7.
- BONACUCINA, G., MARTELLI, S. & PALMIERI, G. F. 2004. Rheological, mucoadhesive and release properties of Carbopol gels in hydrophilic cosolvents. *Int J Pharm*, 282, 115-30.
- BOTTINI, M., D'ANNIBALE, F., MAGRINI, A., CERIGNOLI, F., ARIMURA, Y., DAWSON, M. I., BERGAMASCHI, E., ROSATO, N., BERGAMASCHI, A. & MUSTELIN, T. 2007. Quantum dot-doped silica nanoparticles as probes for targeting of T-lymphocytes. *Int J Nanomedicine*, 2, 227-33.
- BOUSSIF, O., LEZOUALCH, F., ZANTA, M. A., MERGNY, M. D., SCHERMAN, D., DEMENEIX, B. & BEHR, J. P. 1995. A Versatile Vector for Gene and Oligonucleotide Transfer into Cells in Culture and in-Vivo - Polyethylenimine. *Proceedings of the National Academy of Sciences of the United States of America*, 92, 7297-7301.
- BREEDVELD, P., BEIJNEN, J. H. & SCHELLENS, J. H. 2006a. Use of P-glycoprotein and BCRP inhibitors to improve oral bioavailability and CNS penetration of anticancer drugs. *Trends Pharmacol Sci*, 27, 17-24.
- BREEDVELD, P., BEIJNEN, J. H. & SCHELLENS, J. H. M. 2006b. Use of P-glycoprotein and BCRP inhibitors to improve oral bioavailability and CNS penetration of anticancer drugs. *Trends in Pharmacological Sciences*, 27, 17-24.
- BROADWELL, R. D. & BALIN, B. J. 1985. Endocytic and exocytic pathways of the neuronal secretory process and trans-synaptic transfer of wheat germ agglutinin-horseradish peroxidase in vivo. *J Comp Neurol*, 242, 632-50.
- BRUNAUER, S., EMMETT, P. H. & TELLER, E. 1938. Adsorption of Gases in Multimolecular Layers. *Journal of the American Chemical Society*, 60, 309-319.
- BRUNET-MAHEU, J. M., FERNANDES, J. C., DE LACERDA, C. A., SHI, Q., BENDERDOUR, M. & LAVIGNE, P. 2009. Pluronic F-127 as a cell carrier for bone tissue engineering. *J Biomater Appl*, 24, 275-87.
- BRUSCHI, M. L., JONES, D. S., PANZERI, H., GREMIAO, M. P., DE FREITAS, O. & LARA, E. H. 2007. Semisolid systems containing propolis for the treatment of periodontal disease: in vitro release kinetics, syringeability, rheological, textural, and mucoadhesive properties. *J Pharm Sci*, 96, 2074-89.
- BYRON, P. R. & PATTON, J. S. 1994. Drug delivery via the respiratory tract. *J Aerosol Med*, 7, 49-75.
- CAI, Q., LIN, W.-Y., XIAO, F.-S., PANG, W.-Q., CHEN, X.-H. & ZOU, B.-S. 1999. The preparation of highly ordered MCM-41 with extremely low surfactant concentration. *Microporous and Mesoporous Materials*, 32, 1-15.
- CAMPION, R. P. 1975. The Influence of Structure on Autohesion (Self-Tack) and other forms of Diffusion into Polymers. *The Journal of Adhesion*, 7, 1-23.
- CARIO, E. 2012. Nanotechnology-based drug delivery in mucosal immune diseases: hype or hope? *Mucosal Immunology*, 5, 2.
- CARTER, L. A., MACDONALD, J. L. & ROSKAMS, A. J. 2004. Olfactory horizontal basal cells demonstrate a conserved multipotent progenitor phenotype. *J Neurosci*, 24, 5670-83.
- CEDERVALL, T., LYNCH, I., FOY, M., BERGGÅRD, T., DONNELLY, S. C., CAGNEY, G., LINSE, S. & DAWSON, K. A. 2007. Detailed identification of plasma proteins adsorbed on copolymer nanoparticles. *Angewandte Chemie*, 119, 5856-5858.
- CHANG, J. Y., OH, Y. K., CHOI, H. G., KIM, Y. B. & KIM, C. K. 2002. Rheological evaluation of thermosensitive and mucoadhesive vaginal gels in physiological conditions. *Int J Pharm*, 241, 155-63.
- CHAPMAN, C. D., FREY, W. H., 2ND, CRAFT, S., DANIELYAN, L., HALLSCHMID, M., SCHIOTH, H. B. & BENEDICT, C. 2012. Intranasal Treatment of Central Nervous System Dysfunction in Humans. *Pharm Res*.
- CHEARWAE, W., SHUKLA, S., LIMTRAKUL, P. & AMBUDKAR, S. V. 2006. Modulation of the function of the multidrug resistance-linked ATP-binding cassette transporter ABCG2 by the cancer chemopreventive agent curcumin. *Mol Cancer Ther*, 5, 1995-2006.
- CHEKHONIN, V. P., GURINA, O. I., YKHOVA, O. V., RYABININA, A. E., TSIBULKINA, E. A. & ZHIRKOV, Y. A. 2008. Polyethylene glycol-conjugated immunoliposomes specific for olfactory ensheathing glial cells. *Bull Exp Biol Med*, 145, 449-51.

- CHEN, J., DAI, W. T., HE, Z. M., GAO, L., HUANG, X., GONG, J. M., XING, H. Y. & CHEN, W. D. 2013a. Fabrication and Evaluation of Curcumin-loaded Nanoparticles Based on Solid Lipid as a New Type of Colloidal Drug Delivery System. *Indian Journal of Pharmaceutical Sciences*, 75, 178-184.
- CHEN, T. C., DA FONSECA, C. O. & SCHONTHAL, A. H. 2016. Perillyl Alcohol and Its Drug-Conjugated Derivatives as Potential Novel Methods of Treating Brain Metastases. *Int J Mol Sci*, 17.
- CHEN, X., CHENG, X., SOERIYADI, A. H., SAGNELLA, S. M., LU, X., SCOTT, J. A., LOWE, S. B., KAVALLARIS, M. & GOODING, J. J. 2014. Stimuli-responsive functionalized mesoporous silica nanoparticles for drug release in response to various biological stimuli. *Biomaterials Science*, 2, 121-130.
- CHEN, X., ZHI, F., JIA, X., ZHANG, X., AMBARDEKAR, R., MENG, Z., PARADKAR, A. R., HU, Y. & YANG, Y. 2013b. Enhanced brain targeting of curcumin by intranasal administration of a thermosensitive poloxamer hydrogel. *J Pharm Pharmacol*, 65, 807-16.
- CHEN, Y. & LIU, L. 2012. Modern methods for delivery of drugs across the blood-brain barrier. *Adv Drug Deliv Rev*, 64, 640-65.
- CHERNIACK, E. P. 2012. A berry thought-provoking idea: the potential role of plant polyphenols in the treatment of age-related cognitive disorders. *Br J Nutr*, 108, 794-800.
- CHI, S. C. & JUN, H. W. 1991. Release rates of ketoprofen from poloxamer gels in a membraneless diffusion cell. *J Pharm Sci*, 80, 280-3.
- CHIEN, Y. W. & CHANG, S. F. 1987. Intranasal drug delivery for systemic medications. *Crit Rev Ther Drug Carrier Syst*, 4, 67-194.
- CHO, H. J., BALAKRISHNAN, P., PARK, E. K., SONG, K. W., HONG, S. S., JANG, T. Y., KIM, K. S., CHUNG, S. J., SHIM, C. K. & KIM, D. D. 2011. Poloxamer/cyclodextrin/chitosan-based thermoreversible gel for intranasal delivery of fexofenadine hydrochloride. *J Pharm Sci*, 100, 681-91.
- CHOUDHURY, D., GANGULI, A., DASTIDAR, D. G., ACHARYA, B. R., DAS, A. & CHAKRABARTI, G. 2013. Apigenin shows synergistic anticancer activity with curcumin by binding at different sites of tubulin. *Biochimie*, 95, 1297-309.
- CHOW, H. H., ANAVY, N. & VILLALOBOS, A. 2001. Direct nose-brain transport of benzoylecgonine following intranasal administration in rats. *J Pharm Sci*, 90, 1729-35.
- CHOW, H. S., CHEN, Z. & MATSUURA, G. T. 1999. Direct transport of cocaine from the nasal cavity to the brain following intranasal cocaine administration in rats. *J Pharm Sci*, 88, 754-8.
- CHU, Y. H., CHANG, C. L. & HSU, H. F. 2000. Flavonoid content of several vegetables and their antioxidant activity. *Journal of the Science of Food and Agriculture*, 80, 561-566.
- CHUNG, T. H., WU, S. H., YAO, M., LU, C. W., LIN, Y. S., HUNG, Y., MOU, C. Y., CHEN, Y. C. & HUANG, D. M. 2007. The effect of surface charge on the uptake and biological function of mesoporous silica nanoparticles in 3T3-L1 cells and human mesenchymal stem cells. *Biomaterials*, 28, 2959-66.
- COOPER, G. 2000. *The Cell: A Molecular Approach*. 2nd edition, Sunderland (MA), Sinauer Associates.
- COSTANTINO, H. R., ILLUM, L., BRANDT, G., JOHNSON, P. H. & QUAY, S. C. 2007. Intranasal delivery: physicochemical and therapeutic aspects. *Int J Pharm*, 337, 1-24.
- CRANK, J. P., G.S. 1968. *Diffusion in polymers*, London, Academic Press.
- CURRAN, R. M., DONNELLY, L., MORROW, R. J., FRASER, C., ANDREWS, G., CRANAGE, M., MALCOLM, R. K., SHATTOCK, R. J. & WOOLFSON, A. D. 2009. Vaginal delivery of the recombinant HIV-1 clade-C trimeric gp140 envelope protein CN54gp140 within novel rheologically structured vehicles elicits specific immune responses. *Vaccine*, 27, 6791-6798.
- DAHLIN, M., BERGMAN, U., JANSSON, B., BJORK, E. & BRITTEBO, E. 2000. Transfer of dopamine in the olfactory pathway following nasal administration in mice. *Pharm Res*, 17, 737-42.
- DALBY, R. & SUMAN, J. 2003. Inhalation therapy: technological milestones in asthma treatment. *Adv Drug Deliv Rev*, 55, 779-91.
- DALE, O., HOFFER, C., SHEFFELS, P. & KHARASCH, E. D. 2002. Disposition of nasal, intravenous, and oral methadone in healthy volunteers. *Clin Pharmacol Ther*, 72, 536-45.
- DAUCHY, S., DUTHEIL, F., WEAVER, R. J., CHASSOUX, F., DAUMAS-DUPORT, C., COURAUD, P. O., SCHERRMANN, J. M., DE WAZIERS, I. & DECLEVES, X. 2008. ABC transporters, cytochromes P450 and their main transcription factors: expression at the human blood-brain barrier. *J Neurochem*, 107, 1518-28.

- DAVIDSON, G. W. R., PEPPAS, P. 1986. Solute and water diffusion in swellable copolymers versus relaxation controlled transport in phema-co-mma copolymers. *Journal of Controlled Release*, 3, 243-258.
- DAVIS, S. S., WASHINGTON, C., WEST, P., ILLUM, L., LIVERSIDGE, G., STERNSON, L. & KIRSH, R. 1987. Lipid emulsions as drug delivery systems. *Ann N Y Acad Sci*, 507, 75-88.
- DE KEE, D., LIU, Q. & HINESTROZA, J. 2005. Viscoelastic (Non-Fickian) Diffusion. *The Canadian Journal of Chemical Engineering*, 83, 913-929.
- DE LORENZO, D. 1970. The Olfactory Neuron and the Blood-Brain Barrier. In: FOUNDATION., C. (ed.) *Taste and smell in vertebrates*. London,: Churchill.
- DE LUCA, M. A., LAI, F., CORRIAS, F., CABONI, P., BIMPIDIS, Z., MACCIONI, E., FADDA, A. M. & DI CHIARA, G. 2015. Lactoferrin- and antitransferrin-modified liposomes for brain targeting of the NK3 receptor agonist senktide: preparation and in vivo evaluation. *Int J Pharm*, 479, 129-37.
- DEMUTH, P., HURLEY, M., WU, C., GALANIE, S., ZACHARIAH, M. R. & DESHONG, P. 2011. Mesoscale porous silica as drug delivery vehicles: Synthesis, characterization, and pH-sensitive release profiles. *Microporous and Mesoporous Materials*, 141, 128-134.
- DERJAGUIN, B. V., TOPOROV, Y. P., MULLER, V. M. & ALEINIKOVA, I. N. 1977. On the relationship between the electrostatic and the molecular component of the adhesion of elastic particles to a solid surface. *Journal of Colloid and Interface Science*, 58, 528-533.
- DEVKAR, T. B., TEKADE, A. R. & KHANDELWAL, K. R. 2014. Surface engineered nanostructured lipid carriers for efficient nose to brain delivery of ondansetron HCl using Delonix regia gum as a natural mucoadhesive polymer. *Colloids and Surfaces B: Biointerfaces*, 122, 143-150.
- DHURIA, S. V., HANSON, L. R. & FREY, W. H., 2ND 2010. Intranasal delivery to the central nervous system: mechanisms and experimental considerations. *J Pharm Sci*, 99, 1654-73.
- DJUPESLAND, P. G. 2013. Nasal drug delivery devices: characteristics and performance in a clinical perspective-a review. *Drug Deliv Transl Res*, 3, 42-62.
- DOLBERG, A. M. & REICHL, S. 2016. Expression of P-glycoprotein in excised human nasal mucosa and optimized models of RPMI 2650 cells. *Int J Pharm*, 508, 22-33.
- DOUGLAS, S. J., DAVIS, S. S. & ILLUM, L. 1987. Nanoparticles in drug delivery. *Crit Rev Ther Drug Carrier Syst*, 3, 233-61.
- DU, L., YANG, Y. H., XU, J., WANG, Y. M., XUE, C. H., KURIHARA, H. & TAKAHASHI, K. 2016. Transport and uptake effects of marine complex lipid liposomes in small intestinal epithelial cell models. *Food Funct*, 7, 1904-14.
- DUMORTIER, G., GROSSIORD, J. L., AGNELY, F. & CHAUMEIL, J. C. 2006a. A Review of Poloxamer 407 Pharmaceutical and Pharmacological Characteristics. *Pharmaceutical Research*, 23, 2709-2728.
- DUMORTIER, G., GROSSIORD, J. L., AGNELY, F. & CHAUMEIL, J. C. 2006b. A review of poloxamer 407 pharmaceutical and pharmacological characteristics. *Pharm Res*, 23, 2709-28.
- DUTHEIL, F., JACOB, A., DAUCHY, S., BEAUNE, P., SCHERRMANN, J. M., DECLEVES, X. & LORIOT, M. A. 2010. ABC transporters and cytochromes P450 in the human central nervous system: influence on brain pharmacokinetics and contribution to neurodegenerative disorders. *Expert Opin Drug Metab Toxicol*, 6, 1161-74.
- FAN, J., FANG, G., WANG, X., ZENG, F., XIANG, Y. & WU, S. 2011. Targeted anticancer prodrug with mesoporous silica nanoparticles as vehicles. *Nanotechnology*, 22, 455102.
- FARGHALI, A., SWIDERSKA-SRODA, A., LOJKOWSKI, W., RAZIN, A.-F. M., KHEDR, M. & ABOUAITAH, K. E. 2016. pH-controlled Release System for Curcumin based on Functionalized Dendritic Mesoporous Silica Nanoparticles. *Journal of Nanomedicine & Nanotechnology*, 2016.
- FERON, F., PERRY, C., MCGRATH, J. J. & MACKAY-SIM, A. 1998. New techniques for biopsy and culture of human olfactory epithelial neurons. *Arch Otolaryngol Head Neck Surg*, 124, 861-6.
- FERRANDIZ, M. L. & ALCARAZ, M. J. 1991. Anti-inflammatory activity and inhibition of arachidonic acid metabolism by flavonoids. *Agents Actions*, 32, 283-8.
- FLEISHER, B., UNUM, J., SHAO, J. & AN, G. 2015. Ingredients in Fruit Juices Interact with Dasatinib Through Inhibition of BCRP: A New Mechanism of Beverage-Drug Interaction. *Journal of Pharmaceutical Sciences*, 104, 266-275.
- FOLTYNIE, T., BRAYNE, C. E., ROBBINS, T. W. & BARKER, R. A. 2004. The cognitive ability of an incident cohort of Parkinson's patients in the UK. The CamPaIGN study. *Brain*, 127, 550-60.

- FOO, M. Y., CHENG, Y. S., SU, W. C. & DONOVAN, M. D. 2007. The influence of spray properties on intranasal deposition. *J Aerosol Med*, 20, 495-508.
- FOOD, U. & ADMINISTRATION, D. 2002. Guidance for industry: Nasal spray and inhalation solution, suspension, and spray drug products—Chemistry, manufacturing, and controls documentation. *Fed. Regist*, 1-49.
- FRANSON, N. M. & PEPPAS, N. A. 1983. Influence of copolymer composition on non-fickian water transport through glassy copolymers. *Journal of Applied Polymer Science*, 28, 1299-1310.
- FREY, W. H. 1997a. *Method for administering neurologic agents to the brain*.
- FREY, W. H. 1997b. *Neurologic agents for nasal administration to the brain*. WO1991007947 A1.
- FREY, W. H. 2001. *Method for administering insulin to the brain*.
- GANGULI, M., CHANDRA, V., KAMBOH, M. I., JOHNSTON, J. M., DODGE, H. H., THELMA, B. K., JUJAL, R. C., PANDAV, R., BELLE, S. H. & DEKOSKY, S. T. 2000. Apolipoprotein E polymorphism and Alzheimer disease: The Indo-US Cross-National Dementia Study. *Arch Neurol*, 57, 824-30.
- GERION, D., HERBERG, J., BOK, R., GJERSING, E., RAMON, E., MAXWELL, R., KURHANEWICZ, J., BUDINGER, T. F., GRAY, J. W., SHUMAN, M. A. & CHEN, F. F. 2007. Paramagnetic Silica-Coated Nanocrystals as an Advanced MRI Contrast Agent. *The Journal of Physical Chemistry C*, 111, 12542-12551.
- GIZURARSON, S. 1990. Animal models for intranasal drug delivery studies. A review article. *Acta Pharm Nord*, 2, 105-22.
- GIZURARSON, S. 2012. Anatomical and histological factors affecting intranasal drug and vaccine delivery. *Curr Drug Deliv*, 9, 566-82.
- GONG, C. Y., SHI, S., DONG, P. W., ZHENG, X. L., FU, S. Z., GUO, G., YANG, J. L., WEI, Y. Q. & QIAN, Z. Y. 2009. In vitro drug release behavior from a novel thermosensitive composite hydrogel based on Pluronic f127 and poly(ethylene glycol)-poly(ϵ -caprolactone)-poly(ethylene glycol) copolymer. *BMC Biotechnology*, 9, 1-13.
- GOVINDARAJAN, V. S. 1980. Turmeric - Chemistry, Technology, and Quality. *Crc Critical Reviews in Food Science and Nutrition*, 12, 199-301.
- GRADINARU, L. M., CIOBANU, C., VLAD, S., BERCEA, M. & POPA, M. 2012. Synthesis and rheology of thermoreversible polyurethane hydrogels. *Central European Journal of Chemistry*, 10, 1859-1866.
- GRAFF, C. L. & POLLACK, G. M. 2005. Functional evidence for P-glycoprotein at the nose-brain barrier. *Pharm Res*, 22, 86-93.
- GRELA, K. P., MARCINIAK, D. M. & PLUTA, J. 2014. Stability evaluation of thermosensitive drug carrier systems based on Pluronic F-127 polymer. *Acta Pol Pharm*, 71, 167-80.
- GROSS, E. A., SWENBERG, J. A., FIELDS, S. & POPP, J. A. 1982. Comparative morphometry of the nasal cavity in rats and mice. *J Anat*, 135, 83-8.
- GROSSMAN, J. 1994. The evolution of inhaler technology. *J Asthma*, 31, 55-64.
- GROUP, I. E. W. Validation of analytical procedures: text and methodology Q2 (R1). Proceedings of the International Conference on Harmonisation of Technical Requirements for Registration of Pharmaceuticals for Human Use, 2005. 25-27.
- GRÜN, M., LAUER, I. & UNGER, K. K. 1997. The synthesis of micrometer- and submicrometer-size spheres of ordered mesoporous oxide MCM-41. *Advanced Materials*, 9, 254-257.
- GUIDELINE, I. H. T. 2005. Validation of analytical procedures: text and methodology. *Q2 (R1)*, 1.
- GULFAM, M. & CHUNG, B. G. 2014. Development of pH-Responsive Chitosan-Coated Mesoporous Silica Nanoparticles. *Macromolecular Research*, 22, 412-417.
- GUO, Y., LAUBE, B. & DALBY, R. 2005. The effect of formulation variables and breathing patterns on the site of nasal deposition in an anatomically correct model. *Pharm Res*, 22, 1871-8.
- GUPTA, N. K. & DIXIT, V. K. 2011a. Bioavailability enhancement of curcumin by complexation with phosphatidyl choline. *J Pharm Sci*, 100, 1987-95.
- GUPTA, N. K. & DIXIT, V. K. 2011b. Development and evaluation of vesicular system for curcumin delivery. *Arch Dermatol Res*, 303, 89-101.
- GUPTA, V., ASEH, A., RIOS, C. N., AGGARWAL, B. B. & MATHUR, A. B. 2009. Fabrication and characterization of silk fibroin-derived curcumin nanoparticles for cancer therapy. *Int J Nanomedicine*, 4, 115-22.

- HAGERSTROM, H. & EDSMAN, K. 2003. Limitations of the rheological mucoadhesion method: The effect of the choice of conditions and the rheological synergism parameter. *European Journal of Pharmaceutical Sciences*, 18, 349-357.
- HAO, N., JAYAWARDANA, K. W., CHEN, X. & YAN, M. 2015. One-step synthesis of amine-functionalized hollow mesoporous silica nanoparticles as efficient antibacterial and anticancer materials. *ACS applied materials & interfaces*, 7, 1040-1045.
- HARDY, J. G., LEE, S. W. & WILSON, C. G. 1985. Intranasal drug delivery by spray and drops. *J Pharm Pharmacol*, 37, 294-7.
- HARRIS, A. S., NILSSON, I. M., WAGNER, Z. G. & ALKNER, U. 1986. Intranasal administration of peptides: nasal deposition, biological response, and absorption of desmopressin. *J Pharm Sci*, 75, 1085-8.
- HATCH, T. F. 1961a. Distribution and deposition of inhaled particles in respiratory tract. *Bacteriol Rev*, 25, 237-40.
- HATCH, T. F. 1961b. Distribution and deposition of the inhaled particles in respiratory tract. *Bacteriological Reviews*, 25, 237-240.
- HE, Q., ZHANG, J., SHI, J., ZHU, Z., ZHANG, L., BU, W., GUO, L. & CHEN, Y. 2010. The effect of PEGylation of mesoporous silica nanoparticles on nonspecific binding of serum proteins and cellular responses. *Biomaterials*, 31, 1085-1092.
- HE, Q. J. & SHI, J. L. 2011. Mesoporous silica nanoparticle based nano drug delivery systems: synthesis, controlled drug release and delivery, pharmacokinetics and biocompatibility. *Journal of Materials Chemistry*, 21, 5845-5855.
- HE, Q. J., ZHANG, Z. W., GAO, Y., SHI, J. L. & LI, Y. P. 2009. Intracellular Localization and Cytotoxicity of Spherical Mesoporous Silica Nano- and Microparticles. *Small*, 5, 2722-2729.
- HE, X. L., WANG, Y. H., BI, M. G. & DU, G. H. 2012. Chrysin improves cognitive deficits and brain damage induced by chronic cerebral hypoperfusion in rats. *European Journal of Pharmacology*, 680, 41-48.
- HEIM, K. E., TAGLIAFERRO, A. R. & BOBILYA, D. J. 2002. Flavonoid antioxidants: chemistry, metabolism and structure-activity relationships. *J Nutr Biochem*, 13, 572-584.
- HERTOG, M. G. L., HOLLMAN, P. C. H. & VANDEPUTTE, B. 1993. Content of Potentially Anticarcinogenic Flavonoids of Tea Infusions, Wines, and Fruit Juices. *Journal of Agricultural and Food Chemistry*, 41, 1242-1246.
- HESS, D. R. 2005. Metered-dose inhalers and dry powder inhalers in aerosol therapy. *Respir Care*, 50, 1376-83.
- HJ, F. 1966. Irreversible Thermodynamics of Internally Relaxing Systems in the Vicinity of the Glass Transition. In: DENNELLY RJ, H. R. A. P. I. (ed.) *Non-Equilibrium Thermodynamics, Variational Techniques, and Stability*. University of Chicago Press.
- HODAEI, D., BARADARAN, B., VALIZADEH, H. & ZAKERI-MILANI, P. 2015. Effects of polyethylene glycols on intestinal efflux pump expression and activity in Caco-2 cells. *Brazilian Journal of Pharmaceutical Sciences*, 51, 745-753.
- HOPFENBERG, H. 1974. Super case II transport of organic vapors in glassy polymers. In: HB, H. (ed.) *Permeability of plastic films and coatings to gases, vapors, and liquids*. New York: Plenum Press.
- HORCAJADA, P., RÁMILA, A., PÉREZ-PARIENTE, J., VALLET, R., AMP, X & M. 2004. Influence of pore size of MCM-41 matrices on drug delivery rate. *Microporous and Mesoporous Materials*, 68, 105-109.
- HORVAT, S., FEHER, A., WOLBURG, H., SIPOS, P., VESZELKA, S., TOTH, A., KIS, L., KURUNCZI, A., BALOGH, G., KURTI, L., EROS, I., SZABO-REVESZ, P. & DELI, M. A. 2009. Sodium hyaluronate as a mucoadhesive component in nasal formulation enhances delivery of molecules to brain tissue. *Eur J Pharm Biopharm*, 72, 252-9.
- HOSNY, K. M. & BANJAR, Z. M. 2013. The formulation of a nasal nanoemulsion zaleplon in situ gel for the treatment of insomnia. *Expert Opin Drug Deliv*, 10, 1033-41.
- HOSNY, K. M. & HASSAN, A. H. 2014. Intranasal in situ gel loaded with saquinavir mesylate nanosized microemulsion: preparation, characterization, and in vivo evaluation. *Int J Pharm*, 475, 191-7.
- HU, Y., WANG, J., ZHI, Z., JIANG, T. & WANG, S. 2011. Facile synthesis of 3D cubic mesoporous silica microspheres with a controllable pore size and their application for improved delivery of a water-insoluble drug. *J Colloid Interface Sci*, 363, 410-7.

- HU, Y., ZHI, Z., ZHAO, Q., WU, C., ZHAO, P., JIANG, H., JIANG, T. & WANG, S. 2012. 3D cubic mesoporous silica microsphere as a carrier for poorly soluble drug carvedilol. *Microporous and Mesoporous Materials*, 147, 94-101.
- HUANG, D. M., HUNG, Y., KO, B. S., HSU, S. C., CHEN, W. H., CHIEN, C. L., TSAI, C. P., KUO, C. T., KANG, J. C., YANG, C. S., MOU, C. Y. & CHEN, Y. C. 2005. Highly efficient cellular labeling of mesoporous nanoparticles in human mesenchymal stem cells: implication for stem cell tracking. *Faseb Journal*, 19, 2014-+.
- HUANG, X. L., TENG, X., CHEN, D., TANG, F. Q. & HE, J. Q. 2010. The effect of the shape of mesoporous silica nanoparticles on cellular uptake and cell function. *Biomaterials*, 31, 438-448.
- HUANG, X. Y., YOUNG, N. P. & TOWNLEY, H. E. 2014. Characterization and Comparison of Mesoporous Silica Particles for Optimized Drug Delivery. *Nanomaterials and Nanotechnology*, 4.
- HUDSON, S. P., PADERA, R. F., LANGER, R. & KOHANE, D. S. 2008. The biocompatibility of mesoporous silicates. *Biomaterials*, 29, 4045-55.
- HUH, S., WIENCH, J. W., YOO, J.-C., PRUSKI, M. & LIN, V. S. Y. 2003. Organic Functionalization and Morphology Control of Mesoporous Silicas via a Co-Condensation Synthesis Method. *Chemistry of Materials*, 15, 4247-4256.
- HUO, C., OUYANG, J. & YANG, H. 2014. CuO nanoparticles encapsulated inside Al-MCM-41 mesoporous materials via direct synthetic route. *Scientific Reports*, 4, 3682.
- HUO, Q., FENG, J., SCHÜTH, F. & STUCKY, G. D. 1997. Preparation of Hard Mesoporous Silica Spheres. *Chemistry of Materials*, 9, 14-17.
- HUSSAIN, A. A. & DITTERT, L. W. 2001. Intranasal administration of raloxifene and tamoxifen. Google Patents.
- IBRAHIM, H. K., ABDEL MALAK, N. S. & ABDEL HALIM, S. A. 2015. Formulation of Convenient, Easily Scalable, and Efficient Granisetron HCl Intranasal Droppable Gels. *Mol Pharm*, 12, 2019-25.
- IKECHUKWU UGWOKE, M., KAUFMANN, G., VERBEKE, N. & KINGET, R. 2000. Intranasal bioavailability of apomorphine from carboxymethylcellulose-based drug delivery systems. *Int J Pharm*, 202, 125-31.
- IKECHUKWU UGWOKE, M., SAM, E., VAN DEN MOOTER, G., VERBEKE, N. & KINGET, R. 1999. Nasal mucoadhesive delivery systems of the anti-parkinsonian drug, apomorphine: influence of drug-loading on in vitro and in vivo release in rabbits. *Int J Pharm*, 181, 125-38.
- ILLUM, L. 2000. Transport of drugs from the nasal cavity to the central nervous system. *Eur J Pharm Sci*, 11, 1-18.
- ILLUM, L. 2003. Nasal drug delivery--possibilities, problems and solutions. *J Control Release*, 87, 187-98.
- ILLUM, L. 2012. Nasal drug delivery - recent developments and future prospects. *J Control Release*, 161, 254-63.
- ILLUM, L. & DAVIS, S. S. 1992. Intranasal insulin. Clinical pharmacokinetics. *Clin Pharmacokinet*, 23, 30-41.
- ISLAM, M. T., RODRIGUEZ-HORNEDO, N., CIOTTI, S. & ACKERMANN, C. 2004. Rheological characterization of topical carbomer gels neutralized to different pH. *Pharm Res*, 21, 1192-9.
- IVARSSON, D. & WAHLGREN, M. 2012. Comparison of in vitro methods of measuring mucoadhesion: ellipsometry, tensile strength and rheological measurements. *Colloids Surf B Biointerfaces*, 92, 353-9.
- J, C. 1967. *The mathematics of diffusion*, Oxford, Clarendon Press.
- JAIN, A. K., KHAR, R. K., AHMED, F. J. & DIWAN, P. V. 2008. Effective insulin delivery using starch nanoparticles as a potential trans-nasal mucoadhesive carrier. *Eur J Pharm Biopharm*, 69, 426-35.
- JAIN, R., NABAR, S., DANDEKAR, P. & PATRAVALE, V. 2010. Micellar nanocarriers: potential nose-to-brain delivery of zolmitriptan as novel migraine therapy. *Pharm Res*, 27, 655-64.
- JAMBHRUNKAR, S., KARMAKAR, S., POPAT, A., YU, M. H. & YU, C. Z. 2014. Mesoporous silica nanoparticles enhance the cytotoxicity of curcumin. *Rsc Advances*, 4, 709-712.
- JEONG, B., KIM, S. W. & BAE, Y. H. 2002. Thermosensitive sol-gel reversible hydrogels. *Adv Drug Deliv Rev*, 54, 37-51.
- JIA, W. Z., ZHAO, J. C., SUN, X. L., YAO, Z. G., WU, H. L. & XI, Z. Q. 2015. Additive anticancer effects of chrysin and low dose cisplatin in human malignant glioma cell (U87) proliferation and evaluation of the mechanistic pathway. *J BUON*, 20, 1327-36.
- JOGANI, V., JINTURKAR, K., VYAS, T. & MISRA, A. 2008. Recent patents review on intranasal administration for CNS drug delivery. *Recent Pat Drug Deliv Formul*, 2, 25-40.

- JOGANI, V. V., SHAH, P. J., MISHRA, P., MISHRA, A. K. & MISRA, A. R. 2007. Nose-to-brain delivery of tacrine. *J Pharm Pharmacol*, 59, 1199-205.
- JONES, D. S., BRUSCHI, M. L., DE FREITAS, O., GREMIAO, M. P., LARA, E. H. & ANDREWS, G. P. 2009. Rheological, mechanical and mucoadhesive properties of thermoresponsive, bioadhesive binary mixtures composed of poloxamer 407 and carbopol 974P designed as platforms for implantable drug delivery systems for use in the oral cavity. *Int J Pharm*, 372, 49-58.
- JUNGHANNS, J. U. & MULLER, R. H. 2008. Nanocrystal technology, drug delivery and clinical applications. *Int J Nanomedicine*, 3, 295-309.
- KABANOV, A. V., BATRAKOVA, E. V. & ALAKHOV, V. Y. 2002. Pluronic block copolymers as novel polymer therapeutics for drug and gene delivery. *Abstracts of Papers of the American Chemical Society*, 223, U438-U438.
- KAELBLE, D. H. & MOACANIN, J. 1977. Structure and Properties of Biopolymers A surface energy analysis of bioadhesion. *Polymer*, 18, 475-482.
- KANDIMALLA, K. K. & DONOVAN, M. D. 2005. Localization and differential activity of P-glycoprotein in the bovine olfactory and nasal respiratory mucosae. *Pharm Res*, 22, 1121-8.
- KATAYAMA, K., MASUYAMA, K., YOSHIOKA, S., HASEGAWA, H., MITSUHASHI, J. & SUGIMOTO, Y. 2007. Flavonoids inhibit breast cancer resistance protein-mediated drug resistance: transporter specificity and structure-activity relationship. *Cancer Chemother Pharmacol*, 60, 789-97.
- KATZ, L. C., BURKHALTER, A. & DREYER, W. J. 1984. Fluorescent latex microspheres as a retrograde neuronal marker for in vivo and in vitro studies of visual cortex. *Nature*, 310, 498-500.
- KATZ, L. C. & IAROVICI, D. M. 1990. Green fluorescent latex microspheres: A new retrograde tracer. *Neuroscience*, 34, 511-520.
- KAUR, M. 2016. *Phytochemical Mediated Modulation Of Breast Cancer Resistance Protein At The Blood Brain Barrier And Blood Cerebrospinal Fluid Barrier*. Ph.D., Aston University.
- KERN, W., BORN, J., SCHREIBER, H. & FEHM, H. L. 1999. Central nervous system effects of intranasally administered insulin during euglycemia in men. *Diabetes*, 48, 557-63.
- KHAFAGY EL, S., MORISHITA, M., ONUKI, Y. & TAKAYAMA, K. 2007. Current challenges in non-invasive insulin delivery systems: a comparative review. *Adv Drug Deliv Rev*, 59, 1521-46.
- KHAN, M. A., AKHTAR, N., SHARMA, V. & PATHAK, K. 2015. Product development studies on sonocrystallized curcumin for the treatment of gastric cancer. *Pharmaceutics*, 7, 43-63.
- KHARE, A. R. & PEPPAS, N. A. 1995. Swelling/deswelling of anionic copolymer gels. *Biomaterials*, 16, 559-567.
- KHATTAK, S. F., BHATIA, S. R. & ROBERTS, S. C. 2005. Pluronic F127 as a cell encapsulation material: Utilization of membrane-stabilizing agents. *Tissue Engineering*, 11, 974-983.
- KHUTORYANSKIY, V. V. 2011a. Advances in Mucoadhesion and Mucoadhesive Polymers. *Macromolecular Bioscience*, 11, 748-764.
- KHUTORYANSKIY, V. V. 2011b. Advances in mucoadhesion and mucoadhesive polymers. *Macromol Biosci*, 11, 748-64.
- KIM, E. Y., GAO, Z. G., PARK, J. S., LI, H. & HAN, K. 2002. rhEGF/HP-beta-CD complex in poloxamer gel for ophthalmic delivery. *Int J Pharm*, 233, 159-67.
- KIM, H. & FASSIHI, R. 1997. A new ternary polymeric matrix system for controlled drug delivery of highly soluble drugs: I. Diltiazem hydrochloride. *Pharm Res*, 14, 1415-21.
- KIM, J., KIM, H. S., LEE, N., KIM, T., KIM, H., YU, T., SONG, I. C., MOON, W. K. & HYEON, T. 2008. Multifunctional Uniform Nanoparticles Composed of a Magnetite Nanocrystal Core and a Mesoporous Silica Shell for Magnetic Resonance and Fluorescence Imaging and for Drug Delivery. *Angewandte Chemie*, 120, 8566-8569.
- KIM, J. A., ÅBERG, C., SALVATI, A. & DAWSON, K. A. 2012. Role of cell cycle on the cellular uptake and dilution of nanoparticles in a cell population. *Nature nanotechnology*, 7, 62-68.
- KIM, S., PHILIPPOT, S., FONTANAY, S., DUVAL, R. E., LAMOUREUX, E., CANILHO, N. & PASC, A. 2015. pH- and glutathione-responsive release of curcumin from mesoporous silica nanoparticles coated using tannic acid-Fe(III) complex. *RSC Advances*, 5, 90550-90558.
- KIMBELL, J. S., SEGAL, R. A., ASGHARIAN, B., WONG, B. A., SCHROETER, J. D., SOUTHALL, J. P., DICKENS, C. J., BRACE, G. & MILLER, F. J. 2007. Characterization of deposition from nasal spray

- devices using a computational fluid dynamics model of the human nasal passages. *J Aerosol Med*, 20, 59-74.
- KIPEN, H. M. & LASKIN, D. L. 2005. Smaller is not always better: nanotechnology yields nanotoxicology. *American Journal of Physiology-Lung Cellular and Molecular Physiology*, 289, L696-L697.
- KLECH, C. M. & SIMONELLI, A. P. 1989. Examination of the moving boundaries associated with non-fickian water swelling of glassy gelatin beads: Effect of solution pH. *Journal of Membrane Science*, 43, 87-101.
- KLECH, C. M. S., A.P. 1989. Examination of the moving boundaries associated with non-fickian water swelling of glassy gelatin beads: Effect of solution pH. *Journal of Membrane Science*, 43, 87-101.
- KLOUDA, L. & MIKOS, A. G. 2008. Thermoresponsive hydrogels in biomedical applications. *European Journal of Pharmaceutics and Biopharmaceutics*, 68, 34-45.
- KOLA, I. & LANDIS, J. 2004. Can the pharmaceutical industry reduce attrition rates? *Nat Rev Drug Discov*, 3, 711-5.
- KONG, Y., MA, W., LIU, X., ZU, Y. G., FU, Y. J., WU, N., LIANG, L., YAO, L. P. & EFFERTH, T. 2009. Cytotoxic Activity of Curcumin towards CCRF-CEM Leukemia Cells and Its Effect on DNA Damage. *Molecules*, 14, 5328-5338.
- KORHONEN, M., NISKANEN, H., KIESVAARA, J. & YLIRUUSI, J. 2000. Determination of optimal combination of surfactants in creams using rheology measurements. *International Journal of Pharmaceutics*, 197, 143-151.
- KORSMEYER, R., GURNY, R., DOELKER, E., BURI, B., PEPPAS, N.A. 1983. Mechanisms of solute release from porous hydrophilic polymers. *International Journal of Pharmaceutics*, 15, 25-35.
- KOTSUCHIBASHI, Y., ZHANG, Y., AHMED, M., EBARA, M., AOYAGI, T. & NARAIN, R. 2013. Fabrication of FITC-doped silica nanoparticles and study of their cellular uptake in the presence of lectins. *J Biomed Mater Res A*, 101, 2090-6.
- KRAUSZ, A. E., ADLER, B. L., CABRAL, V., NAVATI, M., DOERNER, J., CHARAFEDDINE, R. A., CHANDRA, D., LIANG, H., GUNTHER, L., CLENDANIEL, A., HARPER, S., FRIEDMAN, J. M., NOSANCHUK, J. D. & FRIEDMAN, A. J. 2015. Curcumin-encapsulated nanoparticles as innovative antimicrobial and wound healing agent. *Nanomedicine: Nanotechnology, Biology and Medicine*, 11, 195-206.
- KREFT, M. E., JERMAN, U. D., LASIC, E., LANISNIK RIZNER, T., HEVIR-KENE, N., PETERNEL, L. & KRISTAN, K. 2015. The characterization of the human nasal epithelial cell line RPMI 2650 under different culture conditions and their optimization for an appropriate in vitro nasal model. *Pharm Res*, 32, 665-79.
- KRESGE, C., LEONOWICZ, M., ROTH, W., VARTULI, J. & BECK, J. 1992a. Ordered mesoporous molecular sieves synthesized by a liquid-crystal template mechanism. *nature*, 359, 710-712.
- KRESGE, C. T., LEONOWICZ, M. E., ROTH, W. J., VARTULI, J. C. & BECK, J. S. 1992b. Ordered Mesoporous Molecular-Sieves Synthesized by a Liquid-Crystal Template Mechanism. *Nature*, 359, 710-712.
- KRISTENSSON, K. & OLSSON, Y. 1971. Uptake of exogenous proteins in mouse olfactory cells. *Acta Neuropathol*, 19, 145-54.
- KUMAR, A., GARG, T., SARMA, G. S., RATH, G. & GOYAL, A. K. 2015. Optimization of combinational intranasal drug delivery system for the management of migraine by using statistical design. *Eur J Pharm Sci*, 70, 140-51.
- KUMAR, M., MISRA, A., BABBAR, A. K., MISHRA, A. K., MISHRA, P. & PATHAK, K. 2008. Intranasal nanoemulsion based brain targeting drug delivery system of risperidone. *Int J Pharm*, 358, 285-91.
- KUMARI, A., SHARMA, N., SHARMA, P. K. & GOYAL, N. 2012. Rheological evaluation of thermoreversible and mucoadhesive nasal gels of Zolmitriptan. *Eur Rev Med Pharmacol Sci*, 16, 1022-7.
- KUNDOOR, V. & DALBY, R. N. 2010. Assessment of nasal spray deposition pattern in a silicone human nose model using a color-based method. *Pharm Res*, 27, 30-6.
- KUNDOOR, V. & DALBY, R. N. 2011. Effect of formulation- and administration-related variables on deposition pattern of nasal spray pumps evaluated using a nasal cast. *Pharm Res*, 28, 1895-904.

- KUNNUMAKKARA, A. B., ANAND, P. & AGGARWAL, B. B. 2008. Curcumin inhibits proliferation, invasion, angiogenesis and metastasis of different cancers through interaction with multiple cell signaling proteins. *Cancer Lett*, 269, 199-225.
- KURTI, L., VESZELKA, S., BOCSIK, A., OZSVARI, B., PUSKAS, L. G., KITTEL, A., SZABO-REVESZ, P. & DELI, M. A. 2013. Retinoic acid and hydrocortisone strengthen the barrier function of human RPMI 2650 cells, a model for nasal epithelial permeability. *Cytotechnology*, 65, 395-406.
- LAVORINI, F. 2013. The challenge of delivering therapeutic aerosols to asthma patients. *ISRN Allergy*, 2013, 102418.
- LEE, C.-H., LO, L.-W., MOU, C.-Y. & YANG, C.-S. 2008. Synthesis and Characterization of Positive-Charge Functionalized Mesoporous Silica Nanoparticles for Oral Drug Delivery of an Anti-Inflammatory Drug. *Advanced Functional Materials*, 18, 3283-3292.
- LEE, J. S., LEE, S. U., CHE, C. Y. & LEE, J. E. 2015. Comparison of cytotoxicity and wound healing effect of carboxymethylcellulose and hyaluronic acid on human corneal epithelial cells. *Int J Ophthalmol*, 8, 215-21.
- LEE, J. W., PARK, J. H. & ROBINSON, J. R. 2000. Bioadhesive-based dosage forms: the next generation. *J Pharm Sci*, 89, 850-66.
- LEE, W. H., LOO, C. Y., BEBAWY, M., LUK, F., MASON, R. S. & ROHANIZADEH, R. 2013. Curcumin and its derivatives: their application in neuropharmacology and neuroscience in the 21st century. *Curr Neuropharmacol*, 11, 338-78.
- LEE, W. H., LOO, C. Y., YOUNG, P. M., TRAINI, D., MASON, R. S. & ROHANIZADEH, R. 2014. Recent advances in curcumin nanoformulation for cancer therapy. *Expert Opinion on Drug Delivery*, 11, 1183-1201.
- LEHR, C.-M., BOUWSTRA, J. A., SCHACHT, E. H. & JUNGINGER, H. E. 1992. In vitro evaluation of mucoadhesive properties of chitosan and some other natural polymers. *International Journal of Pharmaceutics*, 78, 43-48.
- LEONARD, A. K., SILENO, A. P., BRANDT, G. C., FOERDER, C. A., QUAY, S. C. & COSTANTINO, H. R. 2007. In vitro formulation optimization of intranasal galantamine leading to enhanced bioavailability and reduced emetic response in vivo. *Int J Pharm*, 335, 138-46.
- LEOPOLD, D. A., HUMMEL, T., SCHWOB, J. E., HONG, S. C., KNECHT, M. & KOBAL, G. 2000. Anterior distribution of human olfactory epithelium. *Laryngoscope*, 110, 417-21.
- LEOPOLD, N. A. & KAGEL, M. C. 1997. Pharyngo-esophageal dysphagia in Parkinson's disease. *Dysphagia*, 12, 11-8; discussion 19-20.
- LEUNG, C. T., COULOMBE, P. A. & REED, R. R. 2007. Contribution of olfactory neural stem cells to tissue maintenance and regeneration. *Nat Neurosci*, 10, 720-6.
- LI, C., LI, C., LIU, Z., LI, Q., YAN, X., LIU, Y. & LU, W. 2014. Enhancement in bioavailability of ketorolac tromethamine via intranasal in situ hydrogel based on poloxamer 407 and carrageenan. *Int J Pharm*, 474, 123-33.
- LI, J., JIANG, Y., WEN, J., FAN, G., WU, Y. & ZHANG, C. 2009. A rapid and simple HPLC method for the determination of curcumin in rat plasma: assay development, validation and application to a pharmacokinetic study of curcumin liposome. *Biomedical Chromatography*, 23, 1201-1207.
- LI, X., KONG, X., WANG, X., SHI, S., GUO, G., LUO, F., ZHAO, X., WEI, Y. & QIAN, Z. 2010. Gel-sol-gel thermo-gelation behavior study of chitosan-inorganic phosphate solutions. *Eur J Pharm Biopharm*, 75, 388-92.
- LIAO, Y.-T., LIU, C.-H., YU, J. & WU, K. C. 2014. Liver cancer cells: targeting and prolonged-release drug carriers consisting of mesoporous silica nanoparticles and alginate microspheres. *International journal of nanomedicine*, 9, 2767.
- LIN, W.-J., WANG, C.-L. & JUANG, L.-W. 2006a. Characterization and comparison of diblock and triblock amphiphilic copolymers of poly(δ -valerolactone). *Journal of Applied Polymer Science*, 100, 1836-1841.
- LIN, W., HUANG, Y.-W., ZHOU, X.-D. & MA, Y. 2006b. In vitro toxicity of silica nanoparticles in human lung cancer cells. *Toxicology and applied pharmacology*, 217, 252-259.
- LIN, W. C., YU, D. G. & YANG, M. C. 2005. pH-sensitive polyelectrolyte complex gel microspheres composed of chitosan/sodium tripolyphosphate/dextran sulfate: swelling kinetics and drug delivery properties. *Colloids Surf B Biointerfaces*, 44, 143-51.

- LINDEMANN, J., KUHNEMANN, S., STEHMER, V., LEIACKER, R., RETTINGER, G. & KECK, T. 2001. Temperature and humidity profile of the anterior nasal airways of patients with nasal septal perforation. *Rhinology*, 39, 202-6.
- LIONG, M., LU, J., KOVOCHICH, M., XIA, T., RUEHM, S. G., NEL, A. E., TAMANOI, F. & ZINK, J. I. 2008. Multifunctional inorganic nanoparticles for imaging, targeting, and drug delivery. *ACS Nano*, 2, 889-96.
- LIPINSKI, C. A. 2000. Drug-like properties and the causes of poor solubility and poor permeability. *J Pharmacol Toxicol Methods*, 44, 235-49.
- LIPINSKI, C. A. 2002. Poor aqueous solubility-an industry wide problem in ADME screening. *American Pharmaceutical Review*, 5, 82-85.
- LIU, Q., SHEN, Y., CHEN, J., GAO, X., FENG, C., WANG, L., ZHANG, Q. & JIANG, X. 2012. Nose-to-brain transport pathways of wheat germ agglutinin conjugated PEG-PLA nanoparticles. *Pharm Res*, 29, 546-58.
- LIU, Z., JIANG, M., KANG, T., MIAO, D., GU, G., SONG, Q., YAO, L., HU, Q., TU, Y., PANG, Z., CHEN, H., JIANG, X., GAO, X. & CHEN, J. 2013. Lactoferrin-modified PEG-co-PCL nanoparticles for enhanced brain delivery of NAP peptide following intranasal administration. *Biomaterials*, 34, 3870-81.
- LOCHHEAD, J. J. & THORNE, R. G. 2012. Intranasal delivery of biologics to the central nervous system. *Adv Drug Deliv Rev*, 64, 614-28.
- LONG, F. A. & RICHMAN, D. 1960. Concentration Gradients for Diffusion of Vapors in Glassy Polymers and their Relation to Time Dependent Diffusion Phenomena^{1,2}. *Journal of the American Chemical Society*, 82, 513-519.
- LÖVESTAM, G., RAUSCHER, H., ROEBBEN, G., KLÜTTGEN, B. S., GIBSON, N., PUTAUD, J.-P. & STAMM, H. 2010. Considerations on a definition of nanomaterial for regulatory purposes. *Joint Research Centre (JRC) Reference Reports*, 80004-1.
- LU, X., QIAN, J., ZHOU, H., GAN, Q., TANG, W., LU, J., YUAN, Y. & LIU, C. 2011. In vitro cytotoxicity and induction of apoptosis by silica nanoparticles in human HepG2 hepatoma cells. *Int J Nanomedicine*, 6, 1889-1901.
- LUESSEN, H. L., DE LEEUW, B. J., LANGEMEYER, M. W., DE BOER, A. B., VERHOEF, J. C. & JUNGINGER, H. E. 1996. Mucoadhesive polymers in peroral peptide drug delivery. VI. Carbomer and chitosan improve the intestinal absorption of the peptide drug busserelin in vivo. *Pharm Res*, 13, 1668-72.
- LUNGARE, S., BOWEN, J. & BADHAN, R. 2016. Development and Evaluation of a Novel Intranasal Spray for the Delivery of Amantadine. *J Pharm Sci*, 105, 1209-20.
- LV, P. P., WEI, W., YUE, H., YANG, T. Y., WANG, L. Y. & MA, G. H. 2011. Porous quaternized chitosan nanoparticles containing paclitaxel nanocrystals improved therapeutic efficacy in non-small-cell lung cancer after oral administration. *Biomacromolecules*, 12, 4230-9.
- MA'MANI, L., NIKZAD, S., KHEIRI-MANJILI, H., AL-MUSAWI, S., SAEEDI, M., ASKARLOU, S., FOROUMADI, A. & SHAFIEE, A. 2014. Curcumin-loaded guanidine functionalized PEGylated I3ad mesoporous silica nanoparticles KIT-6: Practical strategy for the breast cancer therapy. *European Journal of Medicinal Chemistry*, 83, 646-654.
- MACKAY-SIM, A. & KITTEL, P. 1991. Cell dynamics in the adult mouse olfactory epithelium: a quantitative autoradiographic study. *J Neurosci*, 11, 979-84.
- MACREADY, A. L., KENNEDY, O. B., ELLIS, J. A., WILLIAMS, C. M., SPENCER, J. P. & BUTLER, L. T. 2009. Flavonoids and cognitive function: a review of human randomized controlled trial studies and recommendations for future studies. *Genes Nutr*, 4, 227-42.
- MADSEN, F., EBERTH, K. & SMART, J. D. 1998. A rheological assessment of the nature of interactions between mucoadhesive polymers and a homogenised mucus gel. *Biomaterials*, 19, 1083-92.
- MAHMOUDIAN, T. & ZADEH, M. M. 2004. Comparison of intranasal midazolam with intravenous diazepam for treating acute seizures in children. *Epilepsy Behav*, 5, 253-5.
- MAJITHIYA, R. J., GHOSH, P. K., UMRETHIA, M. L. & MURTHY, R. S. 2006. Thermoreversible-mucoadhesive gel for nasal delivery of sumatriptan. *AAPS PharmSciTech*, 7, 67.
- MALMSTEN, M. & LINDMAN, B. 1993. Effects of homopolymers on the gel formation in aqueous block copolymer solutions. *Macromolecules*, 26, 1282-1286.
- MANNO, E. M. 2011. Status epilepticus: current treatment strategies. *Neurohospitalist*, 1, 23-31.

- MANZINI, I. & SCHILD, D. 2003. Multidrug resistance transporters in the olfactory receptor neurons of *Xenopus laevis* tadpoles. *J Physiol*, 546, 375-85.
- MARTIN-LOPEZ, E., ALONSO, F. R., NIETO-DIAZ, M. & NIETO-SAMPEDRO, M. 2012. Chitosan, gelatin and poly(L-lysine) polyelectrolyte-based scaffolds and films for neural tissue engineering. *J Biomater Sci Polym Ed*, 23, 207-32.
- MARTINAC, A., FILIPOVIC-GRCIC, J., VOINOVICH, D., PERISSUTTI, B. & FRANCESCHINIS, E. 2005. Development and bioadhesive properties of chitosan-ethylcellulose microspheres for nasal delivery. *Int J Pharm*, 291, 69-77.
- MARZAIOLI, V., AGUILAR-PIMENTEL, J. A., WEICHENMEIER, I., LUXENHOFER, G., WIEMANN, M., LANDSIEDEL, R., WOHLLEBEN, W., EIDEN, S., MEMPEL, M. & BEHRENDT, H. 2014. Surface modifications of silica nanoparticles are crucial for their inert versus proinflammatory and immunomodulatory properties. *Int J Nanomed*, 9, 2815-2832.
- MATHISON, S., NAGILLA, R. & KOMPPELLA, U. B. 1998a. Nasal route for direct delivery of solutes to the central nervous system: Fact or fiction? *Journal of Drug Targeting*, 5, 415-441.
- MATHISON, S., NAGILLA, R. & KOMPPELLA, U. B. 1998b. Nasal route for direct delivery of solutes to the central nervous system: fact or fiction? *J Drug Target*, 5, 415-41.
- MAYOR, S. & PAGANO, R. E. 2007. Pathways of clathrin-independent endocytosis. *Nature Reviews Molecular Cell Biology*, 8, 603-612.
- MCMARTIN, C., HUTCHINSON, L. E., HYDE, R. & PETERS, G. E. 1987. Analysis of structural requirements for the absorption of drugs and macromolecules from the nasal cavity. *J Pharm Sci*, 76, 535-40.
- MECOCCI, P., TINARELLI, C., SCHULZ, R. J. & POLIDORI, M. C. 2014. Nutraceuticals in cognitive impairment and Alzheimer's disease. *Front Pharmacol*, 5, 147.
- MEDINA, J. H., PALADINI, A. C., WOLFMAN, C., DE STEIN, M. L., CALVO, D., DIAZ, L. E. & PEÑA, C. 1990. Chrysin (5,7-di-OH-flavone), a naturally-occurring ligand for benzodiazepine receptors, with anticonvulsant properties. *Biochemical Pharmacology*, 40, 2227-2231.
- MENG, X., MUNISHKINA, L. A., FINK, A. L. & UVERSKY, V. N. 2009. Molecular mechanisms underlying the flavonoid-induced inhibition of alpha-synuclein fibrillation. *Biochemistry*, 48, 8206-24.
- MERCER, L. D., KELLY, B. L., HORNE, M. K. & BEART, P. M. 2005. Dietary polyphenols protect dopamine neurons from oxidative insults and apoptosis: investigations in primary rat mesencephalic cultures. *Biochem Pharmacol*, 69, 339-45.
- MIKOS, A. G. & PEPPAS, N. A. 1990. Bioadhesive analysis of controlled-release systems. IV. An experimental method for testing the adhesion of microparticles with mucus. *Journal of Controlled Release*, 12, 31-37.
- MILLER, S. C. & DRABIK, B. R. 1984. Rheological properties of poloxamer vehicles. *International Journal of Pharmaceutics*, 18, 269-276.
- MISTRY, A., STOLNIK, S. & ILLUM, L. 2009. Nanoparticles for direct nose-to-brain delivery of drugs. *International Journal of Pharmaceutics*, 379, 146-157.
- MITTAL, P., MANOHAR, R. & RAWAT, A. K. 2006. Comparative study of intranasal midazolam and intravenous diazepam sedation for procedures and seizures. *Indian J Pediatr*, 73, 975-8.
- MOHSENI, M., GILANI, K. & MORTAZAVI, S. A. 2015. Preparation and characterization of rifampin loaded mesoporous silica nanoparticles as a potential system for pulmonary drug delivery. *Iran J Pharm Res*, 14, 27-34.
- MOLINAS, A., SICARD, G. & JAKOB, I. 2012. Functional evidence of multidrug resistance transporters (MDR) in rodent olfactory epithelium. *PLoS One*, 7, e36167.
- MOLL, R., KREPLER, R. & FRANKE, W. W. 1983. Complex cytokeratin polypeptide patterns observed in certain human carcinomas. *Differentiation*, 23, 256-69.
- MONROY, A., LITHGOW, G. J. & ALAVEZ, S. 2013. Curcumin and neurodegenerative diseases. *Biofactors*, 39, 122-132.
- MOORE, G. E. & SANDBERG, A. A. 1964. Studies of a Human Tumor Cell Line with a Diploid Karyotype. *Cancer*, 17, 170-5.
- MOORHEAD, P. S. 1965. Human tumor cell line with a quasi-diploid karyotype (RPMI 2650). *Exp Cell Res*, 39, 190-6.

- MORENO-VEGA, A.-I., #XF3, MEZ-QUINTERO, T., NU, #XF1, EZ-ANITA, R.-E., ACOSTA-TORRES, L.-S., CASTA, #XF1, O, V., #XED & CTOR 2012. Polymeric and Ceramic Nanoparticles in Biomedical Applications. *Journal of Nanotechnology*, 2012, 10.
- MORGEN, M., BLOOM, C., BEYERINCK, R., BELLO, A., SONG, W., WILKINSON, K., STEENWYK, R. & SHAMBLIN, S. 2012. Polymeric nanoparticles for increased oral bioavailability and rapid absorption using celecoxib as a model of a low-solubility, high-permeability drug. *Pharm Res*, 29, 427-40.
- MORIMOTO, K., YAMAGUCHI, H., IWAKURA, Y., MORISAKA, K., OHASHI, Y. & NAKAI, Y. 1991. Effects of viscous hyaluronate-sodium solutions on the nasal absorption of vasopressin and an analogue. *Pharm Res*, 8, 471-4.
- MORRISON, E. E. & COSTANZO, R. M. 1990a. Morphology of the human olfactory epithelium. *The Journal of Comparative Neurology*, 297, 1-13.
- MORRISON, E. E. & COSTANZO, R. M. 1990b. Morphology of the human olfactory epithelium. *J Comp Neurol*, 297, 1-13.
- MORRISON, E. E. & COSTANZO, R. M. 1992. Morphology of olfactory epithelium in humans and other vertebrates. *Microsc Res Tech*, 23, 49-61.
- MORTENSEN, K. & BROWN, W. 1993. Poly(ethylene oxide)-poly(propylene oxide)-poly(ethylene oxide) triblock copolymers in aqueous solution. The influence of relative block size. *Macromolecules*, 26, 4128-4135.
- MORTENSEN, K. & PEDERSEN, J. S. 1993. Structural study on the micelle formation of poly(ethylene oxide)-poly(propylene oxide)-poly(ethylene oxide) triblock copolymer in aqueous solution. *Macromolecules*, 26, 805-812.
- MUTHANE, U., YASHA, T. C. & SHANKAR, S. K. 1998. Low numbers and no loss of melanized nigral neurons with increasing age in normal human brains from India. *Ann Neurol*, 43, 283-7.
- MYTHRI, R. B., HARISH, G., DUBEY, S. K., MISRA, K. & BHARATH, M. M. 2011. Glutamoyl diester of the dietary polyphenol curcumin offers improved protection against peroxynitrite-mediated nitrosative stress and damage of brain mitochondria in vitro: implications for Parkinson's disease. *Mol Cell Biochem*, 347, 135-43.
- NABAVI, S. F., BRAIDY, N., HABTEMARIAM, S., ORHAN, I. E., DAGLIA, M., MANAYI, A., GORTZI, O. & NABAVI, S. M. 2015. Neuroprotective effects of chrysin: From chemistry to medicine. *Neurochem Int*, 90, 224-31.
- NAGARAJAN, R. & GANESH, K. 1996. Comparison of Solubilization of Hydrocarbons in (PEO-PPO) Diblock versus (PEO-PPO-PEO) Triblock Copolymer Micelles. *J Colloid Interface Sci*, 184, 489-99.
- NAKAMURA, F., OHTA, R., MACHIDA, Y. & NAGAI, T. 1996. In vitro and in vivo nasal mucoadhesion of some water-soluble polymers. *International Journal of Pharmaceutics*, 134, 173-181.
- NAKAMURA, K., MAITANI, Y., LOWMAN, A. M., TAKAYAMA, K., PEPPAS, N. A. & NAGAI, T. 1999. Uptake and release of budesonide from mucoadhesive, pH-sensitive copolymers and their application to nasal delivery. *J Control Release*, 61, 329-35.
- NAPIERSKA, D., THOMASSEN, L. C., RABOLLI, V., LISON, D., GONZALEZ, L., KIRSCH VOLDERS, M., MARTENS, J. A. & HOET, P. H. 2009. Size-Dependent Cytotoxicity of Monodisperse Silica Nanoparticles in Human Endothelial Cells. *Small*, 5, 846-853.
- NAROLA, B., SINGH, A. S., SANTHAKUMAR, P. R. & CHANDRASHEKHAR, T. G. 2010. A Validated Stability-indicating Reverse Phase HPLC Assay Method for the Determination of Memantine Hydrochloride Drug Substance with UV-Detection Using Precolumn Derivatization Technique. *Anal Chem Insights*, 5, 37-45.
- NAZAR, H., FATOUROS, D. G., VAN DER MERWE, S. M., BOUROPOULOS, N., AVGOUROPOULOS, G., TSIBOUKLIS, J. & ROLDO, M. 2011. Thermosensitive hydrogels for nasal drug delivery: the formulation and characterisation of systems based on N-trimethyl chitosan chloride. *Eur J Pharm Biopharm*, 77, 225-32.
- NEHOFF, H., PARAYATH, N. N., DOMANOVITCH, L., TAURIN, S. & GREISH, K. 2014. Nanomedicine for drug targeting: strategies beyond the enhanced permeability and retention effect. *Int J Nanomedicine*, 9, 2539-2555.
- NEL, A., XIA, T., MÄDLER, L. & LI, N. 2006. Toxic potential of materials at the nanolevel. *Science*, 311, 622-627.

- NEUHAUS, W., LAUER, R., OELZANT, S., FRINGELI, U. P., ECKER, G. F. & NOE, C. R. 2006. A novel flow based hollow-fiber blood-brain barrier in vitro model with immortalised cell line PBMEC/C1-2. *J Biotechnol*, 125, 127-41.
- NEUWELT, E., ABBOTT, N. J., ABREY, L., BANKS, W. A., BLAKLEY, B., DAVIS, T., ENGELHARDT, B., GRAMMAS, P., NEDERGAARD, M., NUTT, J., PARDRIDGE, W., ROSENBERG, G. A., SMITH, Q. & DREWES, L. R. 2008. Strategies to advance translational research into brain barriers. *Lancet Neurol*, 7, 84-96.
- NEWMAN, S. P. 2005. Principles of metered-dose inhaler design. *Respir Care*, 50, 1177-90.
- NEWMAN, S. P., MOREN, F. & CLARKE, S. W. 1988. Deposition pattern of nasal sprays in man. *Rhinology*, 26, 111-20.
- NG, S. F., ROUSE, J. J., SANDERSON, F. D., MEIDAN, V. & ECCLESTON, G. M. 2010. Validation of a static Franz diffusion cell system for in vitro permeation studies. *AAPS PharmSciTech*, 11, 1432-41.
- NIE, S., HSIAO, W. L., PAN, W. & YANG, Z. 2011. Thermoreversible Pluronic F127-based hydrogel containing liposomes for the controlled delivery of paclitaxel: in vitro drug release, cell cytotoxicity, and uptake studies. *Int J Nanomedicine*, 6, 151-66.
- NONES, J., STIPURSKY, J., COSTA, S. L. & GOMES, F. C. A. 2010. Flavonoids and Astrocytes Crosstalk: Implications for Brain Development and Pathology. *Neurochemical Research*, 35, 955-966.
- NOONEY, R. I., THIRUNAVUKKARASU, D., CHEN, Y. M., JOSEPHS, R. & OSTAFIN, A. E. 2002. Synthesis of nanoscale mesoporous silica spheres with controlled particle size. *Chemistry of Materials*, 14, 4721-4728.
- O'REGAN, M. E., BROWN, J. K. & CLARKE, M. 1996. Nasal rather than rectal benzodiazepines in the management of acute childhood seizures? *Dev Med Child Neurol*, 38, 1037-45.
- OBERDÖRSTER, G., OBEDÖRSTER, E. & OBEDÖRSTER, J. 2005. Nanotoxicology: an emerging discipline evolving from studies of ultrafine particles. *Environmental health perspectives*, 823-839.
- ORIENTI, I., GIANASI, E., ZECCHI, V., CONTE, U. 1995. Release of ketoprofen from microspheres of poly2-hydroxyethyl methacrylate or poly2-hydroxyethyl methacrylate-cob- methacryloyloxyethyl deoxycholate crosslinked with ethylene glycol dimethacrylate and tetraethylene glycol dimethacrylate. *European Journal of Pharmaceutics and Biopharmaceutics*, 41, 247-253.
- OZSOY, Y., GUNGOR, S. & CEVHER, E. 2009. Nasal delivery of high molecular weight drugs. *Molecules*, 14, 3754-79.
- PAN, M. H., HUANG, T. M. & LIN, J. K. 1999. Biotransformation of curcumin through reduction and glucuronidation in mice. *Drug Metab Dispos*, 27, 486-94.
- PANDEY, K. B. & RIZVI, S. I. 2009. Plant polyphenols as dietary antioxidants in human health and disease. *Oxidative Medicine and Cellular Longevity*, 2, 270-278.
- PANDIT, N. K. & MCGOWAN, R. 1998. Gelation of Pluronic (R) F127-polyethylene glycol mixtures: Relationship to PEG molecular weight. *Drug Development and Industrial Pharmacy*, 24, 183-186.
- PAPAHADJOPOULOS, D. 1988. Liposome formation and properties: an evolutionary profile. *Biochem Soc Trans*, 16, 910-2.
- PARDRIDGE, W. M. 1998. CNS drug design based on principles of blood-brain barrier transport. *J Neurochem*, 70, 1781-92.
- PARDRIDGE, W. M. 2005. The blood-brain barrier: bottleneck in brain drug development. *NeuroRx*, 2, 3-14.
- PARDRIDGE, W. M. 2007a. Blood-brain barrier delivery. *Drug Discov Today*, 12, 54-61.
- PARDRIDGE, W. M. 2007b. Blood-brain barrier delivery. *Drug Discovery Today*, 12, 54-61.
- PARDRIDGE, W. M. 2007c. Drug targeting to the brain. *Pharm Res*, 24, 1733-44.
- PARDRIDGE, W. M. 2010. Biopharmaceutical drug targeting to the brain. *J Drug Target*, 18, 157-67.
- PARDRIDGE, W. M. 2012. Drug transport across the blood-brain barrier. *J Cereb Blood Flow Metab*, 32, 1959-72.
- PARK, H. & ROBINSON, J. R. 1987. Mechanisms of mucoadhesion of poly(acrylic acid) hydrogels. *Pharm Res*, 4, 457-64.
- PEPPAS, N. A. & BURI, P. A. 1985. Surface, interfacial and molecular aspects of polymer bioadhesion on soft tissues. *Journal of Controlled Release*, 2, 257-275.
- PEPPAS, N. A. & KHARE, A. R. 1993. Preparation, structure and diffusional behavior of hydrogels in controlled release. *Advanced Drug Delivery Reviews*, 11, 1-35.

- PEPPAS, N. A. & SAHLIN, J. J. 1989. A simple equation for the description of solute release. III. Coupling of diffusion and relaxation. *International Journal of Pharmaceutics*, 57, 169-172.
- PEREZ, A. P., MUNDINA-WEILENMANN, C., ROMERO, E. L. & MORILLA, M. J. 2012. Increased brain radioactivity by intranasal P-labeled siRNA dendriplexes within in situ-forming mucoadhesive gels. *Int J Nanomedicine*, 7, 1373-85.
- PERSIDSKY, Y., RAMIREZ, S. H., HAORAH, J. & KANMOGNE, G. D. 2006. Blood-brain barrier: structural components and function under physiologic and pathologic conditions. *J Neuroimmune Pharmacol*, 1, 223-36.
- PERSSON, H. G. & GATZINSKY, K. P. 1993. Distribution of retrogradely transported fluorescent latex microspheres in rat lumbosacral ventral root axons following peripheral crush injury: a light and electron microscopic study. *Brain Research*, 630, 115-124.
- PICK, A., MÜLLER, H., MAYER, R., HAENISCH, B., PAJEVA, I. K., WEIGT, M., BÖNISCH, H., MÜLLER, C. E. & WIESE, M. 2011. Structure-activity relationships of flavonoids as inhibitors of breast cancer resistance protein (BCRP). *Bioorganic & Medicinal Chemistry*, 19, 2090-2102.
- PIRES, A., FORTUNA, A., ALVES, G. & FALCÃO, A. 2009. Intranasal drug delivery: how, why and what for? *Journal of Pharmacy & Pharmaceutical Sciences*, 12, 288-311.
- PISAL, S. S., PARADKAR, A. R., MAHADIK, K. R. & KADAM, S. S. 2004. Pluronic gels for nasal delivery of Vitamin B12. Part I: preformulation study. *Int J Pharm*, 270, 37-45.
- POLLI, G. P., GRIM, W. M., BACHER, F. A. & YUNKER, M. H. 1969. Influence of formulation on aerosol particle size. *J Pharm Sci*, 58, 484-6.
- PONCHEL, G., TOUCHARD, F., DUCHÊNE, D. & PEPPAS, N. A. 1987. Bioadhesive analysis of controlled-release systems. I. Fracture and interpenetration analysis in poly(acrylic acid)-containing systems. *Journal of Controlled Release*, 5, 129-141.
- POSTE, G. & KIRSH, R. 1983. Site-specific (targeted) drug delivery in cancer therapy. *Bio/Technology*, 1, 869-878.
- POSTE, G., PAPAHAADJOPOULOS, D. & VAIL, W. J. 1976. Lipid vesicles as carriers for introducing biologically active materials into cells. *Methods Cell Biol*, 14, 33-71.
- PRUDHOMME, R. K., WU, G. W. & SCHNEIDER, D. K. 1996. Structure and rheology studies of poly(oxyethylene-oxypropylene-oxyethylene) aqueous solution. *Langmuir*, 12, 4651-4659.
- PUJARA, C. P., SHAO, Z. Z., DUNCAN, M. R. & MITRA, A. K. 1995. Effects of Formulation Variables on Nasal Epithelial-Cell Integrity - Biochemical Evaluations. *International Journal of Pharmaceutics*, 114, 197-203.
- PURVES, D. 2007. *Neuroscience*, New York, W. H. Freeman ; Basingstoke : Palgrave [distributor].
- QI, L., MA, J., CHENG, H. & ZHAO, Z. 1998. Micrometer-Sized Mesoporous Silica Spheres Grown under Static Conditions. *Chemistry of Materials*, 10, 1623-1626.
- QIAN, S., WONG, Y. C. & ZUO, Z. 2014. Development, characterization and application of in situ gel systems for intranasal delivery of tacrine. *Int J Pharm*, 468, 272-82.
- RAVINDRANATH, V. & CHANDRASEKHARA, N. 1980. Absorption and tissue distribution of curcumin in rats. *Toxicology*, 16, 259-65.
- RAVOURU, N., KONDREDDY, P., KORAKANCHI, D. & HARITHA, M. 2013. Formulation and evaluation of niosomal nasal drug delivery system of folic acid for brain targeting. *Curr Drug Discov Technol*, 10, 270-82.
- REGER, M. A., WATSON, G. S., FREY, W. H., 2ND, BAKER, L. D., CHOLERTON, B., KEELING, M. L., BELONGIA, D. A., FISHEL, M. A., PLYMATE, S. R., SCHELLENBERG, G. D., CHERRIER, M. M. & CRAFT, S. 2006. Effects of intranasal insulin on cognition in memory-impaired older adults: modulation by APOE genotype. *Neurobiol Aging*, 27, 451-8.
- REGER, M. A., WATSON, G. S., GREEN, P. S., BAKER, L. D., CHOLERTON, B., FISHEL, M. A., PLYMATE, S. R., CHERRIER, M. M., SCHELLENBERG, G. D., FREY, W. H., 2ND & CRAFT, S. 2008. Intranasal insulin administration dose-dependently modulates verbal memory and plasma amyloid-beta in memory-impaired older adults. *J Alzheimers Dis*, 13, 323-31.
- REICHL, S. & BECKER, K. 2012a. Cultivation of RPMI 2650 cells as an in-vitro model for human transmucosal nasal drug absorption studies: optimization of selected culture conditions. *Journal of Pharmacy and Pharmacology*, 64, 1621-1630.

- REICHL, S. & BECKER, K. 2012b. Cultivation of RPMI 2650 cells as an in-vitro model for human transmucosal nasal drug absorption studies: optimization of selected culture conditions. *J Pharm Pharmacol*, 64, 1621-30.
- REISS, C. S., PLAKHOV, I. V. & KOMATSU, T. 1998. Viral replication in olfactory receptor neurons and entry into the olfactory bulb and brain. *Olfaction and Taste Xii*, 855, 751-761.
- RENNER, D. B., FREY, W. H., 2ND & HANSON, L. R. 2012. Intranasal delivery of siRNA to the olfactory bulbs of mice via the olfactory nerve pathway. *Neurosci Lett*, 513, 193-7.
- ROBEY, R. W., STEADMAN, K., POLGAR, O., MORISAKI, K., BLAYNEY, M., MISTRY, P. & BATES, S. E. 2004. Pheophorbide a is a specific probe for ABCG2 function and inhibition. *Cancer research*, 64, 1242-1246.
- ROUINI, M. R., ARDAKANI, Y. H., MOGHADDAM, K. A. & SOLATANI, F. 2008. An improved HPLC method for rapid quantitation of diazepam and its major metabolites in human plasma. *Talanta*, 75, 671-6.
- SAKANE, T., AKIZUKI, M., TAKI, Y., YAMASHITA, S., SEZAKI, H. & NADAI, T. 1995. Direct drug transport from the rat nasal cavity to the cerebrospinal fluid: the relation to the molecular weight of drugs. *J Pharm Pharmacol*, 47, 379-81.
- SAKANE, T., AKIZUKI, M., YAMASHITA, S., NADAI, T., HASHIDA, M. & SEZAKI, H. 1991. The transport of a drug to the cerebrospinal fluid directly from the nasal cavity: the relation to the lipophilicity of the drug. *Chem Pharm Bull (Tokyo)*, 39, 2456-8.
- SALIB, R. J., LAU, L. C. & HOWARTH, P. H. 2005. The novel use of the human nasal epithelial cell line RPMI 2650 as an in vitro model to study the influence of allergens and cytokines on transforming growth factor-beta gene expression and protein release. *Clin Exp Allergy*, 35, 811-9.
- SALONEN, J., LAITINEN, L., KAUKONEN, A. M., TUURA, J., BJORKQVIST, M., HEIKKILA, T., VAHA-HEIKKILA, K., HIRVONEN, J. & LEHTO, V. P. 2005a. Mesoporous silicon microparticles for oral drug delivery: Loading and release of five model drugs. *Journal of Controlled Release*, 108, 362-374.
- SALONEN, J., LEHTO, V. P. & LAINE, E. 1997. The room temperature oxidation of porous silicon. *Applied Surface Science*, 120, 191-198.
- SALONEN, J., PASKI, J., VAHA-HEIKKILA, K., HEIKKILA, T., BJORKQVIST, M. & LEHTO, V. P. 2005b. Determination of drug load in porous silicon microparticles by calorimetry. *Physica Status Solidi a-Applications and Materials Science*, 202, 1629-1633.
- SAMIA, O., HANAN, R. & KAMAL EL, T. 2012. Carbamazepine mucoadhesive nanoemulgel (MNEG) as brain targeting delivery system via the olfactory mucosa. *Drug Deliv*, 19, 58-67.
- SANTOS, B. L., OLIVEIRA, M. N., COELHO, P. L., PITANGA, B. P., DA SILVA, A. B., ADELITA, T., SILVA, V. D., COSTA MDE, F., EL-BACHA, R. S., TARDY, M., CHNEIWEISS, H., JUNIER, M. P., MOURA-NETO, V. & COSTA, S. L. 2015. Flavonoids suppress human glioblastoma cell growth by inhibiting cell metabolism, migration, and by regulating extracellular matrix proteins and metalloproteinases expression. *Chem Biol Interact*, 242, 123-38.
- SATHISHKUMAR, G., BHARTI, R., JHA, P. K., SELVAKUMAR, M., DEY, G., JHA, R., JEYARAJ, M., MANDAL, M. & SIVARAMAKRISHNAN, S. 2015. Dietary flavone chrysin (5,7-dihydroxyflavone ChR) functionalized highly-stable metal nanoformulations for improved anticancer applications. *RSC Advances*, 5, 89869-89878.
- SCHMALJOHANN, D. 2006. Thermo- and pH-responsive polymers in drug delivery. *Adv Drug Deliv Rev*, 58, 1655-70.
- SCHMOLKA, I. R. 1972a. Artificial skin I. Preparation and properties of pluronic F-127 gels for treatment of burns. *Journal of Biomedical Materials Research*, 6, 571-582.
- SCHMOLKA, I. R. 1972b. Artificial skin. I. Preparation and properties of pluronic F-127 gels for treatment of burns. *J Biomed Mater Res*, 6, 571-82.
- SCOGS 1979. Corn starch. Food and Drug Administration.
- SEVERINO, P., SOUTO, E. B., PINHO, S. C. & SANTANA, M. H. 2013. Hydrophilic coating of mitotane-loaded lipid nanoparticles: preliminary studies for mucosal adhesion. *Pharm Dev Technol*, 18, 577-81.
- SEYBOLD, Z. V., MARIASSY, A. T., STROH, D., KIM, C. S., GAZEROGLU, H. & WANNER, A. 1990. Mucociliary interaction in vitro: effects of physiological and inflammatory stimuli. *J Appl Physiol (1985)*, 68, 1421-6.

- SHARMA, D., MAHESHWARI, D., PHILIP, G., RANA, R., BHATIA, S., SINGH, M., GABRANI, R., SHARMA, S. K., ALI, J., SHARMA, R. K. & DANG, S. 2014. Formulation and Optimization of Polymeric Nanoparticles for Intranasal Delivery of Lorazepam Using Box-Behnken Design: In Vitro and In Vivo Evaluation. *BioMed Research International*, 2014, 14.
- SHETH, P., STEIN, S. W. & MYRDAL, P. B. 2015. Factors influencing aerodynamic particle size distribution of suspension pressurized metered dose inhalers. *AAPS PharmSciTech*, 16, 192-201.
- SHI, N. & PARDRIDGE, W. M. 2000. Noninvasive gene targeting to the brain. *Proc Natl Acad Sci U S A*, 97, 7567-72.
- SHIN, B. K., BAEK, E. J., CHOI, S. G., DAVAA, E., NHO, Y. C., LIM, Y. M., PARK, J. S., HUH, K. M. & PARK, J. S. 2013. Preparation and irradiation of Pluronic F127-based thermoreversible and mucoadhesive hydrogel for local delivery of naproxen. *Drug Dev Ind Pharm*, 39, 1874-80.
- SHIPLEY, M. T., HALLORAN, F. J. & DE LA TORRE, J. 1985. Surprisingly rich projection from locus coeruleus to the olfactory bulb in the rat. *Brain Res*, 329, 294-9.
- SHUKITT-HALE, B. 2012. Blueberries and neuronal aging. *Gerontology*, 58, 518-23.
- SIEPMANN, J. & PEPPAS, N. A. 2001. Modeling of drug release from delivery systems based on hydroxypropyl methylcellulose (HPMC). *Adv Drug Deliv Rev*, 48, 139-57.
- SIRVEN, J. I. & WATERHOUSE, E. 2003. Management of status epilepticus. *Am Fam Physician*, 68, 469-76.
- SLOWING, I., TREWYN, B. G. & LIN, V. S. Y. 2006. Effect of Surface Functionalization of MCM-41-Type Mesoporous Silica Nanoparticles on the Endocytosis by Human Cancer Cells. *Journal of the American Chemical Society*, 128, 14792-14793.
- SLOWING, I. I., VIVERO-ESCOTO, J. L., WU, C.-W. & LIN, V. S. Y. 2008a. Mesoporous silica nanoparticles as controlled release drug delivery and gene transfection carriers. *Advanced Drug Delivery Reviews*, 60, 1278-1288.
- SLOWING, I. I., VIVERO-ESCOTO, J. L., WU, C. W. & LIN, V. S. Y. 2008b. Mesoporous silica nanoparticles as controlled release drug delivery and gene transfection carriers. *Advanced Drug Delivery Reviews*, 60, 1278-1288.
- SMART, J. 1999. The role of water movement and polymer hydration in mucoadhesion. *Drugs and the pharmaceutical sciences*, 98, 11-23.
- SMART, J. D. 2005. The basics and underlying mechanisms of mucoadhesion. *Adv Drug Deliv Rev*, 57, 1556-68.
- SMART, J. D. & KELLAWAY, I. W. 1982. IN VITRO TECHNIQUES FOR MEASURING MUCOADHESION. *Journal of Pharmacy and Pharmacology*, 34, 70P-70P.
- SMART, J. D., KELLAWAY, I. W. & WORTHINGTON, H. E. 1984. An in-vitro investigation of mucosa-adhesive materials for use in controlled drug delivery. *J Pharm Pharmacol*, 36, 295-9.
- SOANE, R. J., FRIER, M., PERKINS, A. C., JONES, N. S., DAVIS, S. S. & ILLUM, L. 1999. Evaluation of the clearance characteristics of bioadhesive systems in humans. *Int J Pharm*, 178, 55-65.
- SOANE, R. J., HINCHCLIFFE, M., DAVIS, S. S. & ILLUM, L. 2001. Clearance characteristics of chitosan based formulations in the sheep nasal cavity. *Int J Pharm*, 217, 183-91.
- SOLANKI, I., PARIHAR, P., MANSURI, M. L. & PARIHAR, M. S. 2015. Flavonoid-based therapies in the early management of neurodegenerative diseases. *Adv Nutr*, 6, 64-72.
- SOPPIMATH, K. S., AMINABHAVI, T. M., DAVE, A. M., KUMBAR, S. G. & RUDZINSKI, W. E. 2002. Stimulus-Responsive "Smart" Hydrogels as Novel Drug Delivery Systems. *Drug Development and Industrial Pharmacy*, 28, 957-974.
- SOUZA, L. C., ANTUNES, M. S., FILHO, C. B., DEL FABBRO, L., DE GOMES, M. G., GOES, A. T., DONATO, F., PRIGOL, M., BOEIRA, S. P. & JESSE, C. R. 2015. Flavonoid Chrysin prevents age-related cognitive decline via attenuation of oxidative stress and modulation of BDNF levels in aged mouse brain. *Pharmacol Biochem Behav*, 134, 22-30.
- STEIN, A., MELDE, B. J. & SCHRODEN, R. C. 2000. Hybrid inorganic-organic mesoporous silicates - Nanoscopic reactors coming of age. *Advanced Materials*, 12, 1403-1419.
- STEWART, W. B. 1985. Labeling of Olfactory-Bulb Glomeruli Following Horseradish-Peroxidase Lavage of the Nasal Cavity. *Brain Research*, 347, 200-203.
- STUART, B. O. 1973. Deposition of inhaled aerosols. *Arch Intern Med*, 131, 60-73.

- SUN, L., WANG, Y., JIANG, T., ZHENG, X., ZHANG, J., SUN, J., SUN, C. & WANG, S. 2013. Novel Chitosan-Functionalized Spherical Nanosilica Matrix As an Oral Sustained Drug Delivery System for Poorly Water-Soluble Drug Carvedilol. *ACS Applied Materials & Interfaces*, 5, 103-113.
- SUN, X. J., PENG, W., YANG, Z. L., REN, M. L., ZHANG, S. C., ZHANG, W. G., ZHANG, L. Y., XIAO, K., WANG, Z. G., ZHANG, B. & WANG, J. 2011. Heparin-chitosan-coated acellular bone matrix enhances perfusion of blood and vascularization in bone tissue engineering scaffolds. *Tissue Eng Part A*, 17, 2369-78.
- SUTTO, Z., CONNER, G. E. & SALATHE, M. 2004a. Regulation of human airway ciliary beat frequency by intracellular pH. *J Physiol*, 560, 519-32.
- SUTTO, Z., CONNER, G. E. & SALATHE, M. 2004b. Regulation of human airway ciliary beat frequency by intracellular pH. *Journal of Physiology-London*, 560, 519-532.
- TAEBNIA, N., MORSHEDI, D., DOOSTKAM, M., YAGHMAEI, S., ALIAKBARI, F., SINGH, G. & ARPANAIEI, A. 2015. The effect of mesoporous silica nanoparticle surface chemistry and concentration on the alpha-synuclein fibrillation. *Rsc Advances*, 5, 60966-60974.
- TAMADDON, L., MOSTAFAVI, S. A., KARKHANE, R., RIAZI-ESFAHANI, M., DORKOOSH, F. A. & RAFIEE-TEHRANI, M. 2015. Design and development of intraocular polymeric implant systems for long-term controlled-release of clindamycin phosphate for toxoplasmic retinochoroiditis. *Adv Biomed Res*, 4, 32.
- TCHEMTCHOUA, V. T., ATANASOVA, G., AQIL, A., FILEE, P., GARBACKI, N., VANHOOTEGHEM, O., DEROANNE, C., NOEL, A., JEROME, C., NUSGENS, B., POUMAY, Y. & COLIGE, A. 2011. Development of a chitosan nanofibrillar scaffold for skin repair and regeneration. *Biomacromolecules*, 12, 3194-204.
- THIEBAUD, N., MENETRIER, F., BELLOIR, C., MINN, A. L., NEIERS, F., ARTUR, Y., LE BON, A. M. & HEYDEL, J. M. 2011. Expression and differential localization of xenobiotic transporters in the rat olfactory neuro-epithelium. *Neurosci Lett*, 505, 180-5.
- THOMAS, N. L. & WINDLE, A. H. 1980. A deformation model for Case II diffusion. *Polymer*, 21, 613-619.
- THOMAS, N. L. & WINDLE, A. H. 1981. Diffusion mechanics of the system PMMA-methanol. *Polymer*, 22, 627-639.
- THOMAS, N. L. & WINDLE, A. H. 1982. A theory of case II diffusion. *Polymer*, 23, 529-542.
- THORNE, R. G., EMORY, C. R., ALA, T. A. & FREY, W. H., 2ND 1995. Quantitative analysis of the olfactory pathway for drug delivery to the brain. *Brain Res*, 692, 278-82.
- THORNE, R. G., PRONK, G. J., PADMANABHAN, V. & FREY, W. H., 2ND 2004. Delivery of insulin-like growth factor-I to the rat brain and spinal cord along olfactory and trigeminal pathways following intranasal administration. *Neuroscience*, 127, 481-96.
- TONNESEN, H. H. & KARLSEN, J. 1985. Studies on curcumin and curcuminoids. VI. Kinetics of curcumin degradation in aqueous solution. *Z Lebensm Unters Forsch*, 180, 402-4.
- UEBING-CZIPURA, A. U., DAWSON, H. D., RUTHERFORD, M. S. & SCHERBA, G. 2009. Transcriptome profile and cytogenetic analysis of immortalized neuronally restricted progenitor cells derived from the porcine olfactory bulb. *Anim Biotechnol*, 20, 186-215.
- UEBING-CZIPURA, A. U., DAWSON, H. D. & SCHERBA, G. 2008. Immortalization and characterization of lineage-restricted neuronal progenitor cells derived from the porcine olfactory bulb. *J Neurosci Methods*, 170, 262-76.
- UGWOKE, M. I., AGU, R. U., VERBEKE, N. & KINGET, R. 2005. Nasal mucoadhesive drug delivery: background, applications, trends and future perspectives. *Adv Drug Deliv Rev*, 57, 1640-65.
- UGWOKE, M. I., EXAUD, S., VAN DEN MOOTER, G., VERBEKE, N. & KINGET, R. 1999. Bioavailability of apomorphine following intranasal administration of mucoadhesive drug delivery systems in rabbits. *Eur J Pharm Sci*, 9, 213-9.
- UGWOKE, M. I., VERBEKE, N. & KINGET, R. 2001. The biopharmaceutical aspects of nasal mucoadhesive drug delivery. *J Pharm Pharmacol*, 53, 3-21.
- VADNERE, M., AMIDON, G., LINDENBAUM, S. & HASLAM, J. L. 1984. Thermodynamic Studies on the Gel Sol Transition of Some Pluronic Polyols. *International Journal of Pharmaceutics*, 22, 207-218.
- VAKA, S. R., SHIVAKUMAR, H. N., REPKA, M. A. & MURTHY, S. N. 2013. Formulation and evaluation of carnosic acid nanoparticulate system for upregulation of neurotrophins in the brain upon intranasal administration. *J Drug Target*, 21, 44-53.

- VALLEE, R. B. & BLOOM, G. S. 1991. Mechanisms of fast and slow axonal transport. *Annu Rev Neurosci*, 14, 59-92.
- VALLET-REGI, M., RÁMILA, A., DEL REAL, R. P. & PÉREZ-PARIENTE, J. 2001. A New Property of MCM-41: Drug Delivery System. *Chemistry of Materials*, 13, 308-311.
- VAN WOENSEL, M., WAUTHOZ, N., ROSIERE, R., AMIGHI, K., MATHIEU, V., LEFRANC, F., VAN GOOL, S. W. & DE VLEESCHOUWER, S. 2013. Formulations for Intranasal Delivery of Pharmacological Agents to Combat Brain Disease: A New Opportunity to Tackle GBM? *Cancers (Basel)*, 5, 1020-48.
- VAN ZANDEN, J. J., VAN DER WOUDE, H., VAESSEN, J., USTA, M., WORTELBOER, H. M., CNUBBEN, N. H. P. & RIETJENS, I. M. C. M. 2007. The effect of quercetin phase II metabolism on its MRP1 and MRP2 inhibiting potential. *Biochemical pharmacology*, 74, 345-351.
- VARSHOSAZ, J., SADRAI, H. & HEIDARI, A. 2006. Nasal delivery of insulin using bioadhesive chitosan gels. *Drug Deliv*, 13, 31-8.
- VIDGREN, M. T. & KUBLIK, H. 1998. Nasal delivery systems and their effect on deposition and absorption. *Adv Drug Deliv Rev*, 29, 157-177.
- VOIUTSKII, S. S. 1963. *Autohesion and adhesion of high polymers*, New York, Interscience Publishers.
- VRENTAS, J. S. & VRENTAS, C. M. 1998. Integral sorption in glassy polymers. *Chemical Engineering Science*, 53, 629-638.
- VYAS, T. K., BABBAR, A. K., SHARMA, R. K. & MISRA, A. 2005a. Intranasal mucoadhesive microemulsions of zolmitriptan: preliminary studies on brain-targeting. *J Drug Target*, 13, 317-24.
- VYAS, T. K., BABBAR, A. K., SHARMA, R. K., SINGH, S. & MISRA, A. 2006a. Intranasal mucoadhesive microemulsions of clonazepam: preliminary studies on brain targeting. *J Pharm Sci*, 95, 570-80.
- VYAS, T. K., BABBAR, A. K., SHARMA, R. K., SINGH, S. & MISRA, A. 2006b. Preliminary brain-targeting studies on intranasal mucoadhesive microemulsions of sumatriptan. *AAPS PharmSciTech*, 7, E8.
- VYAS, T. K., SHAHIWALA, A., MARATHE, S. & MISRA, A. 2005b. Intranasal drug delivery for brain targeting. *Curr Drug Deliv*, 2, 165-75.
- WAKE, W. C. 1976. *Adhesion and the formulation of adhesives*, London, Applied Science.
- WAKE, W. C. 1978. Theories of adhesion and uses of adhesives: a review. *Polymer*, 19, 291-308.
- WANG, Y. J., PAN, M. H., CHENG, A. L., LIN, L. I., HO, Y. S., HSIEH, C. Y. & LIN, J. K. 1997. Stability of curcumin in buffer solutions and characterization of its degradation products. *J Pharm Biomed Anal*, 15, 1867-76.
- WANG, Z., FAN, H., LI, Y. & WANG, Y. 2015. Anti-hepatocarcinoma effects of chrysin loaded solid lipid nanoparticle against H22 tumor bearing mice.
- WANKA, G., HOFFMANN, H. & ULBRICHT, W. 1990. The aggregation behavior of poly-(oxyethylene)-poly-(oxypropylene)-poly-(oxyethylene)-block-copolymers in aqueous solution. *Colloid and Polymer Science*, 268, 101-117.
- WANYIKA, H., GATEBE, E., KIONI, P., TANG, Z. Y. & GAO, Y. 2011. Synthesis and characterization of ordered mesoporous silica nanoparticles with tunable physical properties by varying molar composition of reagents. *African Journal of Pharmacy and Pharmacology*, 5, 2402-2410.
- WASHINGTON, N., STEELE, R. J. C., JACKSON, S. J., BUSH, D., MASON, J., GILL, D. A., PITT, K. & RAWLINS, D. A. 2000. Determination of baseline human nasal pH and the effect of intranasally administered buffers. *International Journal of Pharmaceutics*, 198, 139-146.
- WASOWSKI, C., MARDER, M., VIOLA, H., MEDINA, J. H. & PALADINI, A. C. 2002. Isolation and identification of 6-methylapigenin, a competitive ligand for the brain GABA(A) receptors, from *Valeriana wallichii*. *Planta Med*, 68, 934-6.
- WATANABE, Y., MATSUMOTO, Y., KAWAMOTO, K., YAZAWA, S. & MATSUMOTO, M. 1992. Enhancing effect of cyclodextrins on nasal absorption of insulin and its duration in rabbits. *Chem Pharm Bull (Tokyo)*, 40, 3100-4.
- WEN, M. M. 2011. Olfactory Targeting Through Intranasal Delivery of Biopharmaceutical Drugs to the Brain - Current Development. *Discovery Medicine*, 61, 497-503.
- WERMELING, D. P. 2009. Intranasal delivery of antiepileptic medications for treatment of seizures. *Neurotherapeutics*, 6, 352-8.

- WERNER, U. & KISSEL, T. 1996. In-vitro Cell Culture Models of the Nasal Epithelium: A Comparative Histochemical Investigation of Their Suitability for Drug Transport Studies. *Pharmaceutical Research*, 13, 978-988.
- WESTIN, U., PIRAS, E., JANSSON, B., BERGSTROM, U., DAHLIN, M., BRITTEBO, E. & BJORK, E. 2005. Transfer of morphine along the olfactory pathway to the central nervous system after nasal administration to rodents. *Eur J Pharm Sci*, 24, 565-73.
- WESTIN, U. E., BOSTROM, E., GRASJO, J., HAMMARLUND-UDENAES, M. & BJORK, E. 2006a. Direct nose-to-brain transfer of morphine after nasal administration to rats. *Pharm Res*, 23, 565-72.
- WESTIN, U. E., WESTIN, U. E., WESTIN, U. E., WESTIN, U. E., BOSTRÖM, E., BOSTRÖM, E., BOSTRÖM, E., BOSTRÖM, E., GRÅSJÖ, J., GRÅSJÖ, J., GRÅSJÖ, J., GRÅSJÖ, J., HAMMARLUND-UDENAES, M., HAMMARLUND-UDENAES, M., HAMMARLUND-UDENAES, M., HAMMARLUND-UDENAES, M., HAMMARLUND-UDENAES, M., BJÖRK, E., BJÖRK, E., BJÖRK, E. & BJÖRK, E. 2006b. Direct nose-to-brain transfer of morphine after nasal administration to rats. *Clinical and experimental pharmacology & physiology*, 23, 565-572.
- WHO 2006. *Neurological Disorders: Public Health Challenges*, World Health Organization.
- WILLIAMS III, R. O. & LIU, J. 1999. Formulation of a protein with propellant HFA 134a for aerosol delivery. *European Journal of Pharmaceutical Sciences*, 7, 137-144.
- WILLIAMS, R. J. & SPENCER, J. P. 2012. Flavonoids, cognition, and dementia: actions, mechanisms, and potential therapeutic utility for Alzheimer disease. *Free Radic Biol Med*, 52, 35-45.
- WOLFE, T. R. & MACFARLANE, T. C. 2006. Intranasal midazolam therapy for pediatric status epilepticus. *Am J Emerg Med*, 24, 343-6.
- WOLFMAN, C., VIOLA, H., PALADINI, A., DAJAS, F. & MEDINA, J. H. 1994. Possible anxiolytic effects of chrysin, a central benzodiazepine receptor ligand isolated from *Passiflora coerulea*. *Pharmacol Biochem Behav*, 47, 1-4.
- WU, H., ZHANG, S., ZHANG, J., LIU, G., SHI, J., ZHANG, L., CUI, X., RUAN, M., HE, Q. & BU, W. 2011. A Hollow-Core, Magnetic, and Mesoporous Double-Shell Nanostructure: In Situ Decomposition/Reduction Synthesis, Bioimaging, and Drug-Delivery Properties. *Advanced Functional Materials*, 21, 1850-1862.
- WU, J., WEI, W., WANG, L. Y., SU, Z. G. & MA, G. H. 2007. A thermosensitive hydrogel based on quaternized chitosan and poly(ethylene glycol) for nasal drug delivery system. *Biomaterials*, 28, 2220-32.
- WU, J. C. & PEPPAS, N. A. 1993. Modeling of penetrant diffusion in glassy polymers with an integral sorption Deborah number. *Journal of Polymer Science Part B: Polymer Physics*, 31, 1503-1518.
- WU, S. H., MOU, C. Y. & LIN, H. P. 2013. Synthesis of mesoporous silica nanoparticles. *Chemical Society Reviews*, 42, 3862-3875.
- WU, X., HAN, Z., SCHUR, R. M. & LU, Z.-R. 2016. Targeted Mesoporous Silica Nanoparticles Delivering Arsenic Trioxide with Environment Sensitive Drug Release for Effective Treatment of Triple Negative Breast Cancer. *ACS Biomaterials Science & Engineering*, 2, 501-507.
- XIA, H., GAO, X., GU, G., LIU, Z., ZENG, N., HU, Q., SONG, Q., YAO, L., PANG, Z., JIANG, X., CHEN, J. & CHEN, H. 2011. Low molecular weight protamine-functionalized nanoparticles for drug delivery to the brain after intranasal administration. *Biomaterials*, 32, 9888-98.
- XIAO, J., ZHAI, H., YAO, Y., WANG, C., JIANG, W., ZHANG, C., SIMARD, A. R., ZHANG, R. & HAO, J. 2014. Chrysin attenuates experimental autoimmune neuritis by suppressing immuno-inflammatory responses. *Neuroscience*, 262, 156-64.
- XIE, M. F., ZHOU, W., TONG, X. Y., CHEN, Y. L., CAI, Y., LI, Y. & DUAN, G. L. 2011. High-performance liquid chromatographic determination of memantine hydrochloride in rat plasma using sensitive fluorometric derivatization. *Journal of Separation Science*, 34, 241-246.
- YALLAPU, M. M., GUPTA, B. K., JAGGI, M. & CHAUHAN, S. C. 2010. Fabrication of curcumin encapsulated PLGA nanoparticles for improved therapeutic effects in metastatic cancer cells. *Journal of Colloid and Interface Science*, 351, 19-29.
- YAN, M., RAMSTRÖM, O., LIU, L.-H., WANG, X., LERNER, M. M. & MALUANGNONT, T. 2014. Method for functionalizing materials and devices comprising such materials. Google Patents.

- YANG, B., ZHANG, Y., ZHANG, X., TAO, L., LI, S. & WEI, Y. 2012. Facilely prepared inexpensive and biocompatible self-healing hydrogel: a new injectable cell therapy carrier. *Polymer Chemistry*, 3, 3235-3238.
- YANG, Z. Z., ZHANG, Y. Q., WANG, Z. Z., WU, K., LOU, J. N. & QI, X. R. 2013. Enhanced brain distribution and pharmacodynamics of rivastigmine by liposomes following intranasal administration. *Int J Pharm*, 452, 344-54.
- YAO, L. H., JIANG, Y. M., SHI, J., TOMAS-BARBERAN, F. A., DATTA, N., SINGANUSONG, R. & CHEN, S. S. 2004. Flavonoids in food and their health benefits. *Plant Foods for Human Nutrition*, 59, 113-122.
- YAO, Y., CHEN, L., XIAO, J., WANG, C., JIANG, W., ZHANG, R. & HAO, J. 2014. Chrysin protects against focal cerebral ischemia/reperfusion injury in mice through attenuation of oxidative stress and inflammation. *Int J Mol Sci*, 15, 20913-26.
- YE, Y., LIU, J., CHEN, M., SUN, L. & LAN, M. 2010. In vitro toxicity of silica nanoparticles in myocardial cells. *Environmental Toxicology and Pharmacology*, 29, 131-137.
- YIN, H., ZHANG, H. & LIU, B. 2013. Superior anticancer efficacy of curcumin-loaded nanoparticles against lung cancer. *Acta Biochimica et Biophysica Sinica*.
- YONCHEVA, K., TZANKOV, B., POPOVA, M., PETROVA, V. & LAMBOV, N. 2016. Evaluation of Stability of Mesoporous Silica Nanoparticles and Their Further Formulation in Tablet Form. *Journal of Dispersion Science and Technology*, 37, 113-118.
- YU, K. O., GRABINSKI, C. M., SCHRAND, A. M., MURDOCK, R. C., WANG, W., GU, B. H., SCHLAGER, J. J. & HUSSAIN, S. M. 2009. Toxicity of amorphous silica nanoparticles in mouse keratinocytes. *Journal of Nanoparticle Research*, 11, 15-24.
- YUAN, L., TANG, Q., YANG, D., ZHANG, J. Z., ZHANG, F. & HU, J. 2011. Preparation of pH-responsive mesoporous silica nanoparticles and their application in controlled drug delivery. *The Journal of Physical Chemistry C*, 115, 9926-9932.
- ZAKI, N. M., AWAD, G. A., MORTADA, N. D. & ABD ELHADY, S. S. 2007a. Enhanced bioavailability of metoclopramide HCl by intranasal administration of a mucoadhesive in situ gel with modulated rheological and mucociliary transport properties. *Eur J Pharm Sci*, 32, 296-307.
- ZAKI, N. M., AWAD, G. A., MORTADA, N. D. & ABD ELHADY, S. S. 2007b. Enhanced bioavailability of metoclopramide HCl by intranasal administration of a mucoadhesive in situ gel with modulated rheological and mucociliary transport properties. *European journal of pharmaceutical sciences*, 32, 296-307.
- ZAND, R. S. R., JENKINS, D. J. A. & DIAMANDIS, E. P. 2002. Flavonoids and steroid hormone-dependent cancers. *Journal of Chromatography B-Analytical Technologies in the Biomedical and Life Sciences*, 777, 219-232.
- ZAVERI, M., KHANDHAR, A. & JAIN, S. 2008. Quantification of baicalein, chrysin, biochanin-A and ellagic acid in root bark of *Oroxylum indicum* by RP-HPLC with UV detection. *Eurasian Journal of Analytical Chemistry*, 3, 245-257.
- ZBARSKY, V., DATLA, K. P., PARKAR, S., RAI, D. K., ARUOMA, O. I. & DEXTER, D. T. 2005. Neuroprotective properties of the natural phenolic antioxidants curcumin and naringenin but not quercetin and fisetin in a 6-OHDA model of Parkinson's disease. *Free Radical Research*, 39, 1119-1125.
- ZHAI, W. Y., HE, C. L., WU, L., ZHOU, Y., CHEN, H. R., CHANG, J. & ZHANG, H. F. 2012. Degradation of hollow mesoporous silica nanoparticles in human umbilical vein endothelial cells. *Journal of Biomedical Materials Research Part B-Applied Biomaterials*, 100B, 1397-1403.
- ZHANG, L. W., ZENG, L., BARRON, A. R. & MONTEIRO-RIVIERE, N. A. 2007. Biological interactions of functionalized single-wall carbon nanotubes in human epidermal keratinocytes. *Int J Toxicol*, 26, 103-13.
- ZHANG, P., ZHENG, Y., SHI, J., ZHANG, Y., LIU, S., LIU, Y. & ZHENG, D. 2010. Targeting a novel N-terminal epitope of death receptor 5 triggers tumor cell death. *Journal of Biological Chemistry*, 285, 8953-8966.
- ZHANG, R., LIU, Y., YANG, Z., LI, Y., RONG, X., WANG, L., GUO, C., LI, S., LIU, J. & LI, M. 2015. Construction of nanoparticles based on amphiphilic PEI-PA polymers for bortezomib and paclitaxel co-delivery. *RSC Advances*, 5, 15453-15460.

- ZHANG, S., WANG, X., SAGAWA, K. & MORRIS, M. E. 2005. Flavonoids chrysin and benzoflavone, potent breast cancer resistance protein inhibitors, have no significant effect on topotecan pharmacokinetics in rats or *mdr1a/1b* (-/-) mice. *Drug Metab Dispos*, 33, 341-8.
- ZHANG, S., YANG, X. & MORRIS, M. E. 2004. Flavonoids are inhibitors of breast cancer resistance protein (ABCG2)-mediated transport. *Mol Pharmacol*, 65, 1208-1216.
- ZHANG, Y., WANG, J., BAI, X., JIANG, T., ZHANG, Q. & WANG, S. 2012. Mesoporous silica nanoparticles for increasing the oral bioavailability and permeation of poorly water soluble drugs. *Mol Pharm*, 9, 505-13.
- ZHAO, X. S., LU, G. Q., WHITTAKER, A. K., MILLAR, G. J. & ZHU, H. Y. 1997. Comprehensive study of surface chemistry of MCM-41 using Si-29 CP/MAS NMR, FTIR, pyridine-TPD, and TGA. *Journal of Physical Chemistry B*, 101, 6525-6531.
- ZHAO, Y. Z., LI, X., LU, C. T., LIN, M., CHEN, L. J., XIANG, Q., ZHANG, M., JIN, R. R., JIANG, X., SHEN, X. T., LI, X. K. & CAI, J. 2013. Gelatin nanostructured lipid carriers-mediated intranasal delivery of basic fibroblast growth factor enhances functional recovery in hemiparkinsonian rats. *Nanomedicine*.
- ZHOU, M. & DONOVAN, M. D. 1996. Intranasal mucociliary clearance of putative bioadhesive polymer gels. *International Journal of Pharmaceutics*, 135, 115-125.
- ZHOU, Z. & CHU, B. 1988. Anomalous micellization behavior and composition heterogeneity of a triblock ABA copolymer of (A) ethylene oxide and (B) propylene oxide in aqueous solution. *Macromolecules*, 21, 2548-2554.
- ZLOKOVIC, B. V. 2008. The blood-brain barrier in health and chronic neurodegenerative disorders. *Neuron*, 57, 178-201.
- ZOU, P., HELSON, L., MAITRA, A., STERN, S. T. & MCNEIL, S. E. 2013. Polymeric Curcumin Nanoparticle Pharmacokinetics and Metabolism in Bile Duct Cannulated Rats. *Molecular Pharmaceutics*, 10, 1977-1987.

Appendix A

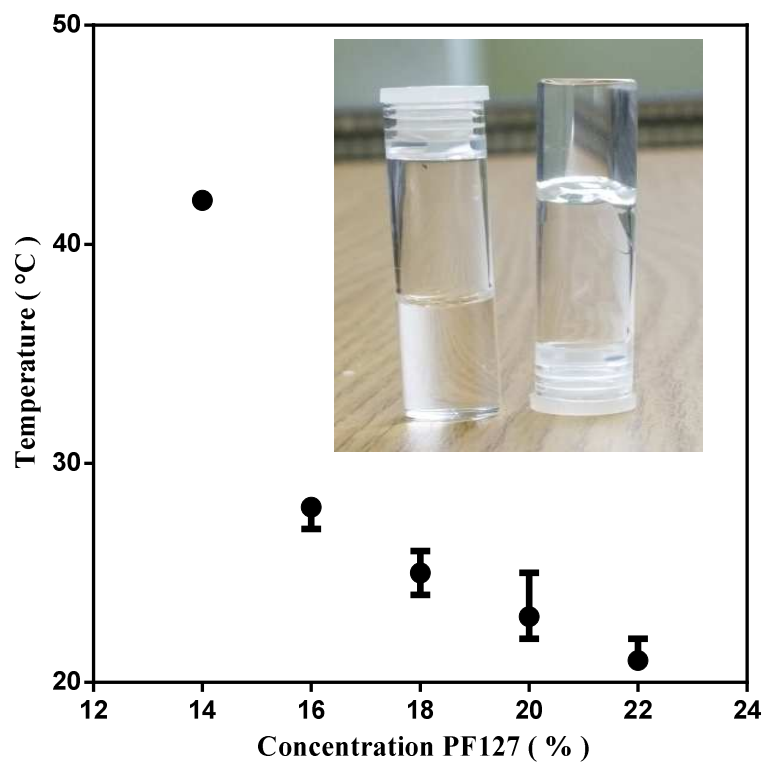


Figure : Effect of PF127 concentration on gelation temperature

1g of solution was weighed in a glass vial and placed in a dry block and heating initiated at 20 °C and increased by 1 °C after every 5 minutes of equilibration time. The $T_{\text{sol-gel}}$ point was defined as the temperature whereby the upper meniscus of the gel did not move upon tilting the vial by 90 °. $n=3$